THE JOINING OF HIGH TEMPERATURE ALLOYS

Thesis submitted in accordance with the requirements of the University of Liverpool for the degree of Doctor in Philosophy

by

Darren James Potter

September 2008

Materials Science, Department of Engineering

Abstract

The Joining of High Temperature Alloys

The reduction of the parasitic leakage of hot gas using static, dynamic and abradable seals is a critical area of gas turbine research. Improved sealing technology allows for greater control of secondary flow systems and so improves performance by increasing the efficiency and power output. The development of these seals does not afford a substantial additional cost to the manufacture of the gas turbine engine and so it is encouraged by the consumer. The concept of utilising honeycomb abradable seals to improve gas turbine engine performance has been under development for many years. Engine operation temperatures were previously restricted to 950°C by the formation of an unstable chromia scale on the substrate alloy. The introduction of nickel brazed FeCrAlY based alloys within the honeycomb seal has facilitated a safe increase in engine operation temperature to 1200°C. This is aided by the formation of a more stable α-alumina scale.

These FeCrAlY foils have been designed with a service lifetime of up to 24,000 hours. However, isothermal oxidation tests on these foils at 1100°C and 1200°C have shown them to fail within much earlier time scales. Degradation of the foils occurs just above the brazed region and causes the remaining honeycomb arrangement to fall out, rendering the seal useless.

Extensive analysis of the failure mechanism has been carried out. The honeycomb component has been tested as a whole and by separating the component into its three main constituents: FeCrAlY foils, braze and base plate. Experiments on the thin FeCrAlY alloy foils (100μm) found void formation beneath the outer protective alumina scale after times varying up to 700 hours at 1200°C. The life limiting factor of these alloys occurs once the substrate aluminium level drops below a critical value (≤0.5 wt%), and can no longer sustain the formation of a protective alumina scale. Oxidation beyond this point resulted in the initiation and growth of a Cr-rich oxide sub-layer. At 1200°C, the Cr-rich sub-scale layer was continuous with voids filled with chromia beneath the alumina scale.

Analysis of the FeCrAlY foils when brazed to a base plate also reveals void formation and filling after similar times at 1200°C. However, the addition of the brazing alloy changes the oxidation mechanism and the filling of the voids is thought to be responsible for the degradation of the FeCrAlY foils and the decreased lifetime of the honeycomb abradable seal.

Scanning Electron Microscopy and EDX analysis have been the main techniques used to evaluate the oxidation mechanisms of the abradable seal. Other analysis techniques used include: EBSD, XRD and optical microscopy.

Content **Page No.**

ACKNOWLEDGEMENTS

Firstly, I would like to thank my supervisor Professor Gordon J. Tatlock for his endless support, guidance and friendship throughout this work.

I would like to acknowledge Margaret Robinshaw and Dr Hameed Al-Badairy for who over the past four years have also provided endless support and guidance.

I would like to thank all the technical staff of the Materials Science Department and Department of Earth and Ocean Sciences, especially a Mr David Atkinson, Dr Peter Beehan, Professor David Prior, and Dr Nicholas Seaton.

I would also like to thank all of my close friends and work colleagues past and present, of whom there are too many to mention individually. All have made my time here very enjoyable.

I will always be eternally grateful to my parents (Marion and Richard) whose belief, love, and financial support, have made my many years of study possible. And to the rest of my family, especially Laura, who have always supported me.

The most important acknowledgement needs to go to my fiancée Joanne. Her love, belief, patience, and endless support over the past four years will always be remembered.

The financial support of the EPSRC is gratefully acknowledged.

1. Introduction: Background Information

The design of modern gas turbine engines is restricted by international legislation and is heavily influenced by end user demands. Both call for an increase in efficiency (i.e. limiting heat loss) and power output without increasing the specific fuel consumption. Researchers are continually developing methods aimed at improving engine components i.e. turbines and compressors, whilst minimising additional costs. Such developments are normally associated with the aeroengine industry. However, more recently, manufacturers of land based gas turbines have become interested in the development of materials employed in high temperature environments.

The reduction of parasitic leakage of hot gas through the hot gas path junctions using static, dynamic and abradable seals is a critical area of gas turbine research. Improved sealing technology allows for greater control of secondary flow systems and so improves performance by increasing the efficiency and power output. The development of these seals does not afford a substantial additional cost to the manufacturer of the gas turbine and so it is encouraged by the end user. The idea of using these seals to improve the engine performance has been under development for many years. Consequently there are numerous different seals commercially available.

Within the gas turbine, hot fluid will co-act with the rotor blades and transfer power to the shaft. If the leakage of this fluid between the tips of the rotor blades and the surrounding shroud structure is minimised, the efficiency is materially increased. The clearance between the blade tips and the shroud is made large enough in the cold state to allow for the thermal expansion of parts, machining tolerances, eccentricities and radial loosening in the bearings.

Aeroengines provide a clearance in the region of 1.5% of the blades' radial length at the beginning of service life. Throughout the lifetime, it is inevitable that the clearance will diminish. Even with advances in creep resistant superalloys [1], the rotor blades still elongate. Thermal expansion, extensive radial loading, and to an extent creep, are operational factors which contribute to the lengthening of the blades. This can be detrimental to the clearance of the blade tips and shroud. Thus, with turbines, an abradable shroud around the rotor blade tip is desirable so that the lowest possible cold clearance can be provided. This means that if the blade tips rub against the shroud during operation, the damage will not be catastrophic. If there is operational damage to the seal, the leakage of fluid around the blade tips must be prevented to maintain the engine's performance. Previous work suggests that an increase of 0.1mm in the clearance of the blade tip and shroud of a turbine increases the specific fuel consumption by 0.5% [2]. The abradable seal must therefore adjust the level of clearance after sustaining significant damage.

Abradable seals are used to decrease the operating blade tip clearances. Without the presence of these seals, the shrouds must provide enough clearance to prevent significant contact during operation. Abradable seals allow the cold clearances to be reduced with the assurance that, if contact occurs during operation, the sacrificial part will be the abradable material and not the blade tips [3]. Abradable materials are useful as seals as they allow for further reduction of the blade tip clearances during operation. This reduction in the clearance is caused by the radial expansion of the blades at high temperatures and high operating speeds. The rotor blades also expand to the extent that they exceed cold built clearances, at which point they come into contact with abradable seals. This causes the shroud material to wear away. A self-produced clearance between the blade tip and the seal is then formed, allowing for uninterrupted operation of the turbine blades. This does not result in the loss of efficiency. This wearing of the abradable seal can continue until the radial

expansion of the blades exceeds a specified amount. When this level is exceeded the efficiency of the blades will be lost as hot gas will flow over the blade tips, the geometries of which will all be the same until the eventual replacement of the rotor blades.

Abradable seals are available to gas turbine manufacturers in a variety of forms. These can be classified by their method of application, or according to their temperature capabilities. Polymer based castings are only used in low temperature environments due to temperature limiting factors of polymers i.e. usage in low power compressors. The application of thermal sprayed coatings is dependent on the coating composition as well as its ability to withstand high temperature (760-1150°C) and high pressure working environments found in mid range turbines. The application of fibre/porous fibre metals is similar to thermal sprayed coatings. Their application is, however, limited due to the collapse of the structure caused by the impact of the rotor blades. Brazing/diffusion bonded honeycomb structures are currently used in high temperature (~950°C) turbines.

The mechanism of cutting or wearing the abradable material is dependent on the structural geometries of the component and the relative speeds of the rotor blade tips. Abradable components are designed with their low strength in mind, thus preventing damage to the rotor blade tips. Such design constraints leaves them susceptible to gas and solid particle erosion. The temperature of their current working environment (~950°C) also leaves them susceptible to high temperature oxidation. The design of the abradable seal must therefore account for the working conditions. Factors to be considered in the design of the honeycomb seal are as follows:

- Tensile strength – needs to withstand high forces but wear upon impact of the blade.

- Thermal expansion – needs a low coefficient of thermal expansion (CTE) to maintain clearance.
- Creep resistance – avoid shape change to the seal to maintain its high performance.
- Fatigue resistance – the cyclic nature of the component necessitates a high endurance limit.
- Density/geometry – the material must be light enough so as not to add excess weight to the gas turbine engine.
- Formability – the honeycomb cells must be corrugated.
- Joinability – the strong bond that joins the components must withstand the high operating temperatures.

Abradable seals which display some or all the mechanical properties listed above are readily available. However, the need for greater efficiency of the gas turbine engine necessitates higher operation temperatures. The end users demand operating temperatures in the region of 1100°C, using materials that provides satisfactory performance for at least 24,000 hours. Operation above the normal 950°C results in greater deformation of the seal during rubs as the honeycomb material softens. A reconsideration of the current honeycomb seal is therefore essential. The honeycomb seal is constructed from foils of corrugated, oxidation resistant material. The foils are spot welded together and then brazed to a backing plate or some other hot gas component (Figure 3.1). The high temperature degradation of the foil material is a critical factor in determining the lifetime of the abradable seal, and the high temperature degradation of new foil materials forms the basis of this thesis.

Currently, turbine shroud seals operate at temperatures up to 950°C. This is possible because the shroud alloy contains chromium, which forms a protective chromium oxide scale. Unfortunately increasing the operating temperature to 1100°C means that chromia forming alloys are no longer useful, due to the

volatility of the chromia scales above 950°C. Therefore alumina-forming alloys are necessary. This oxide is stable at temperatures in the region of 1100°C. Alloy candidates for such honeycomb seals include FeCrAl and NiCrAl based materials.

2. Literature Review

2.1 Oxidation Theory

The exposure of a metal or alloy to an oxygen containing environment (such as air) can cause a chemical reaction. This is known as an oxidation reaction and can occur over a range of atmospheres and temperatures.

The oxidation process is a reaction where a metal and oxygen chemically combine and result in the formation of a metal oxide. Control of such a chemical reaction is governed by kinetics and the laws of thermodynamics.

The simplest metallic oxidation reaction can be seen in Equation 2-1.

$$M(s) + \frac{1}{2}O_2(g) = MO(s) \qquad (2\text{-}1)$$

The term "oxidation" is also used if a metal atom combines with any atom or molecule and loses electrons, or if a metal goes from one valence state to a higher one, i.e. loses electrons.

2.2 Basic Thermodynamic Considerations

The occurrence of an oxidation reaction is dependent upon the second law of thermodynamics. The second law is written in terms of Gibbs free energy (G′) of a system, Equation 2-2,

$$G' = H' - T\,S' \qquad (2\text{-}2)$$

where H′ is the enthalpy and S′ is the entropy of the system, and T is the absolute temperature. Since high temperature oxidation reactions usually occur

in an environment of constant temperature and pressure, the following values for changes in free energy (ΔG) will hold true: if $\Delta G' < 0$, a spontaneous reaction is expected; if $\Delta G' = 0$, the system is in an equilibrium condition; and if $\Delta G' > 0$, thermodynamically the reaction is impossible.

Equation 2-3 is a typical example of how to consider a chemical reaction.

$$wW + xX = yY + zZ \tag{2-3}$$

where w, x, y, and z, are the number of moles of the species W, X, Y, and Z respectively.

The calculation for the change in Gibbs free energy comes from the following Equation 2-4.

$$\Delta G' = \Delta G° + RT\, ln\left(\frac{a_Y^y . a_Z^z}{a_W^w . a_X^x}\right) \tag{2-4}$$

where ΔG° is the free-energy change when all species are present in their standard states; R is the gas constant; and a is the thermodynamic activity. The thermodynamic activity (e.g. $a_W{}^w$) describes the deviation from the standard state and may be expressed for a given species z as in Equation 2-5,

$$a_z = \frac{p_z}{p_z^\circ} \tag{2-5}$$

Here p_z is either the vapour pressure over a condensed species or the partial pressure of a gaseous species and p_z° is the same quantity corresponding to the standard state of z. Expressing a_z by Equation 2-5 requires the reasonable approximation of ideal gas behaviour at the high temperatures and relatively low pressures usually encountered [4]. The standard free-energy change is expressed for a reaction such as Equation 2-3 by 2-6,

$$\Delta G° = y\Delta G_Y^\circ + z\Delta G_Z^\circ - w\Delta G_W^\circ - x\Delta G_X^\circ \qquad (2\text{-}6)$$

where ΔG_Y°, etc., are standard molar free energies.

For special cases of equilibrium ($\Delta G' = 0$), Equation 2-4 reduces to Equation 2-7.

$$\Delta G° = -RT\, ln\left(\frac{a_Y^y . a_Z^z}{a_W^w . a_X^x}\right)_{eq} \qquad (2\text{-}7)$$

If the reaction is in equilibrium, the above equation is sometimes written using the equilibrium constant (K).

$$\Delta G° = -RT \ln K \qquad (2\text{-}8)$$

2.3 Mechanisms of Oxidation

The reaction between a bare metal substrate and oxygen at the metal-gas interface will form a metal oxide. This is illustrated in equation 2-1. A metal oxide reaction product, if formed around the perimeter of the metal, will separate the two reactant species. This is illustrated in figure 2.1. In order for the reaction to continue, transport of metal, oxygen or both species through the scale must occur. The metal oxide may then grow from either the metal oxide/gas interface, the metal/metal oxide interface, or less commonly reported, within the oxide scale itself. The terms outwardly, and inwardly growing oxides are commonly used and arise from the movement of the dominant diffusing reactant.

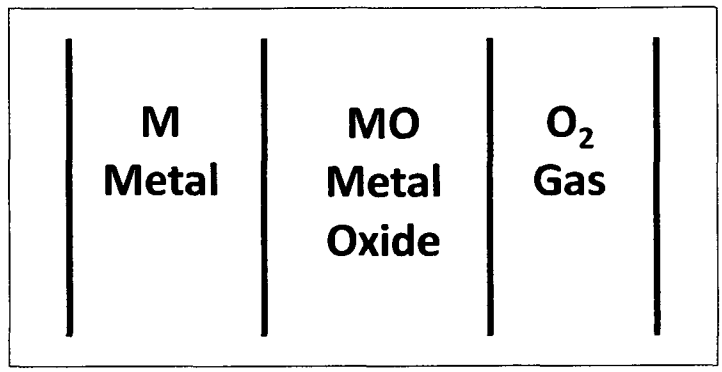

Figure 2.1: Schematic representation of a formed oxide separating the two reactant species

The mechanism of further oxide formation is seen to be an integral part of a complete understanding of high temperature oxidation. For oxides which form at either metal/oxide and oxide/gas interfaces, the rate of the chemical reactions is time dependent and is rapid in the initial stages and decreases as the oxide thickness is increased.

2.4 Diffusion in Oxides

The definition of diffusion is the movement of a species (atoms for example) from a higher concentration to a lower concentration within a material. In order for a diffusing atom to reach its new site, energy must be supplied so that the atom will overcome an energy barrier. This is known as the activation energy (Q). Heating a system can supply an atom with the energy needed to exceed this barrier. The flux of atoms can be calculated by Fick's first law (Equation 2-9):

$$J = -D\frac{dC}{dx} \tag{2-9}$$

where:

J = defined as the mass or, equivalently, the number of atoms/moles diffusing through and perpendicular to a unit cross-sectional area of solid per unit time (moles/m^2.s);

$\frac{dC}{dx}$ = the concentration gradient (moles/m^4); and

D = the diffusion coefficient (m^2/s).

The diffusion coefficient for a reaction is temperature dependent and can be calculated using Equation 2-10.

$$D = D_0 . \exp\left(-\frac{Q}{R.T}\right) \tag{2-10}$$

where:

D_0 = the maximum diffusion coefficient (at infinite temperature);

Q = the activation energy (J/mole);

R = the gas constant (8.31J/mole.K); and

T = the absolute temperature (K)

There are three different types of diffusion in an alloy system; bulk diffusion, grain boundary diffusion, and surface diffusion. All three are thermally promoted processes with rates increasing with increasing temperature. Bulk diffusion occurs when atoms from all parts of the bulk alloy begin to move. Bulk diffusion is more difficult to initiate than other types of diffusion as atoms are closely packed together within alloy grains. Grain boundary diffusion is the movement of the diffusing species along grain boundaries. Grain boundaries are less closely packed than alloy grains and therefore offer less resistance to diffusion. Surface diffusion has still lower activation energy. This process can be generally thought of in terms of particles jumping between adjacent absorption sites on a surface.

Diffusion processes in oxides and oxygen diffusion vary from one oxide to another. Many authors have reported on the rates of oxygen diffusion in many different oxides [5, 6]. High temperature oxidation and tracer experiments using the stable O^{18} isotope are common in these studies. Oxides are ionic and crystalline and have varying degrees of stoichiometry. They can also vary in composition. Diffusion rates through an oxide are significantly affected by the stoichiometry and impurity content of the oxide. The following section will highlight some of these oxide defects and how they affect the development of the scale.

2.5 Defects in Oxides (Transport Mechanisms)

The transport of ions through ionic solids may be explained by several mechanisms. These can be divided into mechanisms belonging to stoichiometric oxides and those belonging to non-stoichiometric oxides.

2.5.1 Stoichiometric Oxides

Oxides which fall into this category show no deviation from stoichiometry, where the metal to non-metal ratio does not deviate from that specified in the chemical formula. The main two predominant defects in stoichiometric oxides are known as Schottky and Frenkel defects.

2.5.1.1 Schottky Defects

Schottky defects allow ionic mobility because of ionic vacancies on the lattice. Electroneutrality is maintained by the equal concentration/number of vacant sites upon both cationic and anionic sub-lattices. It is expected that both anions and cations will be mobile as vacancies exist on both sub-lattices.

2.5.1.2 Frenkel Defects

Defects of this sort are characterised by the existence of a vacancy in the cation lattice. The anion lattice is assumed perfect and electroneutrality of the system is preserved by the existence of an interstitial cation. Therefore, the equivalent number of interstitial cations must exist for the same number of vacant cation lattice sites. This class of defect assumes that only the cations are mobile, via the movement of both vacancies and interstitials.

Stoichiometric defects in an oxide would not provide a significant mechanism to explain material transport during oxidation reactions. Neither defect allows a method by which electrons may migrate.

The movement of atoms or ions and electrons must be considered for an oxidation reaction to occur. There are two main classifications of oxide scale growth. The first being the growth of new oxide at the oxide/gas interface, this requires cation migration through the oxide. The second being oxide growth at the metal/oxide interface, this requires anion migration through the scale.

Defects in oxides which are used to explain the transport of ions and electrons are described as non-stoichiometric.

2.5.2 Non-Stoichiometric Oxides

The term non-stoichiometric oxide implies that the ratio of metal to non-metal atoms is not the same as that of the given chemical formula. However, the compound still remains electrically neutral. Defects in this class of oxides are usually confined to either the metal or non-metal lattices. There are two types of non-stoichiometric oxides and are referred to as semi-conductors. They are known as n-type or p-type semi-conductors.

2.5.2.1 Negative (n-type) Semiconductors

The term negative or the more commonly used n-type semiconductor is derived from the fact that this classification of oxide transports its electrical charge mainly by electrons. This type of oxide has either an excess of metal or a deficit of non-metal.

1. Metal excess: The additional metal ions on the cation lattice are positioned as interstitials. These have an equal number of electrons existing in the conduction band. The formula may be written as $M_{1+x}O$.

2. Oxygen deficit: In these oxides, oxygen vacancies exist within the anion lattice. These vacancies form during the discharge and subsequent evaporation of oxygen ions along with the insertion of electrons into the conduction band [4]. The formula may be written as MO_{1-x}.

2.5.2.2 Positive (p-type) Semiconductors

This classification of oxide transports its electrical charge mainly by positive charge carriers. This type of oxide has either a deficit of metal or an excess of non-metal.

1. Metal deficit: With this class of oxide, vacancies are formed on the cation lattice. Subsequent electron holes are then formed, giving rise to conduction. The formation of electron holes lies in the ability of most metals, but especially transition metals, to exist in several valence states. The formula may be written as $M_{1-x}O$.

2. Excess of non-metal: In this case oxygen ions exist as interstitials. This type of oxide defect is not common and very few oxides belong to this classification. One example is CuO at 1000°C [4]. The formula may be written as MO_{1+x}.

2.6 Next Generation Gas Turbine Abradable Seals

Abradable seals are becoming ever popular in the gas turbine market. Increasing fuel prices necessitate improved efficiencies from such engines [7-9]. Honeycomb abradable seals are excellent at reducing the parasitic leakage of hot gas through hot gas path junctions. They are a relatively simple sealing method, and offer reduced clearances between rotor blades and shroud (increasing efficiency) at low costs and with minor engineering implications [9]. Efficiency is also increased during the service life of the component. Efficiency is increased by the radial expansion of the rotor blades and the reduction of cold build clearances. Blades will eventually exceed cold built clearances, at which time they will come into contact with the abradable seals. Material is then removed from the seal leaving a groove [2]. Any parasitic leakage paths are now closed ensuring that all hot gas flows over the turbine blades. This is represented schematically in figure 2.2.

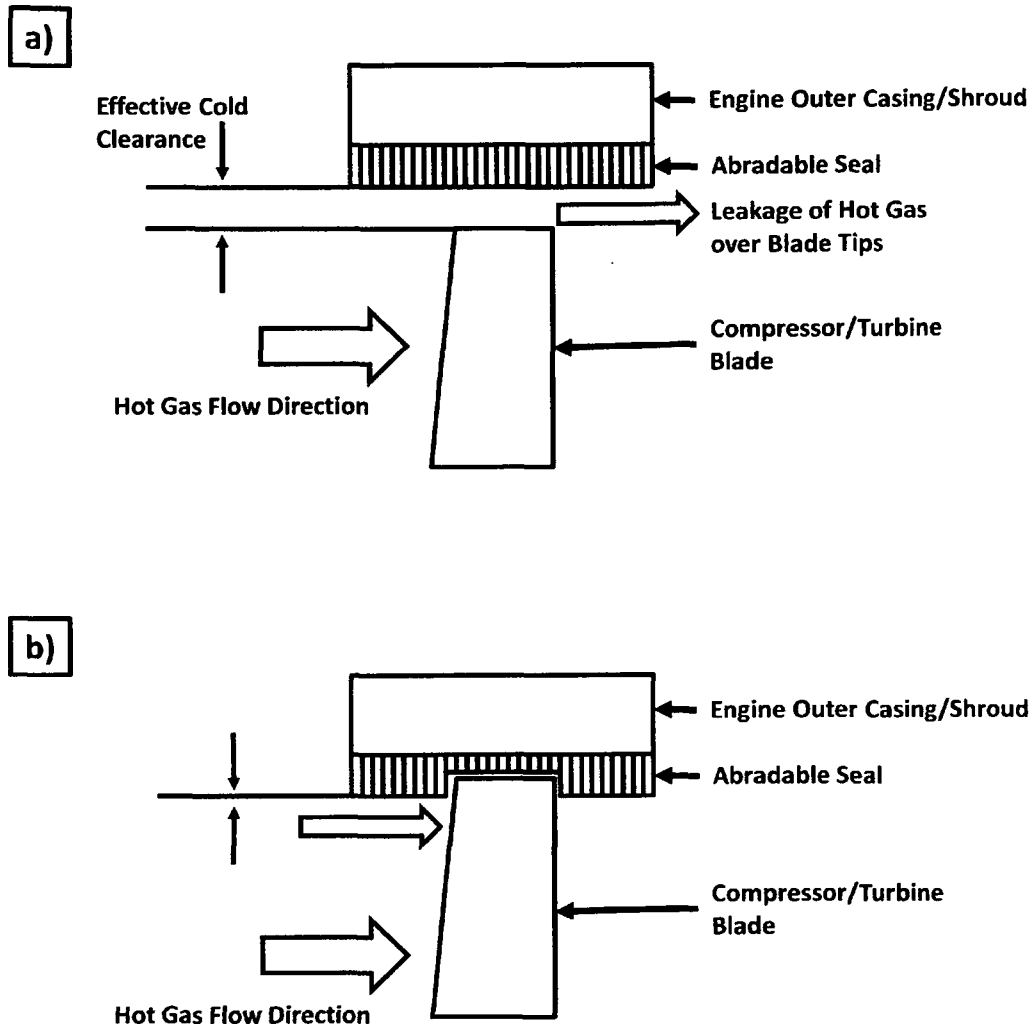

Figure 2.2: Schematic representation of an abradable seal reducing blade tip clearances. a) Represents the cold built clearances between compressor/turbine blades and an abradable seal at the beginning of service life, and b) represents the wear of the seal during service life and the closure of cold built clearances

2.7 Abradable Seal Positioning and Gas Turbine Layout

Figure 2.3 indicates the locations of sealing technologies which are currently incorporated into gas turbine engines. Honeycomb abradable seals are currently used in stages 2 and 3 of the turbine section of E-class gas turbines (Figure 2.4).

High temperature oxidation is not the only design parameter of honeycomb abradable seals. Impact by rotating blade tips during operation causes the seal to deform. Cutting and wearing of abradable seals is of great interest to aerospace manufacturers and has been investigated by specially designed test rigs [8]. This is of such importance that since 1996, many of new E-class gas turbine engines have been designed with turbine blades which incorporate cutter teeth to reduce turbine blade damage during rubs [1]. However, only the high temperature oxidation of new honeycomb abradable seals will be reported upon in this thesis. The oxidation of the newly developed seals is thought to be more critical than the occurrence of turbine blade impacts.

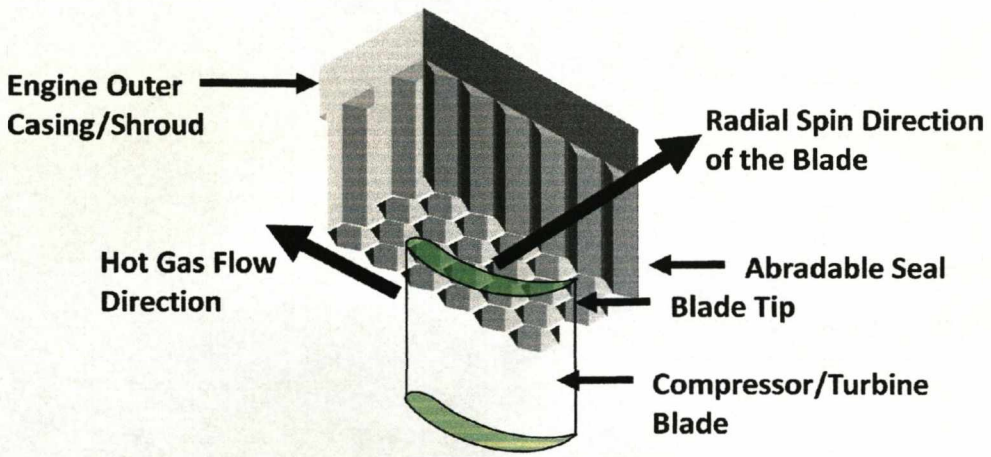

Figure 2.3: A 3-D representation of a honeycomb abradable seal placement above a compressor/turbine blade

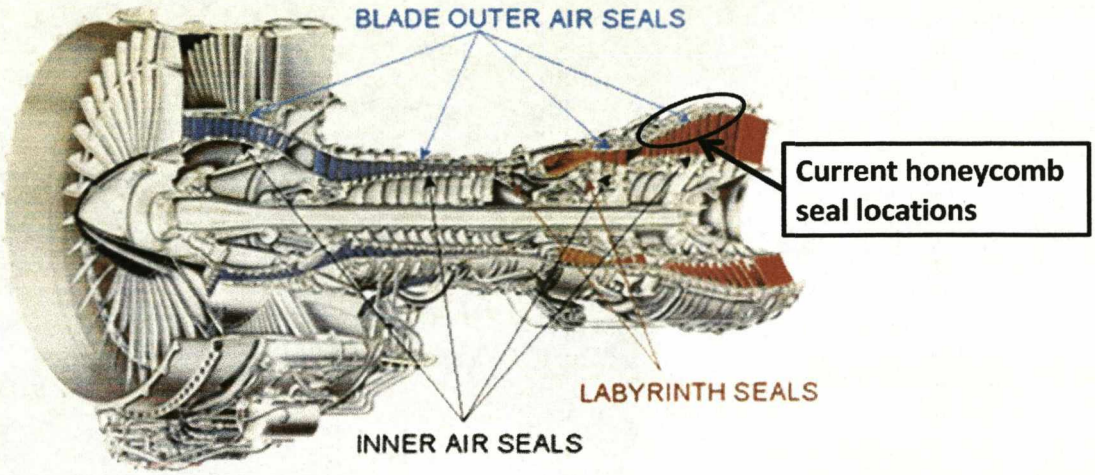

Figure 2.4: Locations of sealing technologies currently incorporated into E-class gas turbine engines.

The construction of a honeycomb abradable seal, as described in Section 3.2, requires brazing. Many in-house investigations have been conducted, and careful attention to the amount and placement of brazing filler metal, brazing time and temperature have been made.

2.8 Joining Problems Associated with Honeycomb Abradable Seals

One issue with honeycomb brazing is the quality and amount of braze alloy used. Nickel brazes are used for honeycomb abradable seals because of their high temperature corrosion resistance and high joint strength. The compositions of such brazes (see Section 2.19) can cause the formation of borides, silicides, and phosphides within the brazed joints. These products have a high hardness compared to the rest of the construction and can cause substantial damage to gas turbine blade tips if contact occurs. It is therefore crucial that braze filler alloys

do not fill the honeycomb cell nodes to a level greater than 25% of corrugated foil height.

Excess braze filler alloy can easily erode the thin walls of the honeycomb foils. This is due to the aggressive nature of the brazing alloy [10] and often occurs when dissimilar metals are involved. This necessitates careful monitoring of the brazing procedure.

The main issue with the brazing of honeycomb abradable seals is the seal operating temperature. Brazing, as will be discussed, is a diffusion joining process. As the desired in-service operating temperature is >1050°C, diffusion of braze alloy constituents will continue over the in-service lifetime until an equilibrium microstructure is reached [11]. Little work has been published on brazing alloy constituents and how they can affect a component's oxidation resistance. Such braze constituents, e.g. silicon, are commonly reported to improve an alloy's oxidation resistance when incorporated into alloy systems [12-16]. Some authors disagree and have published some detrimental effects of silicon additions [17].

2.9 FeCrAl Alloys - Ferritic Stainless Steels

FeCrAl alloys are aluminium containing ferritic chromium steels. They possess good high temperature oxidation resistance and strength. These are important factors in their application. The discovery of such alloys arises from work on austenitic stainless steels (FeCrNi). These alloys contain a large amount of chromium to provide oxidation and corrosion resistance over a range of temperatures by producing a passivating chromia (Cr_2O_3) film. The nickel content in the alloy stabilises the austenitic phase of the steel, and therefore prevents any volume change of the component on cooling. The addition of aluminium to these alloys (FeCrNiAl) provides further oxidation and corrosion

resistance on depletion of the chromium from the bulk material. These alloys, however, prove to have no mechanism of strengthening and embrittle at elevated temperatures. This problem led to the development of FeCrAl alloys which have excellent oxidation resistance. The oxidation resistance comes from a protective chromia or alumina (Al_2O_3) oxide scale, depending on the operating temperature. Below 950°C the bulk alloy uses passivating mixed oxides of mainly alumina and chromia. However, above 950°C, the alloy relies on its aluminium content to provide a protective alumina scale. These FeCrAl alloys also rely on much smaller alloying additions to improve a variety of properties:

- Additions of titanium (Ti), zirconium (Zr), and niobium (Nb) – these stabilise the ferritic lattice structure and provide toughness at high temperatures.
- Additions of lanthium (La), cerium (Ce), hafnium (Hf), yttrium (Y), and zirconium (Zr) – tie up any sulphur present in the alloy and provide improvements in oxide scale adherence at high temperatures.

Commercially, the chemical composition of these alloys varies according to their intended application. Additions of titanium, niobium and zirconium may produce stresses in the passive oxide film at high temperatures. This is due to their high affinities for oxygen, which can lead to the spallation of more stable oxide layers by the formation of oxide nodules or ridges. For this reason, these alloying elements are only added in small amounts. For operation above 950°C these alloys rely heavily on the formation of a protective alumina scale. Total coverage of the alloy by this scale ensures a very low and stable oxide growth rate. At any time during growth, the alumina scale can be damaged or spall due to a build up of excessive stresses in the oxide. If this happens, as long as there is a sufficient amount of aluminium in the bulk alloy, the oxide will self-repair. If, however, there ever reaches a time where the aluminium content of the bulk alloy drops below a critical level, this healing process will stop and less stable

oxides will begin to form. This process is called breakaway oxidation [18-20]. Breakaway oxidation is defined in Section 2.13.

Breakaway oxidation occurs in FeCrAl alloys when chromia and iron oxides form at an excessive rate. This depletes the vital elements from the bulk material and eventually leads to failure of the structure. This becomes the critical factor in determining the lifetime of the component. An obvious way to further increase the lifetime would be to increase the aluminium content of the alloy. Increasing the aluminium content above 8 wt.% (weight percent), however, causes embrittlement to the alloy. This is why most commercial alloys contain ~5-6 wt.% aluminium. Another important factor in their application as honeycomb abradable seals is the geometry of the foils. Thin FeCrAl alloy foils (70μm) form the honeycomb cell walls of the test samples. This foil geometry dictates a small reservoir of aluminium in the alloy and can be consumed quickly at high temperature for protective oxide formation. Other mechanisms of delaying breakaway oxidation have been discovered through the addition of rare earth metals such as yttrium (Y) and hafnium (Hf) (see Section 2.12).

2.10 NiCrAl Alloys – Haynes 214

Nickel based alloys are excellent candidates for high temperature applications. Such alloys have been designed to provide good oxidation resistance for a wrought austenitic material whilst still allowing for conventional joining and forming of the material. Once again these alloys have been developed from a very simple model alloy known as Nichrome. These nickel-chromium (Ni-Cr) alloys are commonly employed in heating elements due to their high resistivity, excellent oxidation resistance, and high melting temperature. They are, however, restricted to operating temperatures not exceeding 950°C and are found to have relatively low strength at elevated temperatures [21, 22].

Developments of these basic nickel-chromium alloys have produced extremely strong and oxidation resistant materials for high temperature usage. Such alloys are known as "superalloys" and are employed as turbine blades for example, because of their creep resistance. The nickel based alloy used for the honeycomb shroud/base plate is not developed to the same complexity of these nickel superalloys, but the principles of their development and high temperature attributes are the same.

Initial developments showed that the additions of aluminium and titanium formed intermetallic particles with the nickel. Aluminium additions were found to produce two types of intermetallic precipitates: γ' (Ni_3Al) and β (NiAl). The γ' precipitates raise the high temperature strength of the material due to the misfit and strain they inflict upon the microstructure. The high level of chromium in the alloy lowers the melting temperature of the γ' precipitates and restricts the operating temperature of the alloy. Low levels of chromium are also found to decrease strength and corrosion resistance at high temperatures.

Fabrication of the Haynes 214 alloy, used in the base plate of the abradable seals in this work, does not use precipitation strengthening to provide its high temperature properties, but it is susceptible to age hardening. If the alloy is exposed to intermediate temperatures of 595-925°C, second phase γ' precipitates form. This can be disastrous, as the alloy will then be prone to strain-age cracking. Also, if solution treated at less than 1095°C, the alloy composition will result in the formation of carbides along grain boundaries. This causes embrittlement to the alloy matrix. The resulting conditions designate the optimal heat treatment for this alloy: solution treat at 1095°C followed by rapid cooling (quenching) to room temperature to achieve optimum properties. It is claimed that Haynes 214 alloy can be exposed for short time periods at 1315°C with some reduction in strength. These types of alloys have very good attributes

at high temperatures. However further developments are still ongoing. The composition of the NiCrAl based alloys has been optimised for the best mechanical properties. This suggests the need for other mechanisms for further improving these alloys and has lead to the introduction of diffusion and thermal barrier coatings on surfaces, along with optimum additions of reactive elements to the alloy. These add-ons allow increased high temperature use, without necessitating further developments to the alloy microstructure.

2.11 Oxidation Background of FeCrAl Alloys

Interest in FeCrAl alloys derives from their outstanding oxidation performance. Their ability to form a protective alumina scale makes FeCrAl alloys excellent candidates to replace ceramic substrates as the substrates for honeycomb-style catalytic converters where operating temperatures can exceed 1000°C. FeCrAl alloys can be produced by many different routes, such as via powder metallurgy, mechanically alloying and conventional melting.

The excellent high temperature performance of FeCrAl thin foils makes them excellent candidates to replace not only ceramic materials as substrates for automotive catalytic converters but also for use as honeycomb abradable seals [23]. The typical thickness of such foils is between 50μm and 100μm. Such foils only have a small reservoir of aluminium, and therefore alumina scales grown on such substrates do not grow to a thickness that will induce spallation.

The amount of chromium in FeCrAl alloys (~20 wt.%) is necessary to stabilise the ferrite phase at temperatures >1400°C. The difference in metallic crystal structure between ferrite and austenite is key to the rates of diffusion within the alloy substrate. The body centre cubic structures (BCC) of ferrite increase the rate of diffusion of elements with high oxygen affinities, whereas the more densely packed face centre cubic (FCC) structure of the austenite phase reduces

the rate of diffusion to the alloy-scale interface. Chromium may deplete locally during breakaway oxidation.

Oxidation of ternary alloy systems is found to be heavily influenced by the element with the second strongest affinity to oxygen i.e. chromium [24]. The chromium additions to a FeCrAl alloy system are very important. Chromium assists in the formation of an external oxide and stops any inward movement of oxygen, and thus the formation of internal oxides. The establishment of this passivating external oxide reduces the oxygen partial pressure below the surface scale to a level where only the element with the highest oxygen affinity can react.

2.12 Adherence of Alumina Oxide Scales

Many authors have studied the development, growth rate and adherence of alumina scales upon FeCrAl alloys together with the effects of impurity elements such as S, P, C, etc [25-27]. Other papers commonly report upon the favourable minor additions of reactive elements, such as Y, Hf, Zr, La, etc. as these are crucial to the alumina scale adherence. Extensive research regarding reactive element effects has been ongoing for more than 30 years and many of the mechanisms are still under debate [28-30]. In 2005, a European funded project (SMILER) performed some extensive research on combining the effects of incorporating two or more reactive elements into a FeCrAl alloy system. The optimisation of reactive element additions has been found to significantly extend the lifetime of FeCrAl alloys [30-32]. The project also concentrated on the common problems of incorporating several impurities, namely C and Si, into the alloy system and how these affect alumina scale adherence.

FeCrAl alloys containing minor additions of reactive elements present excellent resistance to oxide scale spallation. Stott et al. published the results of

lanthanum and molybdenum alloying additions in FeCrAl alloy systems [33]. This resulted in increased times to the onset of breakaway oxidation. Improvements in oxide scale adherence were recorded. During their testing period, no scale spallation was detected. Their weight gain tests actually presented a weight loss without any apparent scale spallation. It was assumed that decreases in weight were associated with loss of material as a vapour phase.

One life limiting factor of thin FeCrAl foils is when the aluminium reservoir within the alloy reaches a critical level [17] and ceases to heal the protective alumina scale. Time at high temperatures is decreased significantly if the Al_2O_3 scale is poorly adhered and spalls extensively in service. Numerous publications discuss the benefits of reactive element additions, such as lanthanum and yttrium [19, 34, 35] on improving scale adherence. They commonly report of the improved integrity and spallation resistance of Al_2O_3 scales.

Alumina scale adherence is affected by carbon-content. FeCrAl alloys with increased levels of carbon exhibit high levels of alumina scale spallation, more extensive formation of local oxide protrusions and a higher critical aluminium content at which the alloy ceases protective oxide formation. Significant amounts of scale spallation are exhibited on cooling of such alloy systems [28-30].

The undesirable attributes of increased carbon levels in FeCrAl alloys can be related to the formation of Cr-rich carbides along grain boundaries and at the scale/metal interface. Kochubey et al. performed tests on a model alloy with high carbon content and suggested the amount of carbide formation at the scale/metal was influenced by the sample cooling rate [36, 37].

Minor alloying additions of Zr are reported to counteract the undesirable effects of carbon impurities. This reactive element addition is reported to promote the formation of more stable carbides. Alumina scales can be modified by additions of Zr. It is incorporated into the alumina scale and effectively reduces the oxide grain size. This modification of the oxide scale structure leads to an enhanced oxidation resistance and presents excellent resistance against spallation under thermal cycling conditions [31, 33].

Terminologies such as convolution [38-41], buckling [42], rumpling and wrinkling [43] are often associated with alumina scales formed on FeCrAl alloys. The addition of small amounts of reactive elements helps to promote a flat and well adhered alumina scale and effectively eliminate convolution.

Oxide scale convolution is caused by stress generation and can cause further stress generation due to oxide scale growth. Growing oxides are subject to compressive or tensile loading, depending upon the position of the scale on the undulating interface. The oxide scale at the top of the undulating wave is subjected to tensile stress, whilst scale compression is experienced within the "troughs" of the waves. This tensile stress can be a significant driving force for internal pore formation, scale delamination and crack propagation and scale spallation during cooling [39, 44, 45].

Several authors have given explanations for the formation of convoluted oxide scales [32, 40, 46]. A general consensus is that oxide growth stresses induce plastic deformation of the substrate and cause the formation of a wavy scale-substrate interface [38]. Wood et al. originally proposed that growth stress may occur due to the lateral growth of the alumina scale [46]. It is widely accepted that α-alumina scale growth is predominantly by the inward movement of oxygen; however, it is also accepted that some aluminium does diffuse outwardly through the scale and may oxidise within the scale or at the scale-gas

interface. Although the Al diffusion is a minor component, its transport can cause significant growth stress [43, 47, 48]. Such high compressive stresses applied to scales of only a few microns in thickness cause undulation. Similar observations are commonly found in the semi-conductor industry during thin film depositions at elevated temperatures [49-51].

2.13 Breakaway Oxidation of Alumina Forming Alloys

Breakaway oxidation is simply defined as the formation of a non-protective oxide scale upon a system which has ceased to form its protective oxide. In an FeCrAl alloy system, this is defined by the formation of iron/chromium oxide, when the aluminium level in the alloy substrate drops below a critical level necessary to sustain a protective alumina scale. Extensive research on the prediction of breakaway oxidation for FeCrAl alloys have been carried out [52-56].

Breakaway oxidation for FeCrAl alloys is defined as the end of protective oxide formation and the rapid formation of unstable oxides at high temperatures. These are essentially iron-rich oxides and will consume the remaining alloy substrate over a relatively short period. Any chromium remaining in the alloy once breakaway oxidation commences will form chromium-rich internal oxide precipitates. These can offer no protection to the remaining alloy substrate.

Once initiated, breakaway oxidation will rapidly consume a FeCrAl substrate. During breakaway oxidation many authors report the formation of relatively large voids in the residual substrate, along with the significant spallation of the protective oxide scale [34].

The two mechanisms for failure by breakaway oxidation are classed as intrinsic chemical failure (InCF) and mechanically induced chemical failure (MICF) [56-

60]. Thin foils are associated with intrinsic chemical failure. Commonly, the oxide on thin foil samples does not tend to spall. Here, oxide growth continues until all the aluminium is consumed down to a critical level where chromia formation starts [23, 34, 61].

With reference to FeCrAl foils, Mechanically Induced Chemical Failure (MICF) is a term used when the protective alumina scale cracks or spalls, and breakaway oxidation is initiated because the alloy is unable to reheal the protective scale. Intrinsic Chemical Failure (InCF) is regarded as true chemical failure as the substrate is exhausted of all protective oxide forming constituents.

Chemical failure results from the depletion of aluminium in an alloy substrate below a critical value. Approximately ≤ 0.5 wt.% for thin foil samples. The critical parameters involved with the chemical failure of alumina are:

a) the available aluminium content of the alloy, and
b) the relaxation of oxidation induced stress by alloy substrate creep deformation

Thin foil samples are defined as having thicknesses less than 0.2mm [20]. For thicker samples, as well as the consumption of aluminium from the substrate, oxide scale thickness becomes a critical parameter. If the scale exceeds a critical thickness then it may spall, promoting further aluminium exhaustion from the substrate. The thickness of an alloy dictates it's time to breakaway oxidation [56, 57].

Failure of alumina scales formed on thick FeCrAl-RE alloys can be attributed to the time when the growing alumina scales pass a critical thickness. Stresses built up in the scale cause it to spall, although this may be decelerated by stress relief emanating from substrate plastic deformation [58, 60].

There are three main factors which influence the breakaway oxidation of alumina forming FeCrAl-RE alloys:

a) alloy Al concentration,
b) temperature, and
c) sample geometry.

A common observation is that upon rectangular specimens, breakaway oxidation will often start at the corners [35].

During breakaway oxidation, iron-rich oxide scales are established, whilst the substrate is depleted of chromium. This consumption of chromium can cause the austenite phase of the stainless steel to stabilise. This retards diffusion of chromium to the alloy's surface and causes chromia to form as an internal oxide precipitate. Chromia would otherwise form as an external layer that would offer slightly more protection to the alloy substrate for a short time period.

The rate of alloy wastage by breakaway oxidation has been found to be suppressed by the additions of molybdenum. This addition is found to stabilise the ferrite phase near the alloy-scale interface. This maintains a high rate of diffusion of chromium to the interface and facilitates the establishment of a healing and partially protective chromium rich oxide layer at the base of the breakaway oxide scale [34]. For FeCrAl alloy systems without such additions, the onset of breakaway oxidation can cause the depletion of chromium near the alloy-scale interface. At such high temperatures (>1000°C), this allows the austenite phase to stabilise. Diffusion of chromium through austenite is very slow, and chromia formation is now observed as internal oxide precipitates rather than as a continuous external layer. The chromium diffusion in ferritic steels is about 2 orders of magnitude faster than in austenitic steels [62-65]. Cr diffuses more rapidly in ferrite than in austenite [66-68]. These internal

precipitates provide no protection to the remaining alloy substrate, and breakaway oxides are allowed to consume the component at a rapid rate.

2.14 Growth of Alumina Scales

Common sources of stress on an alumina forming alloy system are those which arise during scale formation or growth, and thermal stresses which arise during cooling due to the thermal expansion mismatch between alloy and oxide. As the thermal expansion coefficient of alumina is much lower than that of any alloy system on which it forms.

A number of mechanisms are available to reduce any growth or thermal stresses generated in a protective oxide system. The most important are: (a) cracking of the oxide; (b) spalling of the oxide from the alloy substrate; (c) plastic deformation of the substrate; and (d) plastic deformation of the oxide [20, 69].

The following equation (Equation 2-11) was proposed by Al-Badairy et al. [20] and is used later in this work. Its purpose is to calculate approximately the amount of aluminium consumed from a substrate alloy by the growing alumina scale, for a given oxide thickness. Therefore, the equation is also useful in determining the level of Al remaining in the substrate alloy. The equation is suggested for use only with flat samples, and neglects any edge effects. The main assumption for consideration is that all aluminium is consumed by scale formation. The equation is as follows:

$$Al_r = \frac{Al_m \cdot \rho_m \cdot x_m - 2Al_s \cdot \rho_s \cdot x_s}{\rho_m \cdot x_m - 2Al_s \cdot \rho_s \cdot x_s} \tag{2-11}$$

where:

Al_m = weight fraction of Al in the substrate alloy before oxidation

Al_r = weight fraction of Al remaining in the substrate alloy after oxidation

Al_s = weight fraction of Al in the oxide scale

ρ_m = density of the substrate alloy

ρ_s = density of the oxide scale

x_m = thickness of the substrate alloy

x_s = thickness of the oxide scale

This calculation is very useful in estimating the remaining Al content of the substrate alloy for a given foil and alumina scale thickness. The limitations of this calculation are clear, as this only considers the intrinsic chemical failure of the specimen. Other life prediction factors, such as the gas environment, impurities in the alloy, stress generation, and thermal cycling are also of great importance.

It is generally well accepted that small additions of reactive elements, such as Y, Hf, Ce, etc., substantially improve alumina scale adherence.

- Growth stresses are higher in alumina formed on FeCrAl alloys as compared to that formed on nickel-based alloys [69].
- Y additions do not result in lower growth stresses in the scales in alumina scales on FeCrAl alloys even though the additions decrease the amount of lateral scale growth [20].
- Growth stresses are relaxed by plastic deformation of both the alloy and oxide [70].

2.15 Creep in FeCrAl Alloys and Alumina Scales

Thin foil curvature/deformation is commonly observed after oxidation testing [23]. Commonly associated with weak alloys, these thin foils cannot withstand the strong growth stresses from the oxide. This curvature/deformation reduces the occurrence of oxide scale cracking. If an alloy substrate is weak, stresses generated during oxide scale growth can cause specimens to deform. Strong substrate alloys, such as the oxide dispersion strengthened (ODS) PM2000, are more resilient to oxidation induced deformation [8, 71, 72]. However, weaker alloys exhibit longer in-service lifetimes than the more creep resistant alloys [73].

On thicker samples, where no curvature/deformation is observed, the change in specimen length is a method used to obtain information on the growth stresses. Direct measurements for extensions in sample length are common for determining the creep properties of an alloy substrate. Curvature of thin foils makes determining foil extensions difficult and prevents the recording of accurate change in length measurements. Most authors who attempt to perform such measurements always disclose that their results are only ever semi-quantitative [74]. Most authors rely on modelling to calculate expected foil extensions [75].

Increasing the thickness of a FeCrAl foil will decrease the amount of foil curvature/deformation observed. This will also increase the time to breakaway oxidation by increasing the overall aluminium reservoir of the system. Increasing the thickness of the alloy foils may not always be possible, as increasing foil thickness in a honeycomb abradable seal may cause damage to the turbine blade tips during contact [1, 2].

Strehl et al. presented results for the elongation of Aluchrom I SE thin foils (50μm) at 1250°C for ~6 hours [23]. An extension of foil length of ~12%, prior to the exhaustion of aluminium from the substrate was observed. The results prove that creep processes on thin foil substrates cannot be neglected.

Thin foil samples are found to elongate during oxidation, showing that a competitive relaxation mode takes place according to the mechanical properties of the metallic substrate [75]. If such a specimen is restricted, mechanically or geometrically, in such a way that elongation cannot take place, then interface undulation is common. This is an energetic stress relaxation mode for the substrate alloy. This mode of relaxation causes locally stressed regions during cooling, which often results in oxide scale spallation.

During alumina scale growth, defects can develop within the oxide scale and at the scale-metal interface [69, 74, 76]. These defects can cause spallation of the protective oxide scale, especially during cooling where the coefficient of thermal mismatch between scale and substrate is more noticeable. Often such built-up stresses at the oxide-metal interface are reduced by substrate creep.

2.16 Formation of Chromia under Alumina Scales

The oxidation of thin FeCrAl foils with additions of reactive elements occurs in three stages [77]. First a protective alumina scale is established, this oxide thickens until the aluminium is exhausted from the substrate. Next, a chromia layer will form beneath the original alumina. This layer also thickens, but at a slightly slower rate than the original layer [78]. The final stage of the alloys in-service life is the formation of breakaway oxides (usually iron oxide). These form until the entire thickness of the alloy is consumed.

If aluminium is exhausted from the alloy and the alumina scale remains intact without spalling or the formation of cracks, oxygen will begin to diffuse through the scale. This establishes an oxygen partial pressure that is too low to promote the formation of iron oxides, but high enough to establish chromia formation. Good scale adherence for both alumina and dual layered oxide is due to the large amount of deformation of the substrate alloy.

The formation of a chromia layer directly beneath the alumina scale has regularly been observed [23, 34]. This dual layered oxide can effectively prolong the lifetime of the foil component. The idea that the formation of a chromia layer will still provide protection and prolong component lifetimes has caused some conflict and debate. Breakaway oxidation has normally been associated with a period of rapid weight gain during oxidation. The formation of a chromia layer would significantly affect weight gain experiments. Therefore great care must be taken when determining whether an alloy system has established oxidation mechanisms from weight gain experiments alone [74, 79].

Stott et al. [34] found a dual layered oxide of alumina and chromia prior to breakaway oxidation for lanthanum containing Fe-20Cr-5Al thin foils. They established the oxide species by a combination of TEM diffraction patterns and EDX analysis. Their results for a 50μm thick foil, oxidised for 400 hours at 1150°C gave the following dual layered oxide measurements: (a) an outer alumina layer, described as columnar, of 0.5-0.8μm thick, (b) an intermediate columnar grained layer of alumina of ~3.5μm thick, and (c) a chromia inner layer of ~2μm thick on average. Both layers of alumina contained traces of iron and chromium; however, there was no detectable aluminium in the chromia layer. The alloy substrate beneath the scale also contained no detectable aluminium.

Some results for molybdenum containing FeCrAl alloys [34] have indicated that the thicknesses of these dual layered oxides may not be constant across the sample. It is not uncommon to see large penetrations of chromia oxides into the alloy substrate during any stage of the chromia layer formation. The alloy is effectively going into breakaway oxidation.

The growth mechanism for chromia under alumina scales is not completely understood. However, three separate models are proposed below.

Model 1:- The rate of oxygen diffusion in chromia is faster than that of chromium. Therefore, if chromia forms beneath the alumina scale, the oxygen ions are still the rate determining species [80]. New oxide will form at the metal/oxide interface if the alloy does not transfer to breakaway oxidation.

Model 2:- This model suggests that chromium diffusion is faster than oxygen through chromia scales. If true, fresh oxide would form at the interface between the alumina and chromia layers. The growth model for the chromia layer would be expected to be linear, but is difficult to prove using thermo gravimetric analysis (TGA) [81, 82].

Model 3:- Another suggestion is that chromia formation is a result of the counter flux of chromium and oxygen. It is suggested that new oxide is formed by the reaction of the two species within the existing alumina/chromia scales [83].

Model 4:- A fourth model is suggested for chromia layer formation by Cr directly reducing the alumina scale. This was the original concept of induced chemical failure (InCF) suggested by Evans

et al. [84]. Their work presents the direct reduction of a chromia layer by Fe upon the consumption of Cr from an alloy substrate. An equilibrium condition at the interface during InCF is maintained by an increase in the oxygen activity. This can arise from both the dissociation of chromia at the interface and also possibly from the inward transport of oxygen across the oxide layer. As continued depletion of Cr occurs, the local oxygen activity will increase to a value at which reaction with other elements within the alloy becomes thermodynamically possible.

As the formation of chromia in a FeCrAl alloy system is normally associated with the commencement of breakaway oxidation, very little information has been published. The beneficial effects of this sub-layer formation and its pseudo protective properties have had little appreciation. As long as the alumina outer oxide scale remains intact, formation of a chromia sub-layer will extend alloy in-service life and delay the onset of breakaway oxidation [17, 23, 85].

2.17 Microstructure of Alumina Scales

The α-alumina oxide scales are usually characterised by two types of grain structure. A layer of equiaxed grains, usually only 1-2 grains thick at the scale-gas interface. The remaining inner scale between the equiaxed layer and the metal surface is made up of much larger columnar grains. These sometimes possess axial ratios of 1:6 with their long axes perpendicular to the metal surface [86]. These single grains connect the outer equiaxed layer with the metal substrate.

The equiaxed grains represent the initial nucleation of the α-alumina scale and the columnar grains develop in subsequent growth [87]. They are a

representation of the growth direction of the oxide scale. The alumina scale thickness increases predominantly by the growth of the columnar crystals [86, 87].

Continued growth of α-alumina scales is predominantly by the diffusion of oxygen through the scale [88-91]. Diffusion through the scale is dominated by grain boundary diffusion. This oxygen then reacts with the available Al content of the substrate at the metal-oxide interface. Inert marker experiments have indicated that α-alumina scales grow inward by oxygen diffusion [92, 93].

The thermodynamically stable α-alumina is highly desired for oxidation resistance for alumina forming alloys [94]. The oxidation sequence of the alloy upon exposure to the atmosphere at temperature requires a short period of metastable and transient phases of alumina prior to the establishment of an α-alumina scale [95, 96].

Initially formed alumina undergoes a transformation from a transient state, to a mature state (α-alumina) [97, 98]. There are three types of transient/metastable aluminas all based on the spinel structure [98]:

- γ-Al_2O_3, a defective spinel,
- δ- Al_2O_3, a tetragonal form of spinel having a triple spinel block as a unit cell, and
- θ- Al_2O_3, a monoclinic phase.

The mature α-alumina has a corundum structure. Its unit cell is hexagonal. The transformation from transient alumina to α-alpha alumina is $\gamma \rightarrow \delta \rightarrow \theta \rightarrow \alpha$ [99]. A large reduction in the oxidation rate accompanies the change in oxide morphology, along with a 14% decrease in volume [100].

2.17.1 Microstructure of Alumina Scales:- Crystallographic Preferred Orientation/Texture

Prior et al. studied the microstructure of α-alumina scales formed on model FeCrAl containing Y and Hf at 1200°C [87]. The scales comprised of two distinct layers. An equiaxed grain structure at the outer scale, and columnar grains between these and the metal surface. EBSD analysis of these layers revealed that both layers were found to have a very strong crystallographic preferred orientation (often referred to as texture). They present the results as a fibre texture, were the r-axis is orientated perpendicular to the metal substrate [86]. This result is independent of the microstructure and crystallographic orientation of the metal substrate. A mechanism, where the thermal stresses during heating control α-alumina nucleation, was suggested by this work to explain the α-alumina crystallographic preferred orientation, although a preferred growth direction could also be invoked.

The r-axis is referred to as the $<1\bar{1}01>$. In sapphire single crystals (Al_2O_3), the measured r-axis speed of sound is significantly different from the measured c- and a-axis sound speeds (~7%) [101]. Sapphire is an anisotropic material and has a low symmetry in the r-direction. The elastic properties of the r-axis of sapphire are important for a wide range of technological applications including substrates for thin film deposition.

Over 20 years ago, studies by Smialek et al. presented work on crystallographic preferred orientations for α-alumina scales formed on NiAl and NiCrAl alloys [97]. TEM (transmission electron microscopy) and selected area diffraction (SAD) was used to analyse the crystal orientation of alumina grains. Large data sets for ~300 α-alumina grains (both equiaxed and columnar) yielded diffraction patterns with a reasonably uniform distribution of spots; i.e. no preferred orientations. When the authors analysed on a smaller scale (analysis of ~19

grains), they found that neighbouring grains had remarkably similar orientations. Where all subgrains possessed an orientation near $[10\bar{1}\bar{1}]$. There was no mechanism suggested for the production of this localised texture.

In contradiction, the textures of alumina scales grown on FeCrAl and FeCrAlY alloys were measured by Blachère et al. [102]. Their results suggested that the columnar morphology of the alumina scales on FeCrAlY was not associated with a fibre texture. They also presented α-alumina scales that consisted solely of equiaxed grains. These also had no preferred crystallographic orientation.

A key feature of α-alumina scales, especially after short term oxidation tests (>20 hours), is the formation of macro voids within the oxide sale. These are a common feature of high resolution microscopy studies [103, 104].

2.18 Interfacial Void Formation

The adherence of the alumina scale is also of great importance to the lifetime of the FeCrAl alloys. This adherence is affected by the presence of voids/pores at the metal-oxide interface, which are considered detrimental to the lifetime of the component. The formation of voids/pores at temperatures >1000°C has rarely been discussed [105-108]. Interfacial void formation is usually associated with alloys that do not contain reactive elements. Many authors commonly report upon the benefit of improved oxide scale adherence provided by reactive elements [28, 30], such as Y, Hf, Zr, La, etc. However, the experiments described in this work present void formation at the metal-oxide interfaces of a commercial grade alloy with reactive element additions.

The condensation of vacancies has often been thought to be the main mechanism for void formation. These vacancies can be the result of outward growing oxide scale, or from any unequal diffusion of alloying elements in the

substrate. Vacancies can also be injected into the metal to be annihilated at the metal-oxide interface [109, 110]. Another suggested argument for interfacial void formation at high temperature is the de-lamination of the oxide scale through the creep relaxation of the substrate alloy. Compressive stresses generated in the growing oxide may induce a tensile stress on the substrate alloy [111].

Golightly et al. [43] reported the presence of voids both within alloy grains and at alloy grain boundaries. The surface of these voids was always smooth and displayed features of thermal etching. Some authors report that interfacial void growth is temperature dependent [112]. Increasing the temperature will also increase the growth rate of the voids.

2.18.1 Condensation of Vacancies

Most authors commonly report vacancy condensation as the mechanism for interfacial void formation. These vacancies can coalesce at the metal-oxide interface as a result of:

- outward-cation transport
- any unequal diffusion of alloy constituents
- vacancy injection into the substrate

Many authors [113-116] suggest that void formation is the sole result of the coalescence of vacancies. However some voids, including those seen later in this work, appear to be too large to form as a result of vacancy coalescence. These are often associated with α-alumina scales grown on alloys without reactive element additions [117]. They may be the result of secondary creep effects from the alloy substrate [27].

Dunnington et al. [118] commented on the movement of vacancies during the high temperature oxidation of iron/steels. Initially the high number of vacancies created at the start of oxidation diffused back into the metal producing a vacancy gradient within it. At the beginning of oxidation this gradient is steep. However as oxidation continues, this gradient gradually decreases leaving a high concentration of vacancies at the metal-oxide interface. This coalescence of vacancies at the interface leads to the separation of metal and oxide and the formation of voids.

Tylecote et al. [6] suggested that if voids/scale separation is initiated at one side of a component before the other, then the gap formed will act as a sink for the vacancies collecting on the opposite side. This is illustrated in figure 2.5. This allows for the opposite metal-oxide interface to remain intact and well adhered whilst scale exfoliation and alloy breakaway is initiated from the other side. Tylecote [119, 120] performed a second experiment with similar results. Rather than observing the delamination of an interface acting as a vacancy sink, a series of samples were produced with holes drilled through the centre. After oxidation the samples revealed no delamination of the oxide scale. However, the circular holes at the centre now had the appearance of ovals, with their long axes being normal to the metal/oxide interface. It was proposed that these geometric additions to the samples now acted as a sink for vacancies.

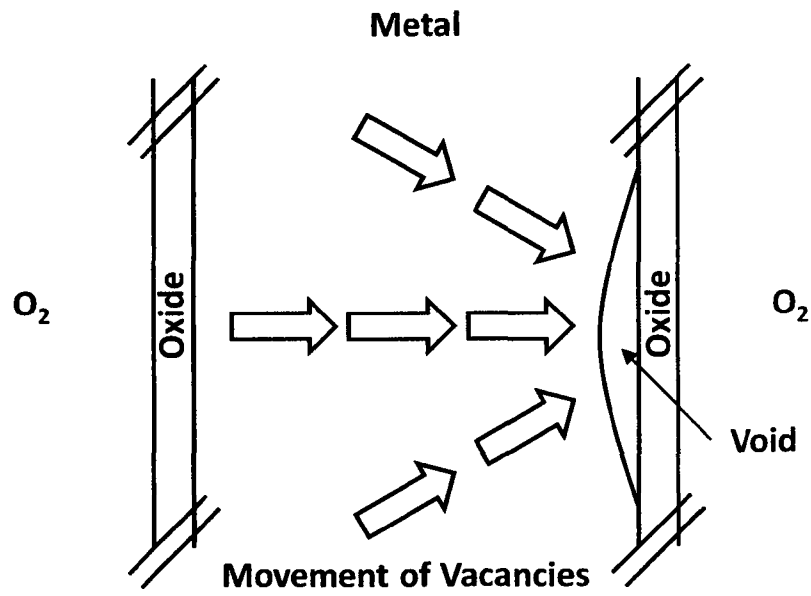

Figure 2.5: Schematic representation of void/scale separation on one side of a sample acting as a vacancy sink for all other vacancies, as suggested by Tylecote et al. [6]

Work by Stringer et al. [121] suggested that the formation/presence of internal oxide particles in an alloy (e.g. oxide dispersion strengthened alloys) can act as a vacancy sink and can prevent or suppress void formation.

For alloys which rely on chromia formation as a protective oxide scale, a vacancy flux directed toward the metal-oxide interface is created as a consequence of the outward diffusion of chromium ions through the oxide [43, 122, 123]. For alumina forming alloys, alpha alumina growth is primarily via the inward diffusion of oxygen and therefore the creation of vacancies is less clear. However, the transient stages of alumina grow by the outward diffusion. Kuenzly et al. [124] proposed that a coalescence of vacancies at the metal-oxide interface results from a Kirkendall effect in the alloy substrate, and this is explained below.

2.18.2 Kirkendall Effect

The fluxes of two alloy constituents do not need to be the same at any given time due to a possible difference in their diffusion coefficients. Consequently, a net flux of matter will be generated through the alloy and a corresponding flux of metal vacancies will arise towards or away from the scale-alloy interface due to this effect [107].

Bruum et al. [105] attributed void formation during the oxidation of NiAl to the Kirkendall effect. As the diffusion rates of Ni and Al in the alloy at high temperature would be different, this would cause a flux of vacancies to the metal-oxide interface.

2.18.3 Void Formation during Initial Stages of Oxidation

Cross-section analysis of alumina formers commonly reveals small voids after short times at high temperatures. These could be a remnant of the volume reduction associated with the transient-stage, θ-α alumina phase transformation [125].

During the initial stages of high temperature oxidation of alumina forming alloys, cation-transported-alumina growth dominates (transient stage) [106, 108] i.e. the outward growth of alumina. Rapid void formation is often recorded during the transient stage.

Micron-sized pores were found after times as little as three minutes on alumina-FeAl interfaces after oxidation at 1000°C. In addition, the metal surfaces of the voids were found to be covered with sulphur. The alloy contained 27 ppm S in the bulk alloy [126, 127].

If sulphur is present in the alloy, sulphur saturation of the metal surfaces of voids is found to occur soon after their nucleation. This effect is reported to lower the surface energy of the voids [106], and the mopping up of the sulphur with reactive elements might explain why void formation is often lower in the presence of reactive elements.

Interfacial void formation on FeCrAl alloys is not expected during the initial stages of oxidation [43] when high oxidation rates, and hence high levels of stress, should cause thin oxide scales to plastically deform. Therefore, scale adhesion should be maintained by the plastic deformation of the oxide. Interfacial void formation is expected after longer oxidation periods due to the lower levels of stress, and the thicker oxide scale. Plastic deformation of thick oxide scales is less common and any condensation of vacancies during the later stages of oxidation may result in interfacial void formation.

Al-Badairy et al. [17, 108] published work on the formation of voids after testing FeCrAl alloys at the lower temperature of 900°C for times up to 50 hours. They suggested that the longer growth time for transition alumina at 900°C prior to the formation of α-alumina, could cause movement of vacancies to the metal/oxide interface causing void formation after short times.

2.18.4 Model Calculations

The formation of interfacial voids can be analysed in terms of surface energies. Pint et al. [117] presented a simplified two-dimensional model for considering interfacial void formation. The model is based on surface energies in a metal-oxide system and is represented schematically in figure 2.6. The stress, σ, required for void growth is:

$$\sigma \geq \gamma_m \cos\varphi + \gamma_{ox} \cos\varphi - \gamma_{int} \qquad (2\text{-}12)$$

where:

γ_m = surface energy associated with the metal

γ_{ox} = surface energy associated with the oxide

γ_{int} = surface energy associated with the metal-oxide interface

and where in equilibrium:

$$\varphi = \cos^{-1}\left(\frac{\gamma_{int}}{\gamma_m + \gamma_{ox}}\right) \tag{2-13}$$

φ = angle of surface separation

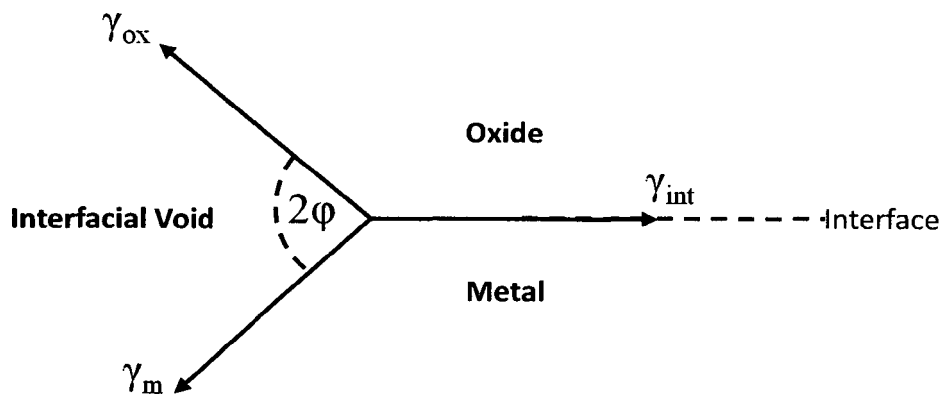

Figure 2.6: Schematic of the surface energies at the edge of an interfacial void.

This model is a very simple approach to understanding interfacial void formation. Additional factors which may need to be considered to understand void formation are the:

- movement of grain boundaries in the oxide and/or metal [128]

- fluxes of diffusing species [43, 93, 129, 130]
- crystallographic orientation of the scale and metal [117]
- defects in the metal [117]

This simplistic model is not without its problems, as interfacial effects are difficult to quantify. Surface energies are only available for pure elements and idealised systems [131, 132].

It is known that the effects of sulphur can be detrimental to an alloy system and increase the risk of void formation [30, 133-136]. The presence of sulphur at the bare metal surface can reduce γ_m, thus making it easier for the void to grow. Also, segregation of sulphur to the metal-oxide interface can increase γ_{int}, which increases the probability of void growth. Reactive elements can inhibit/suppress void formation by preventing sulphur segregation to the metal-oxide interface.

Some research was carried out by Maruyama et al. [137] on the high temperature oxidation (600°C) and void formation in growing magnetite scales. Rather than interfacial void formation, their work concerns void formation within the oxide scale. They propose that internal void formation in magnetite scales can be explained by the divergence of ionic fluxes and the establishment of a chemical potential distribution. They propose a model calculation to quantify the amount and volume of the internal voids formed. These calculations were later improved by Ueda et al. [138] and Akriba et al. [139] who attempted to estimate the positions of the voids. Unfortunately, these models are only valid for outward growing oxide scales and presently the models have only been applied to magnetite and NiO scales.

They have attempted to verify their work experimentally with some success. Voids were always found to form at the metal-oxide interface before they are

incorporated into the fast growing oxide scale. They conclude that the divergence of the iron flux is the quantitative measure of void formation.

2.18.5 Gas Vapour Phase Transport

Hou et al. [106] commented on the alumina scale thickness above voids on FeAl substrates. The scale thickness above a void was identical to the thickness of the oxide scale which remained intact with the substrate. This indicates a continuous supply of aluminium to the oxide above the void to sustain alumina scale growth. This can be achieved by two possible methods - either Al surface diffusion, or by Al-vapour transport.

Hou et al. [106] suggest pore/void enlargement is a result of aluminium evaporation that is required to support scale growth after a critical time of 20 minutes. Using the Knudsen-Langmuir equation [4, 140], and the vapour pressure of aluminium at 1000°C for a Fe-40Al alloy system, they calculated that the gas phase transport of aluminium to the surface is sufficient to maintain scale growth over a void. Before this time, the average pore diameter is only 2μm, and transport of Al must be dominated by surface diffusion.

Convoluted scales which separate from the substrate as shown in figure 2.7, also show signs of continued alumina scale growth [44]. Maintaining the supply of aluminium to the scale in these situations is also thought to be either by vapour phase diffusion or by surface diffusion across the cavity or around the underside of the oxide [44, 106, 108]. Golightly et al. [43] commented on the high level of aluminium necessary in convoluted areas to maintain alumina scale growth above a ridge. As the underside of the convoluted alumina scale is longer than the original length of oxide that was initially adhered to the substrate. An increase in the level of aluminium is necessary to allow the scale to grow at the same rate, as if adhered to the substrate.

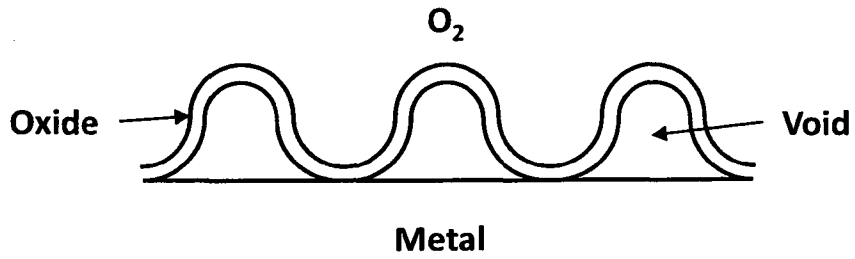

Figure 2.7: Schematic diagram of scale convolution/buckling at the metal-oxide interface

A recent publication by Ehlers et al. [141] regarding high temperature oxidation and the effects of water vapour on low alloy steels presented internal void formation and proposed a mechanism for gas/vapour phase transport of iron within an oxide scale. The effects of water vapour entering a magnetite oxide scale were found to increase the scale porosity and reduce the time to alloy breakaway. The work suggests that "H_2O can create porosity by vaporising a $Fe(OH)_2$ (gas) species and re-depositing in parts of the scale where higher pO_2 (gas) values exist." A schematic representation of this can be seen in figure 2.8.

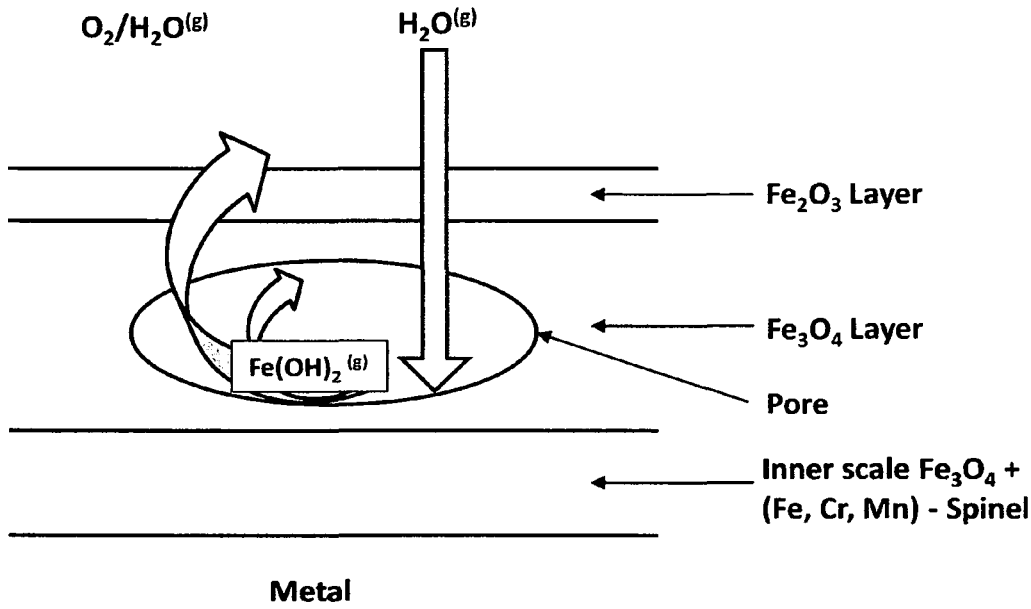

Figure 2.8: Schematic illustration showing proposed mechanism for transport of Fe from inner to outer part of the scale via volatile specie $Fe(OH)_2$ gas, as suggested by Ehlers et al. [141]

The above mechanism represents another possible method of void formation within oxide scales. The transport of material by a volatile species is one method of redistributing material and void growth. Ehlers et al. present very porous scales with many voids in high water vapour containing environments.

2.19 Brazing and Alloy Constituents

Brazing can be classed as a high temperature soldering technique. It is the process in which two or more metals are joined by a mechanical bond with a filler metal that has a melting point typically above 500°C. Its advantages include joining small integral parts for high temperature application that welding cannot achieve without the necessity for machining afterwards. Brazing is a process by which the filler alloy wets the surface. Therefore, small separations

between adjacent surfaces draw the filler metal by a process called capillary action. This process is beneficial for the design of current honeycomb abradable seals.

With great care, brazing can be used on finished machined parts. Demand over the last 40 years for materials that can operate in high temperature corrosive environments has brought with it a call for methods of joining capable of satisfying these stringent service conditions [142]. This demand for excellent high temperature joint strength and corrosion properties in a variety of aggressive environments has necessitated the development of a whole new range of filler metals (see Section 2.19.2). Braze alloys now based on elements such as nickel, gold, palladium and manganese are all in use and are suitable for many different environments.

These new braze alloys had much higher melting points than previous braze alloys. The range of melting points was now 900-1300°C. This made flux brazing impractical, but brazing at low pressures was found to produce joints of high integrity and strength.

This opened the door for a technique called vacuum brazing. Vacuum brazing is now widely accepted in industry and is relied upon to produce joints between materials that are capable of operating under severe conditions. The main advantage of vacuum brazing is that it can braze components together without the need for any further machining. The component produced will have a high joint strength, with a high quality joint finish.

The strength of a braze joint depends upon the wetting action between the filler metal and the surfaces of the metals to be joined. Any contamination or particulates (debris), such as grease, remnant oxides, chemical compounds, etc. can cause a reduced wetting action of the braze filler metal. This would lower

the ability of the filler metal to produce a high quality joint and would reduce joint strength.

Vacuum brazing is used extensively in the aerospace and nuclear industries [143-145]. These both require component manufacture with high quality joints. Some of the most aggressive environments are encountered in these fields of use, therefore, high strength and high quality joints are imperative.

The brazing process requires heating both braze filler metal and substrate alloys to a brazing temperature. Selection of braze filler metal requires a melting point that is less than that of the substrate alloys. Coalescence of component constituents is achieved by melting the braze filler metal, and the action of wetting the filler to the substrate. A molten braze will flow and fill any narrow gap between substrate alloys. These two parts may or may not be of the same material. Brazing often relies upon the brazing alloy to wet and flow into narrow gaps, typically of 0.05mm wide.

Capillary action of a braze filler metal i.e. how far the braze will travel, is reliant upon surface tensions of the braze when molten, and the surface tension of the metal parts. It is also reliant upon the ability of the braze when molten to wet the solid and most importantly, the distance between the two parts which produce the narrow gap. This can be represented by the following equation:

$$H = \frac{2\gamma_L \cos A}{g\rho D} \tag{2-14}$$

where:

$$\cos A = \frac{\gamma_S - \gamma_{L/S}}{\gamma_L} \tag{2-15}$$

and where:

H = vertical distance the braze will travel by capillary action

γ_S = surface tension of solid

$\gamma_{L/S}$ = surface tension of the liquid on a solid

γ_L = surface tension of the liquid

A = angle represents the ability of a liquid to wet the solid

g = acceleration due to gravity

ρ = liquid density

D = distance between plates

2.19.1 Joining Dissimilar Materials

Another advantage of vacuum brazing is that the technique can be used to join very dissimilar metals. For example, it can be used for combining alloys where fusion welding would present metallurgical problems. The joining of dissimilar metals is possible because the two parent metals never actually intermix. The brazing alloy acts as a buffer layer between the two metals and reduces the possibility of forming brittle intermetallic compounds.

One of the main disadvantages of brazing is the corrosion resistance of the joint. Over the past 20 years, nickel-based brazes containing chromium have proven to provide excellent corrosion resistance up to 900°C. However, prior to the invention of such brazes, reliance was placed upon corrosion resistant alloys containing silver. This was due to the galvanic action of the joint. Since the rate of galvanic action is proportional to the areas exposed, the brazed joint should be cathodic with respect to the base material [146].

2.19.2 Brazing Fundamentals – Metallurgy of Ni-based Brazing Filler Metals

Nickel based brazing filler metals were developed in 1947 to provide higher temperature capabilities and improved mechanical properties compared to the available copper- and silver-based filler metals [10]. The additional composition of several alloying elements in nickel-based filler metals serve to optimise the alloy in a number of ways. The role of these alloying elements is described below.

Boron (B) - Boron is used to suppress the melting point of the nickel (1455°C) to below that of most base metals. Lowering the melting point allows nickel-boron filler metals to braze a wide variety of metals. However, a binary nickel-boron braze has several disadvantages, i.e. low tensile strength and low corrosion resistance.

Another disadvantage of boron is that it is very easily diffused because of its molecular size and because of this can be erosive to very thin metal components such as honeycomb abradable seals [147-149].

Ideally, boron will diffuse away from a brazed joint. The boron loss will result in a strong, corrosion resistant braze joint, with melting point higher than the original filler metal [150]. Many commercial braze filler metals rely on the diffusion of boron to increase strength, corrosion resistance and most importantly, to increase the melting temperature of the filler metal [147].

Silicon (Si) – Silicon behaves very similar to boron, by lowering the melting point of the filler metal. This alloying addition

also has disadvantages in a nickel-silicon binary system. It exhibits a low tensile strength and poor ductility.

Nickel (Ni) – Boron (B) – Silicon (Si) Filler Metals –

Both binary Ni-B and Ni-Si systems do not provide the adequate properties necessary for a braze filler metal. When alloyed together as a 3 component system, suitable brazing filler metals can be formed. Silicon additions to these ternary alloys are found to enhance corrosion resistance.

Phosphorus (P) – This alloying addition also behaves as a melting point suppressor, but to a greater extent than either boron or silicon. For example, an addition of 11wt% phosphorus to nickel will decrease its melting point by 575°C. Ni-P binary systems do produce satisfactory braze filler metals and are commercially available.

Chromium (Cr) – Chromium alloying additions are usually added as a third or fourth element to some of the systems already mentioned above. Chromium is recommended to add strength and/or corrosion resistance. This addition is normally associated with longer brazing times, as this allows other braze constituents (i.e. boron) to diffuse away from the joint.

Carbon (C) – Carbon is an undesirable element in most brazing filler metals. The formation of chromium carbides at brazed joints can reduce joint quality, and also reduce corrosion

resistance. Typically, nickel-based filler metals contain <0.1 wt% C.

Carbon additions have also been attributed with slight reductions in melting points and increasing the fluidity of nickel based brazes.

2.19.2.1 Minor Additions

Iron (Fe) – Increases the ductility of braze filler metals

Copper (Cu) – Increases corrosion resistance to aqueous media (in NiCr braze fillers)

Tungsten (W) – Reduces viscosity during brazing and increases high temperature strength

Molybdenum (Mo) – Increases high temperature strength and enhances corrosion resistance

3. Experimental Procedures

3.1 Introduction

The desired outcomes of the experiments were to monitor the performance of the MI2100/BNi-5(AMS 4782)/Haynes 214 honeycomb abradable seal and to understand the degradation mechanism after high temperature oxidation. Isothermal tests at 1100 and 1200°C for times up to 1000 hours were conducted. Cooled samples were analysed and their features such as oxide morphology and spallation were recorded using a combination of optical microscopy, scanning electron microscopy (SEM), and energy dispersive X-ray analysis (EDX). The samples were then cross-sectioned to analyse the oxide for scale thickness, grain structure, cracks, voids and void filling. Electron back-scattered diffraction (EBSD) analysis was an additional technique used to examine sample cross-sections.

As it is the failure of the FeCrAl foil part of the honeycomb abradable seal that defines the component lifetime, a comparative study was run alongside the above research. This exposed 70 micron thick foils of the alloy MI2100, in the as rolled condition, to exactly the same high temperature oxidation testing as the honeycomb abradable seal but without the influence of the brazing alloy.

This chapter is divided into seven main sections: samples and alloys, oxidation procedures, sample preparation and metallography, characterisation, diffusion profiling, and scanning electron microscopy (SEM).

3.2 Samples and Alloys

The honeycomb abradable seal selected for the investigation was thought to be the most suitable for the increase in high temperature application >950°C. The honeycomb abradable seal was supplied by Neomet Limited, UK in the form of a small rectangular section, a replication of one of the many subsections that produce the complete seal around the gas turbine engine shroud.

The component consisted of MI2100 alloy foils, AMS 4782/BNi–5 Brazing alloy, and a Haynes 214 alloy base plate. Honeycomb foils were of 100 micron thickness, corrugated and spot welded at each node, at half foil height, for a ~1.5mm honeycomb cell size diameter. The honeycomb was then vacuum-brazed using a braze tape of 70 microns thickness, onto the 3.5mm thick Haynes 214 alloy to simulate the gas turbine shroud (Figure 3.1). The sample was photographed in its as received state using a flat-bed scanner so that the original conditions were recorded.

A series of honeycomb abradable seal test specimens were prepared from the small rectangular section. A diamond wafer cut-off wheel on a low-speed cutting saw was used to produce test samples with the dimensions of 12mm x 6mm x 10mm (length x width x height). Test samples were then ground to a 1200 grit finish using wet silicon carbide paper for metallographic examination of the brazed joint prior to oxidation.

Additional MI2100 alloy sheet of 70 micron thickness was supplied in the as-rolled condition. From this, test specimens with dimensions 20mm x 10mm were prepared. The oxidation of the thin FeCrAl foil was used as a comparison for the subsequent degradation mechanism of the foils in the honeycomb set-up.

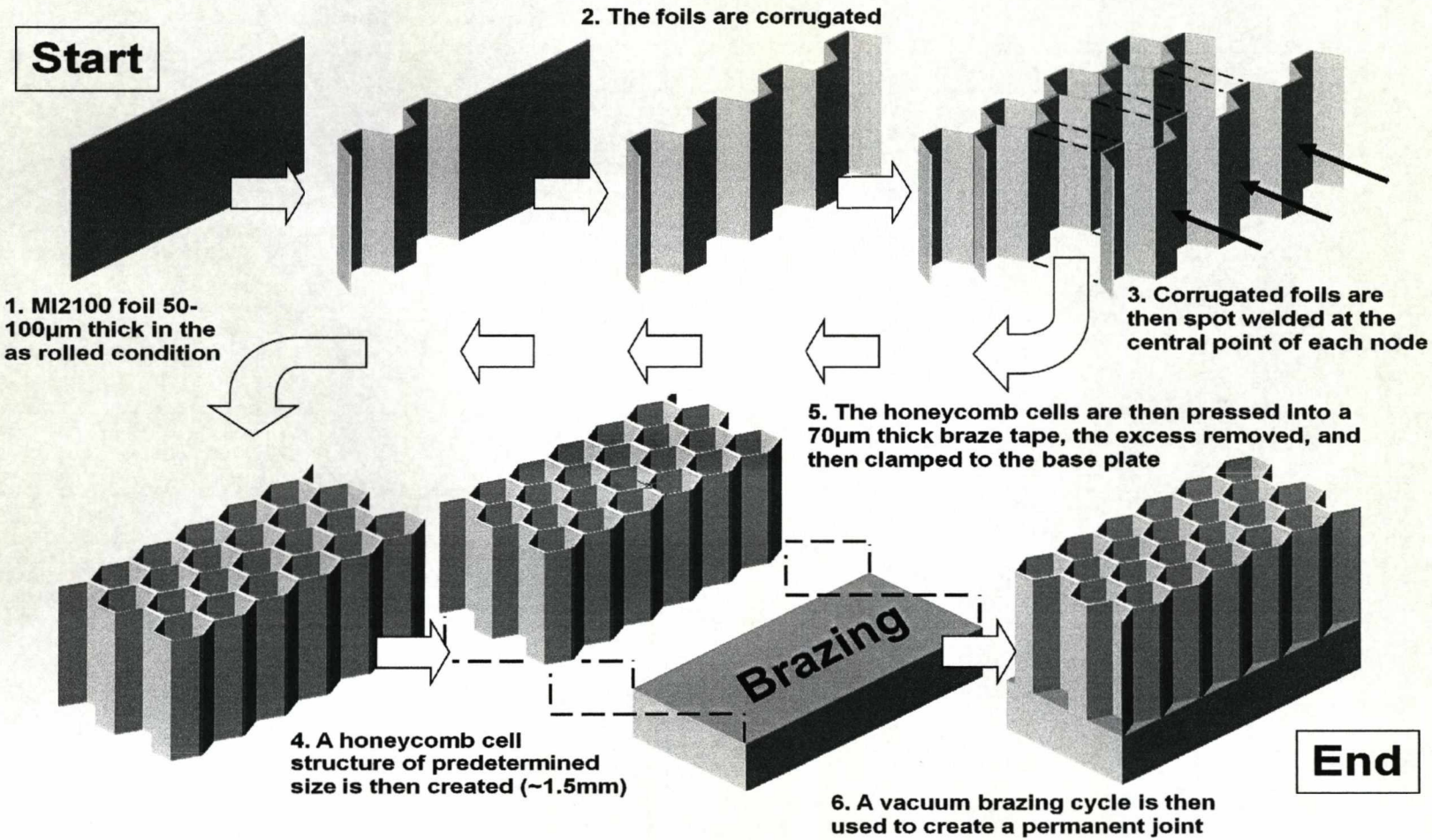

Figure 3.1: Schematic Diagram of the Honeycomb Abradable Seal Construction

3.3 Alloy Composition

The honeycomb abradable seal consists of two commercial alloys, Haynes 214 and AMS 4782/BNi-5, and the model alloy, MI2100. The compositions of the alloys are shown in table 3.1. Compositional analysis of MI2100 was achieved by using Glow Discharge Mass Spectroscopy (GDMS). A 25 element GDMS analysis was conducted by Shiva Technologies Europe, France. No compositional analysis of Carbon, Nitrogen, Oxygen, and Hydrogen content was requested. The results are shown in table 3.1.

3.4 Brazing

The joining of the honeycomb foils to the base plate was achieved by a vacuum brazing technique. Firstly, the honeycomb foils are pressed onto a 70 micron thick braze alloy tape. This process acts like a "pastry cutter" and completely fills one end of the honeycomb cells. The excess braze from around the outer foils is then removed. This combination is then clamped to the desired base plate. The typical vacuum brazing cycle used for joining with AMS4782/BNi-5 can be seen in figure 3.2.

3.5 Isothermal Oxidation

A Carbolite, horizontal tube furnace with an alumina work tube was used for isothermal oxidation. This provided a maximum obtainable operating temperature of 1400°C and a 20 centimetre hot zone (Figure 3.3).

The temperature of the hot zone was verified by a k-type thermocouple throughout the testing of each sample. It confirmed that the correct temperature was maintained at the centre of the furnace with an accuracy of ±10°C.

Table 3.1: Nominal Alloy Compositions

Alloys	wt%										ppm				
	Fe	**Ni**	**Cr**	**Al**	**Si**	**Y**	**Hf**	**Mn**	**Zr**	**B**	**C**	**S**	**N**	**P**	**Ti**
MI2100	Bal.	0.2	20	5	0.62	0.05	0.045	0.11	-	-	-	1.6	-	130	85
AMS 4782 / BNi-5	-	Bal.	19	-	10.2	-	-	-	-	-	600	-	-	-	-
Haynes 214	-	75	16	4.5	0.2	0.01	-	0.5	0.1	0.01	0.5wt%	-	-	-	-
Model alloy A1	Bal.	-	20	5	-	0.05	-	-	-	-	100	5-10	<10	~80	-
Aluchrom YHf	Bal.	-	20	5.5	0.29	0.05	0.04	-	-	-	220	11	40	130	99

Please see Appendix 1 for the additional minor element concentrations for alloy MI2100 as determined by GDMS.

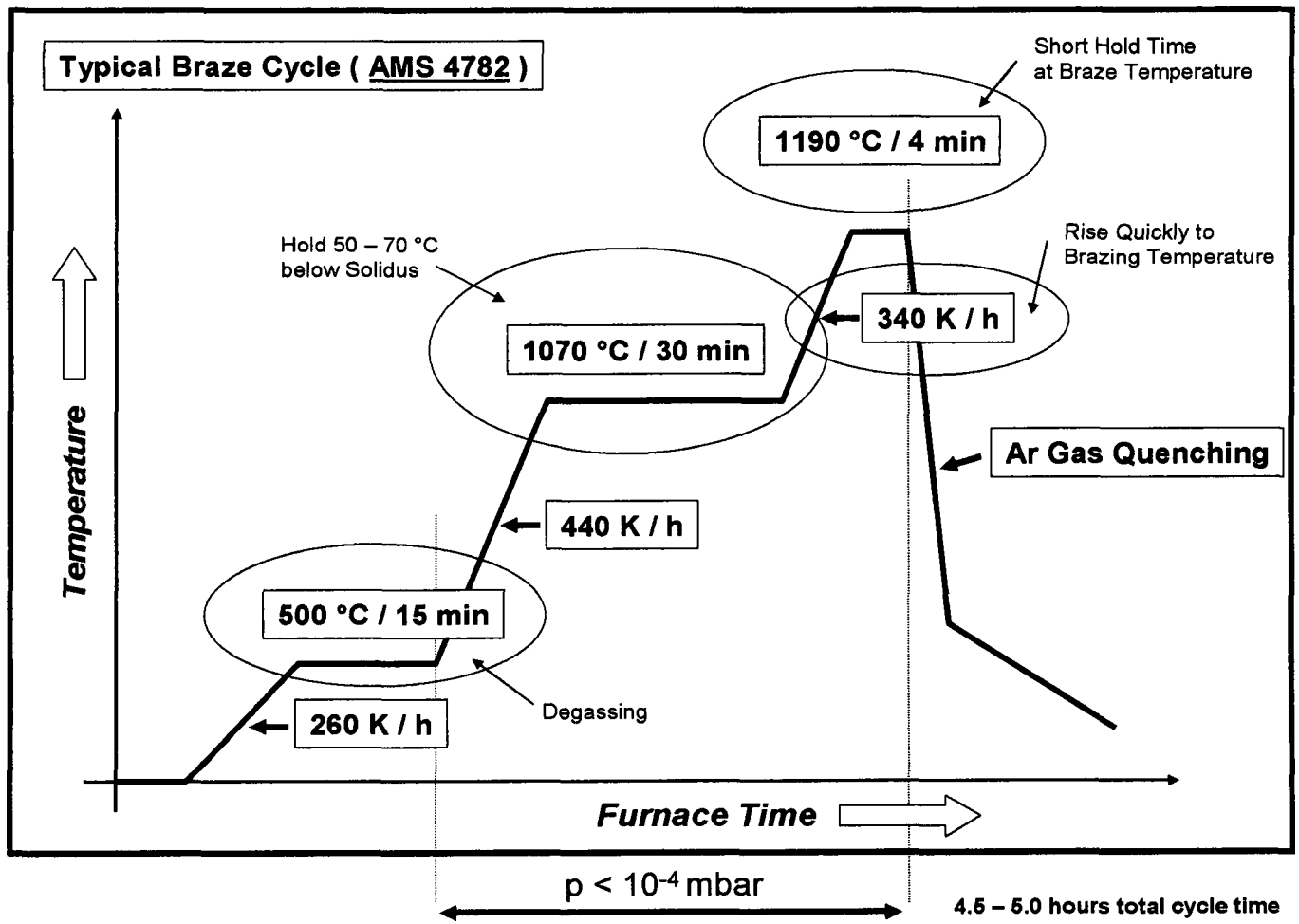

Figure 3.2: Typical Brazing Cycle for alloy AMS 4782 / B Ni-5

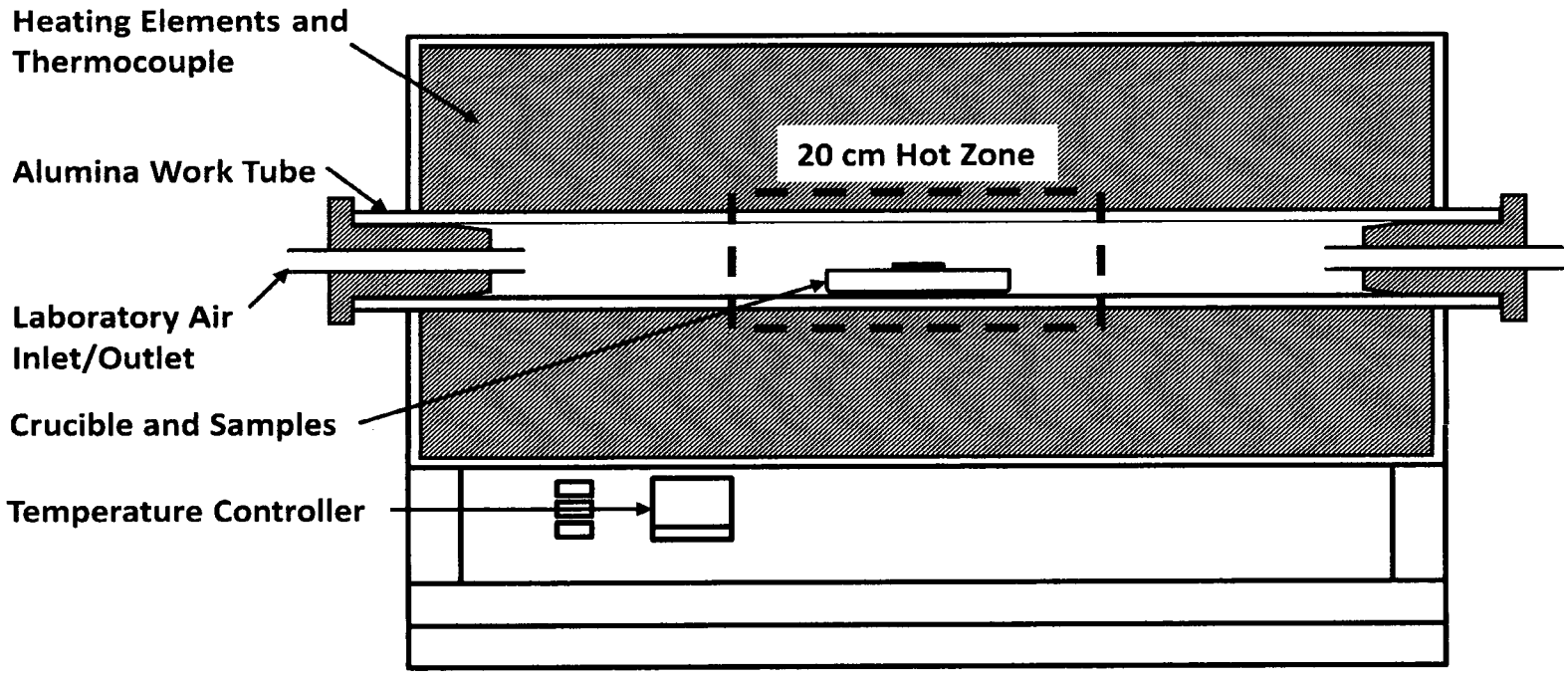

Figure 3.3: Schematic cross-section of a horizontal tube furnace (diagram not to scale)

The operating conditions within the furnace were maintained by closing both entrances to the ceramic tube with large amounts of furnace wool, metallic foil and ceramic tube ends. Throughout testing the furnace atmosphere was always assumed to be laboratory air.

Test samples, prepared from the supplied alloys were chemically cleaned prior to oxidation. Specimens were ultrasonically cleaned in acetone for 30 minutes and degreased using isopropanol. Once decontaminated, the samples were immediately placed in the furnace.

Samples were manually inserted and removed from the furnace hot zone in alumina crucibles. To avoid thermal shock, samples were gradually positioned within the hot zone of the furnace after 10 minutes (600 seconds) of initial insertion to the ceramic tube. The same procedure was followed when removing test pieces. The samples were air-cooled after oxidation.

Samples were oxidised at temperatures ranging from 900°C to 1200°C for times of up to 1000 hours. Previously, excellent performance of the honeycomb abradable seal and MI2100 foils was noted at temperature of up to 1100°C for times greater than 1000 hours. However, the main bulk of accelerated oxidation life testing was studied at 1200°C. The degradation mechanism here was observed within much shorter high temperature exposures.

The exact oxidation temperature and exposure time for a given specimen will accompany the data given in the results chapter.

3.6 Characterisation

Throughout the study, optical and scanning electron microscopy (SEM) were used as the main techniques to analyse all stages of oxidation and subsequent

failure of the thin foil and honeycomb abradable seal samples. This has ranged from preliminary examinations of the outer oxide scales and spallation directly after oxidation testing, to cross-sectional analysis of metallagraphically prepared oxide layers. Optical microscopy enabled geometrical factors of the oxide scale growth and locations of severe attack to be recorded, especially with regard to the abradable seals and void formation in the thin foils. The SEM was used as a tool for high magnification imaging of the very thin oxide scales grown on these alloys. The other facilities which accompanied certain microscopes, such as energy dispersive X-ray analysis (EDX), and electron back scattered diffraction (EBSD) were used simultaneously to generate a more comprehensive analysis of selected locations within the samples.

Honeycomb abradable seals were found to fail at a specific location within the foil in one part of the component each time. The bulk of the studies concentrate on the failure of the model Fe-Cr-Al alloy with and without the brazing alloy. Cross-sectional analysis focused on the formation and growth of interstitial voids at the metal/metal oxide interface. The nucleation of voids at the interface was monitored during alpha alumina scale growth and after aluminium exhaustion from the Fe-Cr-Al substrate.

3.7 Preparation and Analysis

Each oxidised sample was mounted in cross-section after initial investigations. Figure 3.4 shows the cross-section of the honeycomb abradable seal as a reference. Test pieces were cold mounted in epoxy resin. This technique was chosen to avoid any deformation of thin foils. Mounted samples were ground primarily using 180 grit wet silicon carbide paper to a chosen location. They were all then progressively ground and polished to a 1 micron mirror finish. Finally, a choice of either colloidal silica or alumina was used for the final polishing stage (standard of approximately 60nm). The prepared samples were

observed using an optical microscope and the oxide scale thicknesses were measured. Positions of voids and regions of mechanical failure of the oxide scales were marked and recorded using optical micrographs.

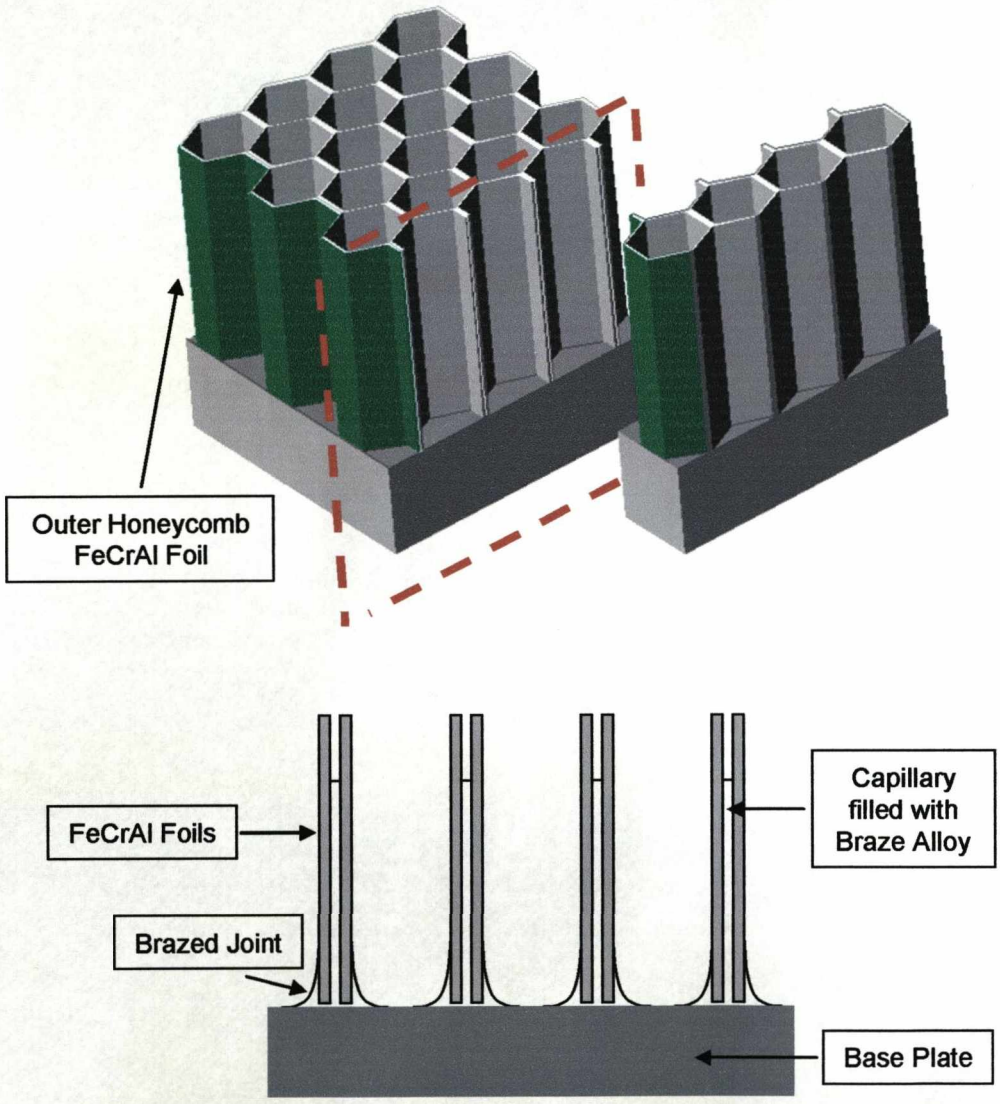

Figure 3.4: Example cross-section of a honeycomb abradable seal sample

Clean, polished samples were carbon coated for scanning electron microscopy (SEM) analysis and images recorded. A number of scanning electron microscopes have been used for the observations. These include:

- a Hitachi S-2460N with an analytical EDX system at an operating voltage of 25KV,
- a Cam Scan X500 crystal probe FEG-SEM, fitted with an analytical EDX system and EBSD (Electron Backscatter Diffraction) facility, and
- a Leo Gemini 1550 FEG-SEM with an analytical EDX system.

3.8 Observations of Void Formation and Filling

The oxide scale morphology, region of oxide scale failures/spallation, interstitial void formation, void growth, and void filling were all imaged and analysed using SEM and EDX. The presence of voids in test samples became a fundamental part of the degradation study. Both secondary electron (SE) and back scattered electron (BSE) imaging were used to analyse such occurrences. During cross-sectional analysis, the interstitial voids were found to be vacant, partially filled, or completely filled with an oxide species differing to the oxide formed by the alloy as a protective scale. SE images were used primarily, whilst BSE imaging was used as an indicator for EDX analysis. EDX spectra were recorded using a 100 second live-time and were quantified using the Wineds Version 1.11 software program. The EDX facility provided qualitative chemical analysis throughout.

3.9 Brittle Fracture of Thin Foil Samples

Brittle fracture was induced in the 70 micron thick Fe-Cr-Al foil samples. This exercise presented the oxide grain structure and void formation beneath the scale without the requirement of extensive metallographic preparation. A

complete series of samples were tested in this way. Exact oxidation times and temperatures will be given in the results section. Samples were submerged in liquid nitrogen for 15 minutes (900 seconds), removed and fractured by an impact force. This was applied by a simple hammer and vice setup. The remaining sandwich of oxide scale and substrate was then gold coated and analysed using SEM and EDX. Void formation was never proved conclusively using this technique, as delamination of the protecting oxide scale from the substrate often occurred.

3.10 Diffusion Profiles of Nickel and Silicon

The nature of the brazing process causes other elements such as nickel and silicon to diffuse into the parent nickel-based and iron-based alloys. The introduction of the brazing alloy produced high diffusion gradients at the mating interface, and subsequent diffusion into the Fe-Cr-Al foil was expected. The inter-diffusion of these and other elements not only occurs during vacuum brazing and the diffusion anneal, but throughout the high temperature exposures as well.

Nickel and silicon diffusion in the honeycomb abradable seal was monitored using EDX point analysis at regular intervals upon polished sample cross-sections. A ratio of either peak heights or peak areas from a series of EDX spectra was plotted in the form of a chemical line scan using Microsoft Excel software. As the EDX system was only qualitative, ZAF corrected peak heights/peak areas ratios with reference to the Chromium K alpha peak were used. Apart from the area near the protective oxide system, the chromium level was assumed to remain constant (~20 wt%) and to give rise to no diffusion gradients throughout all sections of the component.

Periodic EDX point analysis was conducted on the sample cross-section. Starting at the very tip of the Fe-Cr-Al honeycomb foils, through the brazed section and finishing within the base plate. EDX spectra from each point were acquired using a beam accelerating voltage of 25KeV and a constant spot size and beam current at a fixed working distance. Spot analysis was conducted at intervals of >10 microns to avoid any overlaps in acquired data. Positioning of the acquisition point was carried out manually by moving the SEM stage in the X or Y direction. The calibrated vernier scale associated with the SEM stage was accurate to ±5 microns. This error is reduced by the ability to reposition the acquisition point to a higher degree of accuracy after repositioning the stage. The accuracy of this depends on the relative working distance, magnification and beam spot size.

Point analysis was carried out upon both double and single walled honeycomb cross-sections (see Figure 3.5). "Line scans" were always conducted through the centre of the single walled honeycomb cross-sections as shown in figure 3.5. Double walled nodes were scanned in a similar way to the single walled cross-sections. The positioning of the scan was always carried out over the area of a single foil and not over the brazed capillary location as shown in the diagram.

3.11 Columnar Grain Sizes

High resolution SEM and FEG-SEM images of polished sample cross-sections were used to measure the shapes and sizes of the columnar grain structures grown within the alpha alumina scale. This study was conducted on samples before and after aluminium exhaustion from the substrate. Oxide scales above interstitial void formations were also examined. Measurements were carried out using Image J 1.37v software. The positions of points used for measuring were user determined. Both columnar grain width and depth from the oxide/gas interface were measured at regular intervals in this way. Alternatively, the

distance from the metal/oxide interface or the alumina/chromia interface could be used. The columnar grain profile was then graphically represented and plotted against the other columnar grain profiles taken from the same sample SEM image.

Care was taken when establishing a mean grain size and overall range of columnar grain profiles. An average of 20 width measurements were acquired from each individual columnar grain measured. Many columnar grains were analysed per sample cross-section. The number of grains analysed varied from sample to sample due to the difficulty in achieving the high standard of polish necessary to observe clearly the oxide grains using a conventional SEM. When acquiring measurements, a cross-section sampling problem was thought possible as shown in figure 3.6. The columnar grain growth in plan view is very random and the grains impinge on each other. A cross-section of the sample that exposes the maximum diameter of all sampled grains is highly unlikely. This must be considered when evaluating the grouped data sets.

3.12 The Use of EBSD and SEM Techniques

EBSD work was used to observe the crystallographic and microstructural data of metal and oxide regions on both honeycomb and thin foil samples. EBSD automated data aided in the assessment of orientation relationships between alumina and chromia oxide layer growth, especially with regard to the thin foil samples.

EBSD maps were acquired by a Cam Scan X500 crystal probe FEG-SEM that had been optimised for electron backscatter diffraction. Seward et al. [151] gives a detailed description of the microscope design. The prominent difference between the X500 and conventional SEM's is that the column and electron-optic axis is inclined at an angle of 70° to the conventional vertical position. This

adjustment maintains the specimen and stage in a horizontal orientation whilst affording the ideal specimen-beam geometry required for EBSD analysis.

Maps (EBSD) were acquired using an accelerating voltage of 20KV, beam currents between 30 – 40nA, and a spot size of 5-10nm. Automated EBSD data was collected by moving the electron beam between analysis points. The Channel 5 software from HKL Technology was used to index EBSD patterns and to display (Band Contrast, All Euler, Grain Size, and Grain Shape) maps and pole figure data (see Section 4.3). Pole figures present individual crystal orientations in a given direction and use colour contours to show the strength of the texture compared to a random texture. Some data processing [152-154] was used to remove erroneous data from maps.

The Cam Scan X500 was also fitted with an analytical EDS system. This EDS system and Inca software program v.17 (Oxford Instruments), permitted point analysis, lines scans and chemical mapping of the selected regions. This facility could also be run during EBSD map acquisition.

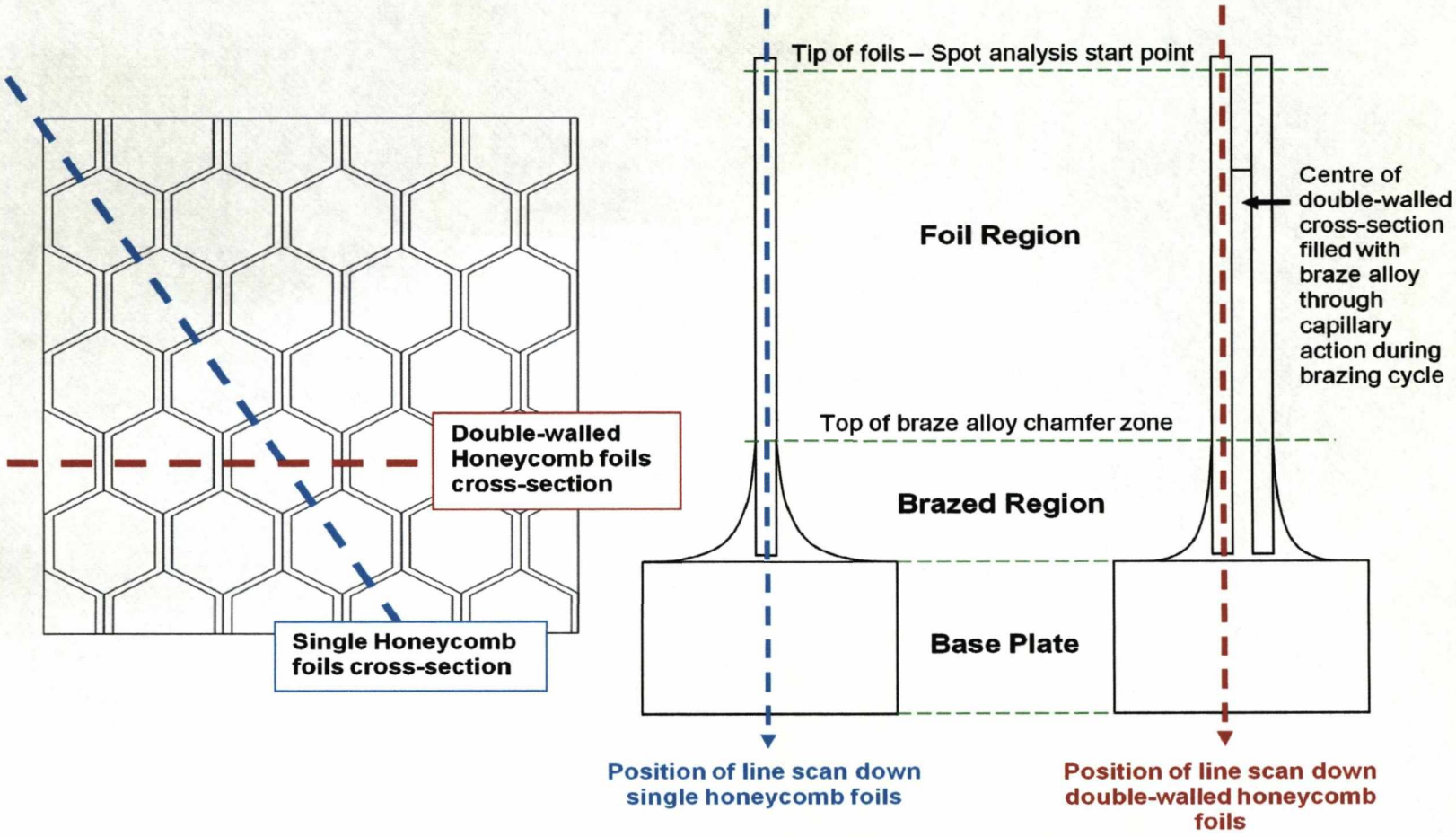

Figure 3.5: Position of line scans

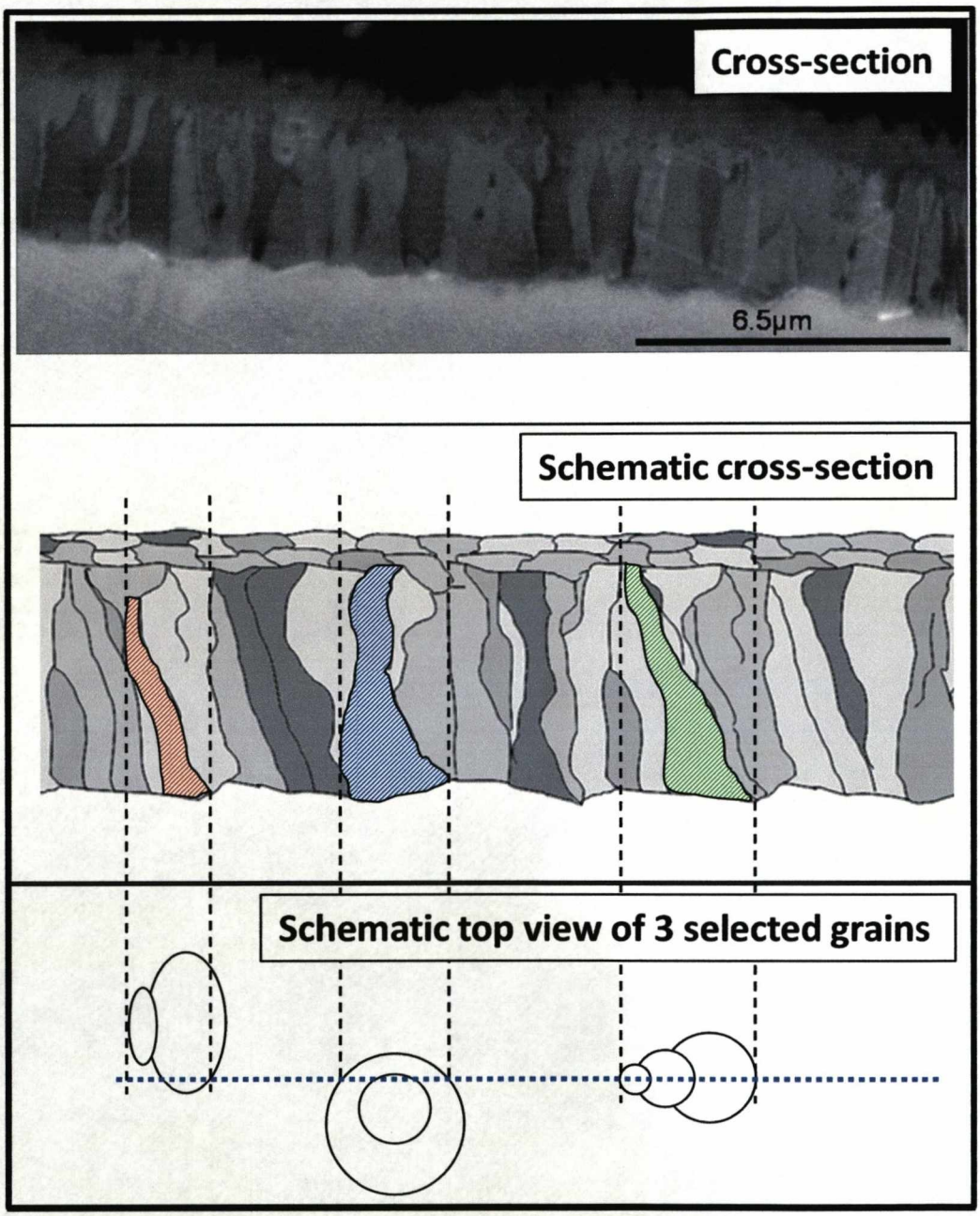

Figure 3.6: A schematic example of the sampling problem with column grain cross-sections

4. The Scanning Electron Microscope (SEM)

The scanning electron microscopy (SEM) is a useful analytical tool for studying the surface, or the near surface of bulk specimens. It works on the principle of accelerating a beam of electrons at energies between 1 and 30 keV. These electrons collide with and penetrate the specimen's surface and are absorbed or scattered by the atoms within a certain interaction volume. Detectors record the radiation emitted by this interaction volume which may be several microns in depth and diameter and can provide different information about the specimen. Almost all the kinetic energy which was carried by the primary electron will end up as heat in the specimen [155]. However, as a result of inelastic scattering of primary electrons, other various forms of radiation are emitted.

4.1 Elastic Scattering

Elastic scattering involves the change of direction of a primary electron, without any change to its energy. The strength of scattering by an atom depends on its atomic number.

4.2 Inelastic Scattering

Inelastic scattering occurs when a primary, incident electron loses a detectable amount of energy ΔE. This involves the transfer of energy (or loss of energy) to electrons or atoms of the specimen. A small portion of this energy will be used to generate other forms of radiation such as X-rays, light (photons), and secondary electrons. These forms of radiation can be acquired for imaging and chemical analysis. This radiation has to escape the specimen if it is to be detected and used for imaging/chemical analysis. These secondary effects are either in the forms of electrons or electromagnetic radiation.

4.2.1 Secondary Electrons

Secondary electrons form the most abundant and commonly used signal in scanning electron microscopy. They are defined as detected electrons with energies below ~50eV [155]. Secondary electrons which are detected are usually emitted from atoms which are a short distance away from the surface and near the incident beam where the primary electrons enter the specimen. This is represented in figure 4.1. However, as they are defined by their energy, they could also be mistaken for primary electrons that at the end of their trajectory have escaped from the sample with very low energies.

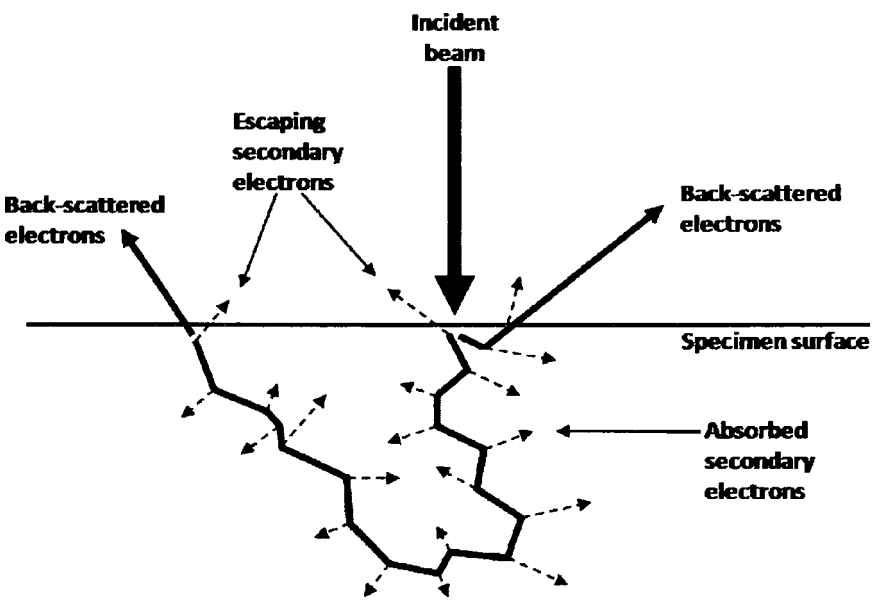

Figure 4.1: Inelastic scattering of primary electrons within an interaction volume [155]

4.2.2 Back-scattered Electrons

The definition of a back-scattered electron is a primary electron which leaves the surface of the specimen before releasing all its energy, as shown in figure 4.1. Back-scattered electrons are more commonly scattered from the specimen surface whilst their energy is still high. Back-scattered electrons commonly originate from regions slightly larger than those from which secondary electrons may be emitted. Such signals are useful for imaging, diffraction and compositional imaging.

Compositional information is obtained from specimens with back-scattered electrons as the back-scattered coefficient η varies monotonically with atomic number Z. This is advantageous when analysing e.g. alloys with multiple phases present.

4.2.3 X-rays

The incidence of primary electrons may cause the removal of an electron from an orbital in an atom. These atoms will then be in an excited, high energy state. The relaxation of excited atoms will occur when the empty electron state is filled by an electron from a higher level and the excess energy is release as either:

- Cathodoluminescence
- Characteristic Auger electron
- X-ray radiation

X-rays represent the change between the two energy states and are also characteristic of a specific element. Most X-ray radiation will be emitted from the entire interaction volume of a sample, as X-rays are not easily absorbed by a

specimen. Therefore, X-rays are acquired from larger volumes than secondary and back-scattered electrons.

EDX is the principal detection system used to acquire the broad range of X-rays emitted by an interaction volume from a sample. Measuring the energy of each X-ray allows the qualitative analysis of a specimen. The number of X-rays of a specific energy detected per second can be linked to the relative amounts of an elemental species present and maybe used for semi-quantitative analysis.

4.3 EBSD

The signals from back-scattered electrons of the highest energy (i.e. those that have been elastically scattered), originate near the incident beam. These back-scattered electrons are capable of yielding crystallographic information about the sample. This arises from the effects of diffraction of the scattered electrons as they leave the sample, and can be used to form Kikuchi patterns such as those obtained via TEM (Transmission electron microscopy). The technique is called electron back-scatter diffraction (EBSD) and is developing rapidly as a widely used analytical tool. The technique is very dependent upon the orientation of the crystal/sample with respect to the incident beam.

EBSD relies on the interaction of primary electrons from the SEM electron beam with the samples surface. Back-scattered electrons can be classed as electrons that have been reflected back from the sample due to elastic scattering [156], or electrons with less energy than the primary beam due to inelastic scattering [157]. Scattering can be considered in two ways, a large single scattering event where the electron is deflected >90° due to close interaction with an atomic nucleus (Rutherford Scattering) or multiple low angle scattering to add up to more than 90° of deflection.

The atomic number of the elements contained within a sample, have a major effect in determining the strength of the back-scattered electron signal. Elements with a high atomic number, have a bigger nucleus which causes an increased amount of electron scattering. The angle the scanning electron beam makes with the specimen is also important to EBSD (see Figure 4.2). For EBSD analysis, the specimen is tilted to an angle of 70° with respect to the incoming beam. This is to increase the yield of back-scattered electrons.

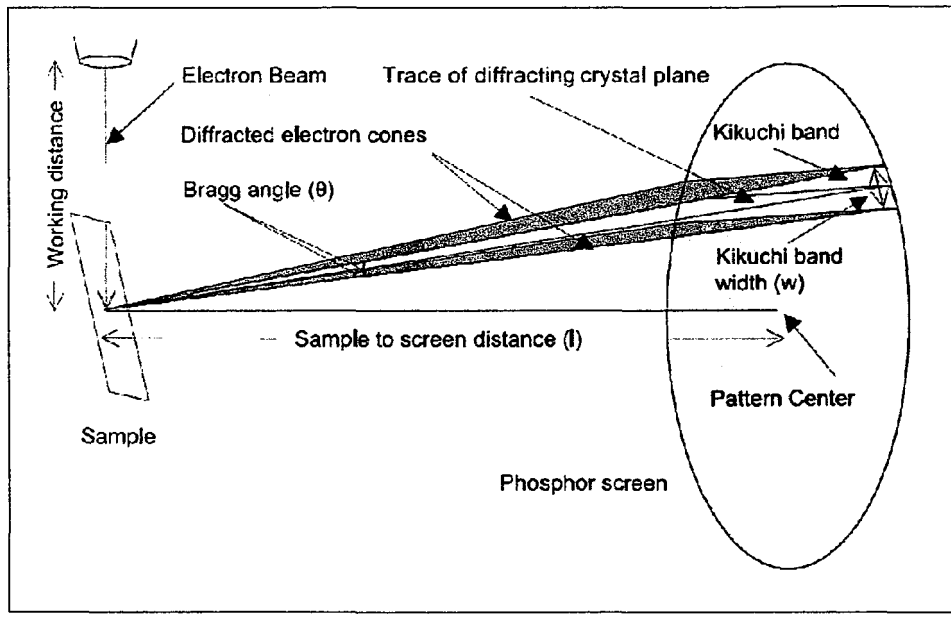

Figure 4.2: A simplistic model of an EBSD facility [158]

Atoms close to the surface of a specimen will inelastically scatter a fraction of the incident electrons with a small loss of energy to form a divergent source of electrons. A small proportion of these electrons are incident on atomic planes of the specimen, at angles which will satisfy the Bragg equation:

$$n\lambda = 2d \sin\theta \qquad (4\text{-}1)$$

where:

$n =$ an integer

$\lambda =$ wavelength of the electrons

$d =$ spacing of the diffracting plane

$\theta =$ angle of incidence of the electrons on the diffracting plane

Back-scattered electrons are diffracted to form a set of paired large angle cones, corresponding to each diffraction plane. Regions of enhanced electron intensity between the two cones produce the image of the characteristic Kikuchi bands of the electron back-scatter diffraction pattern.

The resulting diffraction cones are imaged on a phosphor screen, since the opening angle of the cones from each lattice plane is almost 180° they appear as straight lines on the phosphor screen [159]. A sensitive charge coupled device (CCD) video camera then transfers the patterns to a computer which interprets the crystallographic orientation.

These Kikuchi bands can be indexed by the Miller indices of the diffracting crystal plane from which it formed. Most modern EBSD systems are automated and indexing of Kikuchi bands is achieved automatically by comparing acquired patterns with those from a reference library.

The centre lines of the Kikuchi bands correspond to the projection of the diffracting planes on the phosphor screen. Each point on the phosphor screen corresponds to the intersection of a crystal direction with the screen. In particular, the intersections of the Kikuchi bands correspond to the intersection of zone axes in the crystal with the phosphor screen. These points can be labelled by the crystal direction for the zone axis. The positions of the Kikuchi bands can be used to calculate the orientation of the diffracting crystal.

The advantage of using EBSD is its ability to measure crystal orientation and therefore, its ability to show conclusively the position of all grains and grain boundaries when examining sample microstructures. This is advantageous as standard polishing and chemical etching techniques usually applied to samples which are then examined by SEM and optical microscopy may not always reveal all microstructural features.

The EBSD technique is used to form crystal orientation maps. This is achieved by scanning the electron beam over the sample and measuring the crystal orientation from the diffraction pattern produced from each point. These crystal orientation maps indicate crystal orientations with colour. Points on crystal orientation maps of the same colour represent the same orientation. Similar crystal orientations are represented by similar colours. In these maps a grain is a region of the sample where the crystal orientation is the same within a certain orientation angle tolerance. These types of maps can be processed to show the positions of all grains and grain boundaries within the specified region of microstructure analysis.

The EBSD technique is complementary to conventional analysis techniques by providing information about crystal orientations from bulk specimens. The facility provides a link between microstructure and crystallography, and reduces the amount of sample preparation, which would otherwise be necessary in order to use the TEM for similar analysis.

EBSD is a technique which is ideal for texture analysis. Polycrystalline materials consist of many grains, the orientation of these grains can be random, or it may consist of grains which cluster close to certain crystal orientations. The manner in which these grains cluster is called texture. Texture may arise

from a number of factors including primary casting, and later processing steps, etc.

Crystal orientation data also provides data about sample texture. EBSD can relate the calculated texture or textures present to the microstructure of the material. EBSD can analyse different textures on the same sample microstructure. EBSD is found to be complementary to the standard method of measuring texture using X-ray diffraction.

EBSD can characterise grain boundaries and measure the distribution of various boundary types in a sample. EBSD characterises grain boundaries by a difference in crystal orientation that is greater than the allowed level of tolerance. EBSD can be used to measure statistical data about the type of grain boundaries present. These usually are termed "low" or "high" angle boundaries and depend upon the difference in the crystal orientations of grains either side of the boundary. Grain boundaries which represent small changes in crystal orientation between grains are termed low angle boundaries. Grain boundaries which represent large changes in crystal orientation between grains are termed high angle boundaries.

Band Contrast, All Euler, Grain Size, and Grain Shape maps are produced by the EBSD facility and are explained below:

- Band contrast maps (otherwise known as pattern quality maps) present greyscale images that show the quality of the diffraction patterns indexed during an EBSD scan on a particular sample area. Shades of grey are defined by the strength of the acquired diffraction pattern. Black represents a non-indexed area on these maps. These maps are influenced by a number of factors including local crystalline perfection, sample preparation, surface contamination and the phase and orientation being

analysed. These maps will often reveal features such as grains, grain boundaries and surface damage such as scratches within a selected area.

- All Euler maps present information about the crystallographic orientation of the sample. All Euler maps are colour representations of crystallographic coordinate information from individual grains. Similar colours upon these maps represent similar sets of Euler angle rotations. All Euler maps use Euler angles (φ_1, Φ, and φ_2) and represent the necessary three rotations to superimpose the coordinate system of the crystal upon the coordinate system of the sample.

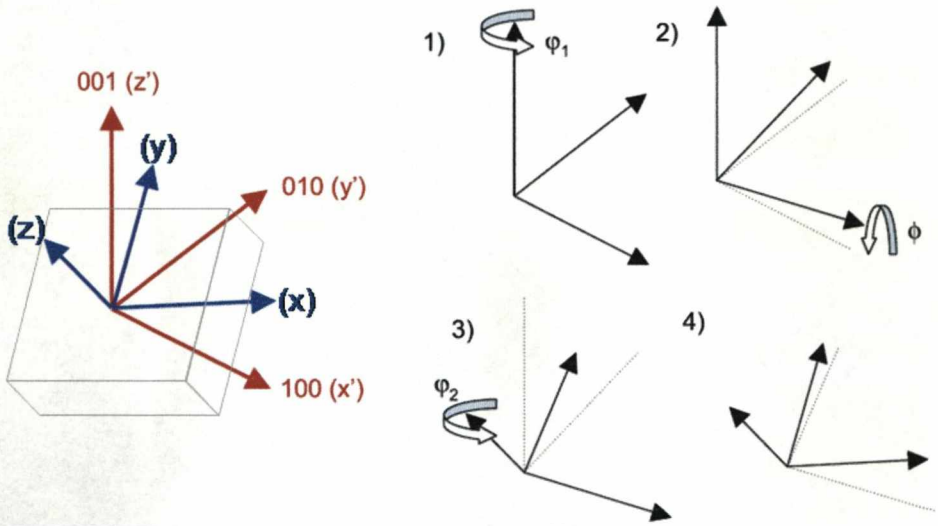

Figure 4.3: This shows the rotations necessary to superimpose the crystal coordinate system (red) onto the sample system (blue). The first rotation ϕ_1 is about the z-axis of the crystal coordinate system. The second rotation is Φ about the new x-axis. The third rotation is ϕ_2 about the new z-axis. The dotted lines show the positions of the axis before the last rotation. Note that the orientation can also be defined by an equivalent set of Euler angles which superimpose the sample coordinate system onto the crystal coordinate system.

- Grain shape maps highlight the aspect ratio of grain structures within the selected regions analysed throughout this work.

- Grain size maps indicate the proportion of grains present of a certain size using colour representation.

EBSD is beginning to replace some of the work which would have been traditionally carried out by TEM. EBSD allows the acquisition of diffraction data from large areas of material from bulk specimens. This technique has many advantages, including the ability to calculate orientations of particular features of a microstructure e.g. α-alumina grains. Its use is becoming more common in the field of oxidation and corrosion.

5. Results

The results section presents the broad analysis from the as-received condition, through to high temperature oxidation and eventual failure of honeycomb abradable seals, consisting of MI2100 foils, BNi-5 braze alloy, and a Haynes 214 alloy base plate. The section shows the results from isothermal oxidation testing of these abradable seals at 1100°C and 1200°C. As little as 300 hours at 1200°C lead to the eventual failure of the abradable seals by thin foil rupture. Cross-section analysis of thin foil failure is also presented and reveals extensive interfacial void formation at the metal/oxide interfaces. The different types of voids formed are shown, along with interfacial void filling. Finally the extent of thin foil degradation is highlighted upon honeycomb end foils.

5.1 As-received Honeycomb Abradable Seal

The condition of the as-received rectangular subsection of honeycomb abradable seal was examined prior to any high temperature oxidation testing. The initial investigation recorded the quality of the brazed joint and the condition of the honeycomb cells. Both external and cross-sectional analyses of the brazed regions, foils and base plates were conducted. Tests looked for erosion of foil material at the braze/foil interface, and any porosity within the brazed zone.
Figure 5.1(a), (b) and (c) are plan view and side-on images of the as-received rectangular subsection of a honeycomb abradable seal sample. These images were recorded using a flatbed scanner. These images give a realistic idea of size and clearly show the position of the spot-welds on the honeycomb foils, as described in Section 3.2.

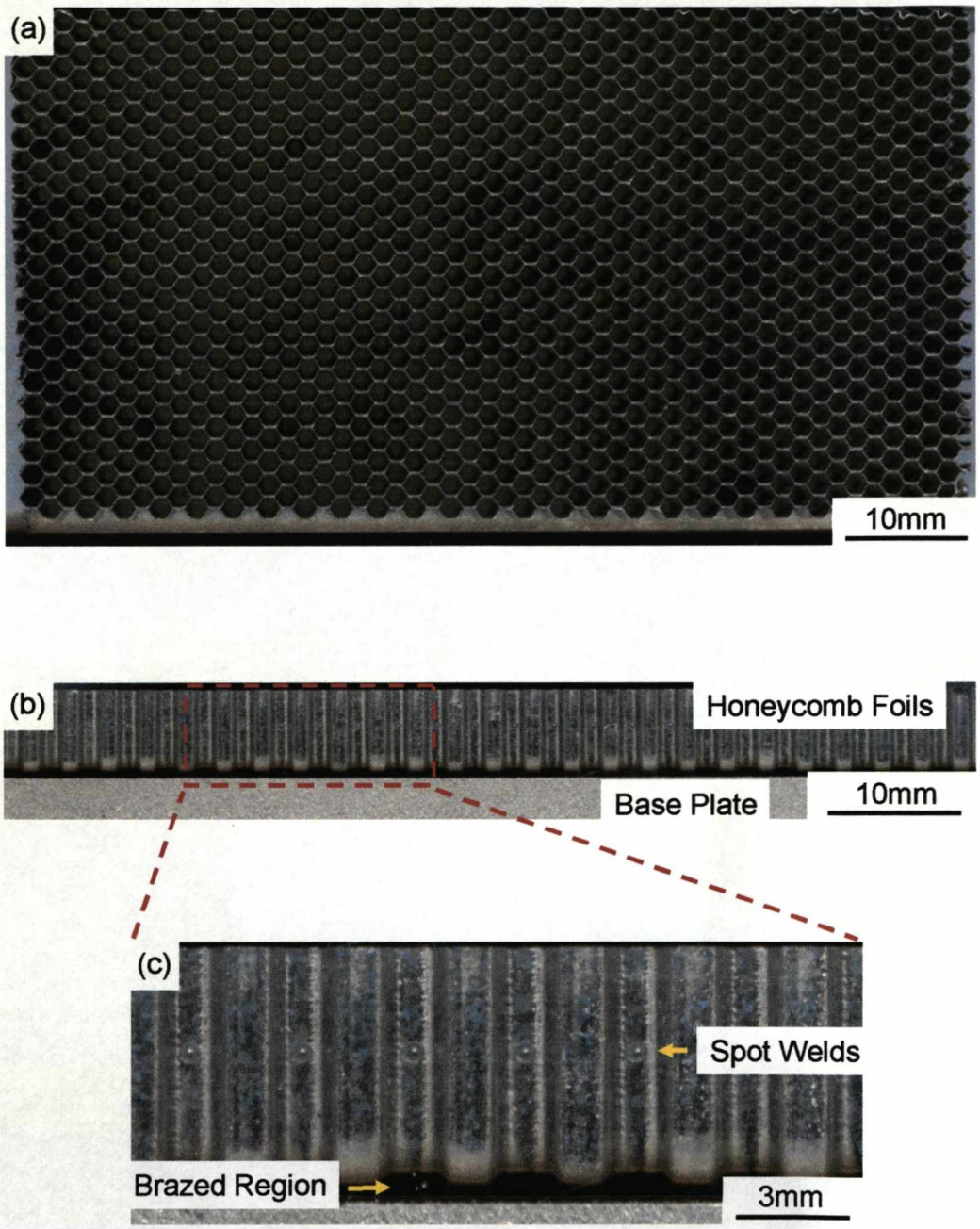

Figure 5.1: Scanned images of the honeycomb abradable seal in the as-received condition shown in (a) Plan view and (b) Side-on view. Image (c) again presents the side-on view with an increased magnification

A small sample of the honeycomb seal construction was cut and metallographically prepared for examination of the brazed joint in cross-section. SEM images reveal a high quality joint between the Haynes 214 base plate and MI2100 foils without any porosity or signs of cracking. Figure 5.2 is a low magnification "composite" SEM image that demonstrates the effective method of joining that brazing provides. The image clearly shows how the wetting of the brazing alloy produces clean chamfered edges at the base of the honeycomb cells which provide a comprehensive joint between foils and base plate. The capillary action of the brazing alloy can also be observed in this micrograph. Capillary action occurs in this component as the spacing between two Fe-20Cr-5Al foils, in a double walled honeycomb node can be less than 20 microns. During vacuum brazing, this small spacing between two parallel foils causes a pressure differential and drives the brazing alloy up the capillary. The spacing between the two parallel foils is not constant. The spot-weld at the centre of the honeycomb node is the only pinned point. Therefore, away from the pinned location, the space between foils gradually increases (Figure 5.3). The brazing alloy can also be found at much larger spacing, up to the point where the double walled node separates. Figure 5.2 demonstrates the different heights achieved by the capillary action at three different nodes. The regions shown are locations of maximum separation of the foils at nodes prior to separation for the honeycomb cell and central cross-sections of nodes as indicated. This demonstrates the non-uniform spacing between foils in the double-walled nodes. This effect can, however, be compounded by a non-perpendicular slice of the samples cross-section. Figure 5.4 shows a rather more uniform effect of the brazing alloy capillary action over a much larger area.

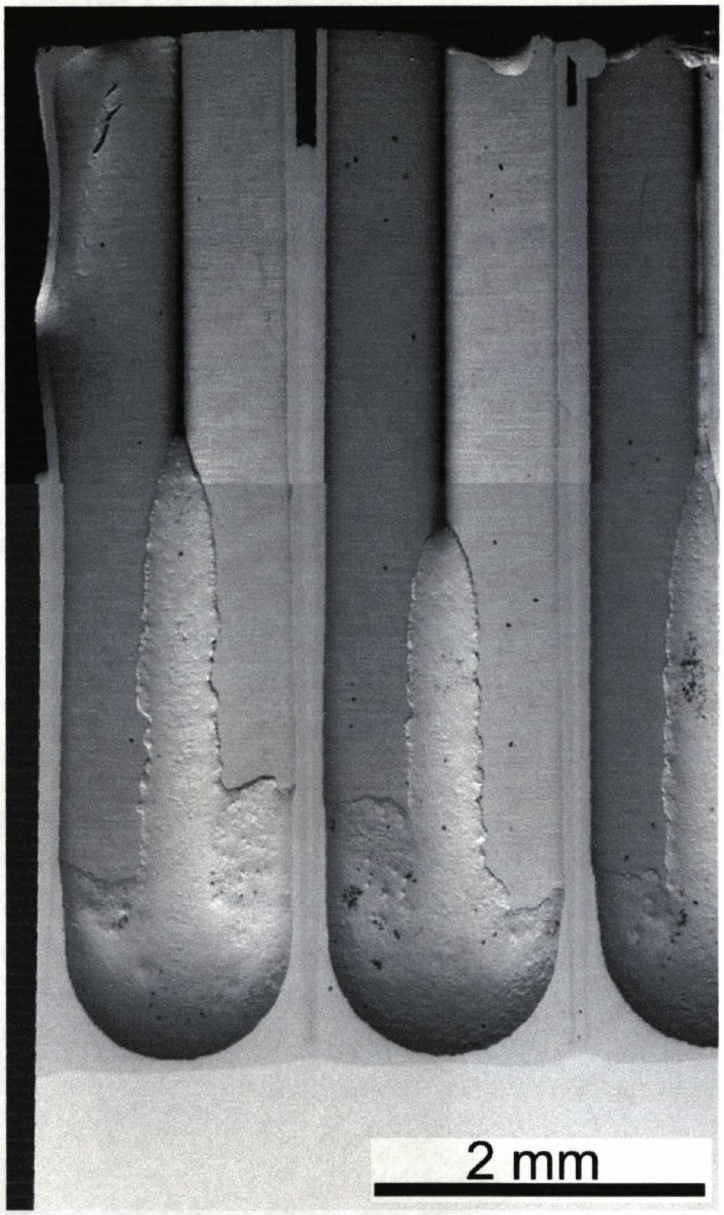

Figure 5.2: Low magnification SEM composite image of an as-received honeycomb abradable seal in cross-section after polishing to a 1 micron standard

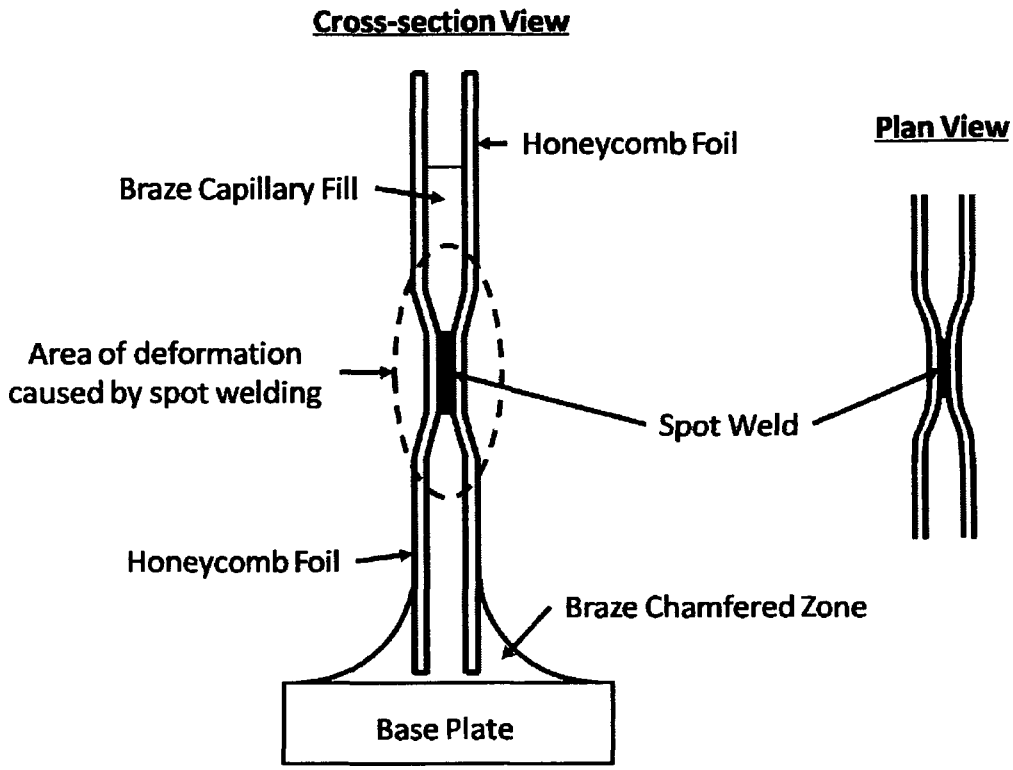

Figure 5.3: Demonstration of the spacing between the two Fe-20Cr-5Al foils at a double-walled honeycomb node

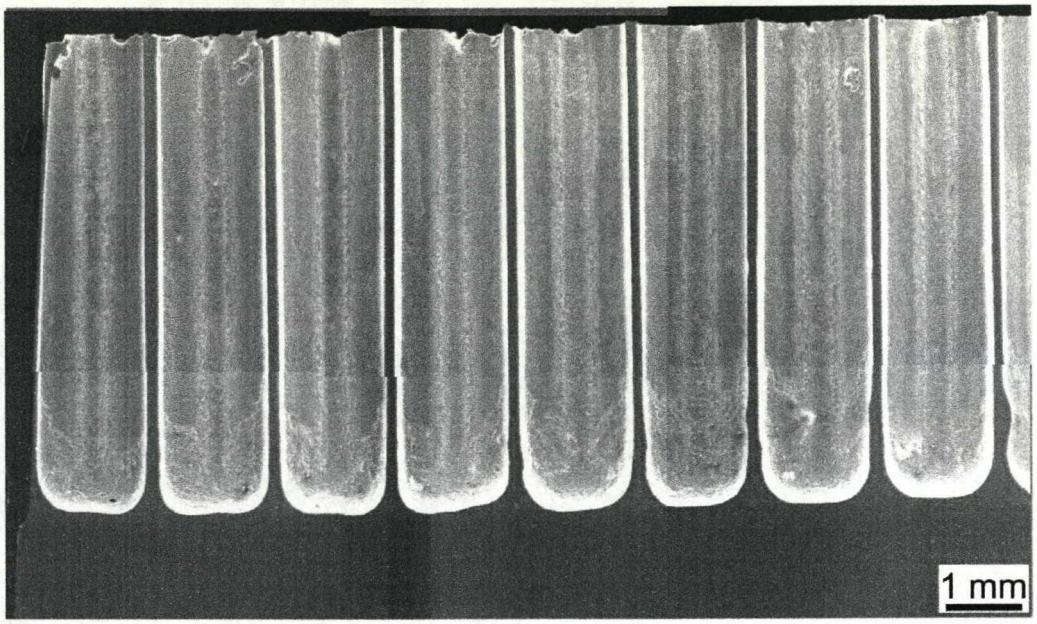

Figure 5.4: Low magnification SEM composite image of an as-received honeycomb abradable seal in cross-section. Sample shows a consistent capillary fill height between all honeycomb cells shown

The three separate components (foils, braze, and base plate) can still be distinguished in figures 5.2 and 5.4. However, the early signs of diffusion between all three constituents, in cross-section, can be seen. The nature of brazing causes a diffusion bond between the materials. Through high temperature exposure (>950°C) this diffusion of braze alloy constituents continues.

Figure 5.5 is a composite optical micrograph of the polished brazed cross-section in its as-received condition. The image presents all three components and the effects of brazing. The clearest observation from the micrograph is the multiple phases present in the braze alloy regions. This effect is very common in brazed components. Short diffusion anneals and testing at high temperatures (1200°C) for times greater than 20 hours has shown the complete inter-diffusion of this multi-phase region. This result will be presented later in this section.

This micrograph also shows the positions of the honeycomb foil ends that are submerged within the brazing region. The brazing process applies pressure to the base of the honeycomb foils, and in the case of the double-walled honeycomb nodes, pushes the two foils close together. This reduces the capillary width at the base of the foils. However, as shown further up the foils in the micrograph, the initial capillary width is gradually restored. The gap between the foils is completely filled with the brazing alloy.

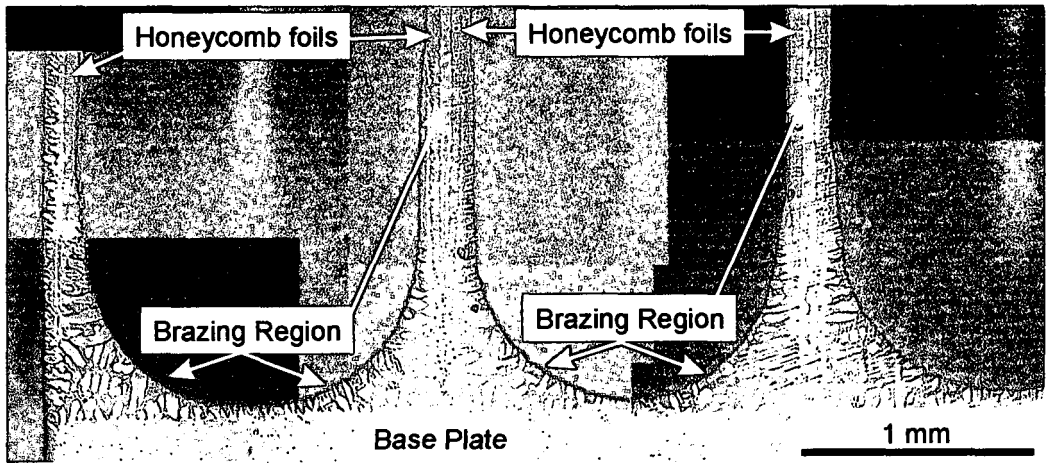

Figure 5.5: Optical micrograph of the brazed joint region clearly showing the presence of a multiple-phase braze region

A single one hour diffusion anneal at 1100°C under a vacuum of 10^{-4} mbar was carried out on the same sample. In cross-section the multi-phase brazed region could still be seen but to a much lesser extent. The distinction of all three parts of the component, especially the braze/base plate interface became more difficult. This is shown in figure 5.6. The images of the multiple phases in the brazing alloy region were recorded, but no chemical analysis conducted. These phases were found to completely diffuse into the substrate matrix after 100 hours oxidation testing in lab air at 1100°C.

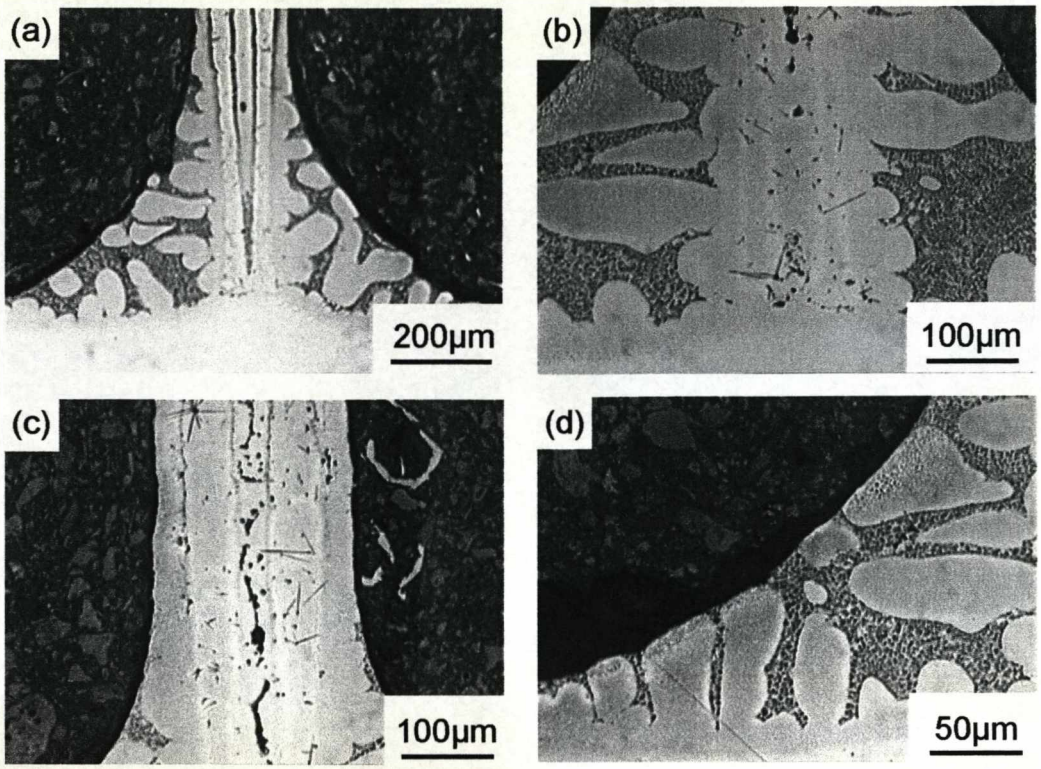

Figure 5.6: Optical micrographs of the polished and etched cross-section of the brazing region. Image (a) shows the entire brazed joint for a double-walled honeycomb node. Images (b), (c), and (d) show the subsequent parts of (a) at higher magnifications

5.2 Oxidation of Honeycomb Abradable Seals

A series of honeycomb abradable seal test samples were oxidised at 1100°C and 1200°C in laboratory air. Oxidation times varied for each temperature. The abradable seal test specimens oxidised at 1100°C were tested for times up to 1000 hours, whilst times of only 600 hours at 1200°C were used.

Oxidation testing of the honeycomb abradable seal at 1200°C at times greater than 300 hours revealed excessive oxidation and attack upon the Fe-20Cr-5Al honeycomb foils just above the brazed region. Testing for longer times at this temperature (>300 hours) presented the detachment of the honeycomb foils from the base plate. Testing indicates that it is not the brazed joint that is failing, but a region within the honeycomb foils. This region is located ~200-500μm above the brazed region.

Oxidation testing of the honeycomb abradable seal at 1100°C for times up to 1000 hours showed excellent oxidation performance for increased engine operating temperatures. The growth of a protective alumina scale was visually evident upon the component, as it exhibited a grey colour. This was attributed to the underlying metallic substrate that was visible through a thin, transparent, and protective oxide layer. This was later verified by EDS analysis.

Visual examination of all honeycomb abradable seal test samples after oxidation at 1100°C confirmed that the honeycomb foils had remained in contact with the base plate. Typical examples of tested honeycomb abradable seals after short times can be seen in figure 5.7. These images present the condition of the abradable seal after oxidation testing and cooling. Oxidation times for these test specimens were only up to 60 hours. The typical test sample end condition can be seen in these three images. The honeycomb foils were all typically grey in colour, representative of a transparent alumina scale, whilst the base plate and

brazed region were always found to have a green colouration, typical of a chromium oxide scale formation. Upon cooling, oxide spallation was observed on all three test samples. An SEM investigation of each of the three sample perimeters showed good oxide scale adhesion on the honeycomb foils, with the exception of some areas located near the brazed region. Figure 5.8 is an example of one of these regions after one hour oxidation at 1100°C and is accompanied by EDX analysis. Oxide growth upon all parts of the component can be seen, most of which is alumina oxide scale with the exception of some chromia and nickel oxide present. Higher magnification SEM images of selected regions show minor spallation of the oxide scales. This was assumed to occur upon cooling. Two examples of this area are shown. One shows a needle like alumina scale, typical of theta alumina. Theta alumina is not stable at these high temperatures and may have formed initially on the surface. This morphology may be remnant on the surface, however the oxide is most likely to have transformed to alpha when heated up. A small portion of this has spalled in figure 5.9, revealing a bare metal surface low down on the honeycomb foils. This example shows evidence of theta alumina spallation above a triple junction grain boundary, after only one hour oxidation at 1100°C. Another occurrence of spallation at this short time is theta alumina loosing contact with the metallic substrate at the expense of alpha alumina (Figure 5.10).

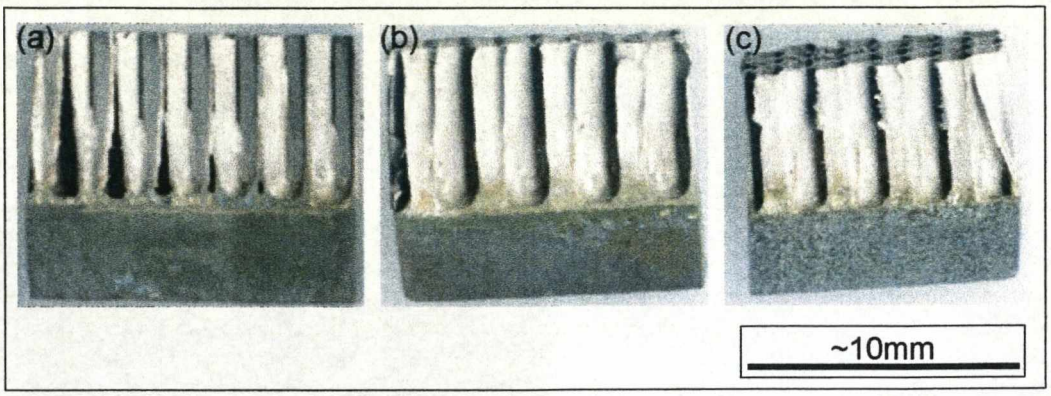

Figure 5.7: Three separate honeycomb abradable seal samples, (a), (b), and (c) have been oxidised for 60 hours at 1100°C

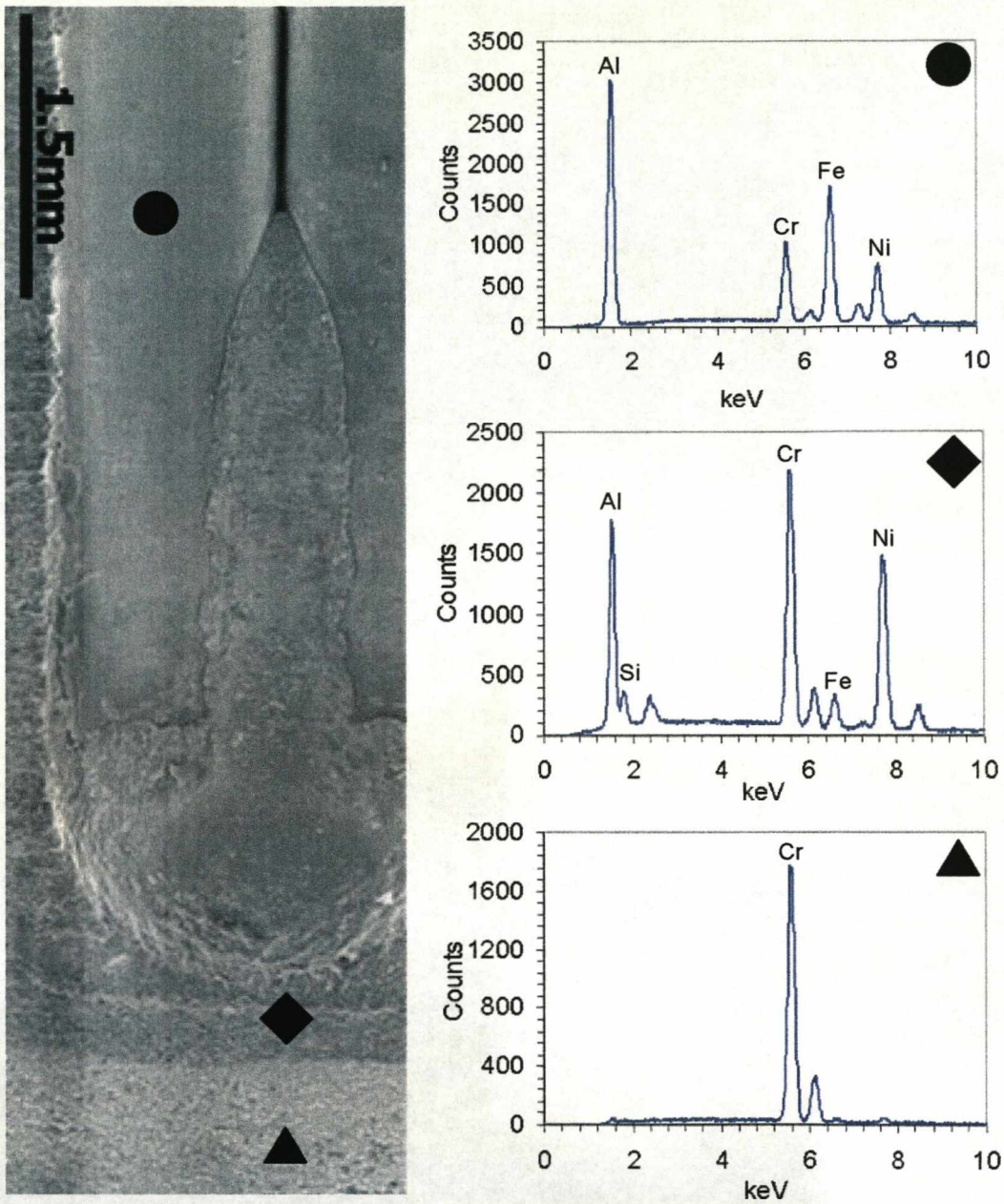

Figure 5.8: Map of a honeycomb node accompanied by EDX spectra after oxidation for 1 hour at 1100°C

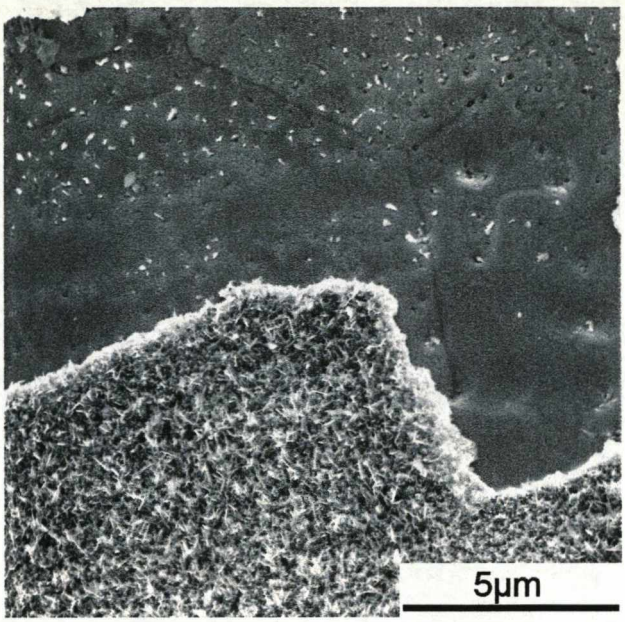

Figure 5.9: Oxide spallation near brazed region. Theta alumina spalled above a grain boundary triple junction on the foils

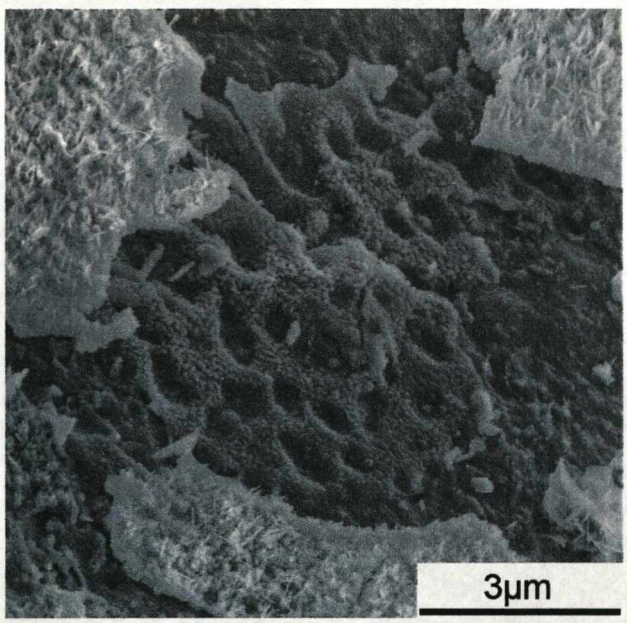

Figure 5.10: Oxide spallation. Theta alumina spallation at the expense of the stable alpha-alumina formation

Up to 450 hours at 1100°C, the honeycomb abradable test samples show excellent oxidation performance. Discolouration and increased levels of oxide growth and spallation low down on the honeycomb foils began after this time. Optical and scanning electron microscopy was used to examine the region. Figure 5.11 is a polarised light optical micrograph that shows the region of the attack above the braze chamfer. Grey colouration is attributed to alumina scale formation, whilst green, yellow, and brown are attributed to the formation of less stable oxides. Attack of this region was greater with increased exposure times at 1100°C. However initial examination of all honeycomb test samples above 450 hours exposure at 1100°C did not reveal failure of the component at this location or any other regions of excessive oxidation upon the outer perimeter.

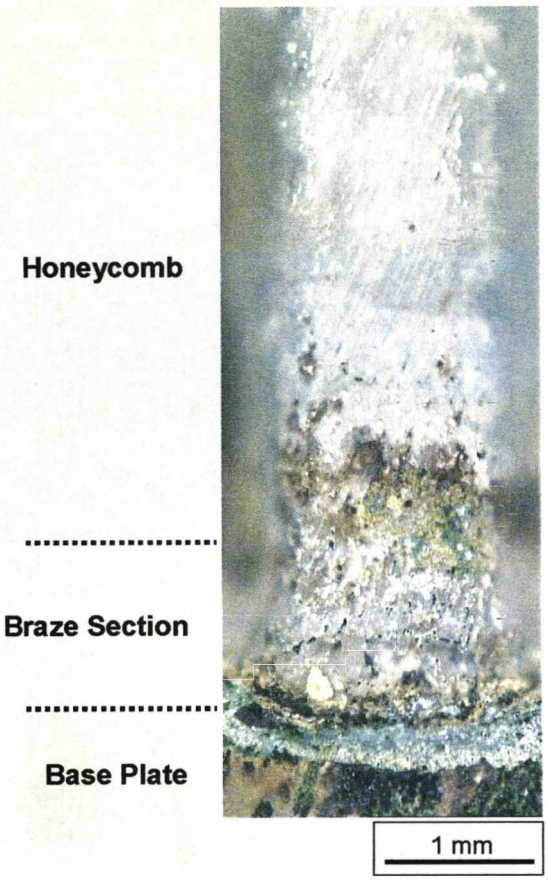

Figure 5.11: Honeycomb abradable seal sample, oxidised for 450 hours at 1100°C. Polarised optical micrograph that shows the region of the attack above the braze chamfer

Tests at 1200°C were performed to observe accelerated oxidation life testing. Additionally if satisfactory performance was recorded, this would be beneficial to further increases in engine operating temperatures.

Failure of the honeycomb abradable seal was recorded at times less than 600 hours at 1200°C, where failure was defined as the detachment of the honeycomb foils from the base plate. Examples of such failure can be seen in figure 5.12a,

b, c, and d. All samples shown here provide evidence of failure at a location on the foils, just above the brazed region, as seen in the 1100°C cases.
Oxide spallation upon cooling was noticeably increased at this temperature.

Polarised light optical micrographs show a significant increase in attack on the foils, just above the brazed region, for much shorter oxidation times. Figure 5.13 is an example of the condition of the honeycomb foils after only 300 hours. The polarised light image shows a dramatic increase in the size of the less stable oxide formations, mainly represented by the green coloured oxide here. SEM and EDX analysis found this region to be chromia, with traces of nickel and iron within the oxide. These could also be in the form of oxide, however, with both foils and braze being high in iron and nickel concentration, the peaks found in the EDX spectra (Figure 5.14) could all be attributed to components of the alloy matrix, picked up from the substrate.

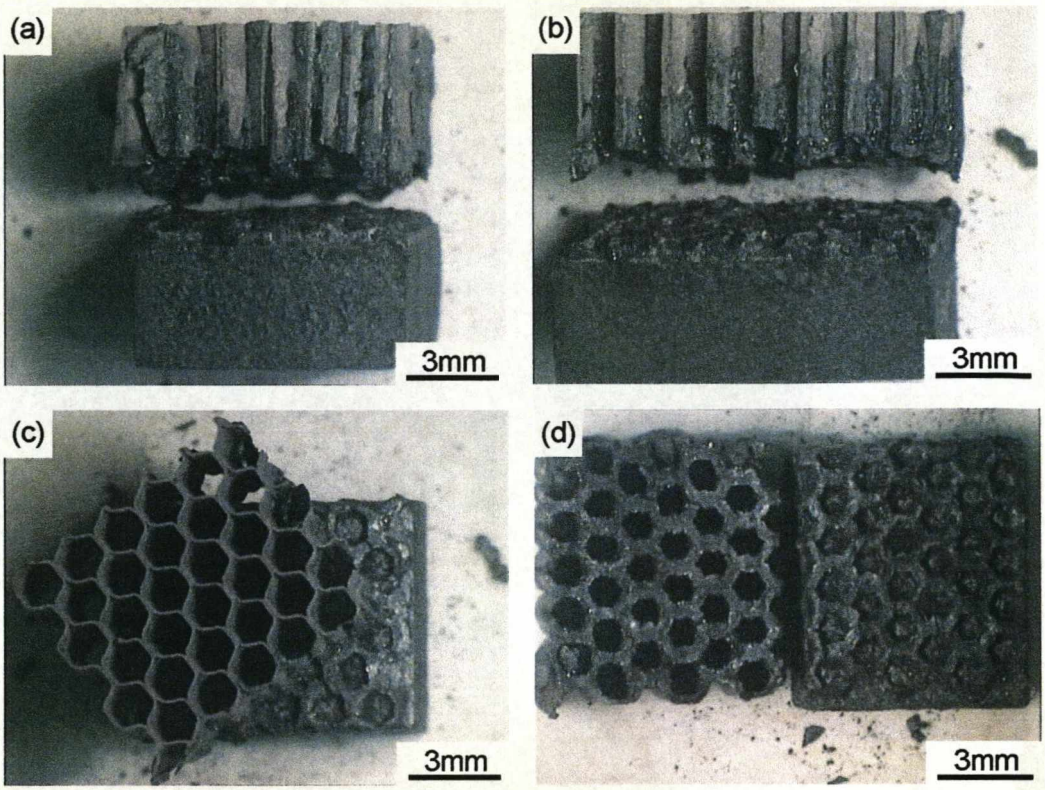

Figure 5.12: Four images of honeycomb seal failure at 1200°C. Samples a, b, c, and d, all failed during oxidation for less than 600 hours.

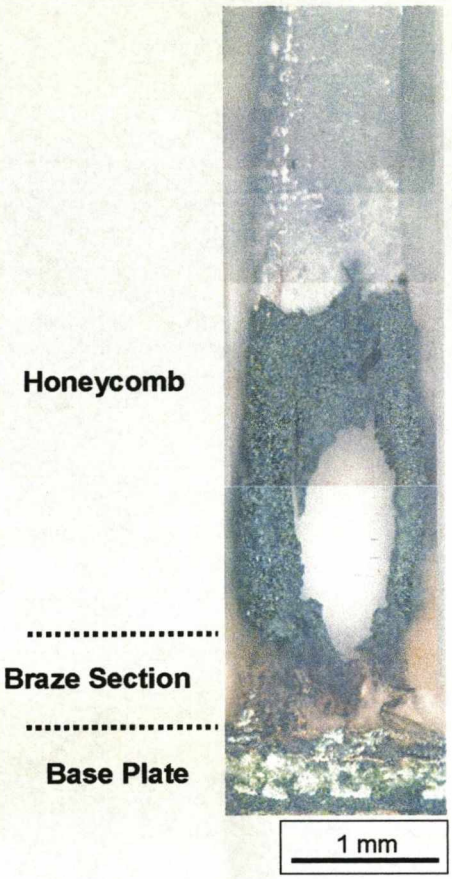

Figure 5.13: Polarised optical micrograph of the external perimeter of a honeycomb abradable seal, oxidised for 300 hours at 1200°C

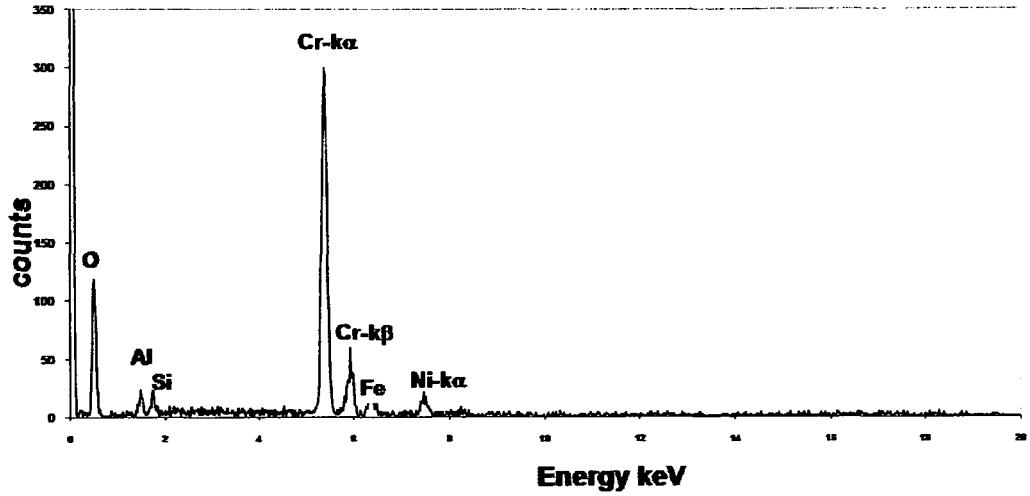

Figure 5.14: EDX spectra of chromia with traces of iron and nickel. Taken from the region shown in the polarised light micrograph above

Since degradation of the foils just above the brazed region could be observed at both temperatures, a comparison of sample cross-sections from 1100°C and 1200°C tests at times when the attack was first observed is shown in figure 5.15. Oxidation times of 460 hours at 1100°C, and 300 hours at 1200°C are shown. Both images present double-walled honeycomb foil nodes and are recorded from a similar position of sample cross-section in each case.

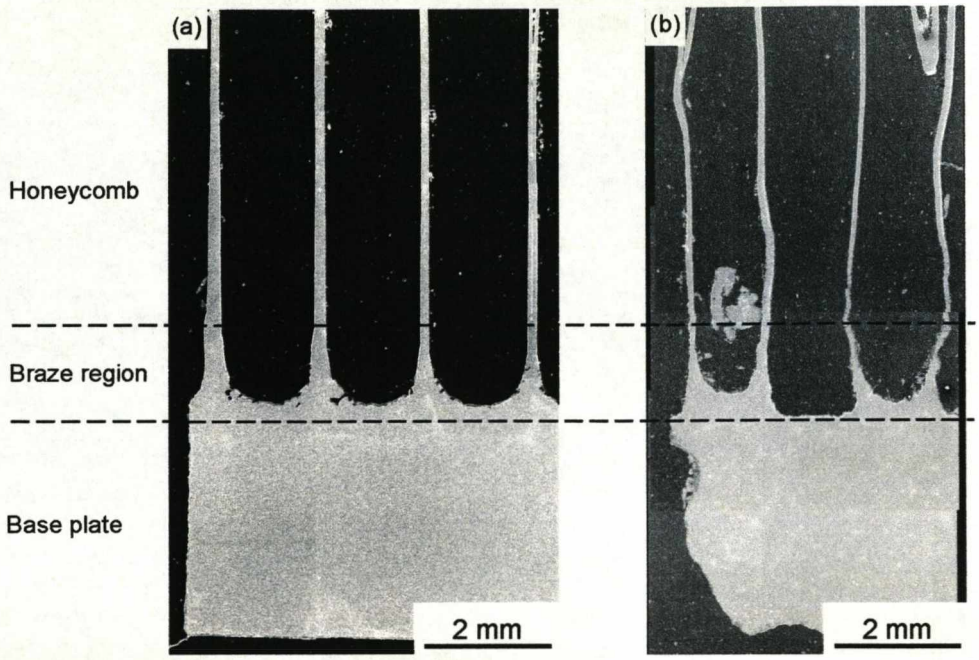

Figure 5.15: Comparison of 1100°C (a) and 1200°C (b) sample cross-sections at the first signs of honeycomb foil degradation

Increased levels of oxidation and attack are more clearly observed on the 1200°C image (Figure 5.15(b)). Double-walled honeycomb nodes show the consumption of metal substrate and foil thinning through high temperature oxidation. The two honeycomb foil nodes to the right of the 1200°C image present almost complete failure and detachment. Indicated in figure 5.13, further oxidation would separate the foil into two parts at ¼ foil height with reference to the Haynes 214 base plate, in this case.

In comparison to the 460 hours at 1100°C test specimen, 300 hours at 1200°C presents a significant increase in foil deformation and curvature. Sample hot mounting procedures under pressure were first thought to be responsible for this.

However, cold mounting under atmospheric pressure produced a similar result. This is thought to be a consequence of creep in the substrate alloy.

Oxidation and degradation of the brazed regions can be observed in both micrographs. Consumption of the brazing alloy occurs through the rapid and unstable formation of nickel and chromium oxides. Removal of more substrate alloy from the brazed region is recorded after tests at 1200°C. Tests at 1100°C present a more localised attack of the brazed regions. This can be described as a "pitting" effect upon the braze alloy chamfers.

The condition of the 1100°C cross-section is significantly better than expected. The early signs of degradation upon the test samples exterior would have suggested a more visible attack through the sample cross-section, much like the foil thinning observed at ¼ foil height after 300 hours at 1200°C. Degradation of the 1200°C sample is clearer to see.

SEM and EDX were used to analyse the conditions of the double-walled honeycomb nodes and the growth of the protective oxide scales. Progressive images of the honeycomb foils, in cross-section, from top to bottom for each sample were recorded. Progressive imaging of one particular end foil demonstrates the level of degradation at 500 micron stages. Figures 5.16 (a) to (i) are taken from the cross-section of an end foil of a honeycomb abradable seal sample that has been oxidised at 1200°C for 300 hours. The position of foil degradation and failure is shown through these images.

Figure 5.16(a) is taken at a location near the top of the honeycomb foil. This image displays two Fe-20Cr-5Al foils that have inter-diffused with the Ni-based brazing alloy to produce a single alloy substrate. Well adhered to this substrate is a 5-8μm thick aluminium oxide layer of uniform thickness. Aluminium oxides were verified using EDX analysis. Even at this low magnification, the

oxide layer consisted of two distinct parts. A layer of equiaxed grains at the gas interface of the oxide, and a layer of large columnar oxide grains below. This formation of alumina is typical of the inward growing alpha phase. The alpha phase formation of alumina is expected at these temperatures. The image also shows two very small voids/pores at the metal/oxide interface on the right hand side. They appear almost semi-circular and are likely to be in the form of a hemi-sphere in 3-dimensions. The radius of the void in 2-dimensions was 1-2μm. The oxide upon the left hand side has a small micro-crack between the gas/oxide and metal/oxide interface. The presence of micro-cracking in the alumina scale is common upon honeycomb foils of this overall condition. It is unknown whether the crack has formed upon cooling or has been initiated during the high temperature exposure. Although the oxide scale thickness will vary, this is a typical description of the honeycomb foil cross-section without any level of degradation.

A section of the sample imaged 500μm further down the foil towards the base plate is shown in figure 5.16(b). A well adhered oxide scale of similar thickness is still present. Interstitial void formation between the metal and oxide interface is clear. The voids are present upon both sides of the honeycomb node and vary in size. The formation of larger voids may be the result of growth and coalescence of several smaller voids. At this location the formation of voids seems to have no impact on the failure of the protective α-alumina oxide layer.

Figure 5.16(c) shows another area 500μm further down the honeycomb foils. Larger voids are present, still generally hemi-spherical in shape. An approximate radius of 5μm is attributed to voids in this image. This location shows evidence of cracks through the oxide scale, near and above void formations. Non-uniform oxide scale thickness is observed on the right side of the substrate. An oxide with reduced thickness is present above a void formed

at the metal oxide interface. Stress generation or the joining of two cracks in the oxide scale could be the reason for this oxide layer spallation.

The next area is shown in figure 5.16(d). Additional to the previous image is the increase in void size, cracks in the scale, and the occurrence of void filling. This was detected using image contrast and BSE imaging. EDX analysis showed the oxide formed within the voids to be silicon rich oxide. Section 5.3 discusses this in more detail.

Figure 5.16(e) shows a dense population of voids upon both sides of the substrate. Both scale cracking above voids and void filling can be observed. Large sections of the protective α-alumina scale have now become detached from the substrate. Some parts of the oxide remain intact. Where oxide has been removed and bare metal has been exposed to the high temperature oxidation environment, the characteristic morphologies of less-stable Cr, Fe, Ni and Si oxide combinations have been recorded. Figure 5.16(f) shows a similar situation (a further 500μm down the foils). Clear in this micrograph is the loss of substrate and the penetration of aggressive, less-stable oxides into the honeycomb node. This example cross-section almost documents the rupture of the foils and the location of the detachment of the Fe-20Cr-5Al foils, at a specific height just above the brazed region.

Progression into figure 5.16(g) shows the top of the braze alloy chamfer. The aluminium oxide scale is no longer adhered to the substrate. Exhaustion of aluminium from the substrate reservoir through oxide scale growth causes the protective oxide to stop growing. If the scale remains adherent, this will provide some extension to the component's lifetime. If the protective oxide cracks, or spalls, less-stable oxides will start to form and cause rapid consumption of the substrate. This region of the honeycomb node will then be enveloped by breakaway oxidation. Sufficient substrate thickness at this region will provide a

slightly prolonged period of attack before rupturing at this point. Figure 5.16(h) is similar to figure 5.16(g) with the formation of highly unstable oxides at the metal/gas interface, although the cross-sectional thicknesses is greater in this region due to the braze alloy chamfers. Rupture at this location is less likely to occur than at the location shown in figure 5.16(f).

Figure 5.16(i) is an important reference image. The image shows the presence of an α-alumina scale upon the braze alloy chamfer, below the region of degradation.

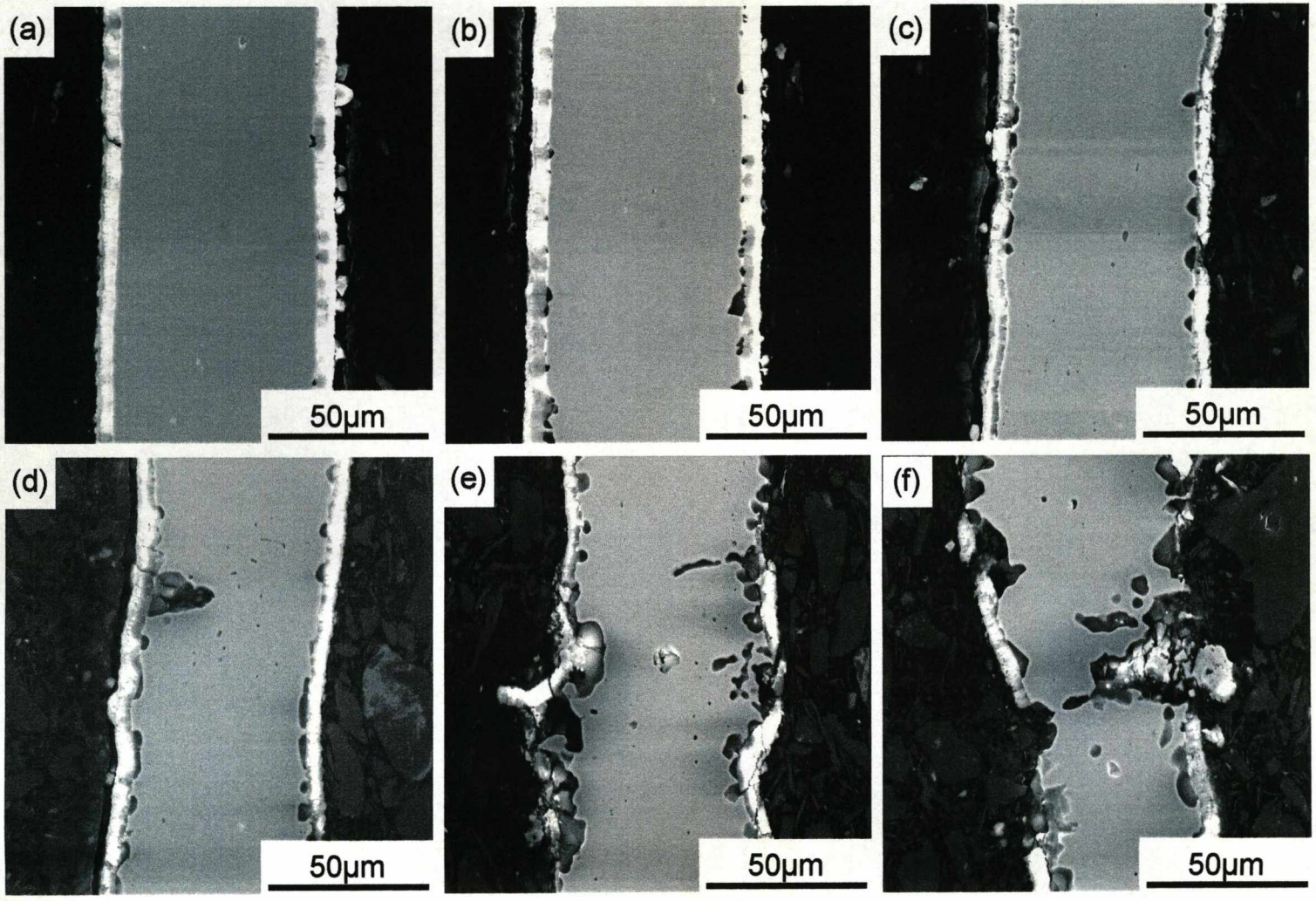
(a)
50μm
(b)
50μm
(c)
50μm
(d)
50μm
(e)
50μm
(f)
50μm

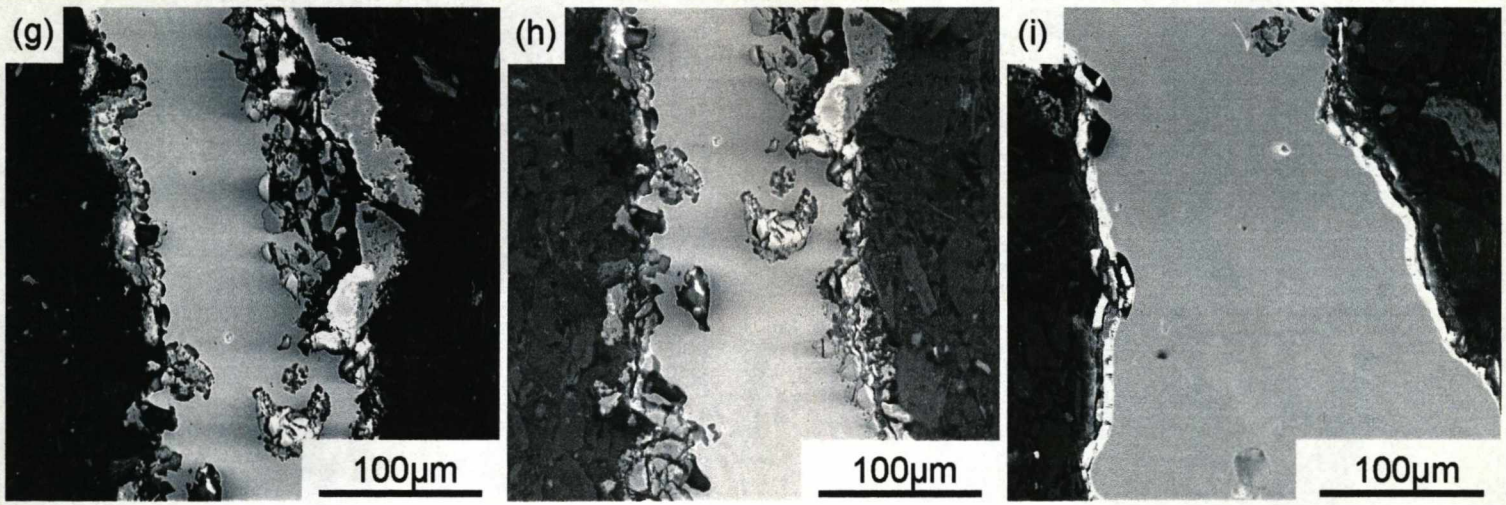

Figure 5.16: Images (a) through to (i), show how degradation effects the Fe-20Cr-5Al foil at a specific location

5.3 Void Formation and Filling – Type I and II Voids

The metallographic examination of mounted polished cross-sectional samples of honeycomb abradable seals which were oxidised at 1200°C, for times greater than 500 hours display void formation directly beneath the protective alumina scale. Interstitial voids have been found to form along the metal/oxide boundary of the brazed honeycomb structures at times as little as 300 hours at 1200°C (as shown in figure 5.16). This example shows a large number of voids positioned near the region of honeycomb foil degradation. The full range of voids (filled, partially filled, and unfilled) can be observed at low magnification in this sequence of images.

At longer times, increased levels of void formation, void growth and coalescence, and void filling can be observed. After formation and growth, a large number of these voids were filled with silica. Figure 5.17 gives three examples of a completely filled void, taken from a honeycomb abradable seal sample oxidised for only 300 hours at 1200°C. EDX analysis confirmed the perimeter oxide as alumina, and the void fill to be silicon rich. These micrographs also show cracks that have propagated through both the silica void fill, and the outer protecting alumina scale. Cracking has occurred along an alumina columnar grain boundary, along the alumina/silica interface, and then through the silica where it stops at the substrate/void interface. It is not known whether these cracks have formed due to stress generation upon cooling, or during the high temperature exposure.

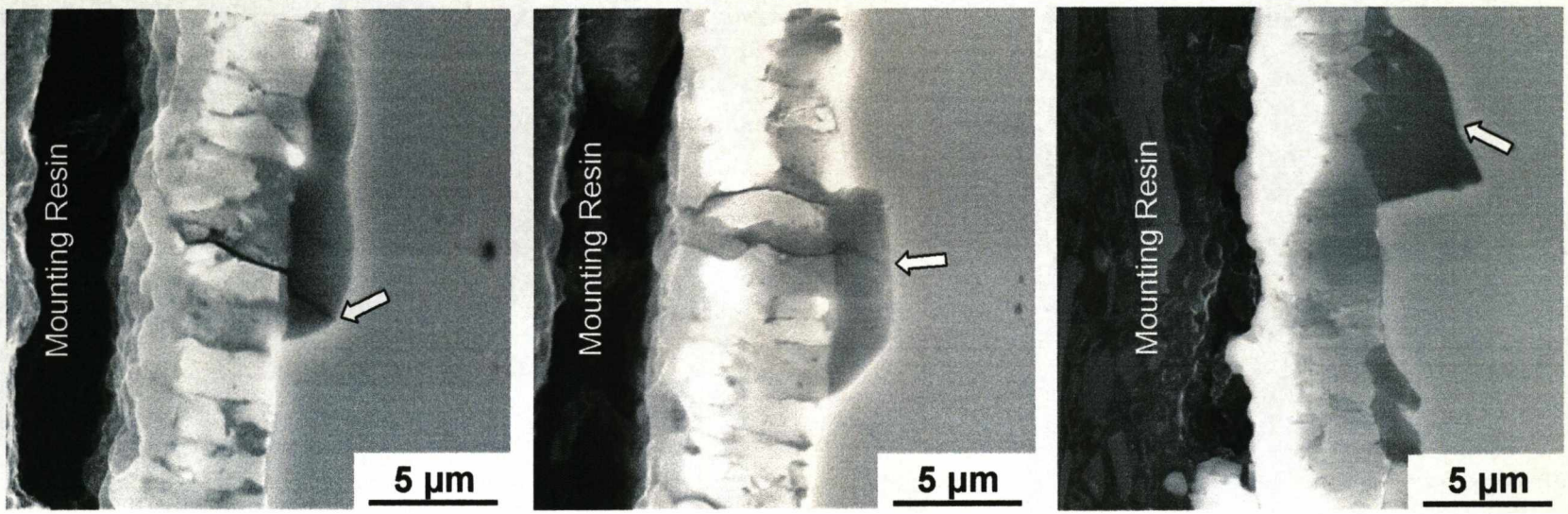

Figure 5.17: Three examples of voids formed beneath the alumina scale upon honeycomb foils/nodes oxidised for 300 hours at 1200°C. All three are completely filled with silica and show evidence of cracking through both the silica and alumina. This is highlighted in each case by a white arrow

Brazed honeycomb foils oxidised at 1200°C for 500 hours show a further mechanism of void formation and filling. Figure 5.18 shows an example of a filled void from one of these test specimens accompanied with the relevant EDX data for chemical analysis of the oxides formed. This example shows a crack in the outer alumina scale with a thin layer of chromia within the void beneath the alumina. This chromia layer is restricted to the void as a discontinuous layer. There is also evidence of chromium oxide growth within the crack in the alumina scale. Further analysis showed that the rest of the void was filled with silica.

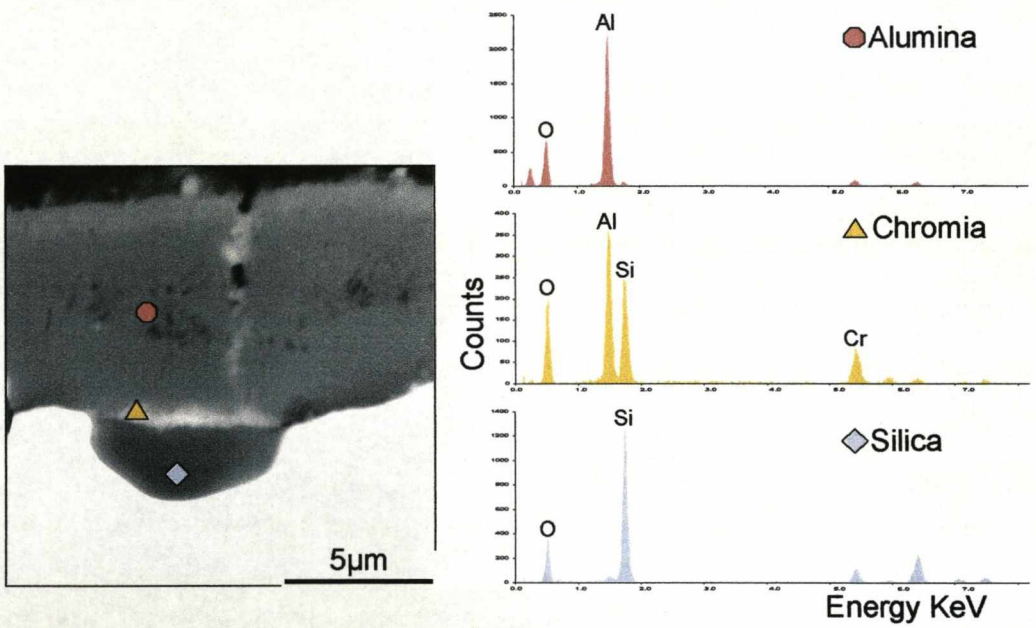

Figure 5.18: BSE image and EDX spectra of a filled void formed after 500h oxidation, in air, at 1200°C. Chromia formation is observed between the silica and the alumina components of the void

Further SEM and EDS examinations revealed that some voids that were only partially filled with silica, as shown, for example, in figure 5.19. These images show both silica and chromia formation in the void. The chromia was found to

form at the underside of the alumina. In tests of a shorter duration (<500 hours), only silica was observed to be growing within the voids. This oxide formation was found to be growing from the substrate side of the voids.

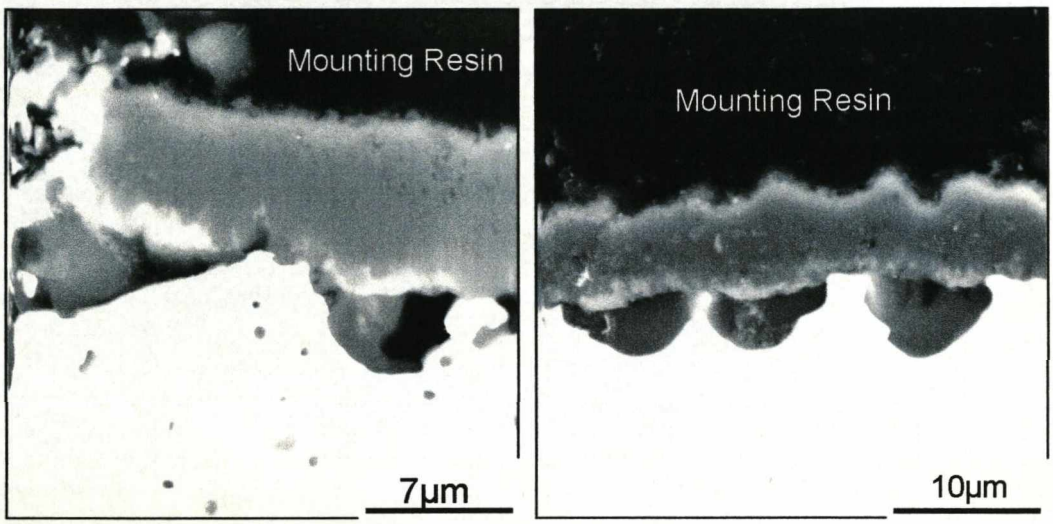

Figure 5.19: BSE images of partially filled voids found after 560 hours at 1200°C.

Large voids observed on polished honeycomb abradable seal cross-sections were usually associated with cracks and the removal of the alumina scale within that region. These voids were often completely filled with silica. Large void formations could always be recorded near the brazed region on the honeycomb foils or upon the outer walls of honeycomb end foils/nodes.

5.3.1 Honeycomb End Foils/Nodes

Honeycomb end foils were found to be affected significantly more than central foils by void formation. The appearance of voids on honeycomb end foils differs slightly from one side of the foil to the other. An example of a sample end foil is highlighted in figure 5.20.

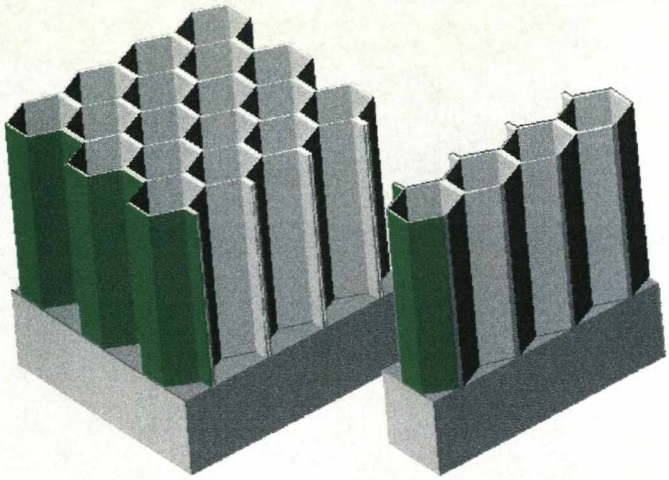

Figure 5.20: Schematic drawing to represent honeycomb end foils/nodes

Interesting observations with regard to honeycomb end foils are best illustrated in Figure 5.21. As well as the increase in number and the size of the voids, there is an increase in alumina scale thickness upon the outer wall of the honeycomb node/foils. The oxide scale is almost double the thickness of that which has formed upon the inner wall of this honeycomb node.

Substantial curvature of the outer most honeycomb foils is observed when compared to more centrally located honeycomb node foils. Plan view and cross-sectional images show the extent of end foil curvature. Examination of the honeycomb abradable seal samples after 500 hours at 1200°C show evidence of end foils curvature. Figure 5.22 is a honeycomb abradable seal sample, oxidised for 560 hours at 1200°C. Both sample end foils show the effect of curvature. The honeycomb foil cell structure in such samples is severely affected, to the extent that some cells collapse.

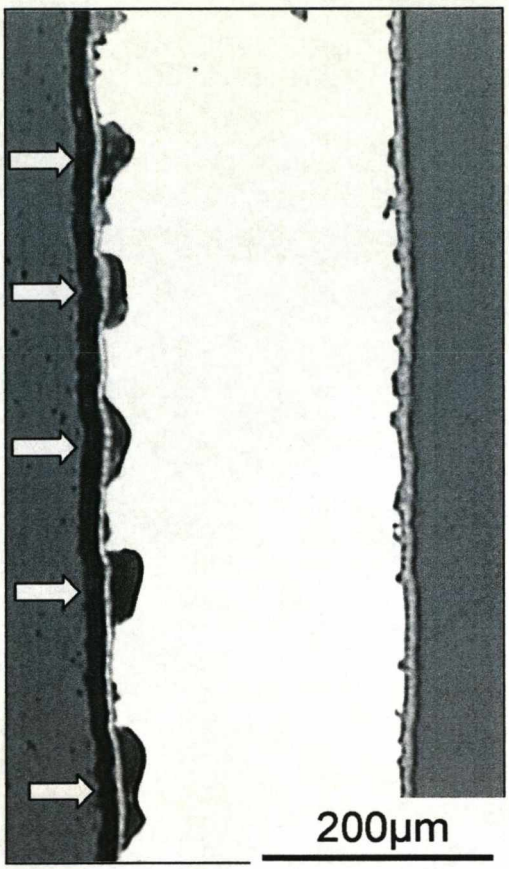

Figure 5.21: Optical micrograph of a honeycomb end foil/node that displays increased void formation upon its outer wall. This honeycomb abradable seal was oxidised for 510 hours at 1200°C

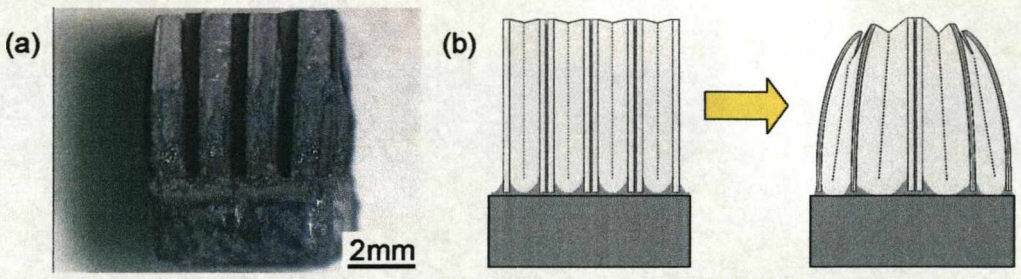

Figure 5.22: Image (a) is the condition of a honeycomb seal after 500 hours at 1200°C, and (b) is a schematic representation of the curvature of honeycomb end foils

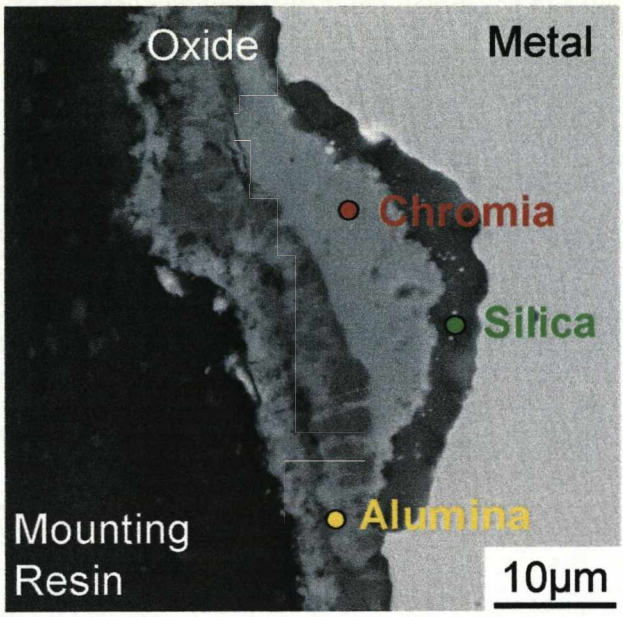

Figure 5.23: Void fill found upon a central honeycomb foil oxidised for 560 hours at 1200°C. The substantial formation of both chromia and silica can be found beneath the alumina scale

This effect was not observed when testing the honeycomb abradable seal at 1100°C. Curvature of sample end foils was not as substantial as in the 1200°C cases. It is thought that a creep mechanism is responsible for the curvature of the honeycomb foils at 1200°C. Increased void numbers, size, and oxide scale thickness, are thought to be interlinked.

A honeycomb abradable seal sample oxidised for 560 hours at 1200°C presented an anomaly to the gallery of completely filled voids (figure 5.23). EDX analysis of the void showed it to be half filled with silica, and half filled with chromia. The silica void fill was confined to the rear of the void and was in direct contact with the alloy substrate. The chromia half of the void-fill is attached to the outer alumina scale and has impinged on the silica void fill without any contact with

the alloy substrate. The silica void fill is in contact with the outer alumina scale, but only at the points of substrate separation.

5.4 Oxidation Testing of Alloy MI2100 at 1200°C

The results from isolated alloy MI2100 thin foils i.e. away from the brazed honeycomb abradable seal setup, oxidised at 1200°C are presented here. Interfacial void formation, and silica void filling was extensive on brazed honeycomb foils. This section oxidises the same alloy in the same environment, without the influence of silicon from the braze. The recorded interfacial void formations and void filling were expected to be different and are presented in this section. Initial observations after isothermal oxidation such as colour change and curvature of the foils are also shown.

Additionally, samples of alloy MI2100 were oxidised away from the honeycomb abradable seal setup to observe the degradation mechanism without the influence of the Ni-based alloys (braze and base plate). Alloy MI2100 was tested at temperatures of 1200°C for times of up to 700 hours. Void formation was observed during these tests and the results will be presented in the following section. However, previous void formation and filling upon the honeycomb abradable seals contrasts with the results for the MI2100 alloy when tested without the influence of the brazing alloy at 1200°C, since a continuous double layered oxide scale of alumina and chromia is now observed after the exhaustion of aluminium from the substrate alloy. Voids are then formed beneath this dual-layer and found to be filled with chromia.

5.4.1 Initial Observations for Alloy MI2100

Initial, visual observations indicated substantial and continuing deformation of the thin alloy foils which were oxidised at 1200°C. This is expected to be a

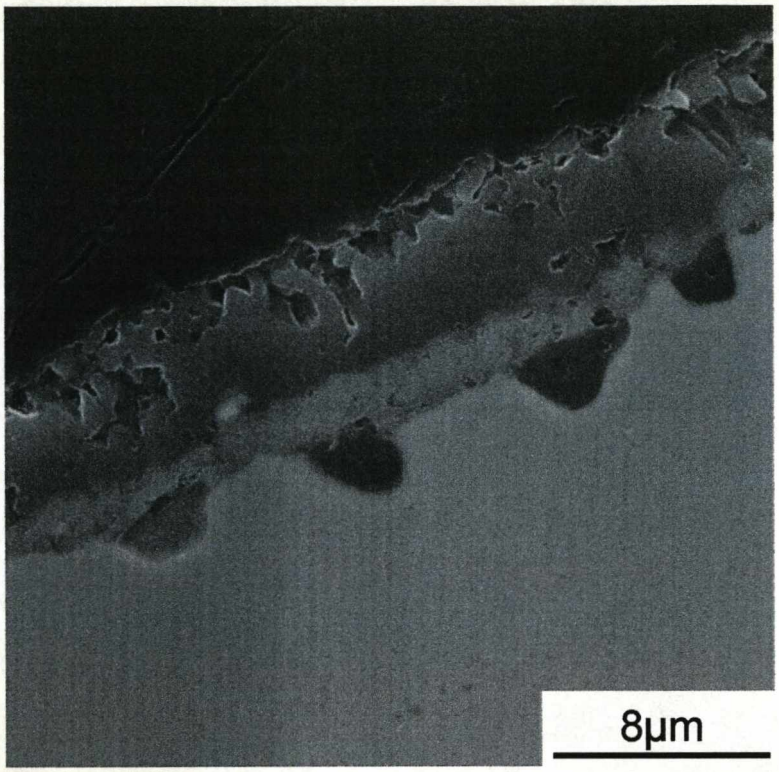

Figure 5.24: Secondary electron image of the cross-section of FeCrAl alloy MI2100 which has been oxidised for 600h at 1200°C. Image shows the formation of a two layered oxide containing alumina and chromia, and the presence of voids beneath this dual layer

5.4.2 Void Formation and Filling

Examination of cross-sectional samples from alloy MI2100 foil after 600h and 700h at 1200°C show a further mechanism of void formation and filling (e.g. Figure 5.25). Below the outer layers of alumina and chromia, a large void has formed between the substrate and the oxide. SEM examination of these voids showed large cracks through the pseudo-protective oxide film and the growth of an oxide upon the substrate side of the void. EDX analysis confirmed this oxide to be chromium rich. On the same micrograph, a band of dark particles

can be seen to be set back into the substrate at a constant distance around the void which chemical analysis revealed were rich in silicon oxide.

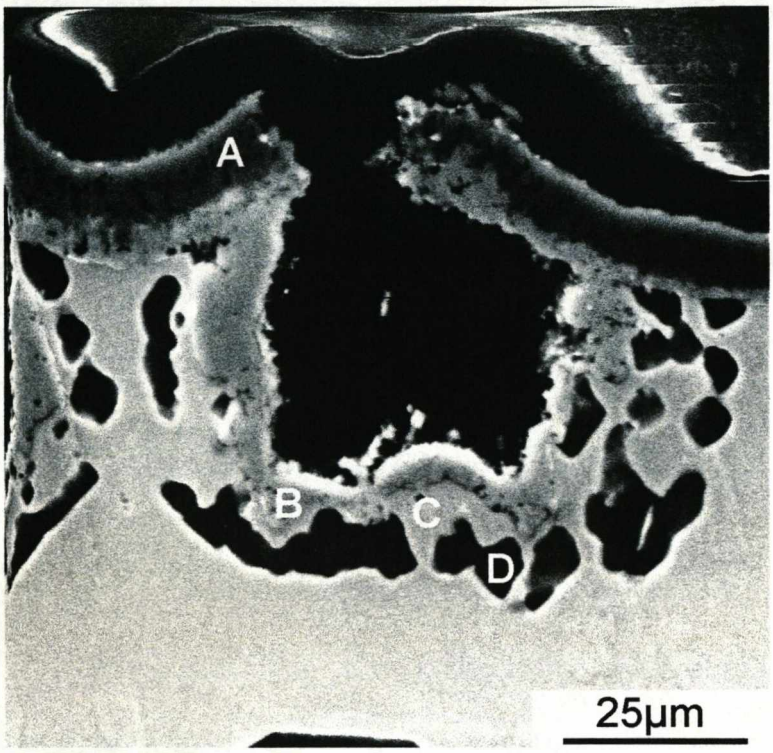

consequence of stress introduced by oxide scale growth and relief by creep of the substrate alloy [27]. Initial curvature of the foils occurred in the rolling direction. Elongation of thin foil length was also observed, however due to substantial curvature no strain measurements (i.e. change in foil length) were recorded. Thin foils that were oxidised for short time periods (up to 300h) exhibited a grey colour. This was the under-lying metallic substrate that was visible through a thin, transparent, and protective alumina layer. Increased oxidation times produced green coloured patches of oxide, especially in areas near corners and edges.

After 600h oxidation in air at 1200°C it was calculated that most of the aluminium in the 70μm thick foil should have been consumed by oxide formation (see Appendix 2). A continuous layer of chromia formed beneath the outer alumina scale, together with a large number of voids (Figure 5.24). At longer times a large number of these voids filled with chromia. The number of voids appeared to differ slightly from one side of the sample to the other.

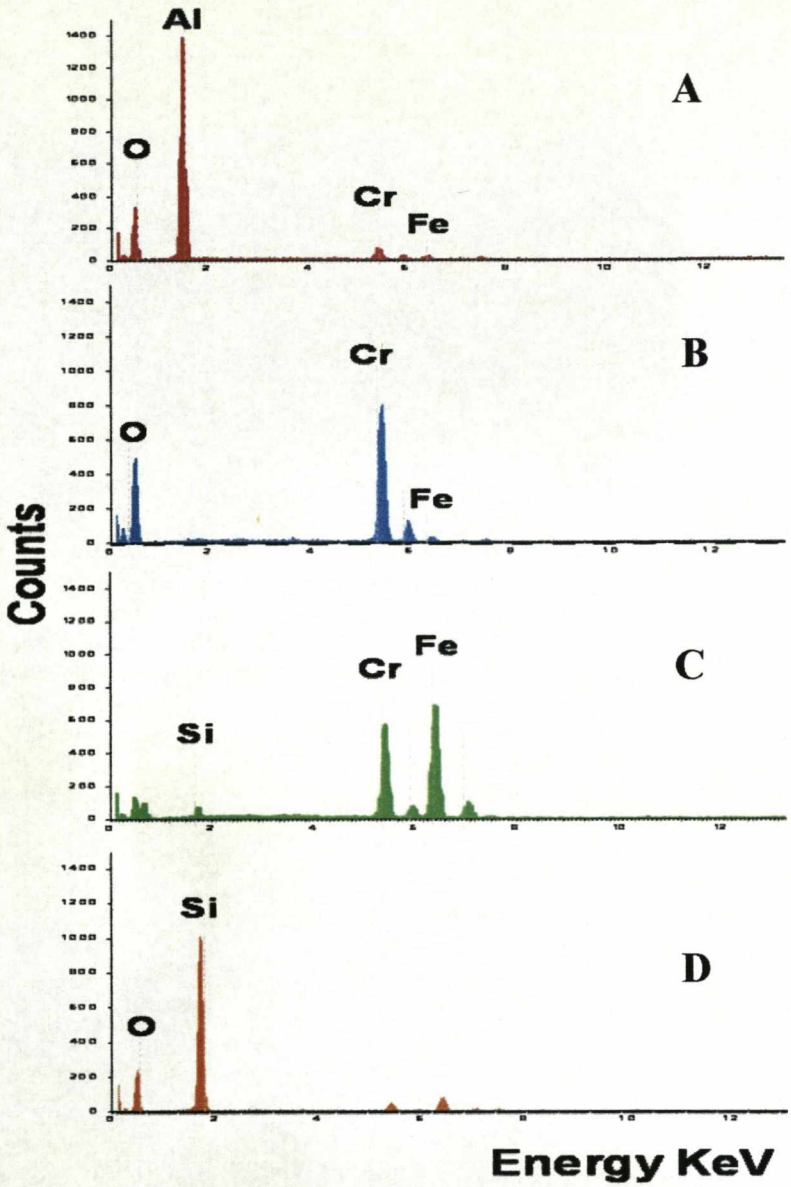

Figure 5.25: Void formation upon FeCrAl alloy MI2100 when oxidised for 600h at 1200°C in air, together with the EDX spectra taken from four regions A-D. Region A is the alumina, B chromia, C substrate alloy, and D silica

Further examination of the same oxidised foils revealed voids of a similar size without either cracks or the presence of silica within the same region. The only chromia present is that which was growing continuously beneath the outer

alumina scale. This internal growth of silicon oxide around the voids appeared to be associated with cracks that had propagated through the dual-layered oxide above the void. It was thought initially that the concentration of silicon within this alloy was insufficient for internal oxide growth. However, literature suggests that additions of ~0.5 wt. % Si in austenitic and ferritic steels will form a thin silica layer beneath chromia during high temperature oxidation [160, 161].

Alloy MI2100 was tested isothermally, for times up to 700h at 1200°C in air. This alloy showed excellent oxide scale adherence whilst alumina was the protecting oxide. After 500 hours and the exhaustion of aluminium from the substrate, a continuous chromia layer started to build under the alumina scale. It was at this point that void formation was clearly seen beneath the chromia layer. These voids may then start to fill with chromia (Figure 5.26). Analysis of numerous voids on the MI2100 alloy, oxidised at 1200°C for 700h revealed that the voids may not only be filled with chromia. A small number have been recorded to have been filled with silica (Figure 5.27). However, it is important to note that the chromia filling mechanism of the voids seems to be the most dominant.

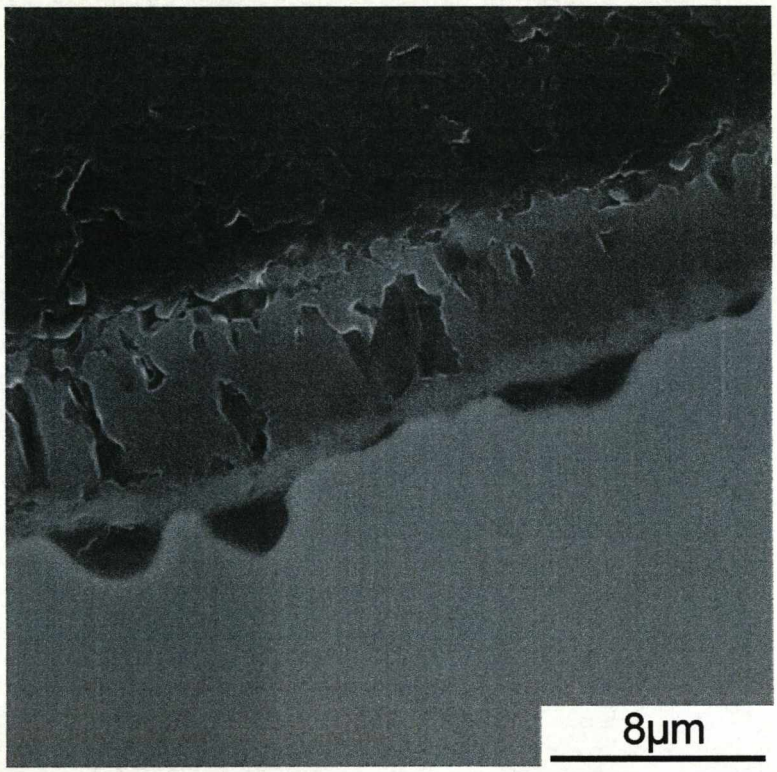

Figure 5.26: Secondary electron image of the cross-section of FeCrAl alloy MI2100 which has been oxidised for 500h at 1200°C. Presence of a continuous layer of chromia formed beneath the alumina scale after exhaustion of aluminium from the substrate. Three unfilled voids can be seen on the micrograph, below the dual layered oxide

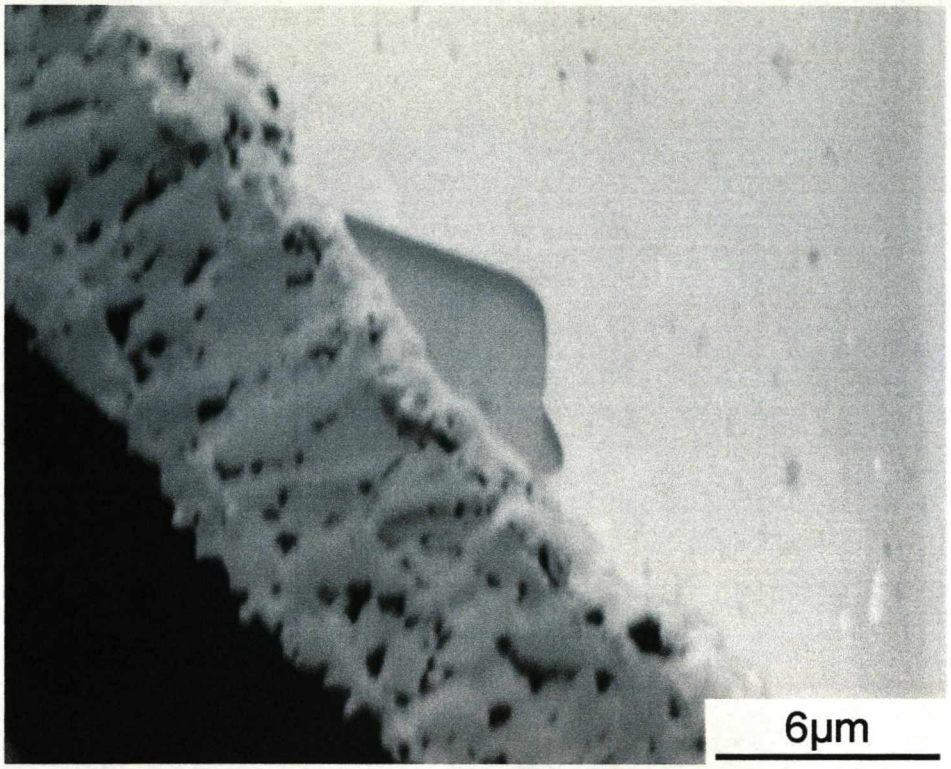

Figure 5.27: Back scattered scanning electron image of a metallographically mounted and polished cross-section of a void formed upon alloy MI2100 after 700h at 1200°C. This void has completely filled with silica

5.5 EBSD Analysis

The following results section presents the structure of both alumina and chromia oxide scales above unfilled and chromia filled voids using EBSD analysis. The structure of chromia void fills is also covered in this section. The EBSD results for oxide structure above and within voids is presented in seven separate subsections. The first three EBSD data analysis sets present the results for alumina and chromia dual layered oxides formed above unfilled voids upon isolated MI2100 alloy foils, oxidised at 1200°C. Three data sets of the structure of oxides above voids are presented to show the reproducibility of the alumina columnar grains and chromia equiaxed grains texture. A further three EBSD data sets present the oxide structure from chromia void fills. Each chromia void fill data set shows the randomness of chromia fill textures observed in three very different types of voids. The final EBSD data set presents the partial chromia void fill analysis from a type II void. The partial chromia fill was analysed both under the alumina scale and whilst directly adhered to the MI2100 alloy substrate. The section presents the texture for both alumina and chromia above voids and within void fills.

The EBSD analyses of the thermally grown oxide scale formations were achieved using the EBSD feature of the Cam Scan X500 crystal probe FEG-SEM. The required high standard of polishing (<60nm standard with a level surface) was unachievable with the cold mounted honeycomb abradable seal samples due to the complex geometry, the differential hardness's of the multi-component system, and the lack of support provided by the cold mounting resin. Therefore, all EBSD map sets in this section are polished oxide scales from singular thin FeCrAl foil samples, oxidised at 1200°C. A recipe for the method of polishing used in sample preparation can be found in Appendix 3. Several different sets of EBSD analyses were taken from each prepared sample. The mapping of α-alumina scales, chromia layer formation beneath the α-alumina

outer scale, dual layered oxides of α-alumina and chromia above unfilled voids, and dual layered oxides above chromia filled voids, can be found in the following section.

5.5.1 EBSD Data Set 1

A 70μm thick MI2100 foil was oxidised at 1200°C for 600 hours. The sample was then mounted in cross-section and polished with great care to a 60μm standard. The sample was found to contain many large voids (>10μm radius) at the metal oxide interface. Figure 5.28 displays the original BSE SEM image of the α-alumina and chromia oxides above the void taken prior to the EBSD mapping. The EBSD mapping of a dual oxide scale above an unfilled void at the interface between the metal and oxide was performed. Band contrast, All Euler, Inverse pole figure, Grain size, Grain aspect ratio (Grain shape), and Grain boundary maps are shown in figure 5.29 with the accompanying Pole figure data. The minimum step size permitted by the Channel 5 software of 0.1μm was used to scan the selected area.

As the alumina and chromia crystal structures are very similar, the Channel 5 software proved to have great difficulty in interpreting the correct crystal structure at certain locations. Such errors in interpretation could not be corrected by the processing and removal of erroneous data. Therefore, the least time consuming option was to set up the Channel 5 software package to only index grains of alumina. Several trial runs in this set-up found that the chromia layer would always index as alumina. Therefore all EBSD maps in this section will be shown to have indexed as completely alumina. Some EBSD maps will be accompanied by EDX spectra/mapping as proof of the presence of the chromia layer.

The Band contrast image (Figure 5.29(a)) shows an oxide scale of only a few micrometers thickness, 5μm < x < 9μm. This is the combined thickness of the chromia and α-alumina scales, highlighted in figure 5.28. The α-alumina is clearly characterised by two types of grain. A layer of equiaxed grains, with a grain size < 2μm occurs in the outer scale surface. This layer is 1-2 grains thick. Between these and the chromia equiaxed layer are larger, elongated α-alumina grains with axial ratios of up to 1:4.5 (Figure 5.29(e)) and long axes perpendicular to the foil orientation. Similar findings are included in the paper by Prior et al. [86]. This two layer structure is observed for α-alumina in all EBSD analysed samples. Figure 5.29(a) shows a small change in alumina scale thickness over the analysed region. Other such test specimens oxidised for shorter times analysed by SEM show that the change in oxide thickness corresponds to the changing length of the columnar grains. Such an occurrence can also be seen in figure 5.29(a).

Chromia layer formation is also labelled upon figure 5.28. This oxide forms an equiaxed grain structure, with a grain size of 1-3μm (Figure 5.29(d)). The layer of chromia seems to thicken towards the right hand side of the band contrast image, where it becomes 2 grains thick. This position corresponds to the centre of the void. The left hand side of the image presents a chromia layer thickness of only 1 grain at this location.

The boundaries between grains are dominated by high angle grain boundaries and the grains contain very little lattice distortion and few sub-grain structures. This corresponds to both α-alumina and chromia oxide scales and is shown in figure 5.29(f).

The pole figures/stereonets are split into 4 separate analysis sets within figure 5.29(g). They correspond to data acquired from the complete data set, the alumina outer equiaxed grains, the inner alumina columnar grains, and the

bottom equiaxed grains of the chromia layer. Interpretation of the pole figures from the alumina outer equiaxed grains suggest no crystallographic preferred orientation/texture within this layer. The data set from the columnar grains of the α-alumina scale is very different to that of the equiaxed grains. The α-alumina columnar grain structures are found to have a strong crystallographic preferred orientation. The crystallographic preferred orientation is characterised by a strong fibre texture. This classification is derived from the preferential alignment of the <1-101> (the r axis) perpendicular to the foil substrate, the formation of clusters/bands around the poles of the Y axis in the [0001] (the c axis), and as a consequence of the c-axis clustering, the data points in the {11-20} (the a axis) are weakly grouped parallel to the trace of the foil in the observation plane.

Analysis of the chromia equiaxed grain structure shown in the fourth pole figure/stereonet shows a very similar crystallographic preferred orientation to that of the columnar grain structures of the α-alumina. This similar texture between the alumina columnar grains and the equiaxed chromia grains has been observed upon all unfilled voids, additional examples will be shown later in this section. This result is also applicable to the formation and growth of chromia oxide layers beneath the α-alumina oxide scale away from void formations, where the chromia oxide layer is in contact with the foil substrate.

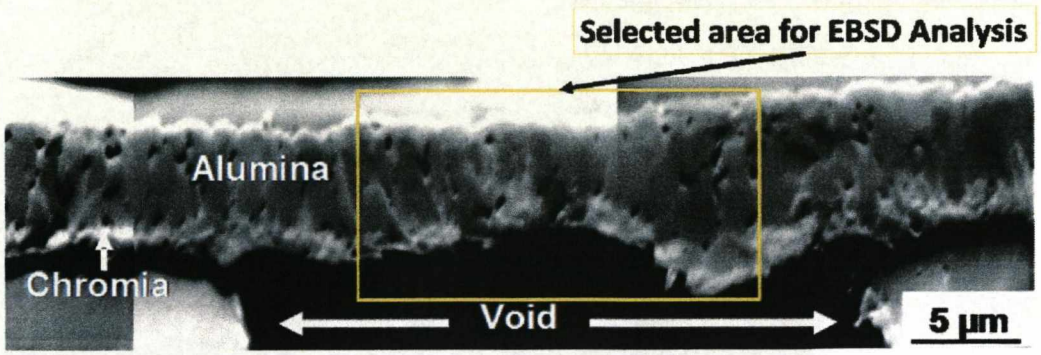

Figure 5.28: BSE image of area 1 selected for EBSD analysis

Band Contrast Map

(a)

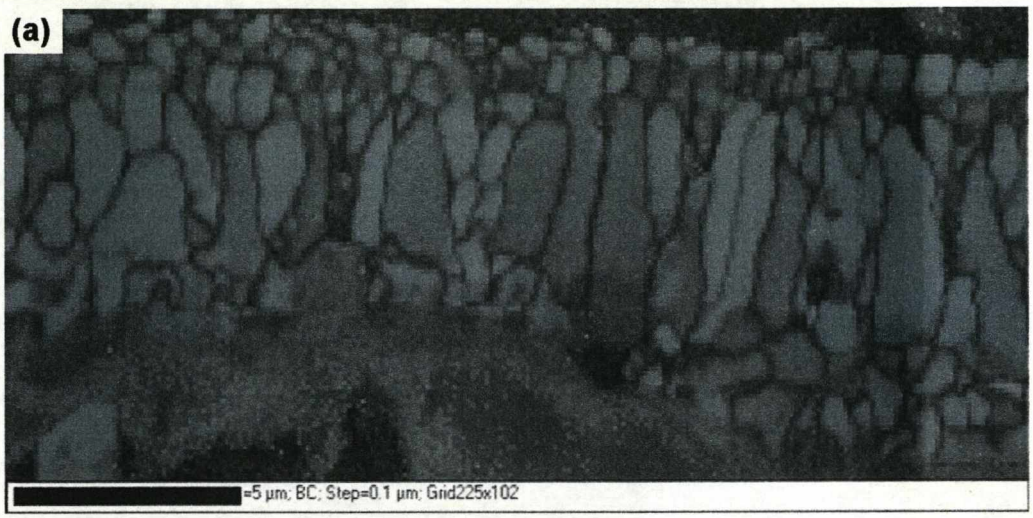

All Euler Map

(b)

Inverse Pole Figure Map

(c)

Legend

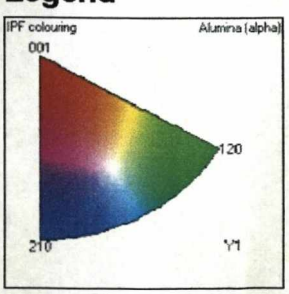

Grain Size Map

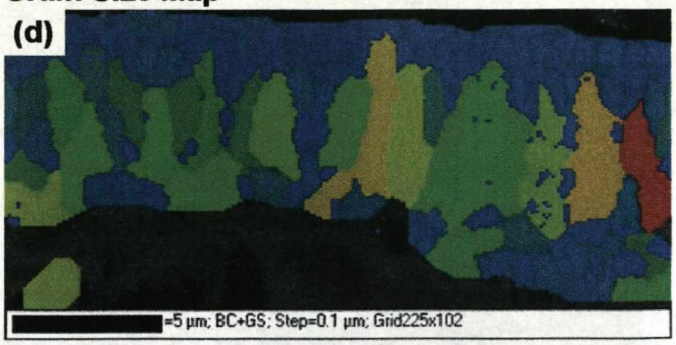

Legend

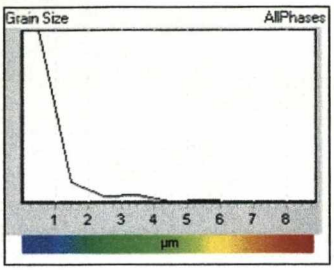

Axial Ratio of Grains (Grain Shape)

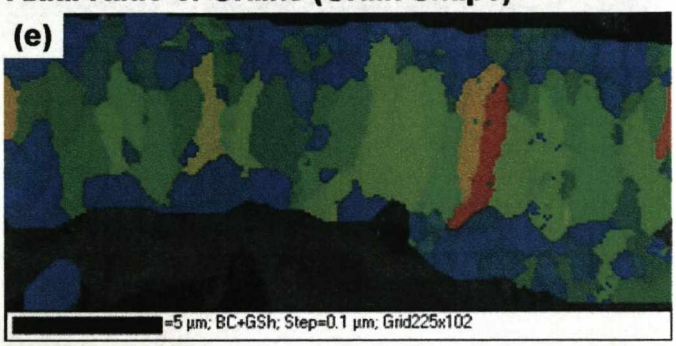

Legend

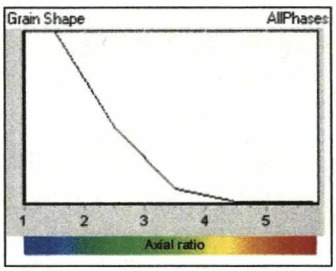

Grain Boundary Map

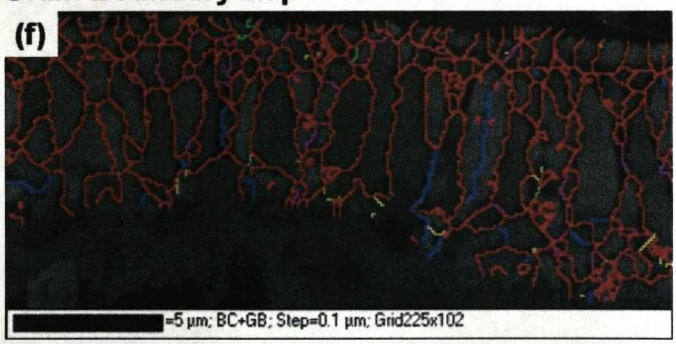

Legend

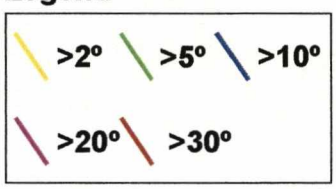

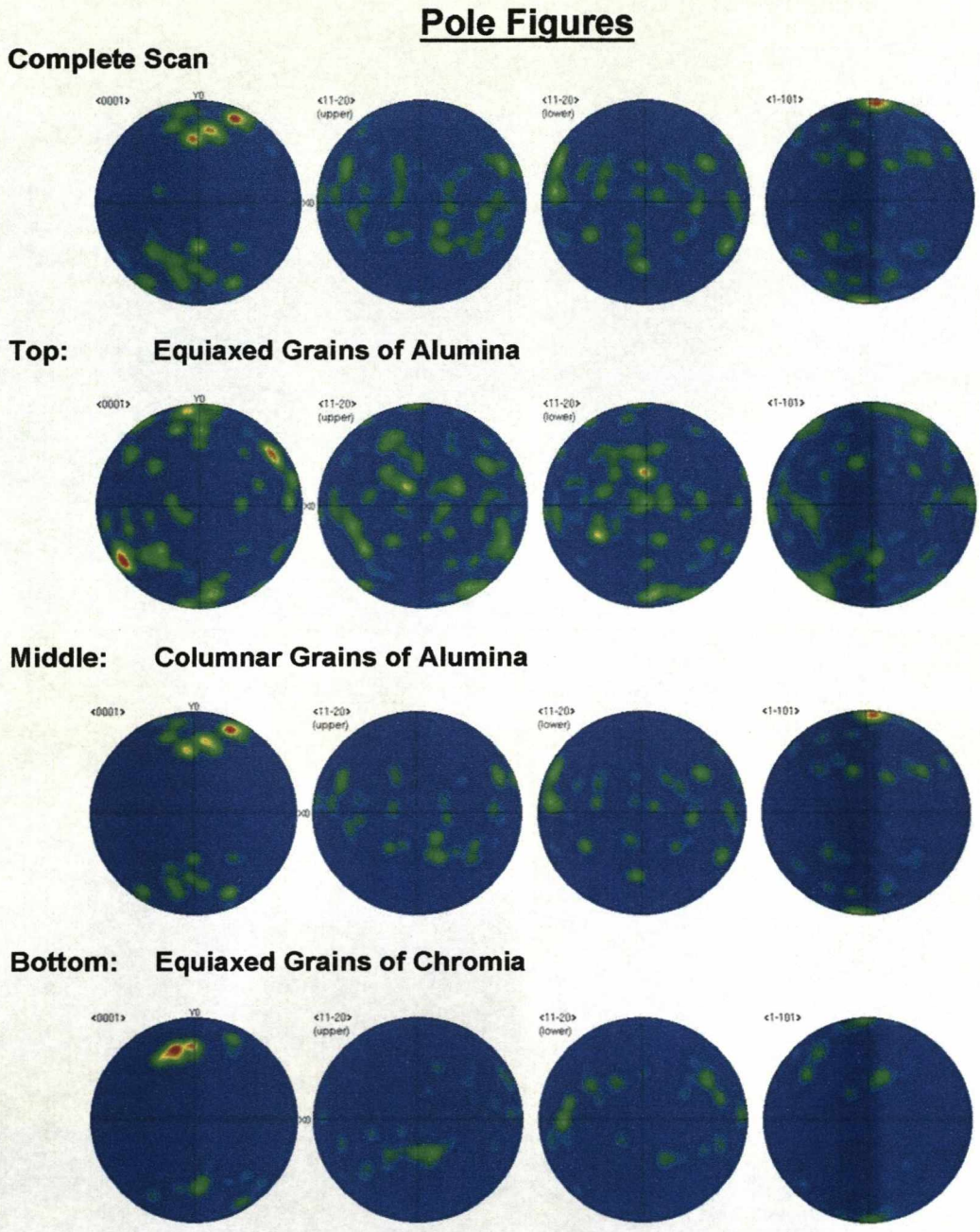

Figure 5.29: EBSD maps and corresponding pole figures of alumina and chromia scales formed above a void. Sample: MI2100 foil after oxidation at 1200°C for 600 hours

5.5.2 EBSD Data Set 2

Additional void formations from other FeCrAl foil samples were analysed using EBSD. A backscattered electron image of a second unfilled void is shown in figure 5.30. Figure 5.31 is an EBSD data set that has been acquired from a test specimen oxidised for 580 hours at 1200°C. This sample was prepared and analysed in the same manner as the first EBSD data set shown in figure 5.29. Figure 5.31 presents the data from three separate EBSD data acquisition sets, using the Channel 5 software facility. EDX spectra of the void area were obtained to show the location of the chromia layer and provide evidence that the equiaxed grain structures beneath the elongated alumina grains are that of chromia. This statement is also supported by the change in contrast of the chromia layer upon the BSE image shown in figure 5.30.

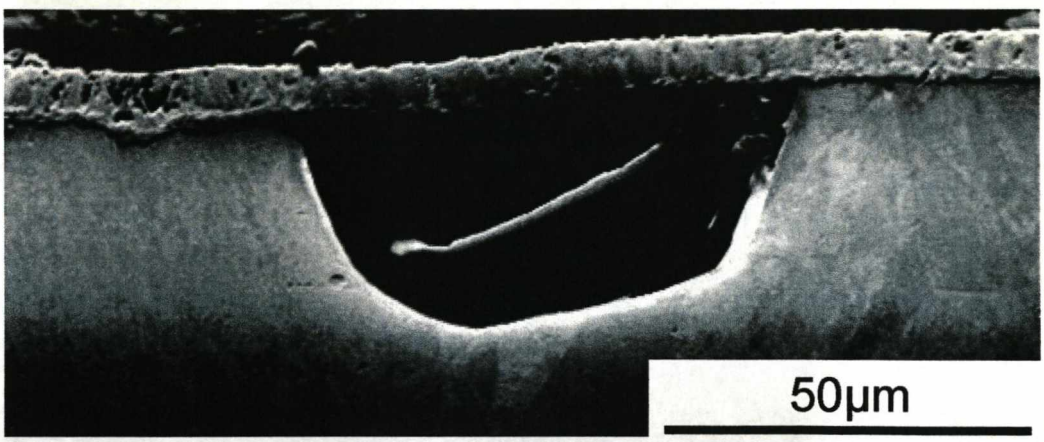

Figure 5.30: Backscattered electron image of an unfilled void. Sample of MI2100 foil after oxidation at 1200°C for 580 hours

Band Contrast Map

(a)

All Euler Map

(b)

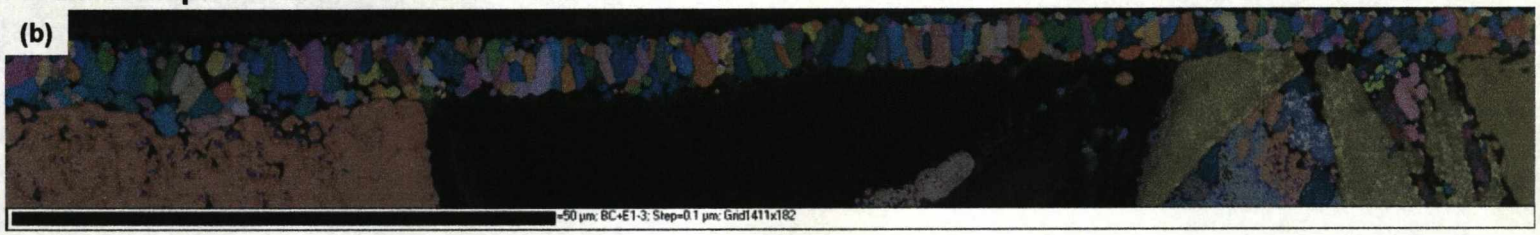

Inverse Pole Figure Map

(c)

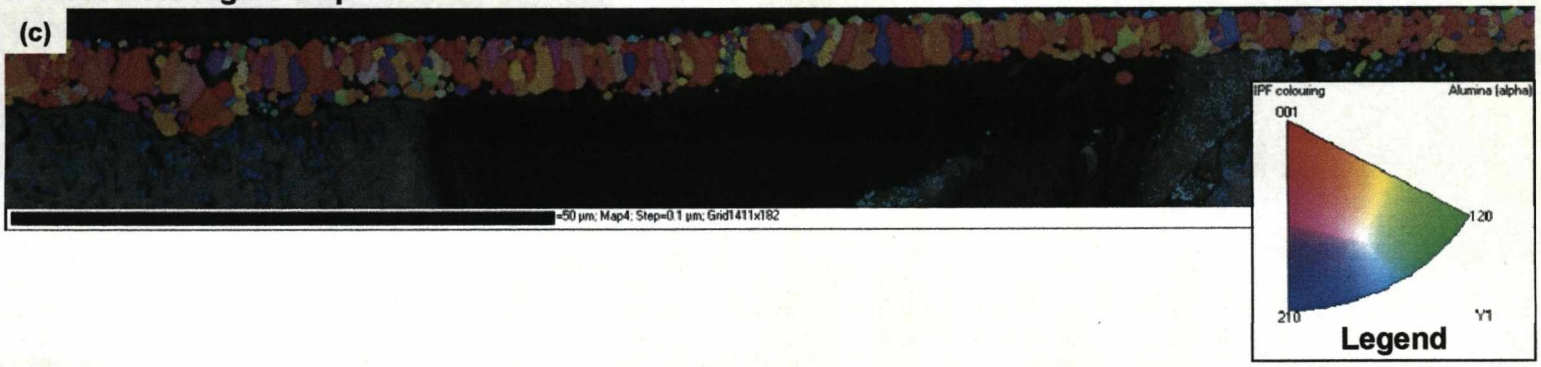

Grain Size Map

(d)

Axial Ratio of Grains (Grain Shape)

(e)

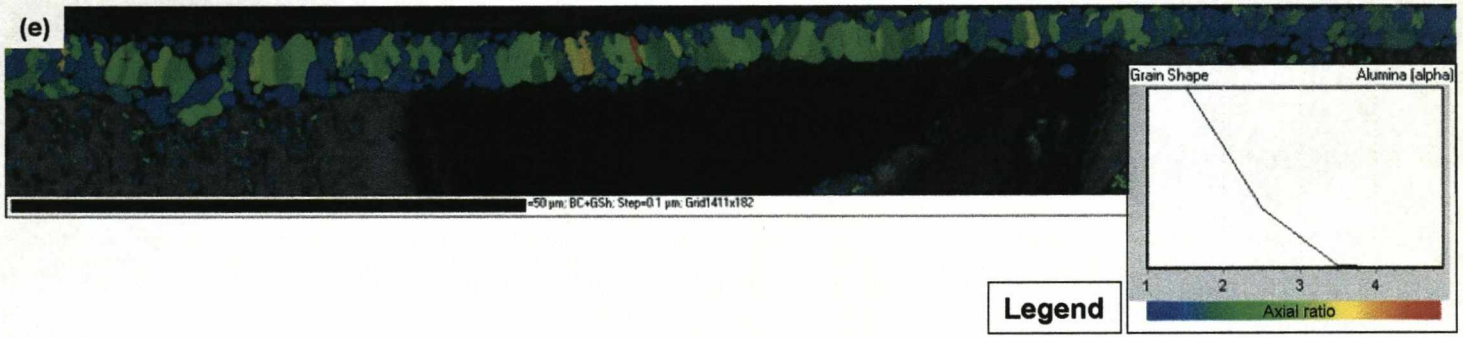

Grain Boundary Map

(f)

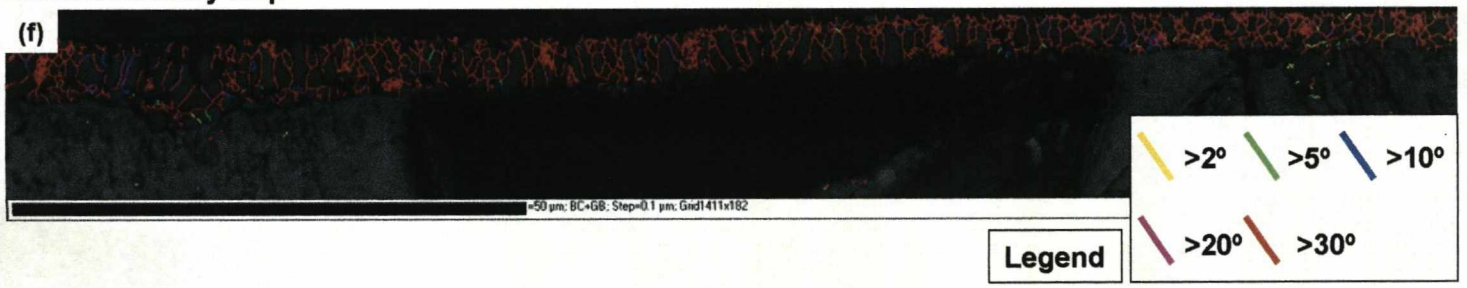

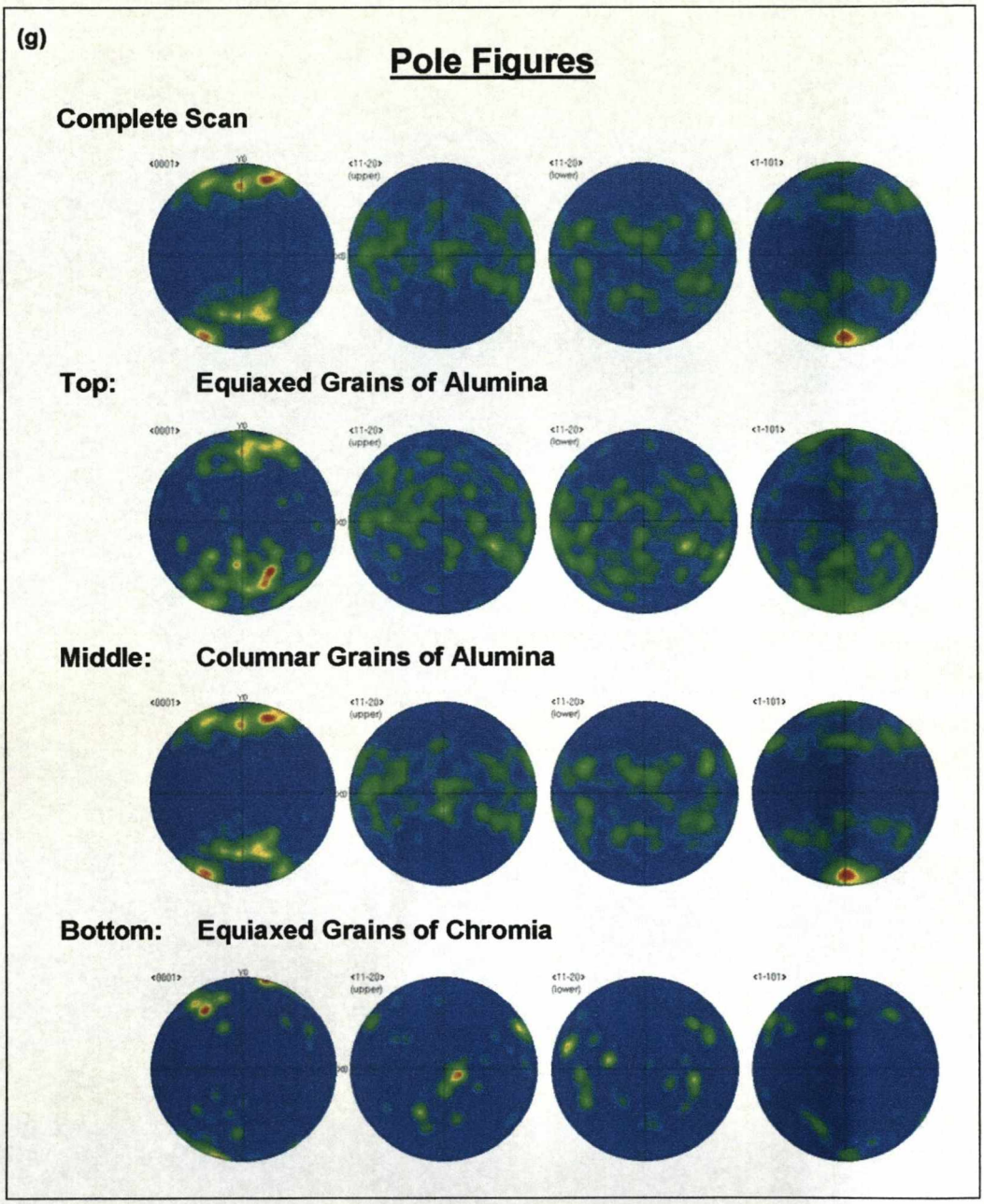

Figure 5.31: EBSD maps and corresponding pole figures of an alumina scale above a void between the metal and oxide. Sample of MI2100 foil, 70 microns thick, and oxidised at 1200°C for 580 hours

The resulting EBSD data maps present the overall condition of the alumina scale with the presence of an intermittent chromia layer. Above the void, the oxide scale was found to be mostly alumina with some small islands of chromia. A clear chromia layer is well established between the alumina and the substrate to the left and right of the void. This unfilled void has a radius >30μm. Figure 5.30 and all EBSD data maps contained in figure 5.31 show a partial filling of the void. This is thought to be polishing debris that has not been removed during the final ultrasonic cleaning stage of sample preparation.

This EBSD data set has indexed a large number of both equiaxed and columnar grain structures contained within the oxides. The grain size map (Figure 5.31(d)) gives the locations of the variety of grain sizes. The legend for this data map is dominated by the number of equiaxed grains over the analysis area. The legend presents data for the greatest population of alumina/chromia grains. These have a grain size of <1.5μm. More reference to the alumina columnar grains can be made in the grain shape map (Figure 5.31(e)). The dual layered oxide both above and away from the void seems to be dominated by high angle boundaries.

The inverse pole figure map (Figure 5.31(c)) and the pole figures/stereonets (Figure 5.31(g)) again show data for similar crystallographic preferred orientations for the alumina and chromia oxide scales. Unfortunately, this data set indexes the majority of its chromia grains away from the void. Over void chromia crystal orientation data is not conclusive from this data set. However, pole figure/stereonet data presents a similar texture for all three parts of oxide (top equiaxed alumina grains/middle columnar grains/bottom equiaxed chromia grains). This is also supported by the colourings of the inverse pole figure map. The crystallographic preferred orientation data is similar to that shown in EBSD Data Set 1 (Figure 5.29) and corresponds to a "fibre texture."

5.5.3 EBSD Data Set 3

Figure 5.32 presents the EBSD results from a pseudo-protective oxide of alumina and chromia layers above an unfilled void. This void is from a polished cross-section FeCrAl foil sample after oxidation at 1200°C for 600 hours. The two layered oxide can be clearly seen upon the BSE image (Figure 5.32(a)). The pseudo-protective oxide is approximately $6\mu m < x < 10\mu m$ thick with good scale adherence around the void interface. The thickest part of the oxide is located above the void where there is no longer any contact between oxide scale and substrate. Figure 5.32 presents the data from three separate EBSD data acquisition sets as indicated in figure 5.32(b), using the Channel 5 software facility.

The band contrast image (Figure 5.32(c)) shows the increase in oxide scale thickness towards the right hand side of the image. This segment of the EBSD analysis set does present the typical three layer structure (equiaxed/columnar/equiaxed) but with additional equiaxed grains moving through the thickness of the oxide rather than the columnar grain structures found elsewhere. From the BSE image these grains are alumina, which may suggest that this is a region of micro-cracking of the oxide, where the alumina has self-healed. This location may be interpreted further in figure 5.32(f).

The boundaries between the oxide grains are dominated by high angle grain boundaries and the grains contain very little lattice distortion and few sub-grain structures. This statement is valid for both the α-alumina and chromia oxide scales shown in figure 5.32(h).

The average grain size is again dominated by the equiaxed grain structure. Using the legend obtained from the grain size map these are commonly $<1.5\mu m$ in length. The grain size map shows two grains indexed in red. These are in

error and are generated by the Channel 5 software. They are actually two grains indexed as one. The grain shape map corresponds to data obtained from other data sets shown in this section. This gives an axial ratio for the alumina columnar grain structures of up to 1:4.5.

The inverse pole figure map (Figure 5.32(e)) and the pole figures/stereonets (Figure 5.32(i)), show a clear similarity in crystallographic preferred orientation between the alumina outer oxide and the chromia layer formed directly beneath it. The pole figure for the chromia layer shows similarities to that of columnar alumina structures and chromia layers formed beneath alumina scales in previous data sets. The pole figure/stereonet data for the equiaxed alumina grains is random. There is no similarity to the orientation observed for the alumina columnar grain structure.

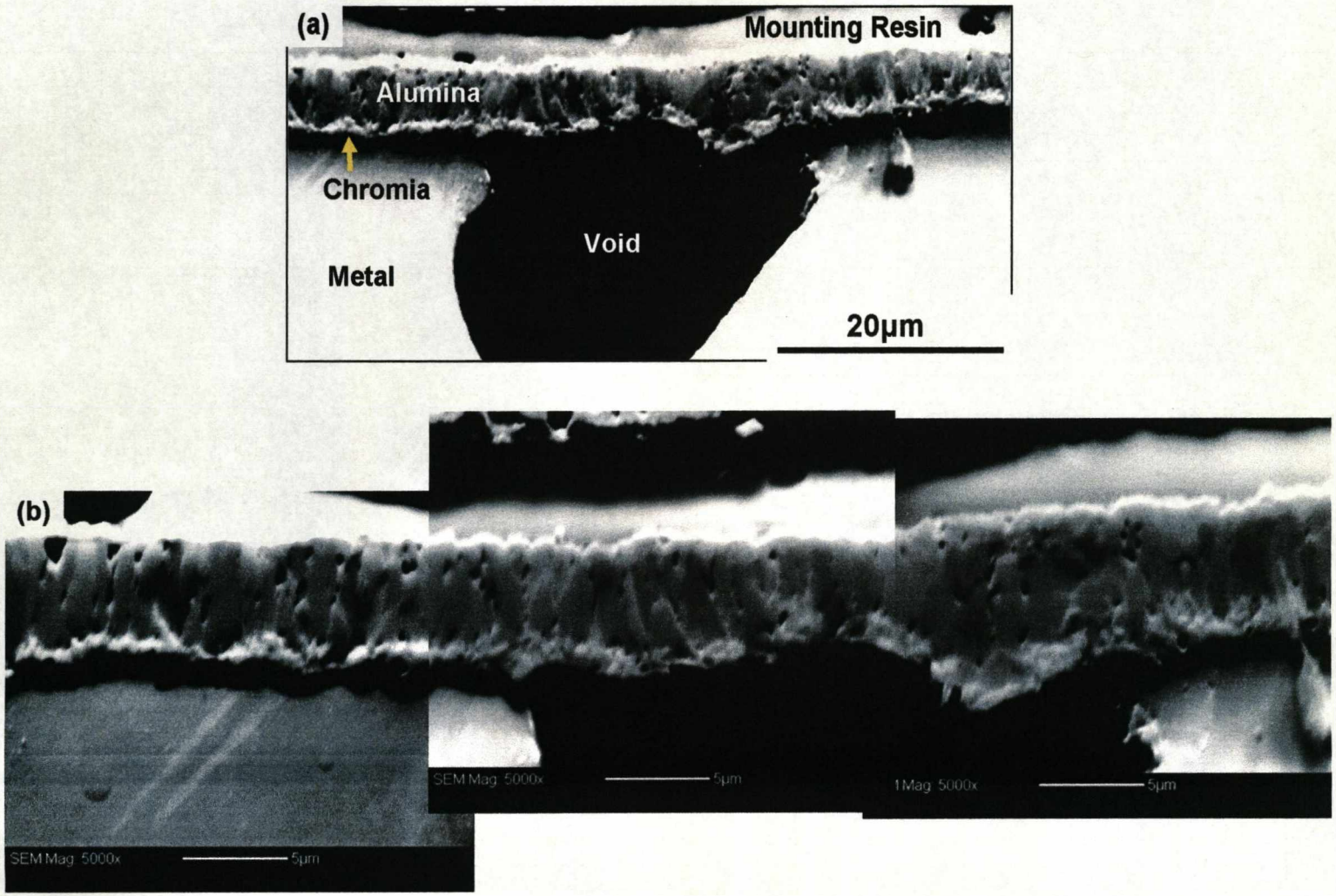
(a)
Mounting Resin
Alumina
Chromia
Metal
Void
20µm
(b)
SEM Mag: 5000x
5µm
SEM Mag: 5000x
5µm
SEM Mag: 5000x
5µm

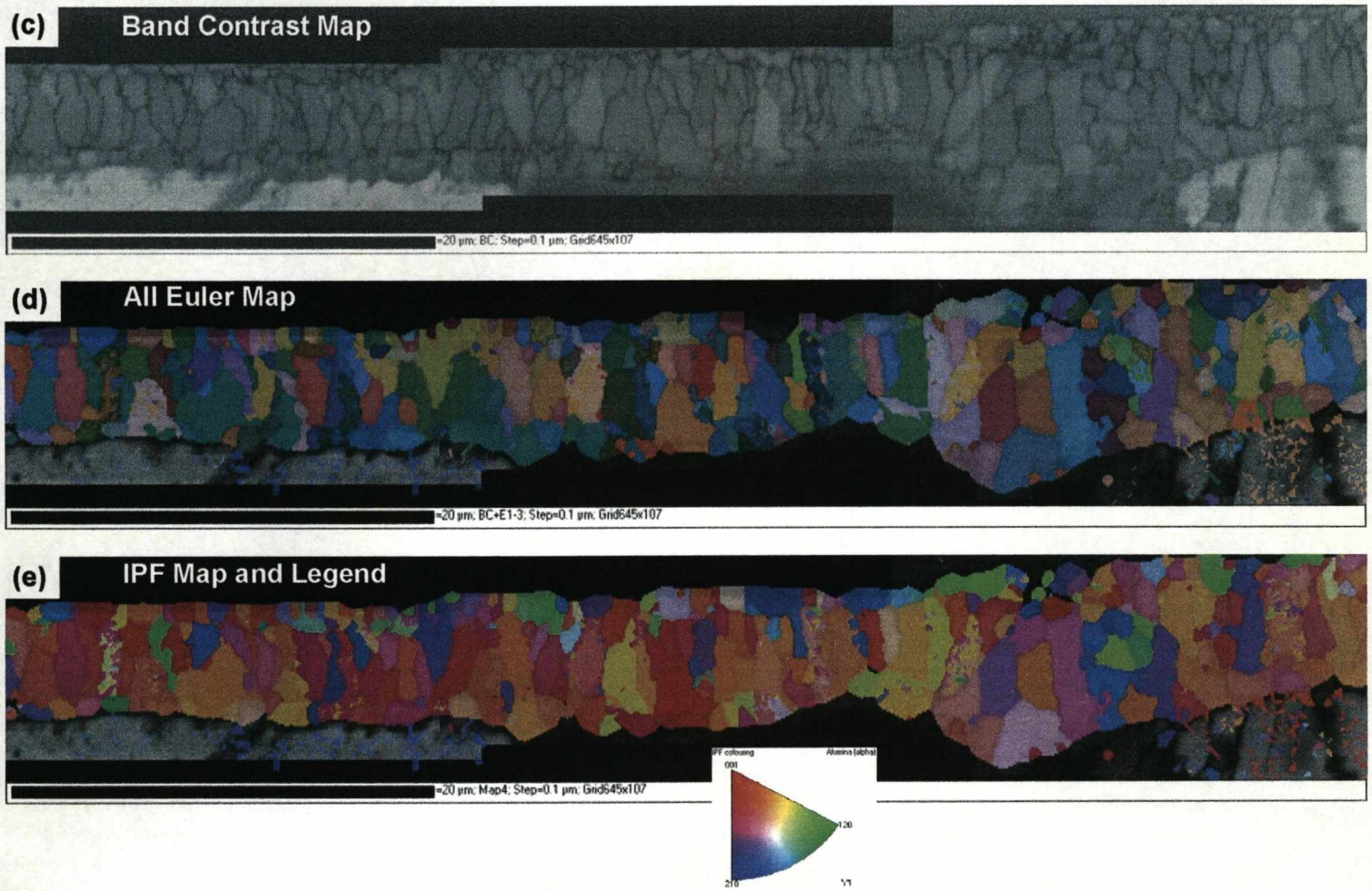
(c)
Band Contrast Map
=20 µm; BC; Step=0.1 µm; Grid645x107
(d)
All Euler Map
=20 µm; BC+E1-3; Step=0.1 µm; Grid645x107
(e)
IPF Map and Legend
=20 µm; Map4; Step=0.1 µm; Grid645x107
IPF colouring
Alumina (alpha)
001
120
210

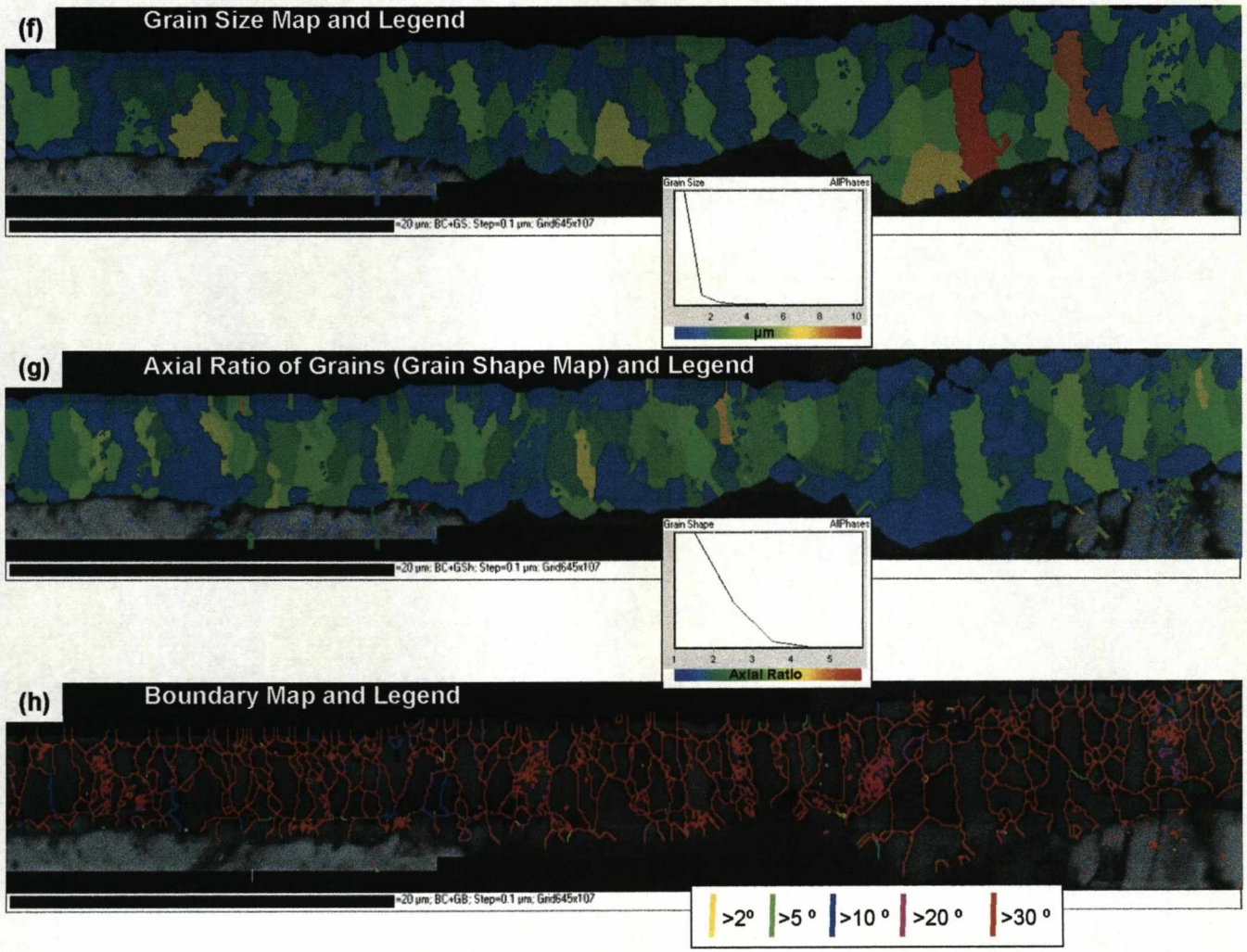
(f)
Grain Size Map and Legend
Grain Size
All Phases
2
4
6
8
10
µm
(g)
Axial Ratio of Grains (Grain Shape Map) and Legend
Grain Shape
All Phases
1
2
3
4
5
Axial Ratio
(h)
Boundary Map and Legend
>2°
>5 °
>10 °
>20 °
>30 °

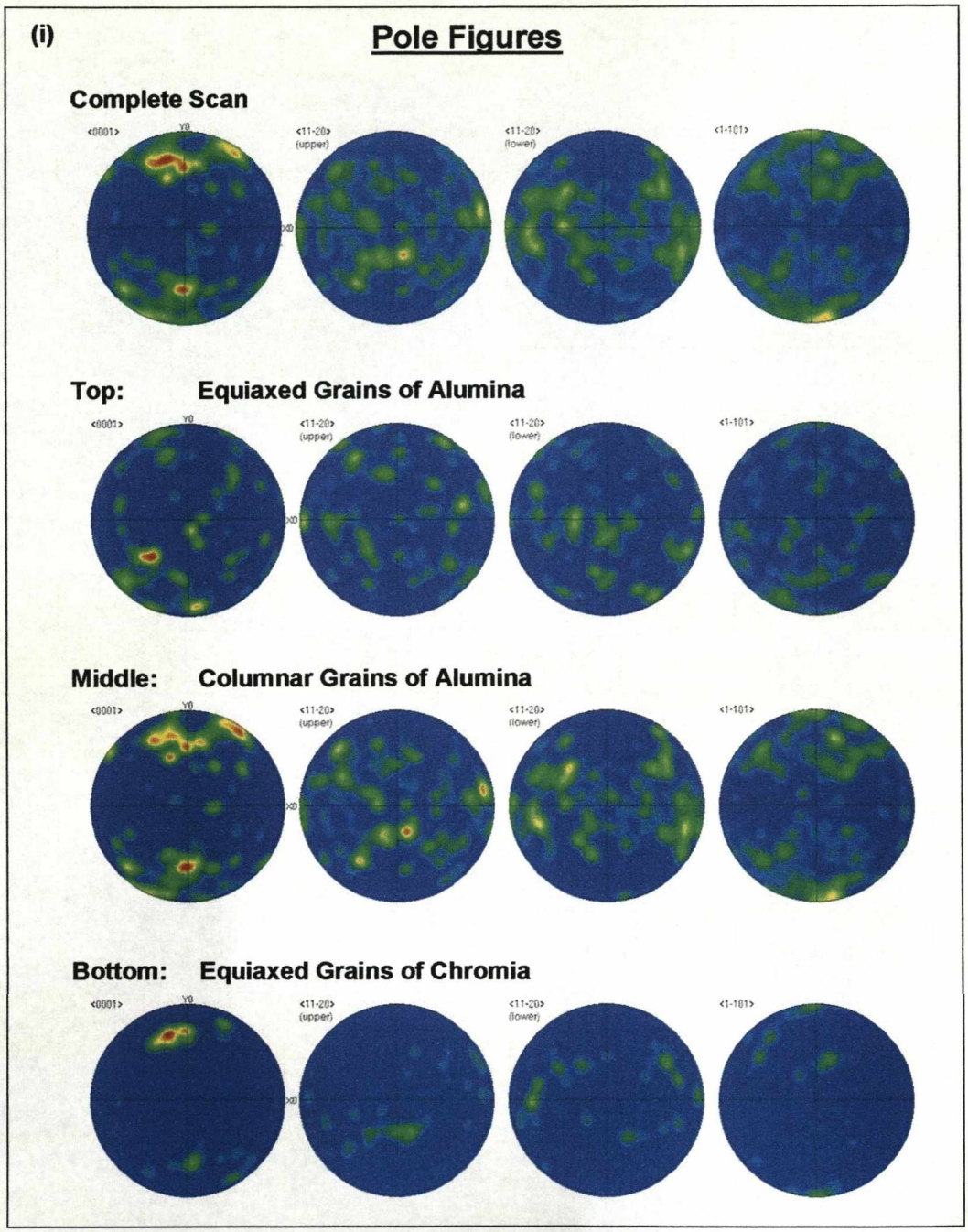

Figure 5.32: Composite EBSD maps of a pseudo-protective scale above a void at the metal/oxide interface. Sample: MI2100 foil 70 micron thick, oxidised at 1200°C for 600 hours

5.5.4 EBSD Data Set 4

Figure 5.33 presents the EBSD results from a chromia filled void. This void is from a polished cross-section through a FeCrAl foil sample after oxidation at 1200°C for 600 hours. Labels upon the BSE image (Figure 5.33(a)) show the main constituents of the void. The appearance of this void is similar to those presented in Section 5.4.2 with a continuous band of silica formed around the void perimeter within the substrate.

A variation of grain size within the chromia void fill is observed within both the band contrast and grain size maps (Figures 5.33(b) and 5.33(e)). Several regions of fine equiaxed grains are separated by larger, more elongated grains. These larger grains of chromia are positioned mostly to the left hand side of the void. The largest elongated grains are in contact with either the metal substrate or the silica band. Clusters of small, equiaxed grains are found in the middle of the void at the very front. This may be the result of different nucleation times and significant changes in the partial pressure of oxygen within the void over time.

Evident from figure 5.33(a) is the removal of alumina scale near the void. If during high temperature exposure and after void formation, the oxide scale cracked and allowed a small leak of hot gas to the void, slow chromia oxide growth may have occurred on all free surfaces of the void. The limited amount of oxygen to the void from the leak would control the growth rate of the chromia grains. Slow oxide growth would lead to a more columnar grain structure as seen here. The sudden change in grain size may have been caused by an increase in the hot gas path to the void. The initial crack/leak may have opened up, increasing the partial pressure of oxygen within the void and causing the rapid chromia formation within the remaining areas.

Using the inverse pole figure data map (Figure 5.33(d)) and the pole figures/stereo nets (Figure 5.33(g)), any crystallographic orientation within this data set can be interpreted. Clear similarities in crystallographic orientation can be observed between the alumina outer oxide and the chromia layer formed directly beneath it within the inverse pole figure map. The pole figure for the chromia layer shows similarities to those of columnar alumina structures and chromia layers formed beneath alumina scales in previous data sets. The texture data set for the columnar alumina grains shown in these images was not recorded.

Analysis of the chromia void fill revealed no preferred crystallographic orientation. The pole figure/stereonet for this set of indexed points is also shown in figure 5.33(g). Even analysis of several small layers of chromia grains directly beneath the initial chromia layer suggests no preferred crystallographic orientation. This is unlike other such chromia void fills where the texture is lost gradually (moving away from the chromia layer). This suggests that the chromia void fill did not occur from vapour transport and new oxide growth did not occur at the underside of the alumina/chromia layer.

The formation of silica was found to be amorphous. Therefore indexing of the silica band using EBSD was not addressed. Out of all acquired EBSD chromia void fill maps, this was the only data set where the silica band looks to be in contact with the chromia. The growth of silica has always been recorded previously as an internal oxide upon oxidised FeCrAl foils.

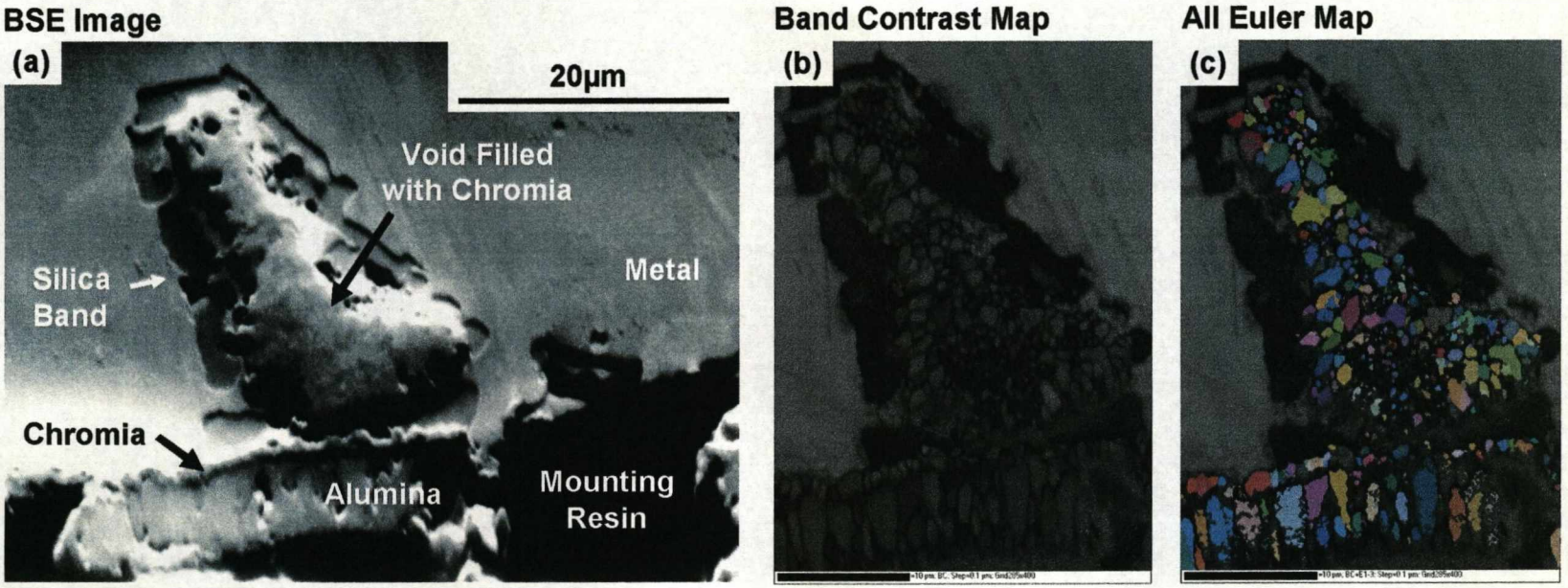
BSE Image
(a)
20μm
Void Filled
with Chromia
Silica
Band
Metal
Chromia
Alumina
Mounting
Resin
Band Contrast Map
(b)
All Euler Map
(c)

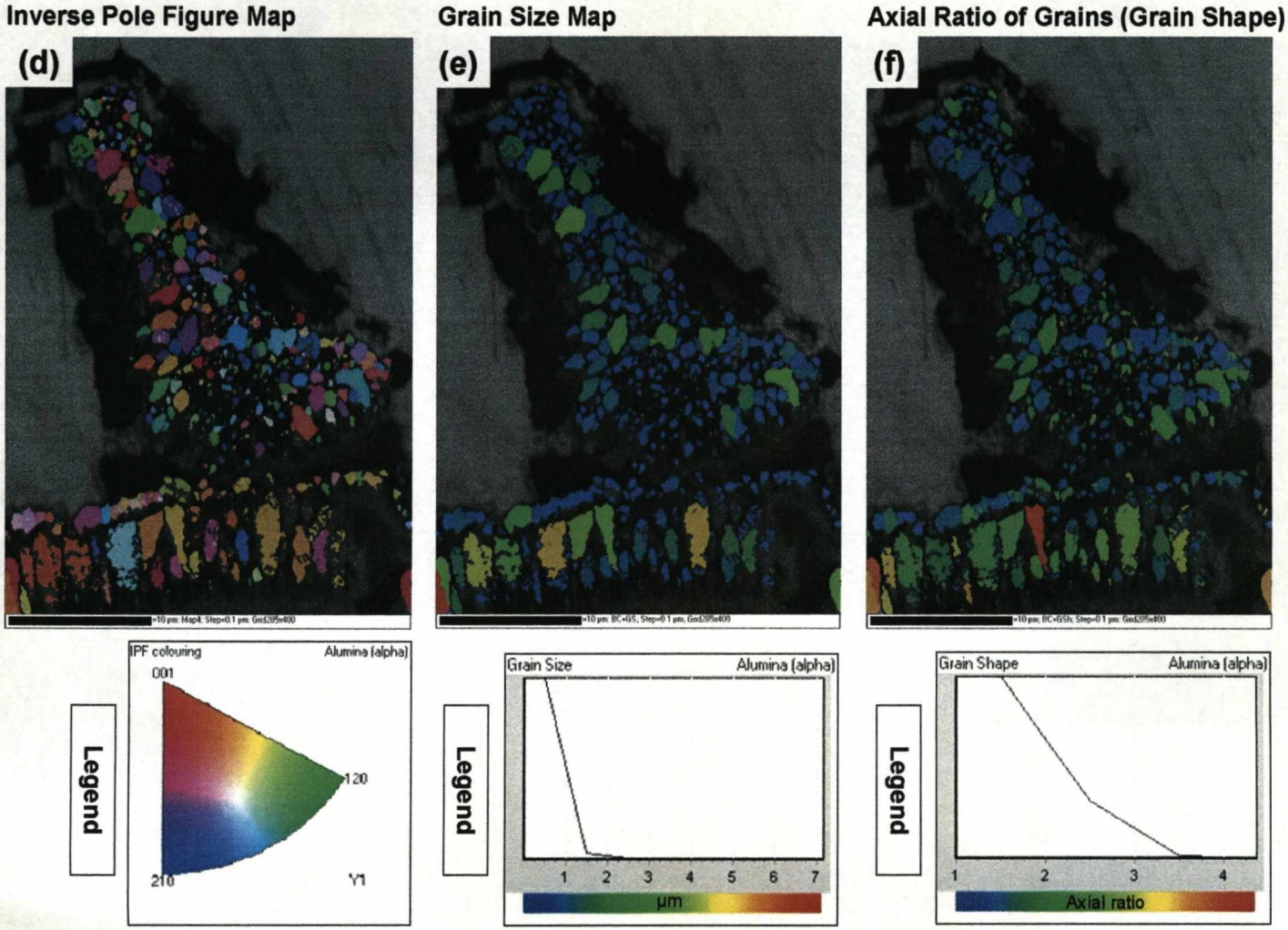
Inverse Pole Figure Map
(d)
Grain Size Map
(e)
Axial Ratio of Grains (Grain Shape)
(f)
Legend
IPF colouring
Alumina (alpha)
001
120
210
Y1
Legend
Grain Size
Alumina (alpha)
1 2 3 4 5 6 7
µm
Legend
Grain Shape
Alumina (alpha)
1 2 3 4
Axial ratio

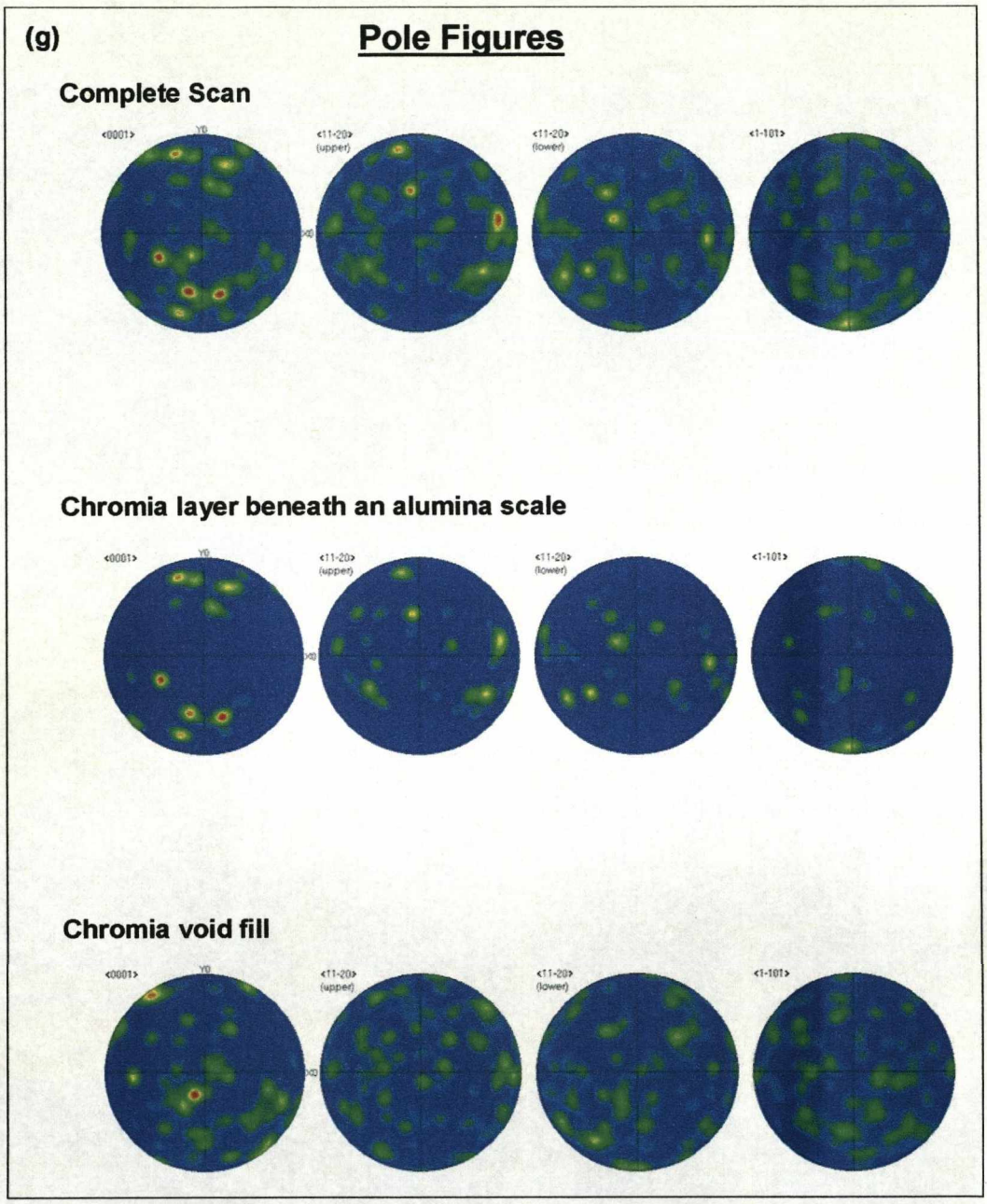

Figure 5.33: EBSD maps and corresponding pole figures of a chromia filled void at the metal/oxide interface. Sample: MI2100 foil 70 microns thick, oxidised at 1200°C for 600 hours

5.5.5 EBSD Data Set 5

Figure 5.34 presents the EBSD results from a second chromia filled void. This void is from a polished cross-section FeCrAl foil sample after oxidation at 1200°C for 600 hours. Labels upon the BSE image (Figure 5.34(a)) show the main constituents of the void. Again silica internal oxides surround the chromia void fill. The silica is present as several particles rather than a continuous band of oxide. These appear as dark regions in the following band contrast, all Euler, and IPF maps. Additional to the silica particles are the regions of void without the presence of chromia void fill. These regions are both located just beneath the alumina outer oxide scale. Micro-cracking of the alumina scale is evident near both oxide-free regions. The outer pseudo-protective oxide is approximately $5\mu m < x < 8\mu m$ thick with good scale adherence around the void interface. The chromia void fill is split into 3 separate regions. It is not known whether this is a consequence of damage induced during sample preparation.

Chromia grain sizes in both band contrast maps (Figures 5.34(b) and 5.34(c)) show variation. Figure 5.34(a) presents a chromia layer beneath the alumina scale that is several grains thick with distinct changes in oxide grain size. This is unlike the average chromia layer thickness found on such samples that is normally 1-2 grains thick. Micro-cracking of the alumina scale and the location of this EBSD scan (close to the void) may have influenced nucleation and growth of chromia grains in this region. Variation of chromia grain size within the void fill is also observed. The grain size data map and legend for this void fill is not presented. The changes in chromia grain sizes are not as clear as those recorded for EBSD data set 4 (Figure 5.33). Iron does not oxidise at the base of the crack in the alumina layer due to the high level of chromium present in the alloy and around the void. Chromium also has the next highest affinity for oxygen after aluminium.

BSE Image

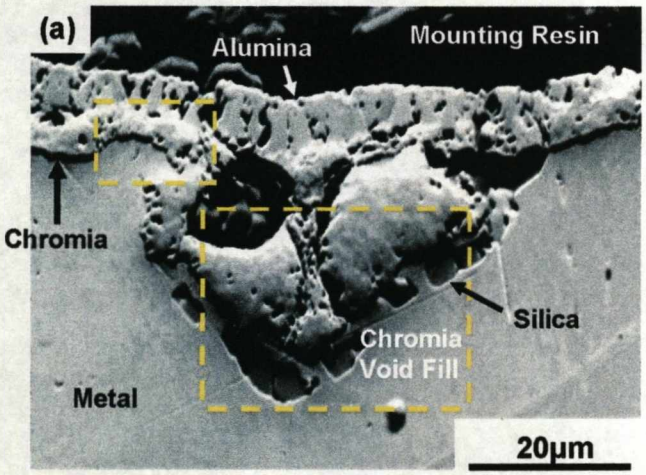

Band Contrast Maps

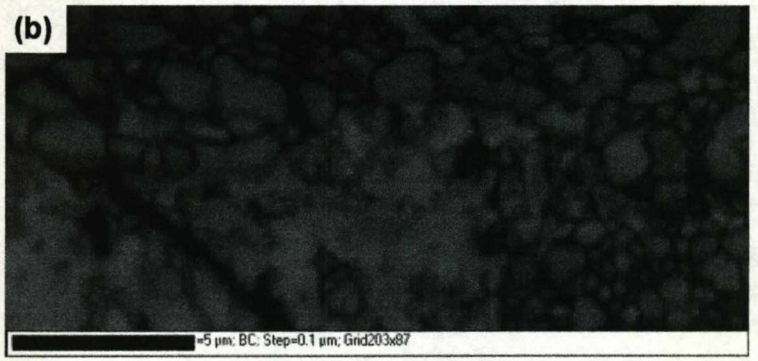

All Euler Maps

(d)

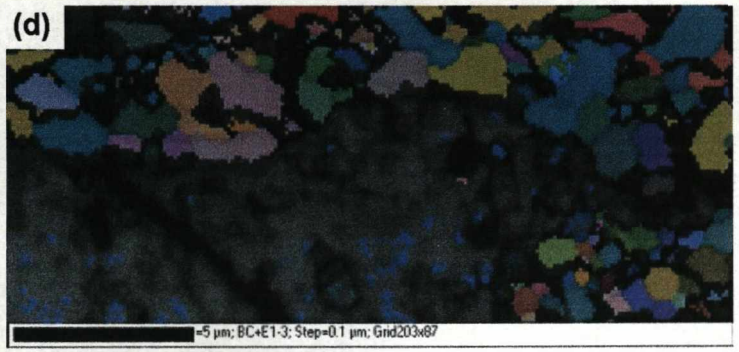

(e)

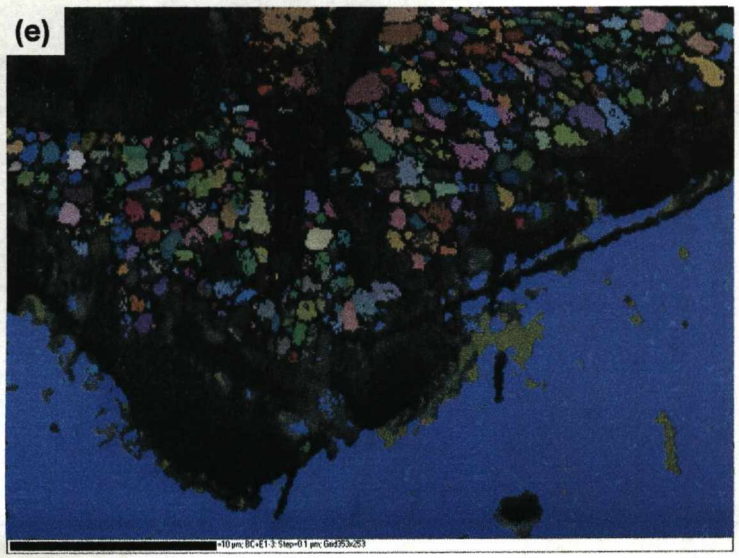

Inverse Pole Figure Maps

(f)

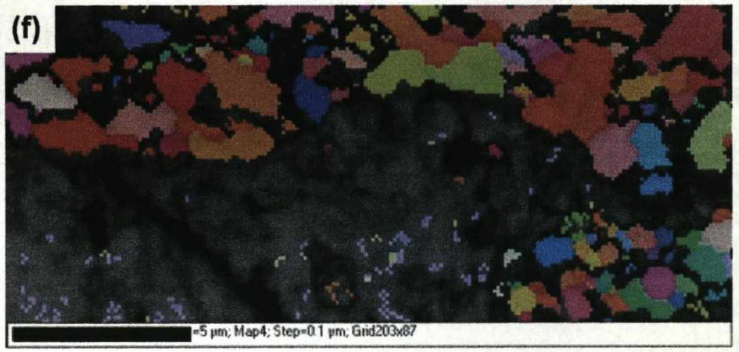

(g)

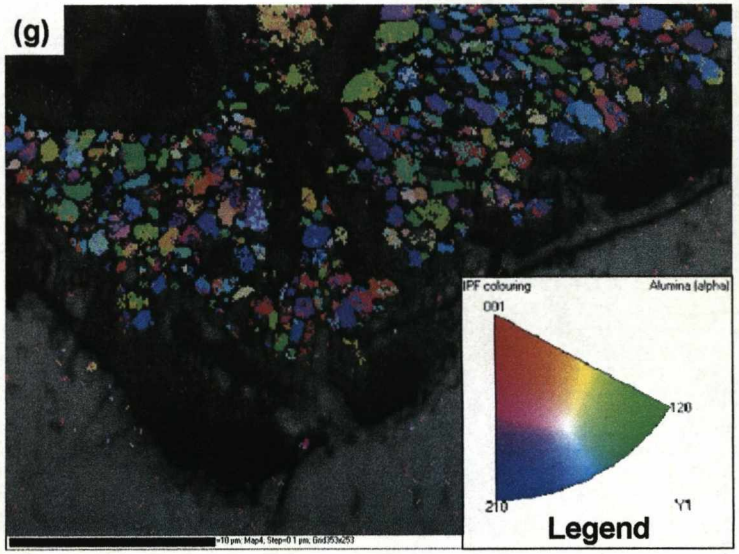

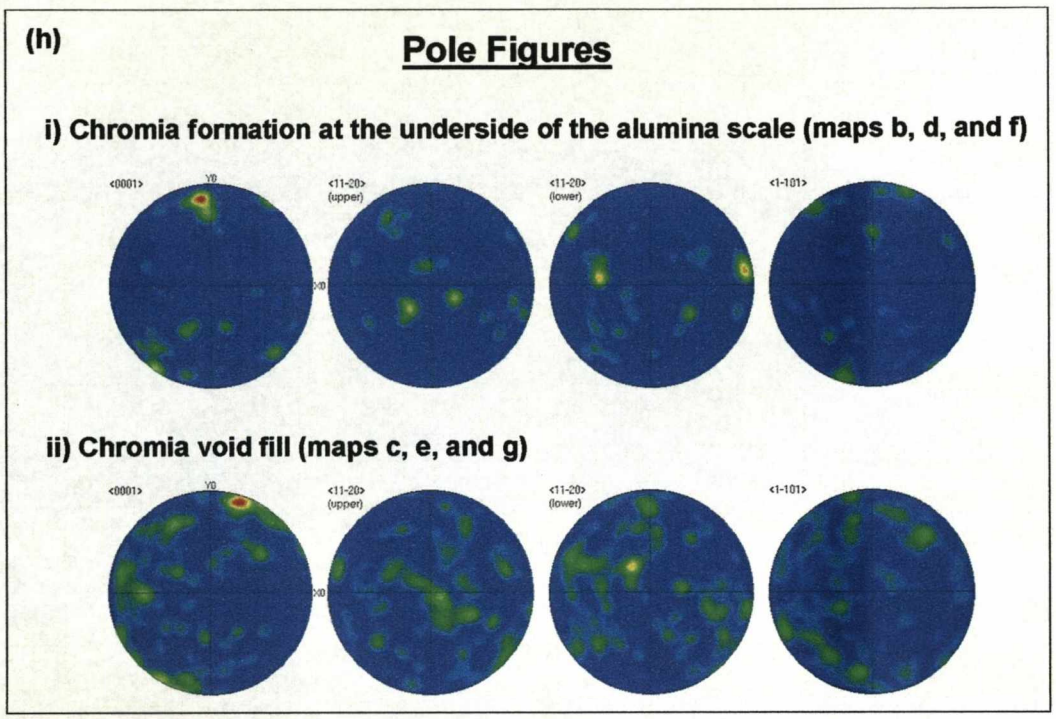

Figure 5.34: EBSD maps and corresponding pole figures of a chromia layer near a void and a chromia void fill. Sample: MI2100 foil 70 microns thick, oxidised at 1200°C for 600 hours

The inverse pole figure map shown in figure 5.34(f) presents some preferred orientation of the chromia grains. This is seen only for those grains positioned within the chromia layer. No preferred orientation is indexed for the chromiagrains indexed in the bottom right of this map. However, the pole figure shown in figure 5.34(h)i) shows no real crystallographic preferred orientation. The indexed data points for this pole figure/stereonet are inclusive of all chromia grains shown in figure 5.34(f). Figure 5.34(g) also presents a random texture for the chromia grains. This is confirmed with the corresponding pole figure shown in figure 5.34(h)ii).

5.5.6 EBSD Data Set 6

Figure 5.35 presents the EBSD and EDS mapping results from another chromia filled void. This void is from a polished cross-section FeCrAl foil sample after oxidation at 1200°C for 640 hours. The BSE image (Figure 5.35(a)) shows the main constituents of the void prior to analysis. This void is slightly smaller than the two previously analysed. If the void is considered hemi-spherical, the radius of this void would be approximately 6μm. The chromia layer beneath the alumina scale is approximately 3-4 microns thick. The condition of the alumina scale in this EBSD data set is not observed. Additionally, the aluminium EDS map (Figure 5.35(h)) does not present well defined aluminium oxide scale boundaries, suggesting damage to the outer oxide scale within this analysis region.

Chromia grain sizes are significantly larger within the chromia layer than those nucleated and grown within the void fill. The average grain size is less than 1μm in diameter within void fill. Grain size in the chromia layer ranged up to 2μm. Figure 5.35(f) presents this data in graphical form. Grain shape data is random and varies across the analysis area. No significant difference between the axial ratio of grains within the chromia layer and void fill is recorded.

BSE Image

(a)

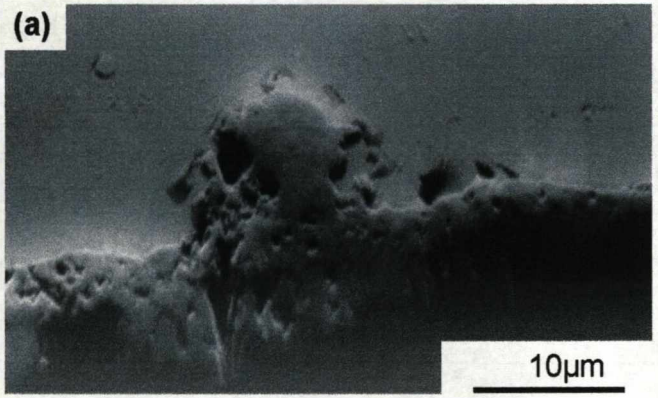

Band Contrast Map

(b)

All Euler Map

(c)

Inverse Pole Figure Map

(d)

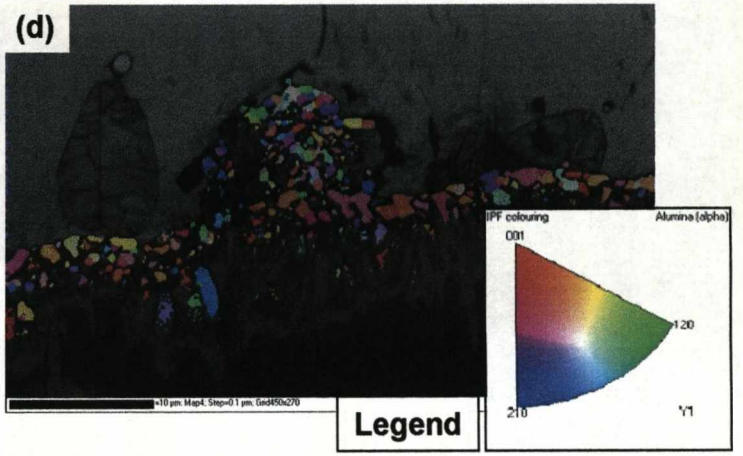

Legend

Axial Ratio of Grains (Grain Shape)

(e)

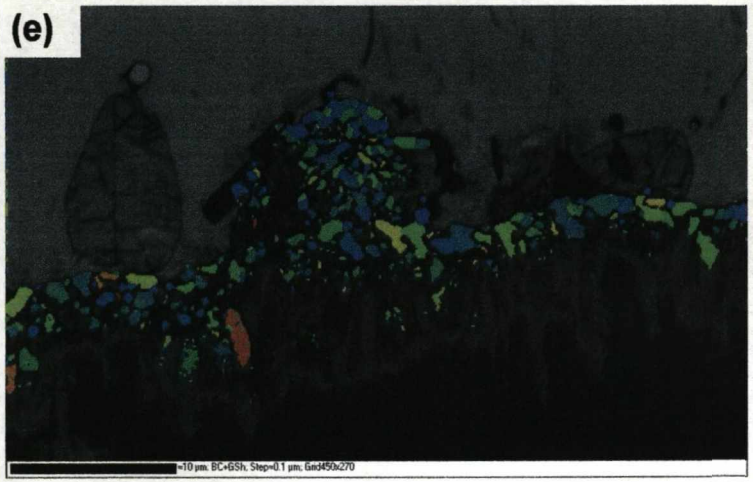

Legend

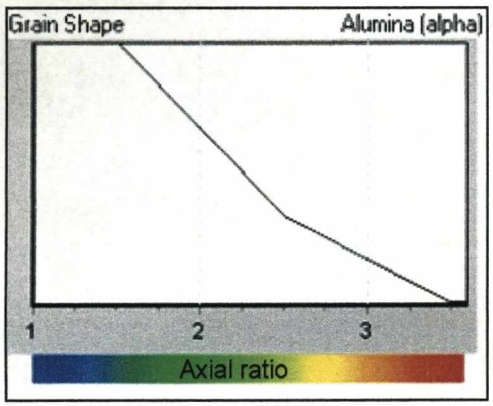

Grain Size Map

(f)

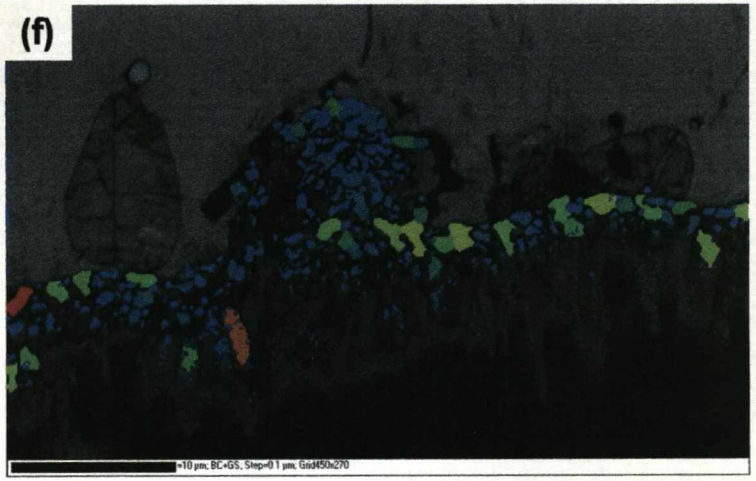

Legend

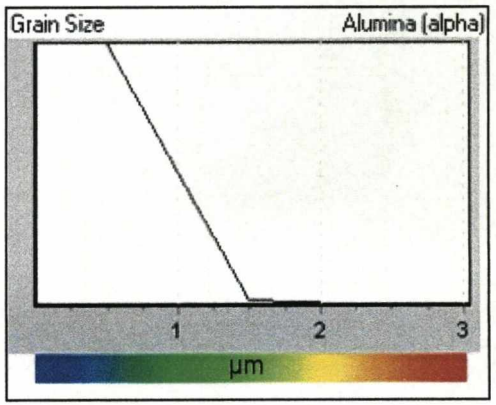

(g)

Pole Figures

Complete Scan

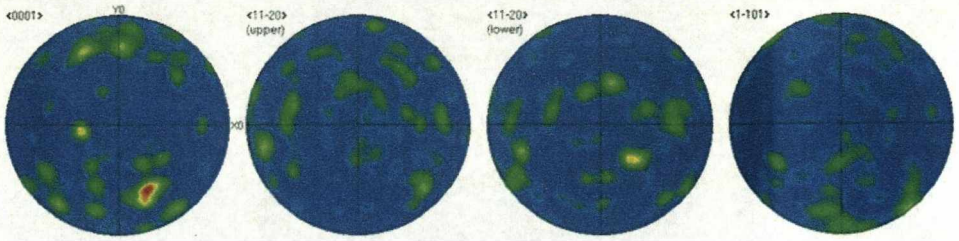

Chromia layer beneath an alumina scale

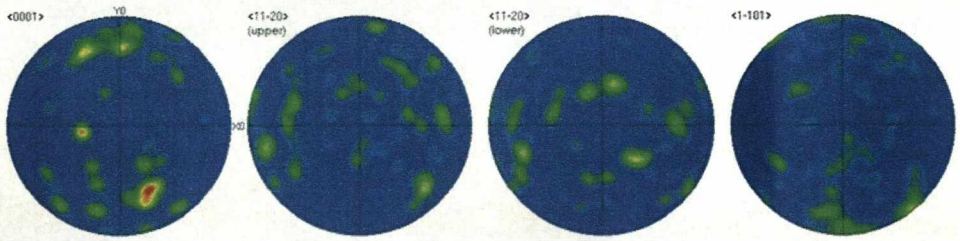

Chromia void fill

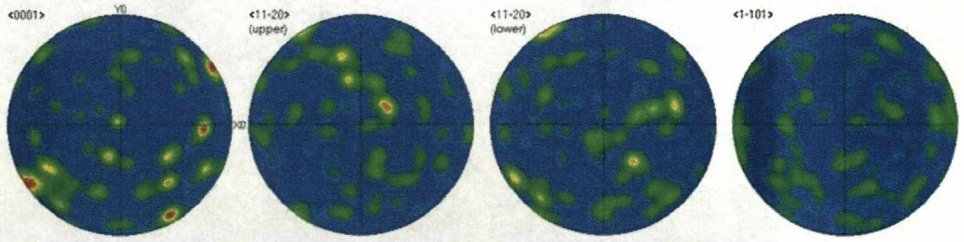

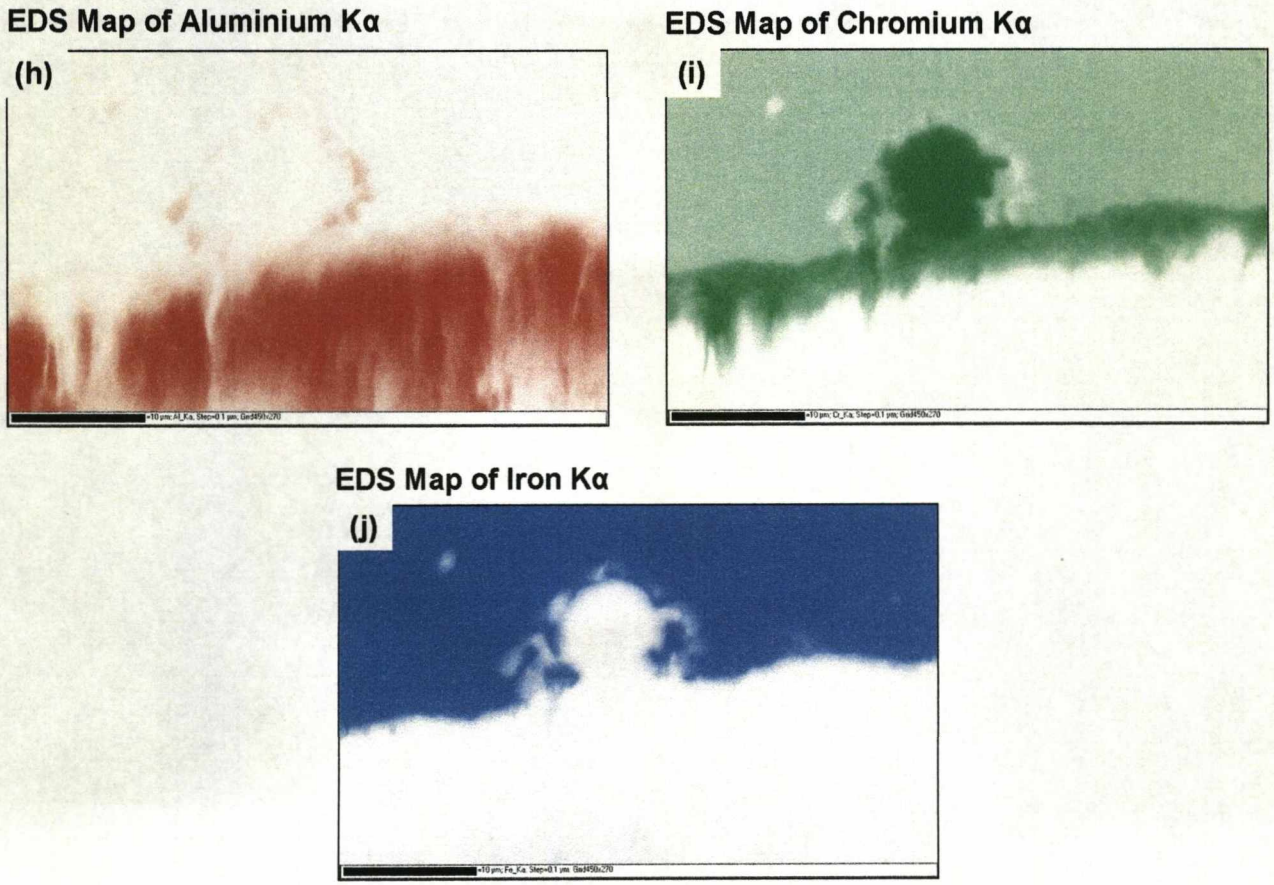

Figure 5.35: EBSD maps, corresponding pole figures, and EDS mapping of a chromia layer and a chromia void fill. Sample: MI2100 foil 70 microns thick, oxidised at 1200°C for 640 hours

The inverse pole figure map (Figure 5.35(d)) and pole figure/stereonet data sets (Figure 5.35(g)) indicate a difference in crystallographic preferred orientation between the chromia layer and the chromia void fill. Although the strength of the pole figure 'Chromia layer beneath an alumina scale' is not as clear as those shown previously, for example as seen in figure 5.29(g), distinct similarities are present. There is a faint trace of alignment of the <1-101> (the r axis) perpendicular to the foil substrate, and the formation of clusters/bands around the poles of the Y axis in the [0001] (the c axis). The pole figure data set 'Chromia void fill' shows no preferred orientation. A complete scan of all indexed chromia grains is also available (Figure 5.35(g)). Layer by layer crystal orientation analysis into the chromia filled void revealed no gradual loss of texture.

EDS maps for Aluminium, Chromium, and Iron were run in conjunction with EBSD analysis and were recorded for the duration of the scan (Figures 5.35(h),(i), and (j)). The scan time was approximately 5 hours. The chromium Kα map is consistent with the positions of the chromia crystals analysed with EBSD. Not present is a Silicon EDS map which may have proven useful in distinguishing the silica particles/band around the void.

Figure 5.35(b) shows the band contrast image for the EBSD analysis. At first glance, this image is quite different to the BSE image (Figure 5.35(a)). Two additional voids located beneath a thin layer of metallic substrate are presented in this map of sample cross-section. There faint outlines can be viewed in the BSE image. No chromia or alumina was indexed using EBSD from these additional voids. The EDS map of Iron Kα (Figure 5.35(j)) records these voids as part of the metallic substrate. The Iron EDS map also shows no change in colour contrast around these sub-layer voids. A small particle containing aluminium is shown on the EDS map near one of these voids.

5.5.7 EBSD Data Set 7

Figure 5.36 presents the EBSD results from half of a partially filled void. This void is from a polished cross-section FeCrAl foil sample after oxidation at 1200°C for 600 hours. The BSE image (Figure 5.36(a)) shows the main constituents of the void. This void is partially filled with chromia. Chromia is present on all free surfaces of the metal substrate. Micro-cracking of the α-alumina scale is evident. A chromia layer can also be observed beneath the alumina over the void. This also forms a continuous band beneath the alumina where contact is restored with the metal substrate. The majority of the void space is vacant. The chromia layer beneath the alumina scale is approximately 3-5 microns thick. Also shown in this BSE image is a much smaller, chromia filled void. No EBSD data was collected from this region. EBSD analysis was taken from two regions of chromia formation. One from the chromia layer formation between alumina and substrate, and the other from a portion of chromia void fill. Both are highlighted on the BSE image. A composite map of the two regions was produced and analysed.

The band contrast map (Figure 5.36(b)) shows that chromia grain sizes are significantly larger within the chromia layer than those nucleated and grown within the void fill. There is some variation of grain size within the partial void fill. The largest grains were found to be in contact with the substrate. With some exceptions, the chromia grain sizes within the void fill seem to reduce moving further into the void. Grain shape data is random and varies across the analysis area. Figure 5.36(d) presents elongated grains of chromia in contact with the metal substrate.

The inverse pole figure map (Figure 5.36(e)) and single pole figure/stereonet data set (Figure 5.36(f)) indicates a random texture for chromia void fill. A separate set of analyses for the chromia layer from this data set (top left

segment) was carried out but was not strong enough to class as a crystallographic preferred orientation. This is unlike those chromia layers previously analysed.

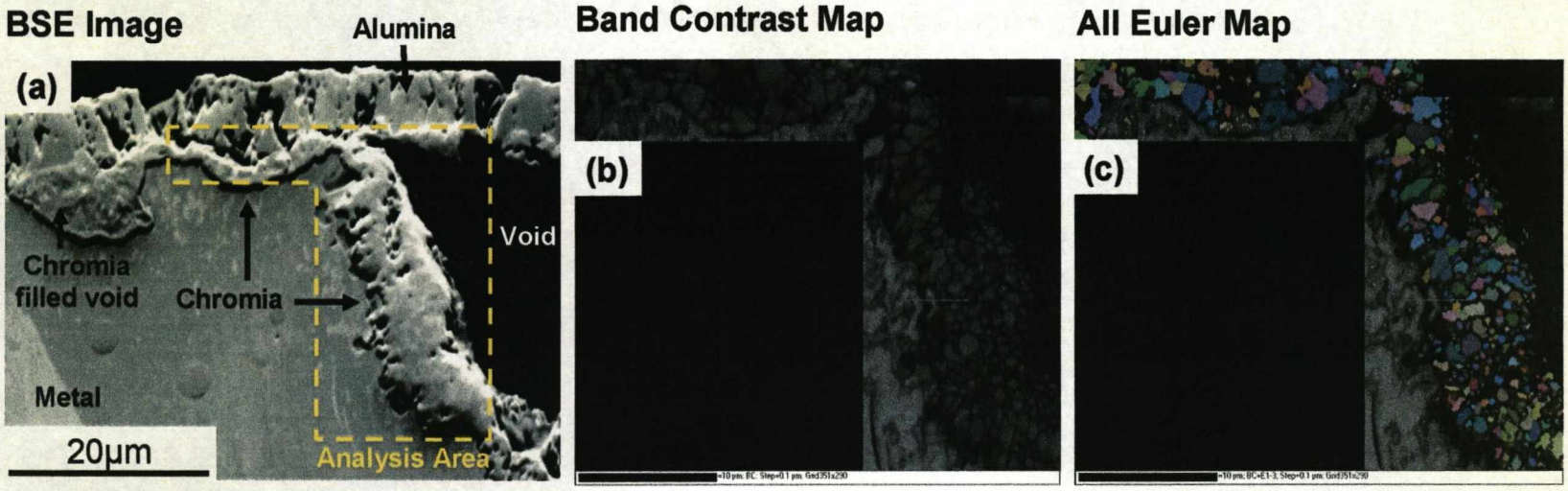
BSE Image
Alumina
(a)
Void
Chromia
filled void
Chromia
Metal
20µm
Analysis Area
Band Contrast Map
(b)
All Euler Map
(c)

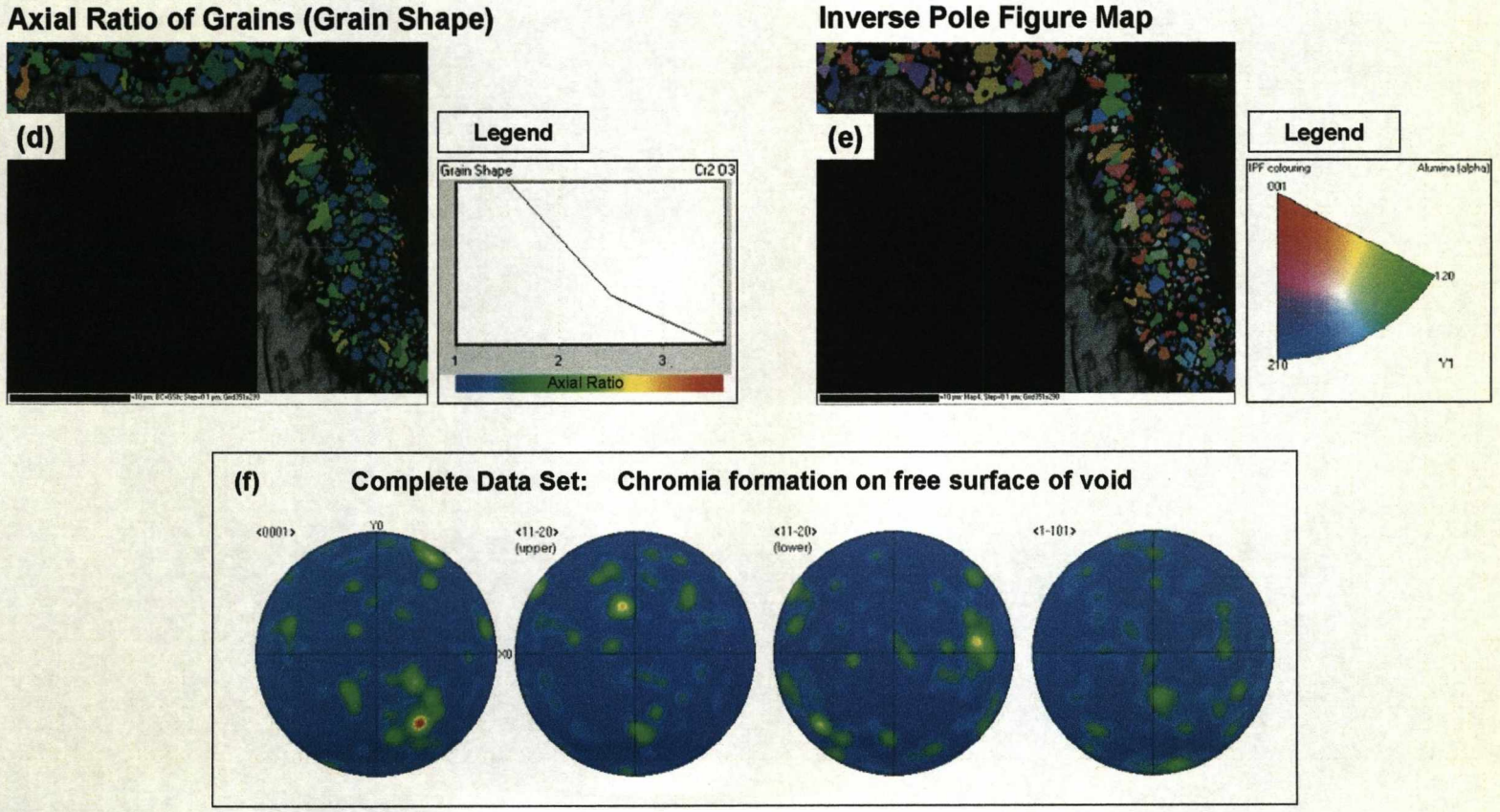

Figure 5.36: Composite EBSD maps and corresponding pole figure of a partial chromia void fill and chromia sub-layer. Sample: MI2100 foil 70 micron thick, oxidised at 1200°C for 600 hours

5.6 Oxidation Testing of Model Alloy A1 at 900°C

Isolated thin FeCrAl alloy foils of a similar alloy were tested at the lower oxidation temperature of 900°C. This results set was used as a comparison to the void formations and filling observed at the higher temperatures (1200°C). The alumina scale morphology was likely to be different at these lower temperatures. Also, phases other than alpha alumina are expected to form at 900°C. The mechanism of alumina scale growth at 900°C was expected to influence void formation. This section presents the results of void formation and the filling of these voids prior to the consumption of aluminium from the alloy substrate. Void formations were recorded at times shorter than those observed on honeycomb foils.

Lower temperature testing at 900°C was conducted. For this a model alloy was used and will be referred to as alloy A1. The alloy's composition is shown in table 3.1. When in the form of 70μm thin foils, short term testing of this alloy also revealed extensive void formation.

5.6.1 Low Temperature Oxidation (900°C)

The metallographic examination of mounted and polished cross-sectional samples from alloy A1 which was oxidised at 900°C for 100h showed discontinuous, scalloped shaped pits containing chromia beneath the outer duplex-alumina scale, as established by the respective EDX analysis (Figure 5.37). This contrasts sharply with the morphology of chromia scales formed on a similar alloy at higher temperatures (1200°C), where a continuous double layered scale is observed (Figure 5.24). In this case voids formed below the chromia layer.

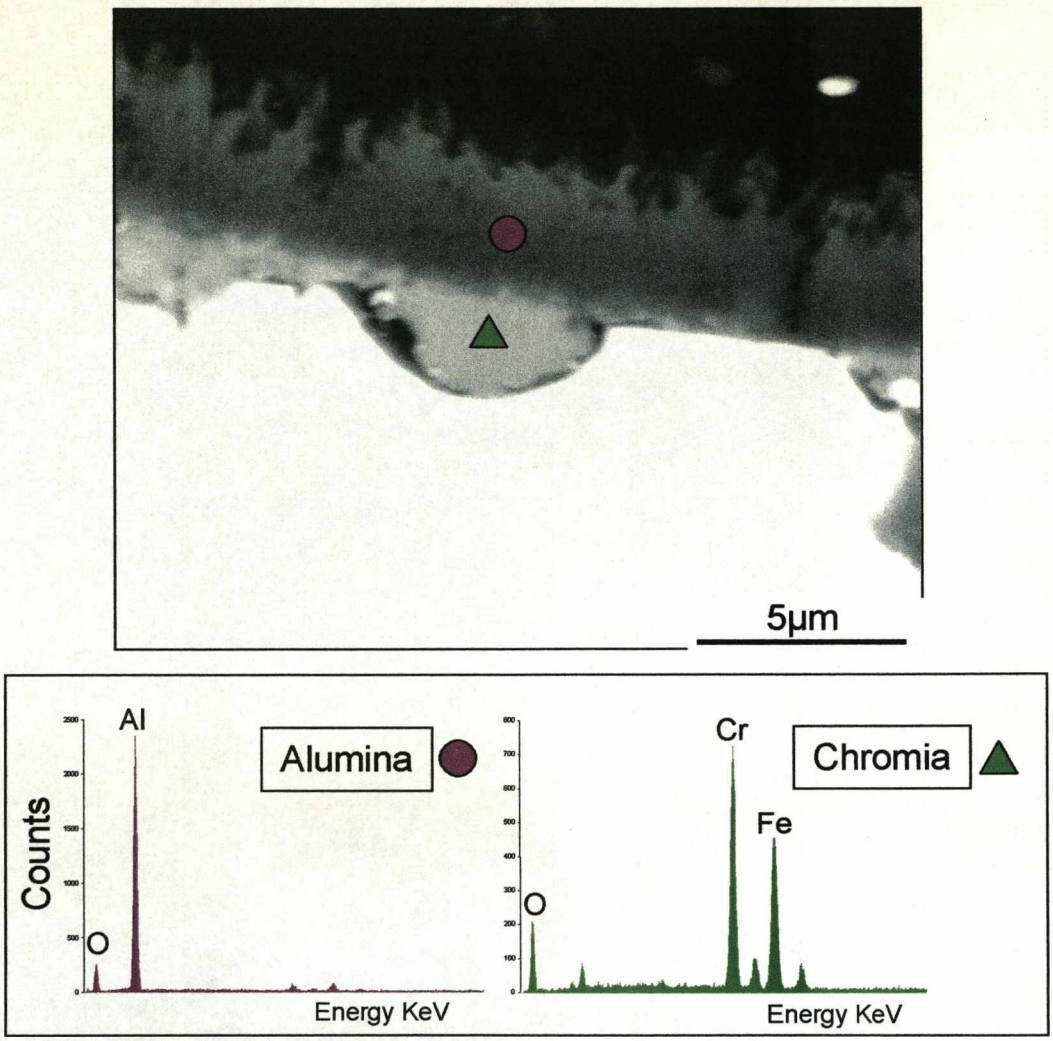

Figure 5.37: Back scattered scanning electron image of a metallographically mounted and polished cross-section of alloy A1 showing a void partially filled with chromia after 100h at 900°C. EDX spectra taken from the regions indicated on the micrograph

Other interesting observations, best illustrated in Figure 5.38, are that the surface of the metal round the edges of the scallop shaped areas is always smooth, the edge of the adjacent chromia layers are usually serrated and small gaps or a series of pores are usually present between the two regions. In

contrast, the interface between the chromia and alumina is usually smooth and pore free.

Further SEM and EDX examinations revealed that some voids were partially filled with chromia, as shown, for example, in Figure 5.37. These areas also often contained small bright particles, which were usually associated with the base of the chromia regions, between the oxide and the metal substrate. EDX analysis showed these bright regions to be silicon rich.

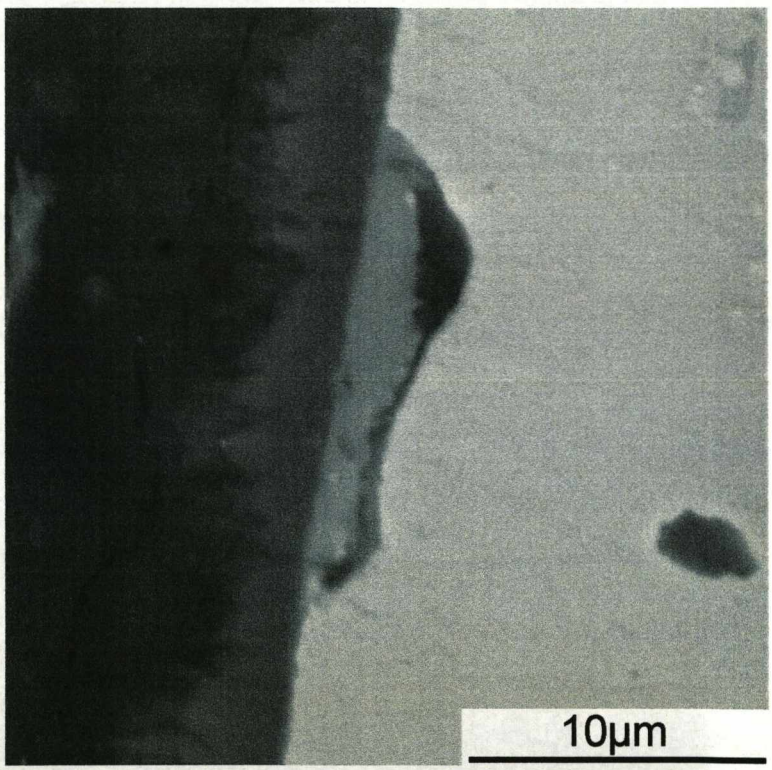

Figure 5.38: Back scattered scanning electron image of a metallographically mounted and polished cross-section of alloy A1 showing a void partially filled with chromia after 100h at 900°C

6. Discussion and Further Results

6.1 As-received Samples

The condition of the as-received samples was encouraging. The combination of MI2100 thin foils and AMS 4782/BNi-5 brazing alloy was a new design. Thin FeCrAl foils had never before been incorporated into a honeycomb abradable seal design and good long term oxidation performance was expected at increased operating temperatures. The vacuum brazing procedure had produced intricate joints of a high quality. These joints were clean, had little porosity, and did not erode the foil material. An even distribution of the brazing alloy was observed through cross-sections of the as-received samples. Capillary action occurs between all double walled honeycomb foils, although the height of the capillary fill did vary across honeycomb structure cross-sections. The spacing between the double walled honeycomb foils (Figure 5.3) is thought to be responsible for this effect. Double walled foils are initially held together by a single spot weld. Some end users request a double spot weld upon honeycomb abradable seal designs with longer foils to reduce the amount of foil separation and increase structural strength. Thin foils begin to separate away from this point. Non-perpendicular sample cross-sectioning may be responsible for the different heights in braze capillary fill although a systematic change in length might then be expected. However, the observed results are still regarded as adequate to provide structural integrity to the structure. A regular and defect-free distribution of braze chamfered zones is also observed. These provide excellent anchoring points for the base of the foils.

The alloy Haynes 214 as a base plate is an interchangeable part of this seal design. Honeycomb abradable seals may also be directly adhered to a cast shroud structure of a similar alloy. Initial observations of the base plate show the Haynes 214 alloy to be a compatible substrate for the brazed honeycomb

foils. Other alloys may be used as a base plate/shroud structures; these will all have a similar composition to the Haynes 214 alloy.

The inter-diffusion between all three components (foils/braze/base plate) can be observed in the as-received samples. The position of all three components is still easily distinguishable, even within the brazed chamfered zone at the base of the foils. Figure 5.6 presents a polished honeycomb sample cross-section after diffusion anneal of 1 hour in an inert atmosphere. The braze chamfered zone became a multi-phase region (Figure 5.6 (d)). Areas rich in Al, Fe, Ni and Si, were detected by EDX. Oxidation testing at 1100°C revealed that these multi phased regions disappeared after 100 hours. This time coincides with what is observed to be the complete inter-diffusion of all three components. No longer can the initial positions of FeCrAl foils and braze alloy be distinguished upon the polished cross-sections. Remnant oxides from the foils have also been consumed or fluxed to the surface. The outer appearance of the structure is not affected by this inter-diffusion.

6.2 Oxidation of Honeycomb Abradable Seals

Honeycomb abradable seals were tested up to 1000 hours at 1100°C. Most tests revealed the honeycomb abradable seals to be covered with an alumina scale upon the foils and braze regions, whilst the base plate was always covered in a green oxide, characteristic of chromia scale presence. In comparison, tests at 1200°C were only conducted up to 600 hours. Detachment of honeycomb foils from the structure occurred at/prior to this time. Tests at 1100°C for times up to 1000 hours, did not show any detachment of the honeycomb foils.

Failure of the brazed joint is not responsible for honeycomb foil detachment at 1200°C. Detachment is caused by the excessive oxidation and rupture of the honeycomb thin foils. Foil rupture is caused by a localised region of breakaway

oxidation and substrate alloy consumption. Foil failure occurs in a region on the foils that is located approximately 200-500μm above the brazed chamfers. Figure 5.13 shows the severity of the increased levels of oxidation observed just above the braze. This honeycomb foil presents a hole surrounded by the formation of a green coloured oxide, typical of chromia. These alloys would normally rely upon alumina formation for high temperature protection. Even at 1100°C, figure 5.11 presents honeycomb foil attack. The same localised region upon the foils did present increased levels of oxidation and the formation of less stable oxides.

Green colouration of both the braze anchor region of the foils and the base plate after oxidation testing was observed. This is representative of chromium oxide formation. The formation of chromia was expected upon the braze alloy as this has no initial aluminium concentration. However, the Haynes 214 alloy does have a reservoir of aluminium and is an expected alumina former at 1100°C and 1200°C. Brief EDX analysis of the base plate presents a mixed oxide scale of predominantly alumina and chromia. As α-alumina is transparent [162], the green colouration of chromia is dominant on the base of the abradable seal.

After oxidation testing, honeycomb abradable seal samples were gradually removed from the furnace, and air cooled. Oxide spallation was always witnessed during the first two minutes of cooling. Spallation occurred during cooling for both test temperatures (1100°C & 1200°C) and after oxidation times as little as 1 hour. Spalled flakes of oxide were always visible by the naked eye. After long exposures at 1200°C, stress relief by oxide spallation caused the sample to recoil and relocate within the test crucible. Oxide spallation during cooling is a common form of stress relief. The complex geometry (i.e. increased number of edges) of the samples is thought to be responsible for the large amounts of spallation observed.

The area of common foil degradation was highlighted using polarised light microscopy in figures 5.11 and 5.13. This technique uses the optical properties (i.e. the refractive index) of the thin oxides. Each colour is then representative of a different or thicker oxide. Greens and yellows represent chromia, and browns represent iron oxide. This denotes the onset of breakaway oxidation.

Overall honeycomb foil degradation is observed at 1200°C. Increased thin foil consumption is clearly observed in figure 5.15(b) where the thickness of the foil cross-sections is dramatically reduced. The increased rate of oxidation at 1200°C consumes the oxide forming elements from the substrate rapidly until they are exhausted from the alloys. This effect reduces the thickness of the foils and decreases their structural integrity. The honeycomb foils shown in figure 5.15(b) are weakened by the alloy consumption for oxidation. These foils now easily deform under their own weight and honeycomb cells can collapse. Degradation of the brazing alloy is also recorded in this image, however all four foils are still well anchored to the base plate. Thin foil rupture would be expected during oxidation shortly after this cross-sectional image was taken. Creep of the substrate alloys is also thought responsible for thin foil curvature and deformation.

Honeycomb foil curvature/deformation was not recorded during tests at 1100°C. However, thin foil curvature was observed upon all the 1200°C test samples. These samples were found to deform at high temperatures, especially upon sample end foils. Hot mounting oxidised samples at 150°C under pressure for metallographic cross-section preparation was found to cause further honeycomb foil deformation. Therefore, cold mounting epoxy was used to confirm the severity of honeycomb foil deformation.

Consumption of the brazing alloy occurs due to the formation of the less stable chromia and nickel oxides. At temperatures above 950°C, chromia is volatile

and is readily removed from the substrate surface. At both test temperatures, the formation of alumina on the honeycomb foils is accompanied by the formation of alumina and chromia on the brazing alloy. Cross-sections of the abradable seal oxidised at 1100°C present the formations of pits and tunnels entering the braze alloy region. In comparison, at 1200°C the attack on the braze alloy is more uniform and the appearance of pits and tunnels is not observed. Excessive oxidation of the braze alloy often occurred. However, the braze region that anchors the base of the thin foils did not experience degradation prior to the failure of honeycomb thin foils.

The tips of the honeycomb abradable seal foils did not undergo any foil degradation or experience breakaway oxidation. The only defects ever present in the alumina scale were small micro-cracks through the oxide which probably occurred during cooling. The alumina scale was always well adhered to the alloy substrate within this region upon the foils and only one or two small voids were ever present.

The number and size of voids formed on the foils increase from the top to the bottom. An increasing dense population of voids can be seen progressively moving down the foils. Voids may coalesce to form larger voids near these regions. Scale cracking and void filling is also observed. Extensive amounts of void formation, void filling, scale cracking and scale spallation is observed near the generalised region of foil attack.

Restoration of an α-alumina scale which is well adhered with little/few voids present is often observed below the region of foil degradation. This region often coincides with an increase in honeycomb foil thickness.

6.3 Void Formation and Filling on Honeycomb Abradable Seals

The severity of interfacial void formation, especially near the regions of foil degradation and rupture were noticed after times as little as 300 hours at 1200°C. Analysis of samples oxidised for longer times revealed an increase in the number and size of the voids. The density of such voiding would suggest that larger voids may be the resultant of the coalescence of smaller neighbouring voids. Void filling was most common with voids formed near the brazed chamfered zone. The locations of voids formed upon these honeycomb foils were generally thought to be random each time. Voids were associated with and without grain boundaries in the substrate.

Foil regions of the honeycomb abradable seals, when oxidised at 1200°C, show interstitial void formation directly beneath the α-alumina scale after only 300h. These may then fill with silica, even though the aluminium level in the foils is still at about 2wt%. However, in most cases these voids are also associated with cracks through the outer alumina scale, and it may be that the remnant aluminium concentration is insufficient to effectively reheal the cracked scale. However, one key feature of all the voids which fill with silica is the growth mechanism within the void. The silica appears to nucleate and grow from the substrate side of the void unlike chromia which appears to always nucleate on the alumina side of the void.

Honeycomb abradable seals oxidised for over 560h at 1200°C exhibit an additional effect in the void filling mechanism. Figures 5.18 and 5.19 are back-scattered electron micrographs and clearly show that two different species have filled the voids in these cases. Both voids are filled largely with silica. However, a thin discontinuous layer of chromia has formed at the underside of the alumina which separates it from the silica. The chromia formation may have occurred after a crack has grown through the alumina scale, as shown in Figure

5.18, although no crack is evident in the image in Figure 5.19 and further work may be necessary to investigate this effect.

Protective α-alumina scale on our variant of the honeycomb abradable seal design was found to suffer from interstitial void formation. The diffusion of silicon from the brazing alloy during oxidation testing was found to have a subsequent effect on the oxidation of the FeCrAl foils and void filling. Silica may grow within the voids and limit the lifetime of the coating by disrupting the protective alumina scale.

The joining of the honeycomb foils to the base plate via brazing, increases the level of silicon in the FeCrAl foils. This was found to alter the void formation and filling behaviour. Voids were found to develop directly beneath the alumina scale. Void development is not a result of aluminium exhaustion in the honeycomb foils. Void formation has been recorded at times as little as 300 hours. The voids were now found to fill with silica rather than chromia. The formation of silica is thermodynamically more stable than chromia at 1200°C. Silica begins to fill the voids from the substrate surface. Another interesting observation is the presence of alumina scale cracking above silica filled voids. Cracking of alumina scales above partially filled voids has not always been observed. Very few partially filled voids with silica have ever been recorded. However, micro-cracking of the outer oxide is the most likely trigger for silica formation. This would allow the movement of oxygen into the void and raise the partial pressure to the necessary level required for silica nucleation and growth.

Oxidised thin foils showed sample curvature after high temperature testing. However, when confined in the honeycomb abradable seal construction, these foils do not exhibit the same curvature and fewer voids are observed. Hence the nucleation of voids in abradable seal foils before the Al is exhausted is most

likely to arise by stress relaxation and relief due to creep of the substrate alloy. However, the complex geometry of the honeycomb foils is also noted. This can prevent such foil curvature. Such geometric restrictions may also explain why honeycomb end foils experience greater foil curvature and interfacial void formations.

Initial investigations suggested that interfacial voids formed upon honeycomb foils are not vacancy voids. These voids appear to be much larger than the vacancy voids described by Hou et al. [106] during the growth of alumina scales. The observed dense population and size of the interfacial voids taken from selected positions of the honeycomb foil cross-sections are at least one order of magnitude larger than those expected due to vacancy condensation alone. Voids presented by Hou et al. are only 2-3μm in diameter, whilst those observed in this work can be greater than 10μm in diameter.

Extensive void formation became more visible microscopically and by the naked eye after 500 hours oxidation at 1200°C. The formation of such voids, at least initially, is not related to the formation of chromia oxide beneath the alumina. Analysis of honeycomb foils did not reveal interfacial void formation prior to 300 hours oxidation at 1200°C. It has been suggested that these voids may form at much earlier times, possibly during the transient alumina oxidation stages, but their size may have been beyond SEM resolution. Substrate deformation and grain growth during oxidation may also cause voids, especially to those associated with substrate grain boundaries. The number and the size of voids increased with increasing oxidation time, increasing the scale thickness, and with increased metal deformation.

The voids occurred during oxidation times where the alumina scale was still well adhered to the metal. The formation of interfacial voids at emergent grain boundaries may be due to the fact that the activation energy for the formation of

such voids is smaller at grain boundary regions than within the centre of alloy grains. In theory, the alumina scale will be under a compressive stress; this causes the metal to creep under a tensile stress and causes void formation. It is also suggests that void formation is related to alloy deformation on honeycomb foils, as tests with thin foils of the creep resistant alloy PM2000 for similar times at 1200°C did not reveal such void formations [162].

Crack propagation through the alumina scales above voids is thought to initiate silica void filling. Cracking of α-alumina scales at 1200°C is very uncommon, however if the thin foils are anchored at the base and the rest of the honeycomb foil creeps, this could induce a mechanical effect which assists with void formation and the mechanical failure of the alumina scale. Mechanical failure in the form of oxide scale cracking would produce hot gas paths through the outer oxide scales, to the voids, and increase the oxygen partial pressure to that necessary for silica nucleation and growth. This would also cause other regions of the alumina scale to spall.

Continued cracks observed through alumina scales and silica void fills (e.g. Figure 5.17) may be the result of secondary effects of the initial cracks in the alumina scale. Impingement of the silica void fill on the outer alumina scale occurs when a void is completely filled. If the alumina scale remains adhered above a silica filled void, during cooling the differences thermal expansion coefficients and tensile loading of alumina, silica and the alloy substrate may cause the crack to propagate further. Cracks are only found to propagate through the oxides and not the alloy substrates. Both alumina and silica are brittle at room temperature.

The thermal expansion coefficients of polycrystalline silica [21] and alumina [163] are much lower than that of the FeCrAl substrate [163]. Additionally, if the crack in the alumina scale did not initiate prior to the silica void fill and

silica filled the void, the crack through both alumina and silica may still be a result of the difference in thermal expansion between oxides and substrate. Silica void filling in this case would be the result of the diffusion of oxygen into the void through the alumina scale or via oxygen movement due to a displacement reaction. Silica is not expected to start void filling at the underside of the alumina if this is the case. Silicon has a lower vapour pressure than chromium and therefore may grow more favourably at the substrate interface of the void [140].

Partially filled voids were not generally observed. Most voids were usually either empty or completely filled with silica during the analysis of honeycomb abradable seal cross-sections. Hence it would appear that once silica nucleation occurs within the void, then void filling will be rapid.

Two types of void filling were commonly observed upon brazed honeycomb foils and are shown schematically in figure 6.1. The following steps below give a brief explanation of void formation and the two filling mechanisms observed. These are to accompany the schematic diagram of interfacial void formation at 1100°C and 1200°C upon brazed honeycomb foils:

1. Growth of protective α-alumina scale until aluminium is exhausted locally from substrate.
2. Voids start to form at the metal/oxide interface and grow during alumina scale growth.
3. If the partial pressure of oxygen is sufficient within the void, silica nucleation and growth will occur. This oxide grows at the substrate interface. Alumina scale cracking above voids is thought to increase the partial pressure of oxygen to the necessary level for silica formation.

4. Type I void formation presents silica growth until the void is completely filled.
5. With Type II voids, after void formation and growth the alumina scale can develop micro-cracks. If this happens a thin layer of chromia develops within the void at the underside of the alumina.
6. Type II voids also present void filling with silica from the substrate interface. It is the silica formation that still dominates the filling of the Type II voids.

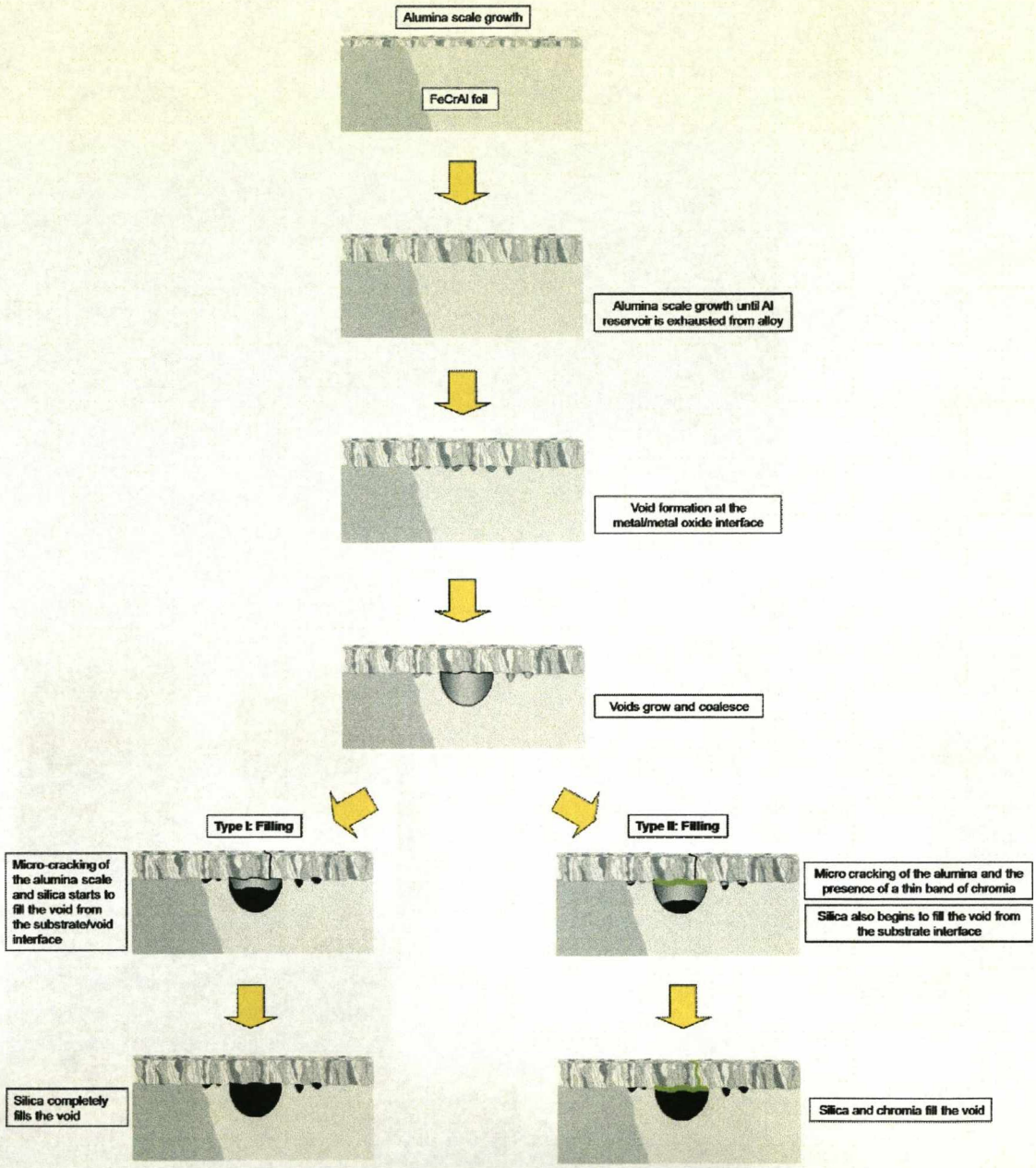

Figure 6.1: Schematic diagram of void formation and filling – brazed honeycomb foils at 1100°C and 1200°C

6.4 Honeycomb End Foils

Tests at 1200°C show that honeycomb end foils are affected significantly more than the more centrally located foils. Observations have also shown that interfacial void formation and void size can be greater upon the end foils and outer walls of honeycomb test specimens. Additionally, an increase in oxide scale thickness is observed on the outer wall of the foil. When compared to the inner wall of the same honeycomb foil, the alumina scale is double the thickness. Substantial end foil curvature is observed upon these test specimens. Tylercote et al. [6] suggested that if a void/pore forms first on one side of a sample, then this will attract other vacancies and form a vacancy sink.

Manufacturers of current honeycomb abradable seals and end users are now specifying honeycomb end foil parameters of double foil thickness. This will increase the aluminium level in the end foils. More centrally located foils will remain at similar dimensions described in this work. It is hoped that this design change will combat these detrimental effects.

End foil curvature and the increase in the number and size of large voids on outer foil walls were not observed during tests at 1100°C. Therefore, it is suggested that a high temperature creep is responsible for curvature of the foils at 1200°C.

6.5 Alloy MI2100: Oxidation and Void formations at 1200°C

The reason why voids form beneath oxide scales is not yet completely understood. The proposed mechanisms for interfacial void formation have been discussed previously by many authors for different alloy systems [105-108]. All present a variety of mechanisms for void formation at the metal/oxide interface, including creep relaxation, influx of vacancies, Kirkendall porosity, etc. Away

from the honeycomb abradable seals, thin foils of alloy MI2100 tested at 1200°C showed little or no void formation until the aluminium level had been exhausted from the substrate and a thin continuous layer of chromia had started to grow on the underside of the alumina. The presence of voids after 600h at 1200°C coincides with the development of a continuous layer of chromia beneath the alumina scale. A combination of the change in oxide growth mechanism and creep of the substrate alloy is thought to be responsible for the formation of interfacial voids.

Other observations of the oxidised thin foils indicate substantial growth of voids along one side of the specimen. This pointed to the source being a creep mechanism relieving stresses due to scale growth causing void formation. The positioning of the voids, however, suggested that this may not be the complete story since voids were also found within the middle of alloy grains as well as on grain boundaries. Voids would have been associated solely with grain boundaries if grain boundary alloy creep was responsible. This random positioning suggests otherwise, although some form of stress relaxation is thought to be responsible for the greater number of voids along one side. Additionally, grain boundaries would not be expected to move after and to be associated with void formations due to an effect of grain boundary pinning [164]. The formation of such voids would decrease the driving force (energy) pushing the boundaries within the polycrystalline structure.

Void formation was soon followed by void filling at the higher temperature of 1200°C. After a continuous layer of chromia is formed beneath the alumina, a void may form. Many voids have been studied; few are found to be vacant but most are completely filled or partially filled with an oxide. For alloys low in silicon, once the aluminium activity in the alloy drops below the critical level [19, 35], the formation of alumina will stop. Then the formation of a layer of chromia will occur beneath the outer oxide. If a void forms behind the layer of

chromia, chromia may start to fill the void. This void filling commences from the base of the oxide by what is proposed as a vapour transport mechanism of chromium [108]. For this vapour transport mechanism to exist, the void region must have a substantially low partial pressure of oxygen. Otherwise the growth of oxide would be expected upon the substrate/void interface. At 1200°C it is not unrealistic to propose a vapour cloud of chromium within the void as long as the pseudo protective oxide scale remains intact. This proposal suggests that, as time increases, oxygen will diffuse through the dual layered oxide and react with the chromium. New chromium rich oxide is then deposited onto the existing chromia layer and grows into the hemi-spherical void. As long as the dual layered scale remains intact, the process may continue until the void is completely filled.

Another possible mechanism for void filling is through surface diffusion of chromium round the void. However, it seems more likely that a vapour transport mechanism may lead to the smooth finishing of the substrate surface, observed in partially filled voids. Surface diffusion around a void would be expected to give a more uneven distribution of void filling.

Another type of void formation is seen within FeCrAl alloy MI2100, which contains ~0.62wt% Si. Similar to the previous mechanism, a void forms beneath the dual layered oxide of alumina and chromia. However, this type of void grows much larger than those shown previously. This excessive growth may be responsible for cracking in the external scale. This crack provides a hot gas path and rapidly increases the partial pressure of oxygen within the now open void, and allows the nucleation of the less stable chromia upon the substrate wall of the void. Interestingly, the growth of silica is also found in the vicinity of these voids, usually as small particles or as a continuous band (this silica nucleation is observed as an internal oxide in the substrate offset by a constant distance around the void). When first observed, these silicon rich

particles were thought to be debris from the polishing suspension used for sample preparation. However, reproducibility of this result and the lack of other silicon rich particles embedded within other regions of the metal substrate make this unlikely.

The presence of silica internal oxide is possibly linked to a localised depletion of chromia round the void together with oxygen diffusion into the substrate. As long as the partial pressure of oxygen in the substrate is high enough at a limited distance away from the void, silica may nucleate and grow. It is noted that further internal oxidation of silica does not appear to occur once a continuous band is formed around the void. The formation of silica is often observed in conjunction with the presence of chromia growth upon the alumina on the outer wall of the void and with large cracks which penetrate the outer dual layered oxide. It is suggested that these are linked to the degradation mechanism of the alloy.

Thermodynamically it is not unexpected to get the growth of alumina, chromia and silica at 1200°C upon a FeCrAl alloy containing silicon. In fact, silica formation would be expected prior to the formation of chromia. The limited amount of silicon ($\leq$0.62wt%) in the alloys may restrict the nucleation and growth of the silica, and chromia void filling is observed instead. However local variations in the silicon content of the alloy may occur and lead to some voids being filled with silica while others are filled with chromia, as has been observed on a limited number of occasions.

The alumina scale is thought to grow predominately by the inward diffusion of oxygen [20, 23, 35, 98, 162]. The chromia scale which forms beneath the alumina, producing a pseudo protective oxide, is suggested to form by the outward movement of chromium atoms once an initial scale has been established [81]. This change in mechanism could cause vacancies to develop

in the substrate alloy and condensation of these vacancies would result in voids at the metal/oxide interface. The extent of voiding may increase if the substrate alloy was to undergo any creep relaxation. It is possible that substrate creep may have an effect upon void formation after the change of oxide species to Cr_2O_3 layer growth. However, the amount of chromium depleted from the substrate during sub-layer formation should not significantly affect the creep resistance of the alloy. Very localised areas of chromium depletion are not expected beneath the metal/oxide interface at 1200°C.

Void filling was recorded at 1200°C in air. MI2100 foil samples oxidised for 600 hours presented a large number of voids that are filled or partially filled with chromia. Void filling was only recorded after the exhaustion of aluminium from the substrate alloy and after the establishment of a continuous chromia layer beneath the alumina. The position of the void is always found beneath the chromia layer. The spacing between voids is rather random and a variety of different sizes is also noted at any one time. This ranged from voids less than 1μm in radius, to voids 20μm in radius (assuming voids are hemi-spherical). The void filling commences from the base of the oxide by what is proposed as a vapour transport mechanism of chromium [17, 85].

FeCrAl foils without reactive element additions are normally associated with extensive void formations prior to aluminium exhaustion from their alloy substrates [23]. Reactive elements are renowned for their improvements in oxide scale adhesion [117]. Alloy MI2100 foils contain additions of Y and Hf, and when oxidised away from the honeycomb abradable seal setup, do not present void formation until after the aluminium is exhausted from the alloy substrate. The condensation of vacancies from the change in oxide growth mechanism of alumina to chromia, as described in Section 2.18, is thought responsible for the formation of interfacial voids below a chromia layer. However, another possible mechanism for void formation is the consumption of

reactive elements. If reactive elements are consumed by incorporation into alumina scales, then upon their exhaustion, scale adhesion may suffer and void formation may arise. This may occur during the formation of the chromia layer beneath the alumina.

The formation of a chromia layer below alumina scales on soft alloy substrates is known to provide limited lifetime extensions [23]. Chromia is also known to be soluble in alumina at 1200°C [165]. Its presence in this work has always generally been observed as two distinct layers. Intrusive growths of chromia can be observed into alumina scales throughout the tests. Needle-like protrusions can be seen in most cases. EDX analysis of the alumina scales in dual oxide formations did detect small levels of chromium. However, no aluminium was detected when analysing the chromia region of the oxides.

Two types of void filling were recorded upon alloy MI2100 foils at 1200°C and are shown schematically in figure 6.2. The following steps below give a brief explanation of void formation and the two filling mechanisms observed. These are to accompany the schematic diagram of interfacial void formation at 1200°C for alloy MI2100 thin foils:

1. Growth of protective α-alumina scale until aluminium is exhausted from substrate.
2. Chromia scale begins to nucleate beneath the α-alumina and forms a continuous layer.
3. At this point, voids start to form at the metal/metal oxide interface and grow due to the change in oxide growth mechanism.
4. Thickness of the chromia layer is unaffected by the presence of voids i.e. uniform layer thickness above voids and adhered to the substrate.

5. As time progresses, a Type I void will fill completely with chromia. The growth of the chromia is from the underside of the alumina via a vapour transport mechanism.
6. Filled Type I voids also show evidence of silica particles being incorporated into the chromia void fill.
7. Type II void formation and filling occur when the pseudo protective oxide cracks above a large void, creating a hot gas path.
8. Chromia formation occurs upon all free metal substrate surfaces within type II voids.
9. At the same time silica internal oxides start to grow just within the substrate around the void.
10. Silica internal oxides form a thin continuous band around the void and chromia growth continues within the void.

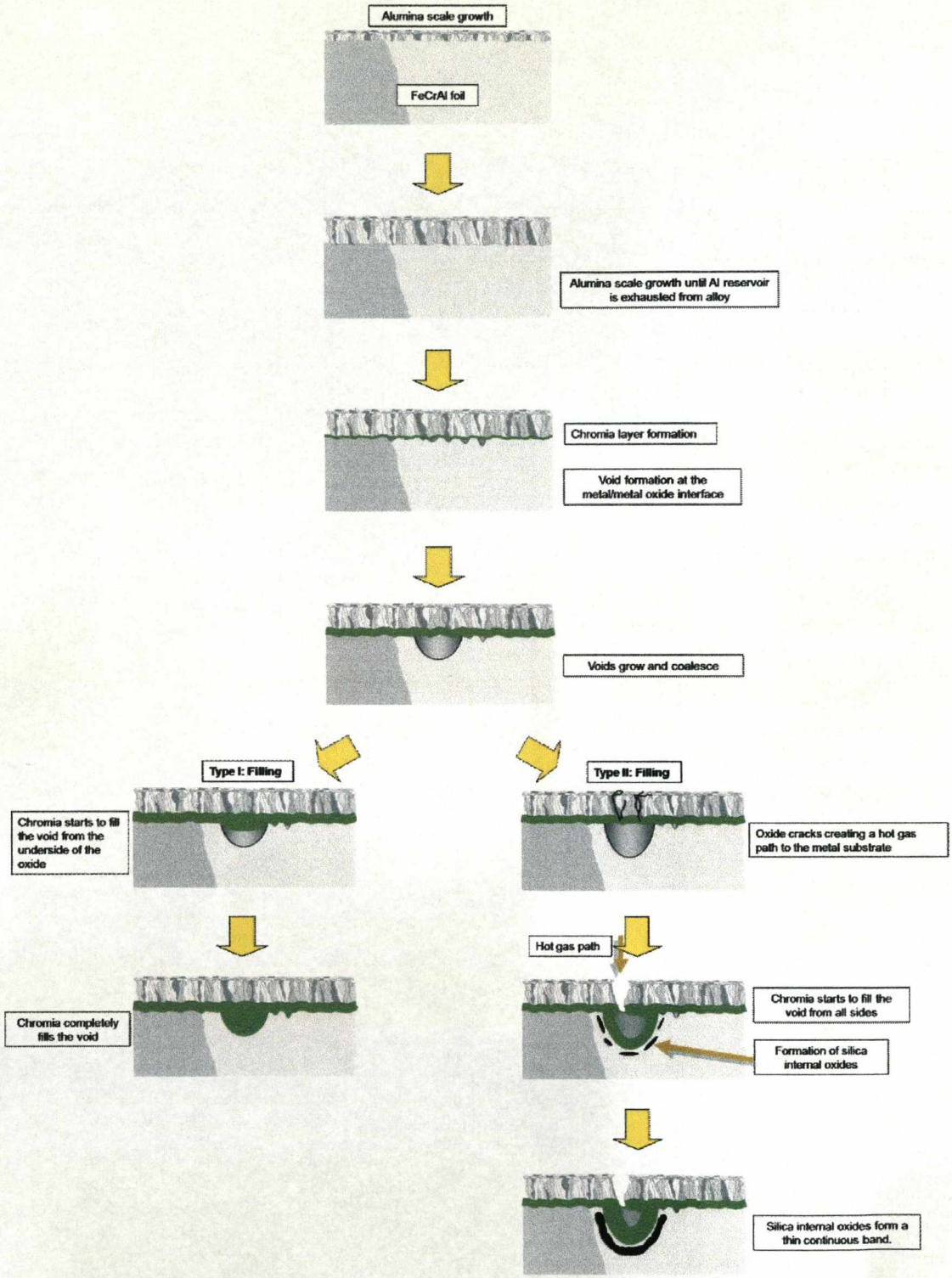

Figure 6.2: Schematic diagram of void formation and filling – alloy MI2100 thin foils oxidised at 1200°C

6.6 Alloy A1: Oxidation and Void formations at 900°C

In comparison, the alloys tested at the lower temperature of 900°C show void formation after only 50h. After this short time there still remained enough aluminium within the metal substrate to sustain the growth of alumina. Tatlock et al [108] suggested that the longer growth time for transition alumina at 900°C prior to the formation of α-alumina, could cause movement of vacancies to the metal/oxide interface causing void formation after short times.

The positioning of the voids at the lower temperature was similar to those voids observed after higher temperature tests. The interfacial voids nucleate at random positions. Some are associated with alloy grain boundaries that emerge at the surface, and others form within outer alloy grains. After observation of sample cross-sections, the voids are again assumed to be hemi-spherical.

Observations from thin foil cross-sections revealed a larger number of voids form on one side of the sample than the other. This may again be a stress-related effect, which could perhaps influence the movement of defects, and hence the subsequent formation of voids. The movement and coalescence of vacancies due to the formation of outward growing transient aluminas is thought to be responsible for void formation after such short times (<50 hours). The inward flux of vacancies and hence void formation is thought to be retarded by the transition to α-alumina formation.

Tests at 900°C present void filling after short times. Void filling occurs soon after void formation. These voids are found to fill with chromia. Void filling was found to commence from the base of the alumina scale.

Even at low temperatures, the growth of alumina scales above interfacial voids is maintained. Whilst the void is unfilled, a vapour transport mechanism of

aluminium is thought responsible for continued alumina scale growth. Once the aluminium activity around the void is reduced void filling will commence.

Partially filled voids were a common observation when testing thin FeCrAl foils at lower temperatures. These reveal the chromia void fill commenced at the underside of the alumina scale. The surface of the chromia fill growing towards the substrate was always smooth. Work by Tatlock et al. [108] suggests this to be evident of a vapour transport mechanism, followed by either the growth of chromia into the void or possibly by a displacement reaction involving the release of aluminium at the base of the alumina layer. The aluminium would then diffuse through the scale to the higher oxygen potential, whilst the released oxygen would maintain the chromia growth.

Thermodynamically, it is possible to explain the successive formation of alumina, followed by chromia and silica, since at 900°C the equilibrium free energy for the metal-oxide dissociation reaction for aluminium is lower [4].

Chromia appears to fill voids at this temperature without the formation of a continuous layer of chromia beneath the alumina, typically seen during thin foil testing at 1200°C. This may be the result of a change in oxidation mechanism, between the two temperatures.

Only one type of void formation and filling mechanism was observed upon alloy Al when oxidised at 900°C. This is shown schematically in figure 6.3. The following steps below give a brief explanation of void formation and the filling mechanism. These are to accompany the schematic diagram of interfacial void formation upon alloy Al at 900°C:

1. Initial transient growth of an alumina scale.

2. After only 50 hours or less, void formation observed directly beneath the alumina scale.
3. Alumina scale can still grow by a method of vapour transport.
4. Soon after void formation, void filling commences. The voids fill with chromia which grows from the underside of the alumina via a vapour transport mechanism.
5. Chromia formation is restricted to the area confined by the void. Chromia does not form at the metal/oxide interface at the same time as it grows in the void. This is possibly due to the localised depletion of aluminium in the substrate near the void.
6. Voids completely fill with chromia.
7. These voids also show evidence of silica particles being incorporated into the base of the chromia void fill.

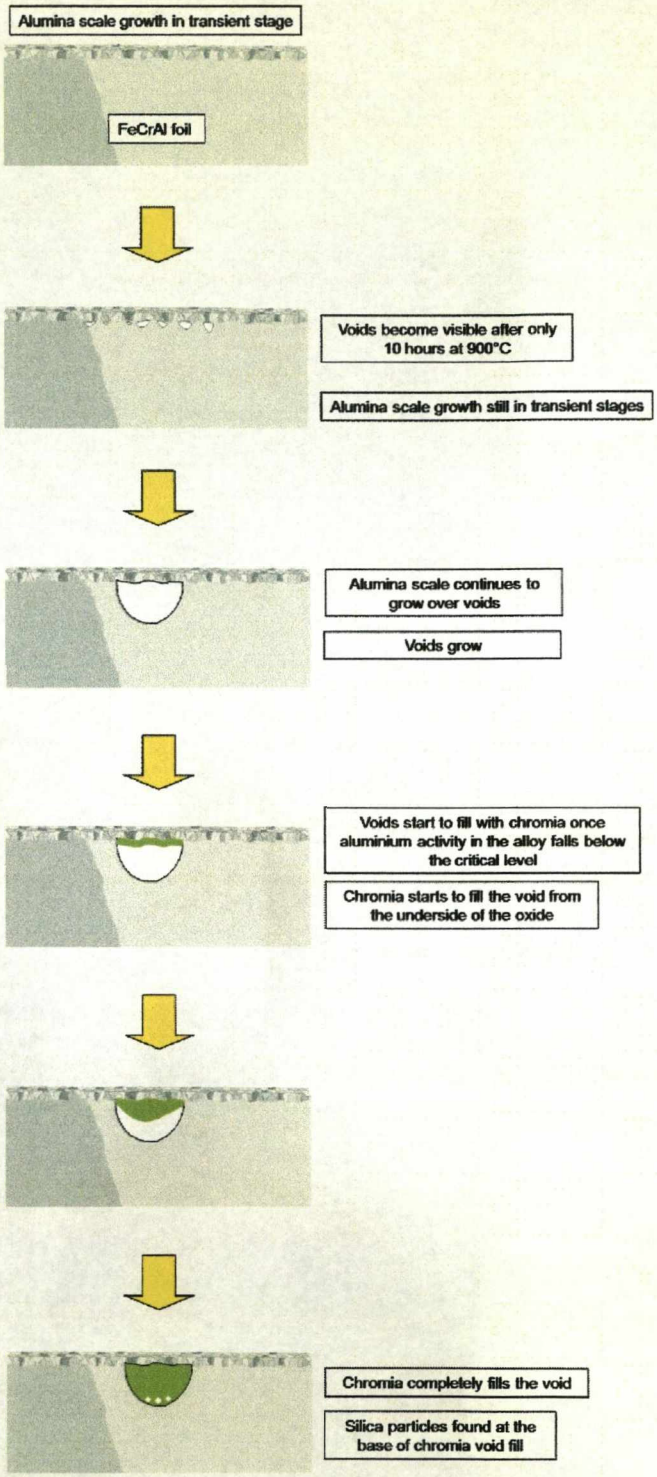

Figure 6.3: Schematic diagram of void formation and filling – FeCrAl foils oxidised at 900°C

6.7 Diffusion of Braze Alloy Constituents – Further Results

The diffusion of nickel and silicon constituents from the brazing alloy through the FeCrAl foils was always considered to be an issue. In the case of nickel, the diffusion of a significant amount could alter the mechanical properties of the ferritic FeCrAl substrate. Silicon carries the risk that it may diffuse through the foil substrate and influence the subsequent oxidation behaviour. The initial diffusion of these two elements, and others, occurs during the four and a half hour brazing procedure. Such a process will cause the permanent joining of the parts via a diffusive reaction. However, the initial brazing process does not afford dramatic changes to the foil composition. Heat treatments and the high temperature testing and operating environments for the honeycomb abradable seal caused further diffusion of braze alloy constituents. The significant differences in alloying elements which remain between the nickel and iron based substrates, and temperatures >950°C, has been found to promote the further and continued diffusion of nickel and silicon during testing.

Experimental diffusion profiling data has been attained for several honeycomb abradable foils, ranging from 450 hours at 1100°C, to foils after 500 hours exposure at 1200°C in lab air. A second set of experimental diffusion calculations were conducted and will be presented first. This was a series of brazed sandwich structures, made up of 1 mm thick sheet of a similar alloy, Aluchrom YHf, and a 70 micron thick BNi-5 brazing alloy. This set of samples was tested at 1100°C for times up to 300 hours. Diffusion profiles were attained using the point analysis method described in Section 3.10. Normally such diffusion profiling would have been studied and made easier by using an electron probe microanalyser (EPMA). Such a facility was not made available during the project time scale. Experimental results were compared to theoretical data throughout.

6.7.1 Brazed Sandwich Structures

The diffusion of braze alloy elements, nickel and silicon was studied in a series of brazed sandwich structures. After brazing, the three sandwich structures were oxidised for 100, 200, and 300 hours at 1100°C in laboratory air. The diffusion of braze alloy constituents was studied over the polished cross-section of each sample, such as that shown in figure 6.4.

A derivative of Fick's second law of diffusion was used to calculate the theoretical diffusion profiles of these sandwich structures. Diffusion coefficients of alloy constituents were acquired from reference sources such as the European funded SMILER project (Contract G5RD-CT-2001-00530), and can be found in Appendix 4. Figure 6.5 presents the theoretical diffusion data sets for the nickel in a brazed sandwich structures. These models assume a finite source of nickel in the braze alloy, and that there is no nickel present in the FeCrAl foils. It is also assume that nickel and silicon entering the FeCrAl foils are not consumed by oxidation of the foils. Three data sets are present: 100, 200, and 300 hours oxidation at 1100°C. All data sets also include the initial diffusion of braze alloy constituents during the brazing cycle. It is assumed that diffusion of braze alloy constituents only occurs at the brazing temperature of 1190°C for 240 seconds (4 minutes) during this cycle.

Figure 6.6 shows the theoretical diffusion profiles for silicon at 1100°C within the brazed sandwich structures. Theses profiles are very similar to those of nickel but with a significantly lower composition by weight. These profiles also assume an initial FeCrAl foil concentration of 0.3 wt. % Si. As shown earlier, silicon is found to significantly affect the oxidation and void filling mechanism of alloy MI2100. If it assumed that there is no silicon present in the FeCrAl foils, theoretical diffusion calculations predict that the very small amount of

silicon will diffuse through a 1mm thick FeCrAl foil at 1100°C in 76,020 seconds (21 hours and 7 minutes).

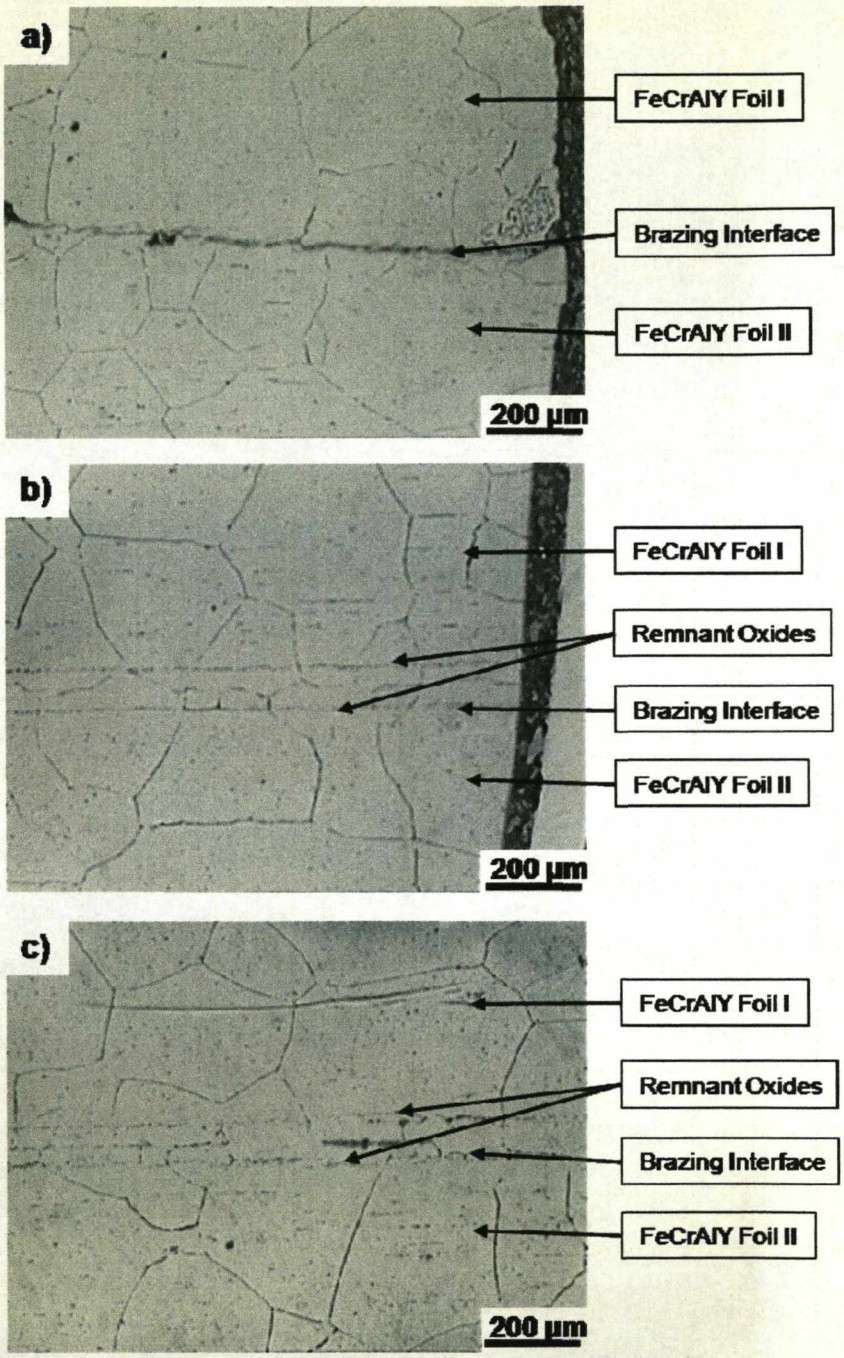

Figure 6.4: Optical micrographs of polished and etched brazed sandwich structure cross-sections, oxidised at 1100°C for a) 100 hours, b) 200 hours, and c) 300 hours

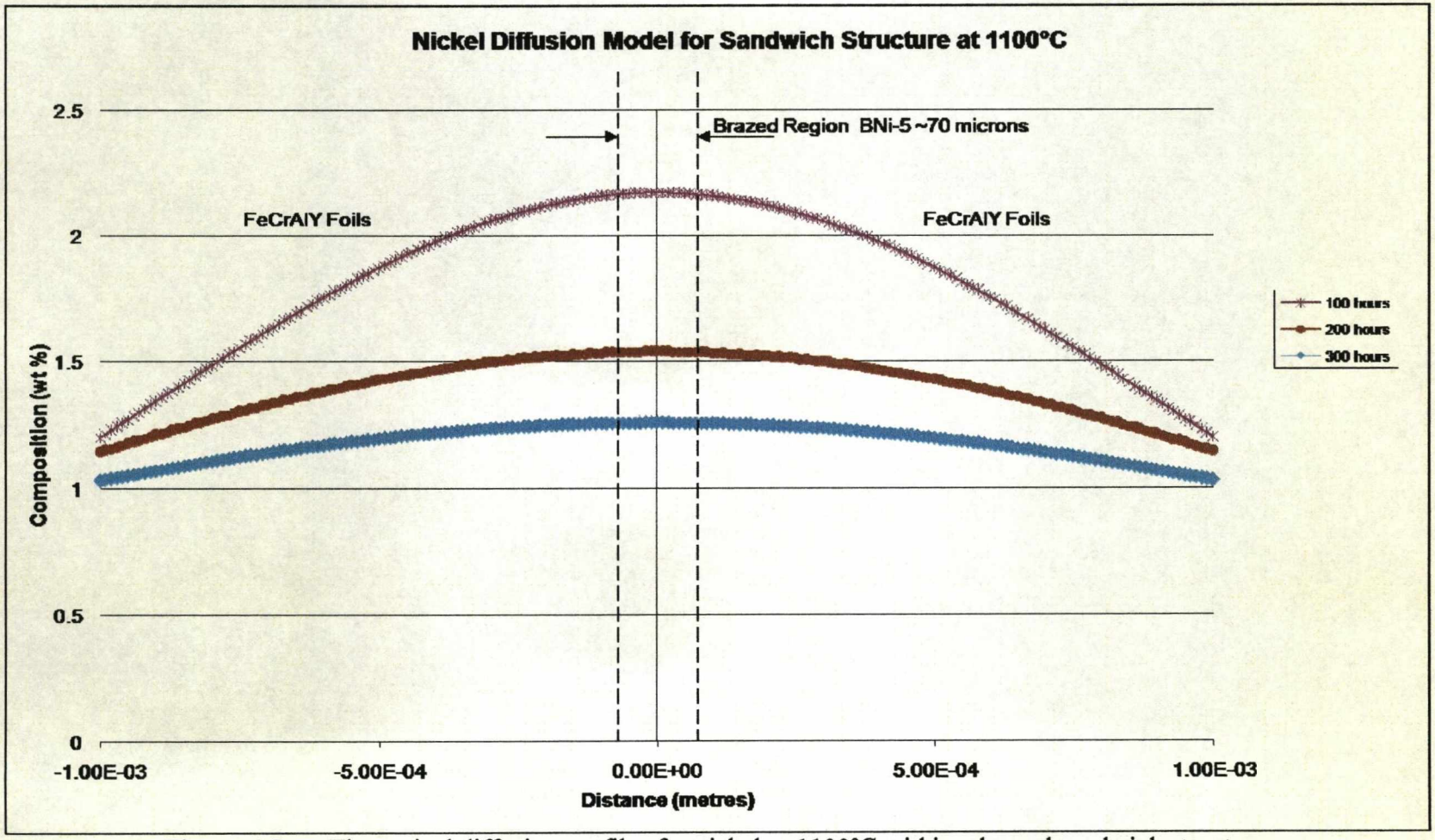

Figure 6.5: Theoretical diffusion profiles for nickel at 1100°C within a brazed sandwich structure

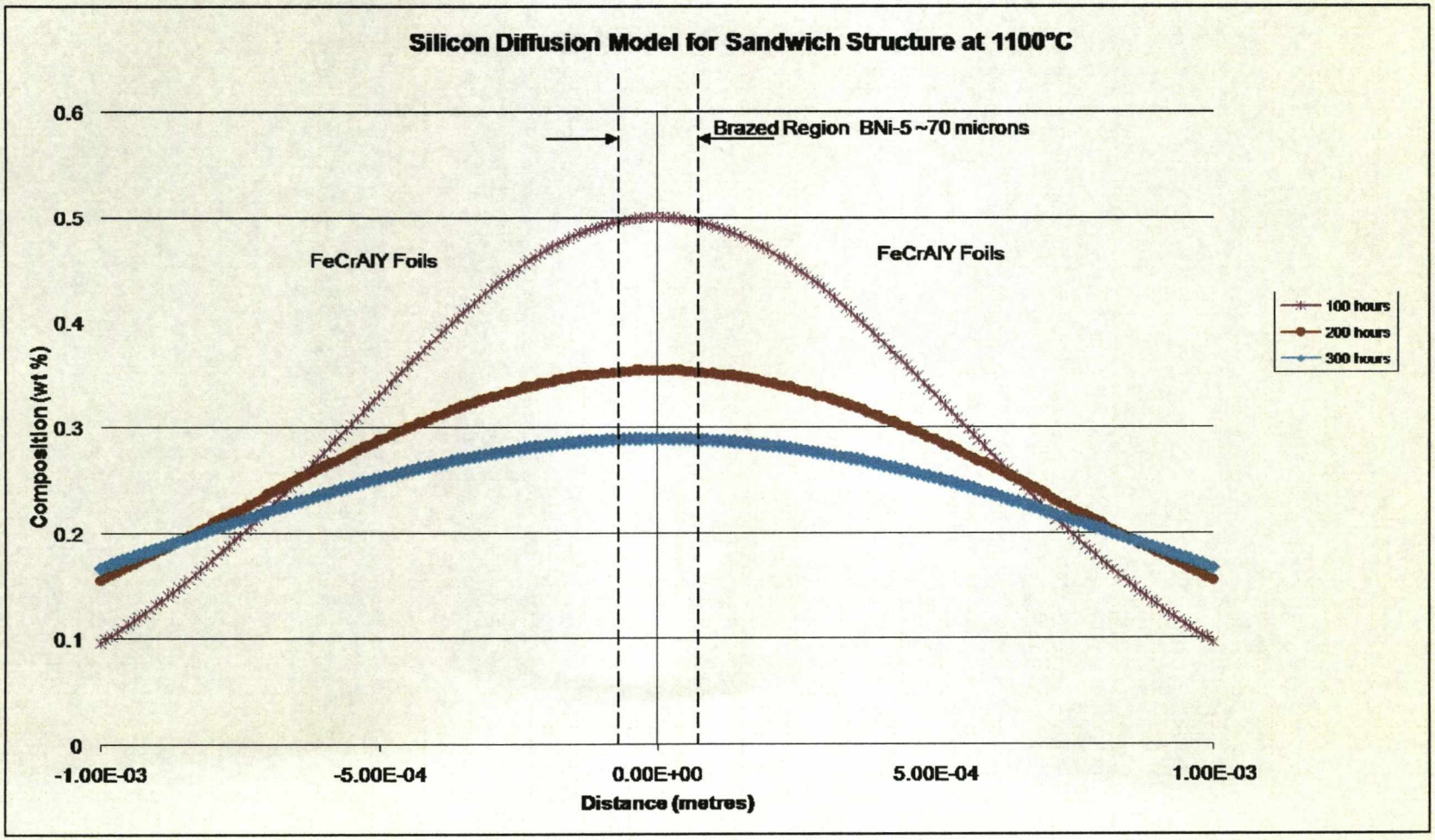

Figure 6.6: Theoretical diffusion profiles for silicon at 1100°C within a brazed sandwich structure

A series of experimental diffusion profiles were acquired using the EDX point analysis from a series of prepared cross-sections. This was carried out in a similar method to that described in section 3.10. Optical images of these sample cross-sections can be observed in figures 6.4(a), 6.4(b), and 6.4(c). These images show the development of a uniform microstructure throughout both FeCrAlY foils and the initial brazing alloy location. EDX point analysis across these cross-sections was used to try and establish diffusion profiles of braze alloy constituents, similar to that of the theoretical diffusion models. As the EDX system was only qualitative, background corrected peak heights ratios with reference to the chromium K alpha peak were used to establish all experimental profiles. The level of chromium through the alloy and braze substrates was assumed constant, except near metal-oxide interfaces. Figure 6.7 and 6.8 show the experimental diffusion profiles of nickel and silicon for direct comparison to the theoretical data sets.

The diffusion profiles of nickel and silicon are very similar. The only difference is the relative compositions of these two constituents diffusing into the foils. Analysis of the experimental diffusion profiles shows that they are not symmetrical. Diffusion of braze alloy constituents to the foil on the right of these experimental diffusion set-ups is less than the foil on the left. This is consistent for both Ni and Si.

In addition to the nickel and silicon experimental diffusion profiles, the aluminium profile across the sandwich structure is presented in figure 6.9. The profile of aluminium is thought to give an insight into any interactions between the aluminium content of the alloys and braze alloy constituents. Although some peaks in aluminium levels near the braze are present on the 100 hour profile. At longer times, these profiles level out and show no interactions of aluminium with braze alloy. This is important as to not tie-up the aluminium content of the alloy which is necessary for protective oxide formation. The peak

in aluminium levels coincides with an increase in nickel signals within the same EDX spectra.

The formation of intermetallic phases within braze alloys is not uncommon. The formation of NiAl and/or Ni_3Al is possible within these diffusion couples. Longer diffusion times (i.e $\geq$200 hours) do not present high levels of aluminium near the braze interface. A more uniform, level profile is observed. It is important to mention that the polished cross-sections also show some remnant oxide which would have been present prior to brazing (Figure 6.4). This may also play a role in increasing the relative levels of Al near or within the Ni-rich braze alloy zone.

Optical microscopy of the 100 hour polished cross-section shows an additional feature on one of its sandwich structure foils. Figure 6.10 shows this feature of the microstructure which is not observed at longer times. This additional phase of the microstructure was observed both within FeCrAlY alloy grains and along grain boundaries. EDX analysis was taken of this "second phase" and compared to the composition of the same foil, within an area clear of this phase (Figure 6.11). These areas were found to be aluminium and nickel-rich.

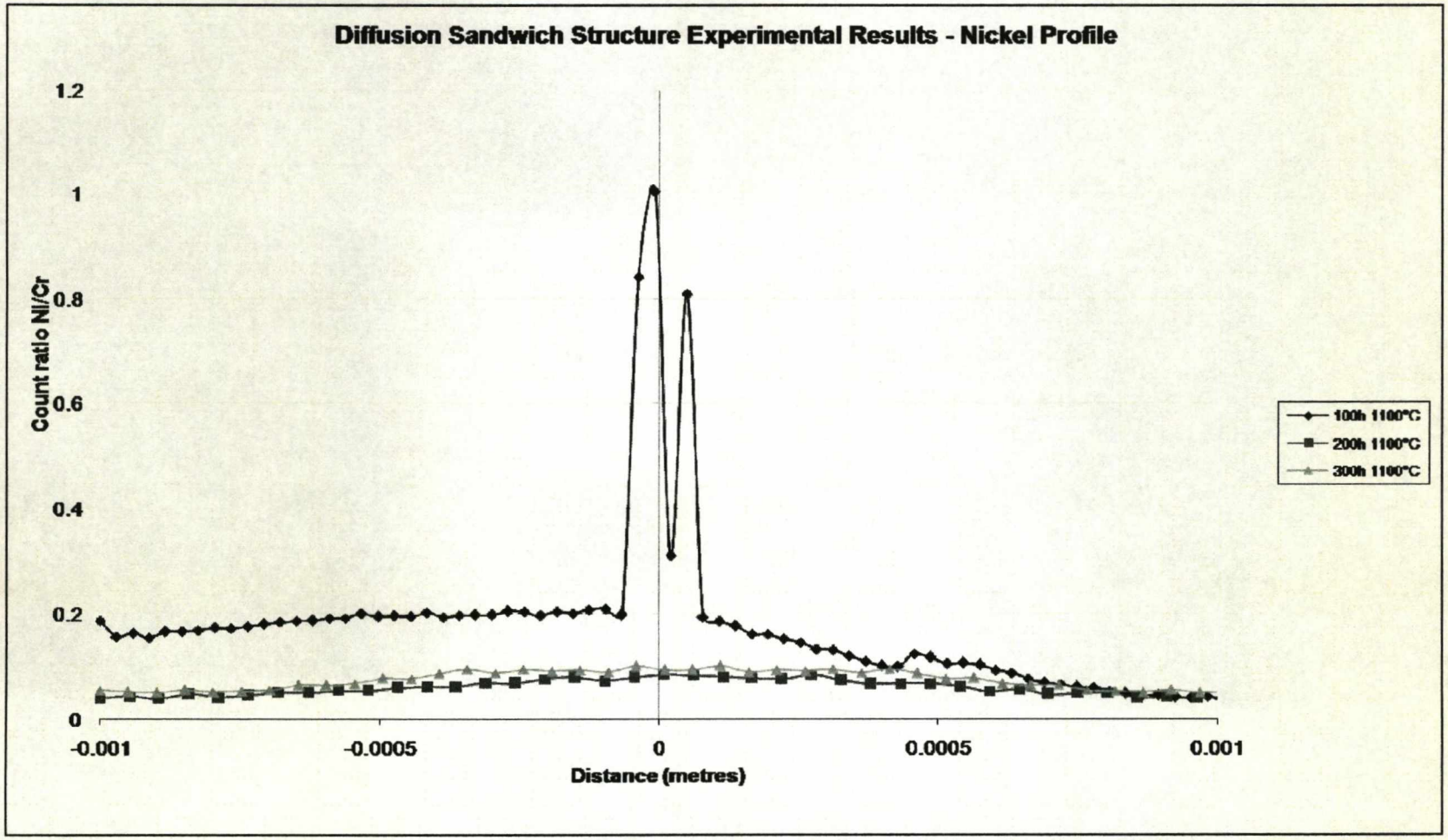

Figure 6.7: Experimental diffusion profiles of nickel at 1100°C within a brazed sandwich structure

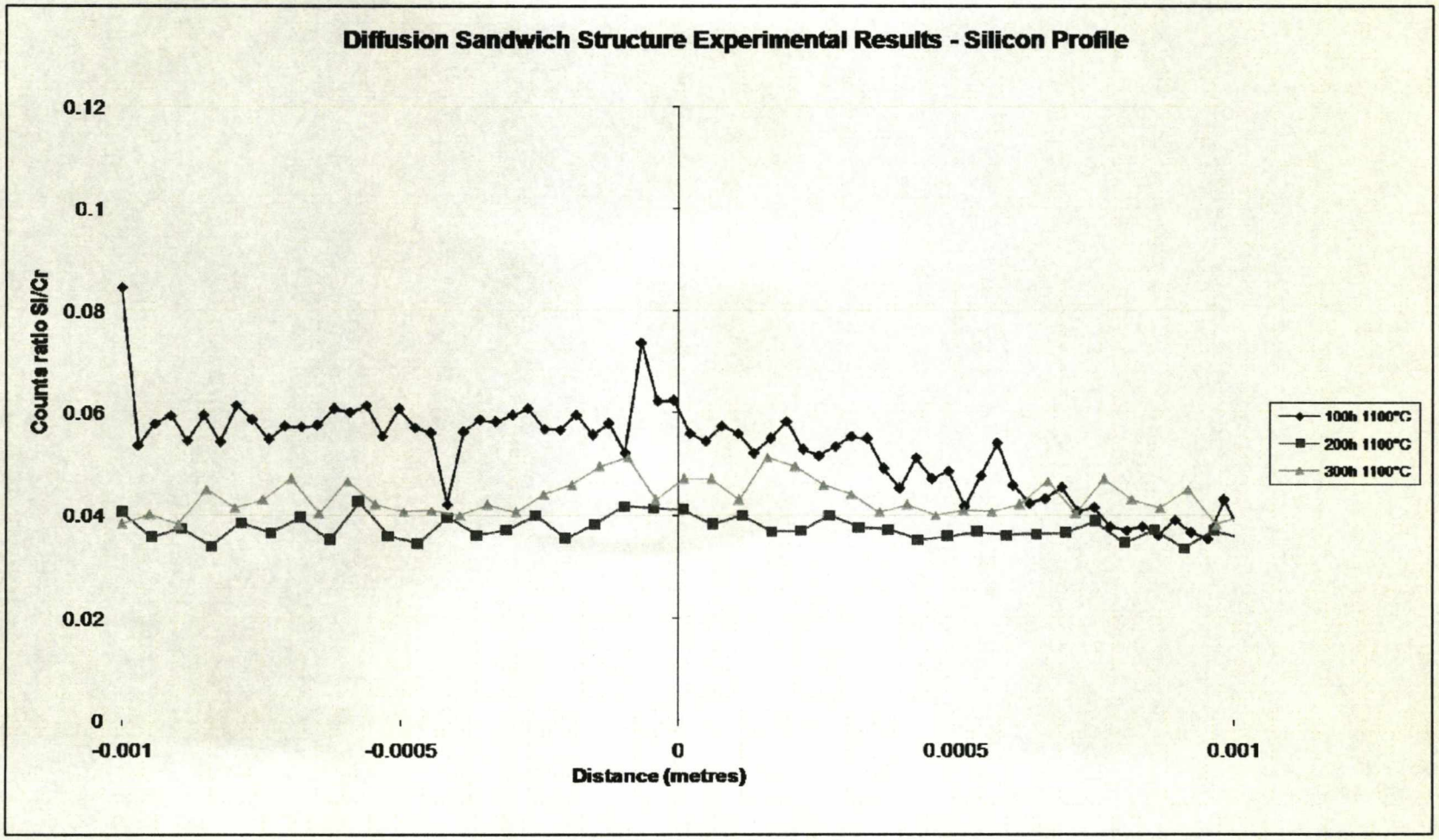

Figure 6.8: Experimental diffusion profiles of silicon at 1100°C within a brazed sandwich structure

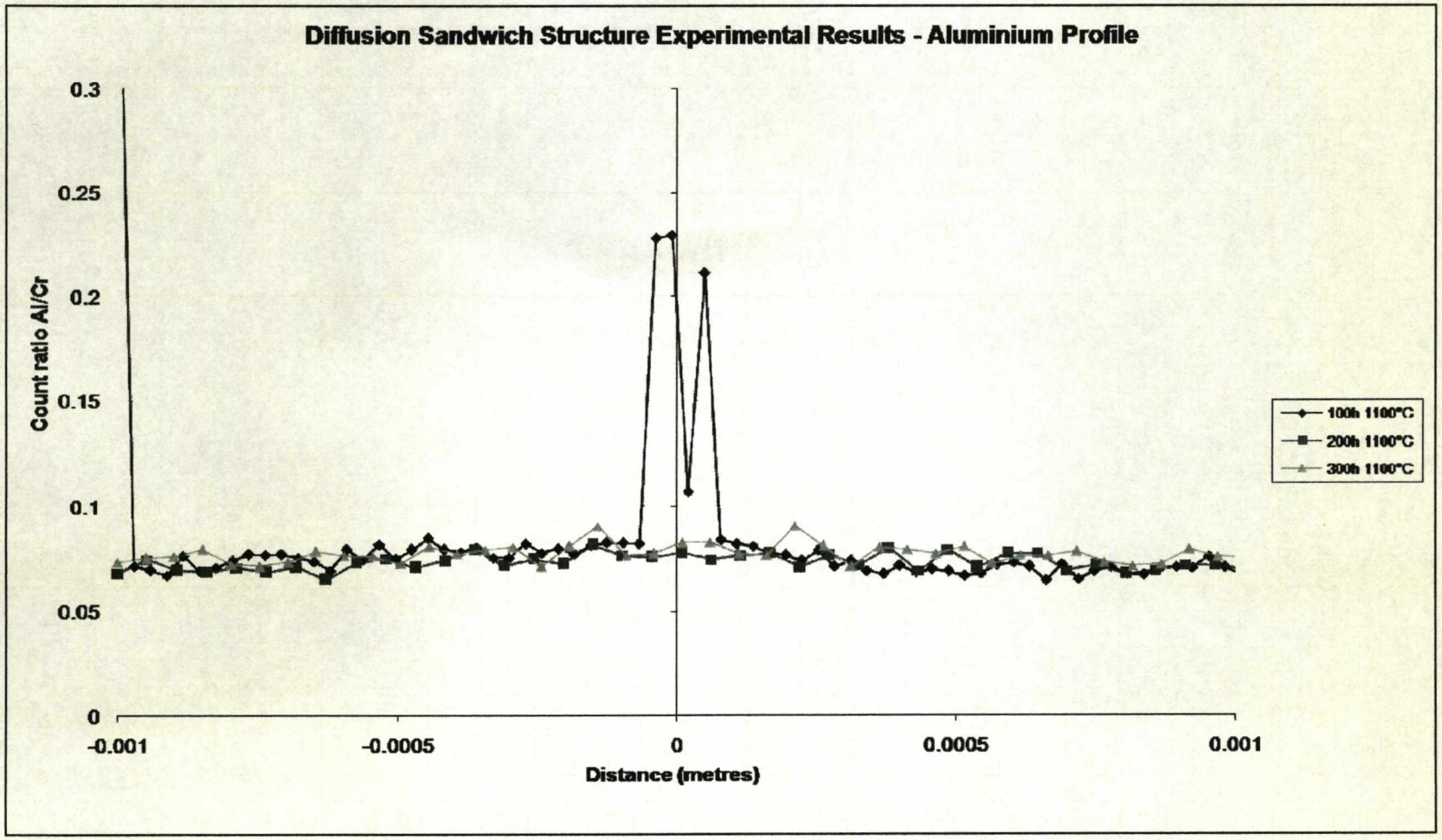

Figure 6.9: Experimental diffusion profiles of aluminium at 1100°C within a brazed sandwich structure

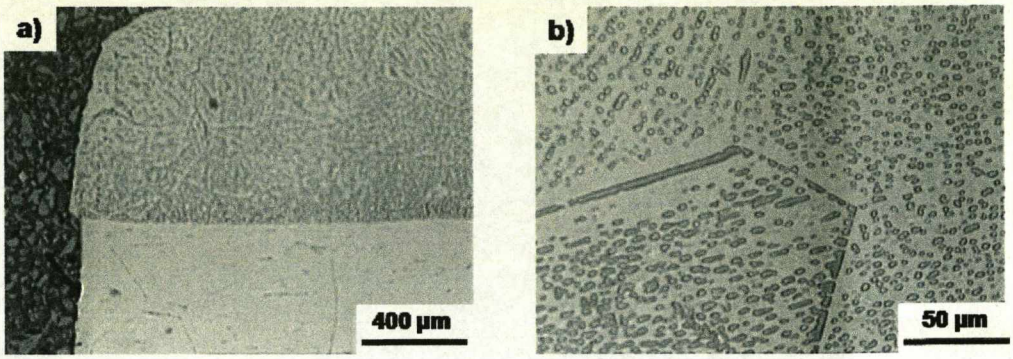

Figure 6.10: Microstructural features of the brazed sandwich structure, oxidised at 1100°C for 100 hours. Image a) shows the presence of a second phase in a single foil, and b) represents a higher magnification of this region

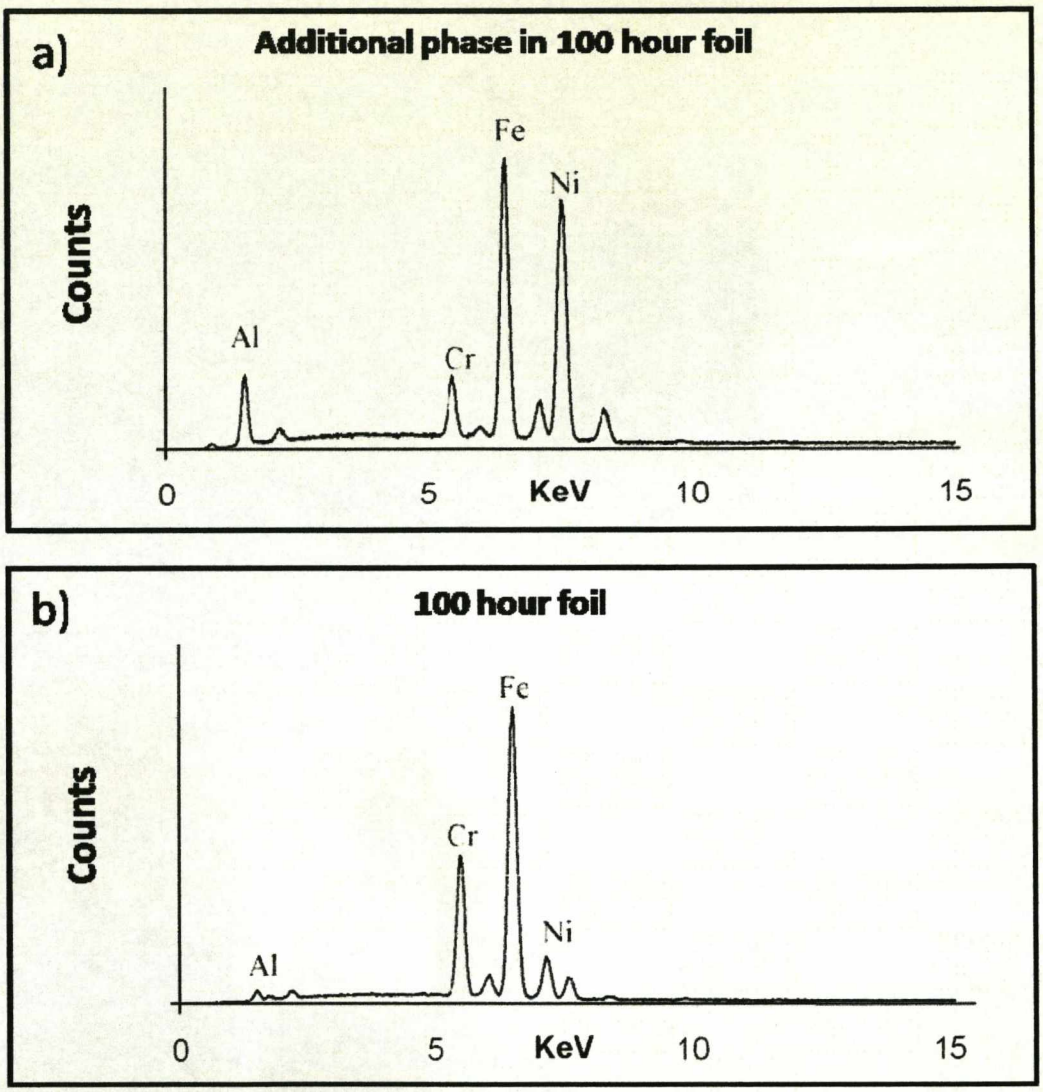

Figure 6.11: EDX analysis of a) diffusive phase present in the 100 hour sample and b) represents a spectrum acquired from the same foil away from the additional phase

6.7.2 Honeycomb Abradable Foils

A composite SEM BSE image of a typical honeycomb foil used for point analysis is shown in figure 6.12. Figure 6.13 shows the experimental point analysis results for a honeycomb foil oxidised at 1200°C for 500 hours. All EDX point analysis and peak height/area ratios are taken with reference to the chromium K alpha peak, as the chromium level was assumed to be constant throughout at ~20 wt. % (see section 3.10). The diffusion profiles of Al, Fe, Mo, Ni, and Si were attained. Although the data acquired was not compositional, figure 6.13 gives results about the relative diffusion of alloy constituents across such a honeycomb foil.

The diffusion profiles of Fe and Ni clearly illustrate the joining of the two dissimilar metals. Also observed on this diffusion map is the high level of Mo present within the base plate. This is thought to be associated with the breakdown of the Haynes 214 alloy but is not thought to be associated with the degradation of the FeCrAl foil material. Scanning electron microscopy (SEM) was used to image this region. Figure 6.14 presents two BSE image and is accompanied by a series of EDX spectra, confirming the high levels of Mo within this diffusion interface.

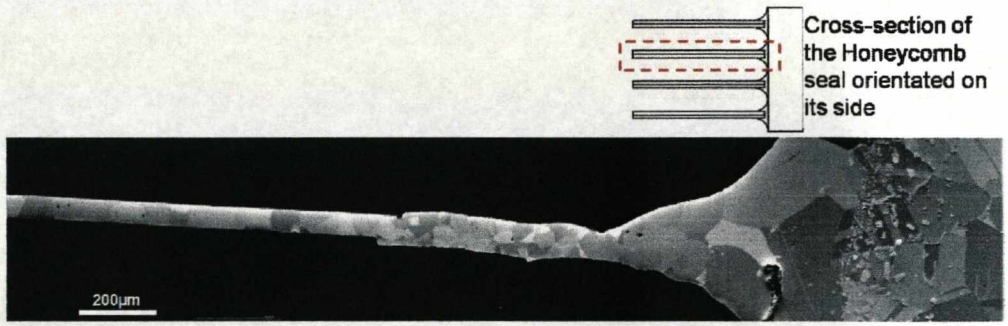

Figure 6.12: BSE image of a honeycomb foil cross-section, oxidised for 450 hours at 1100°C and orientated on its side (as used for diffusion profile maps)

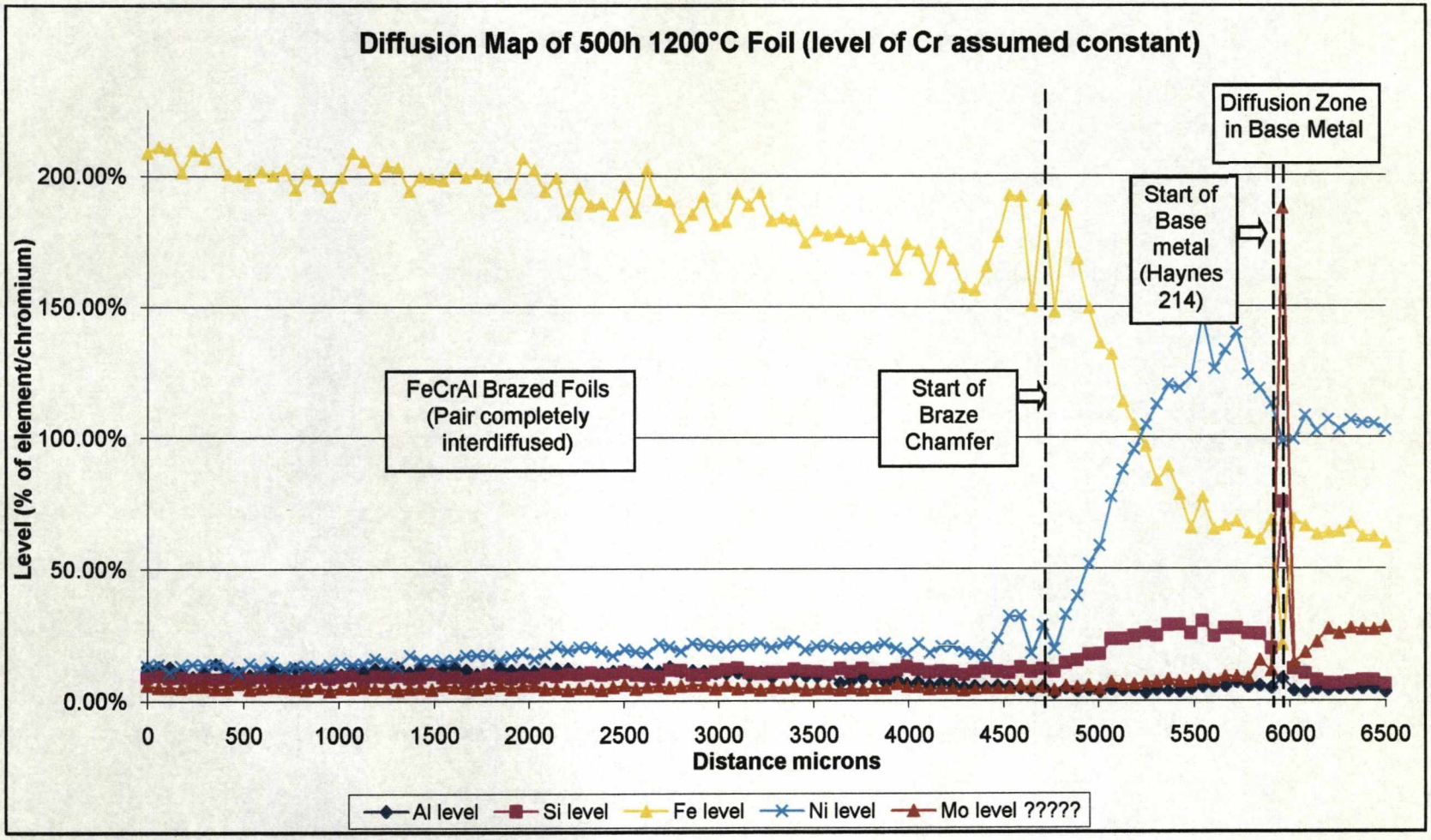

Figure 6.13: Diffusion profiles of elements in a honeycomb foil after 500 hours at 1200°C

A second set of diffusion profile maps of the honeycomb cross-sections was acquired. Experimental diffusion profiles were performed on a honeycomb abradable seal, oxidised for 450 hours at 1100°C. The cross-section of this sample was found to have significant void formation only upon the end/outer foils of the slice analysed. All other honeycomb nodes/cross-sections do not present void formation. Consistent filling of the capillaries between double-walled honeycomb cross-sections/nodes on this sample is not observed and is illustrated in figure 6.15. This is most likely to be the result of poor sample cross-section preparation. The diffusion profile maps of an end foil and a central honeycomb foil without voids and half filled capillary were acquired. Increased levels of Mo are not observed in these two diffusion maps and are therefore not included in this result set. Figure 6.16 presents the diffusion map data for the end/outer honeycomb foils. The distance between step increments of analysis has been increased. Figure 6.17 presents the results for the diffusion profile of the more central honeycomb foils.

In addition to these diffusion maps, a final data set was produced. The polished honeycomb cross-section of the sample oxidised for 450 hours at 1100°C was used to compare the profiles of Al, Fe, Ni, and Si on foils with and without interfacial void formation. This data set can be found in figure 6.18. The graphs clearly highlight the locations where voids are present. The diffusion profiles of all four elements are similar, however it seems that the level of aluminium is less in the end foils near the presence of voids.

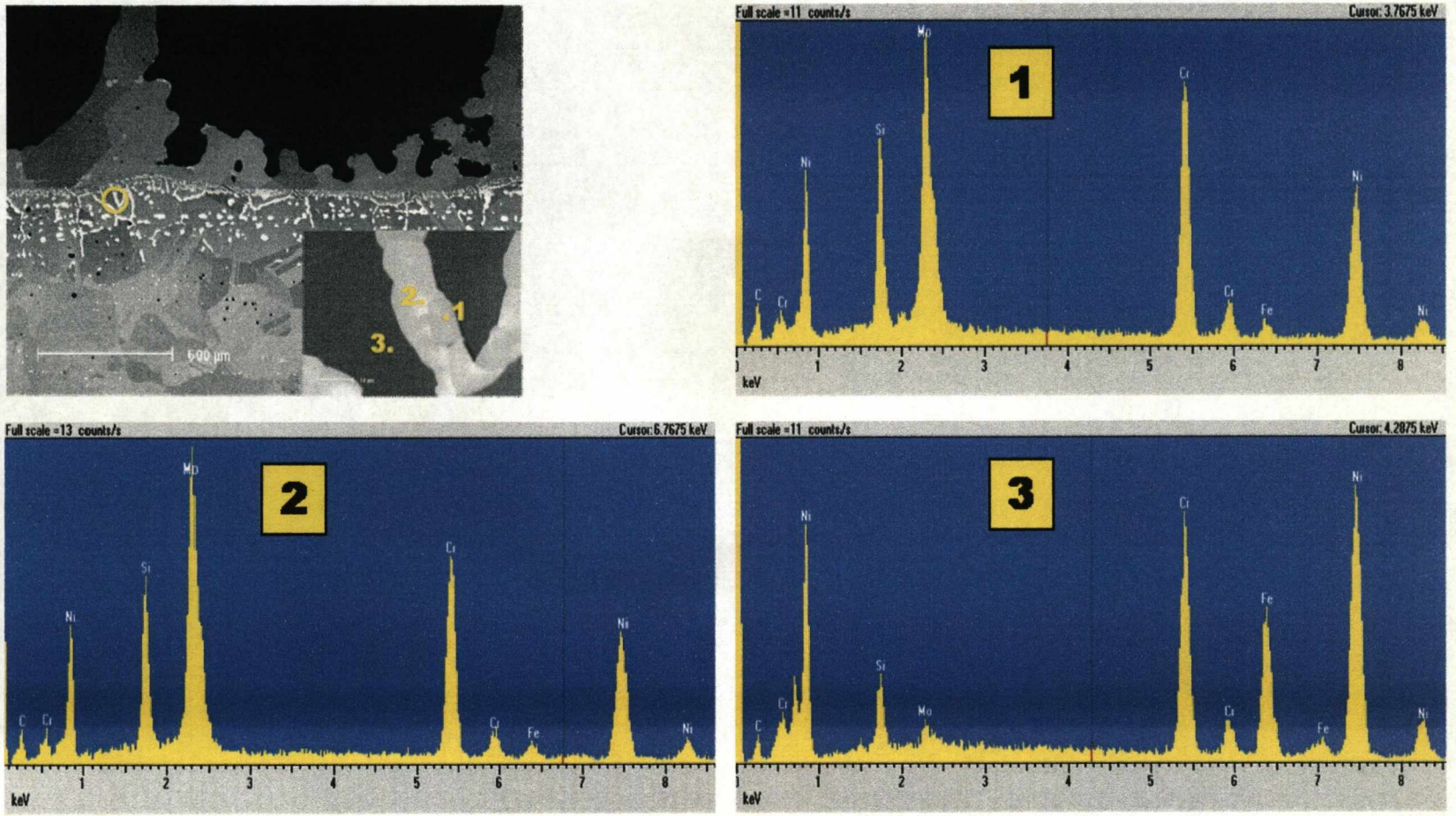

Figure 6.14: Molybdenum-rich diffusion zone in base plate – BSE images and additional EDX spectra of sample oxidised for 500 hours at 1200°C

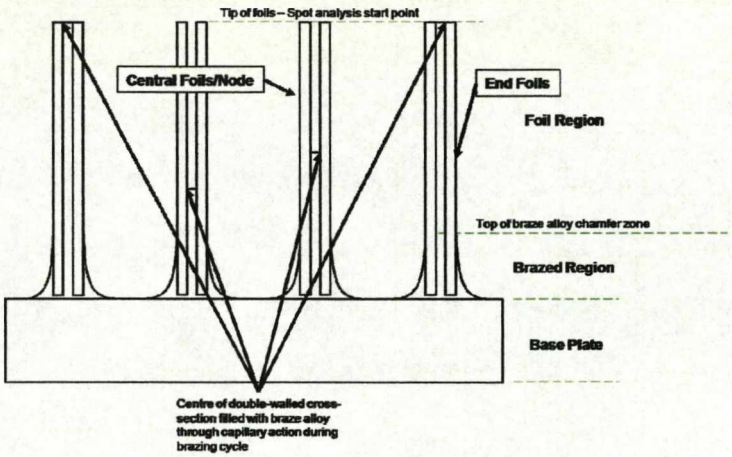

Figure 6.15: Schematic representation of inconsistent filling of the capillaries between double-walled honeycomb cross-sections/nodes

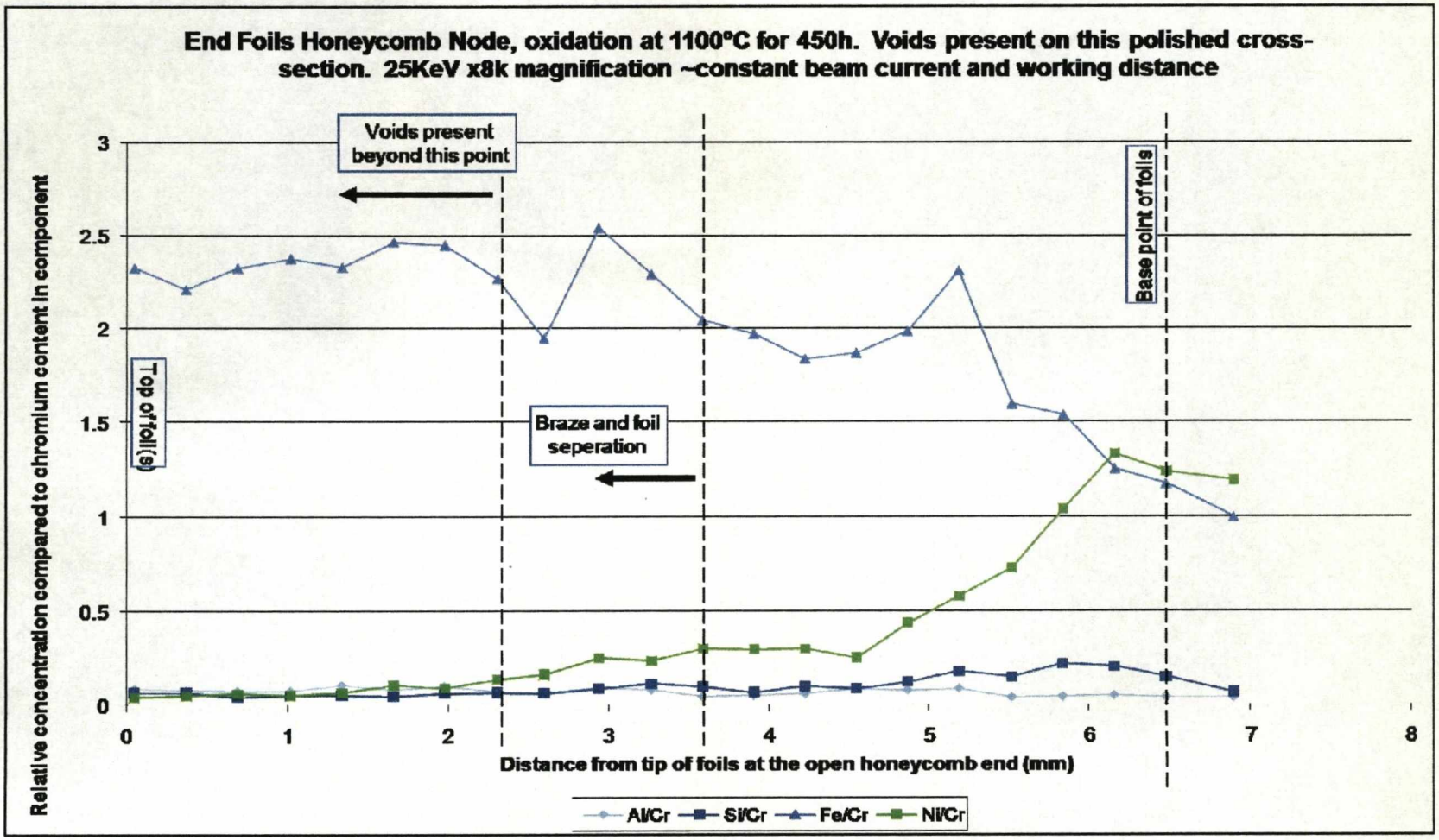

Figure 6.16: Diffusion profiles of elements in a honeycomb end/outer foil after 450 hours at 1100°C

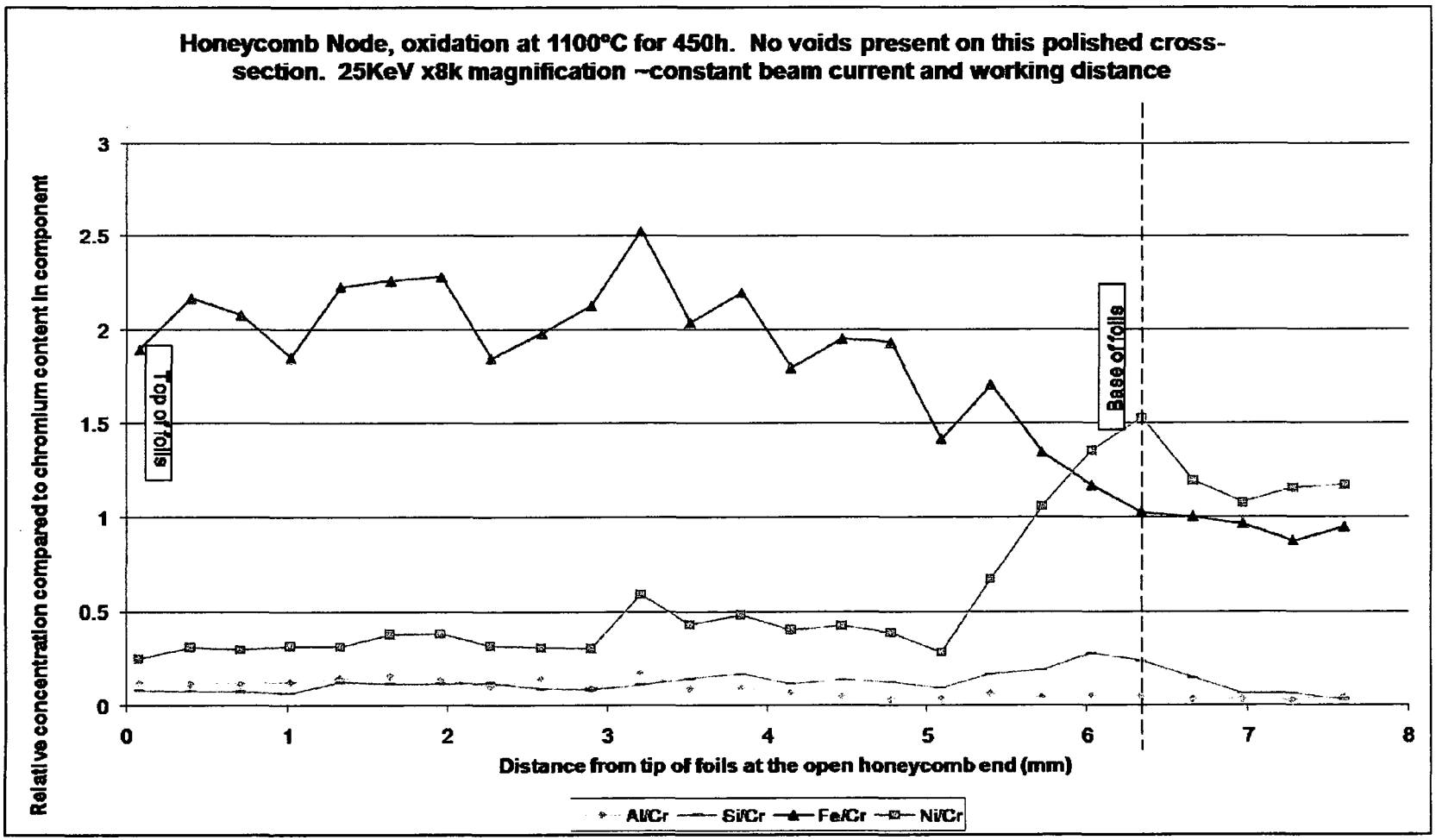

Figure 6.17: Diffusion profiles of elements in a central honeycomb foil after 450 hours at 1100°C

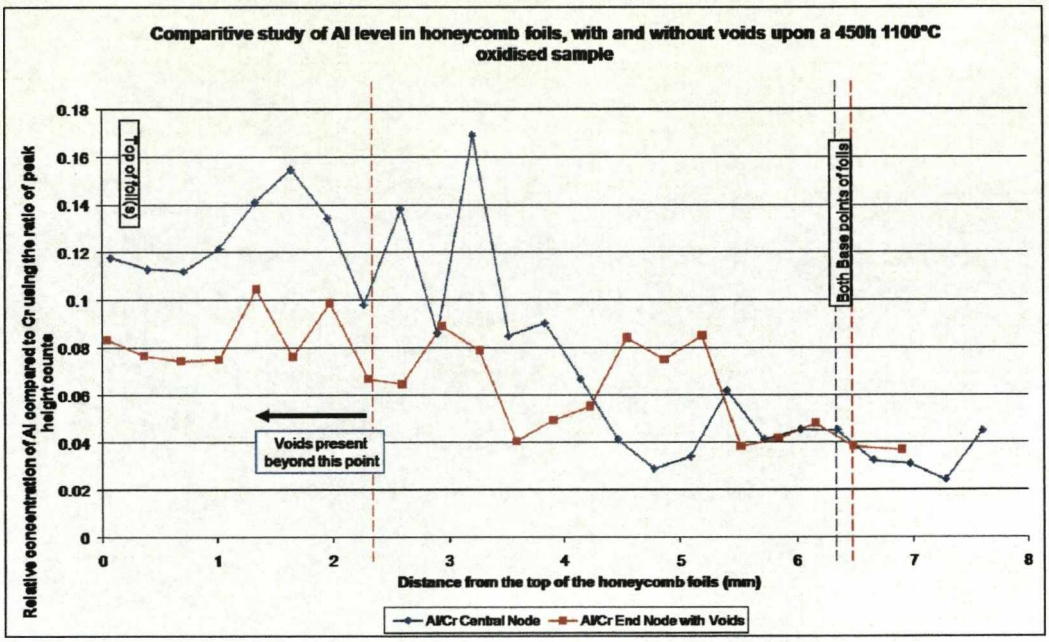
Comparitive study of Al level in honeycomb foils, with and without voids upon a 450h 1100°C oxidised sample
Relative concentration of Al compared to Cr using the ratio of peak height counts
Top of foil(s)
Both Base points of foils
Voids present beyond this point
Distance from the top of the honeycomb foils (mm)
Al/Cr Central Node
Al/Cr End Node with Voids

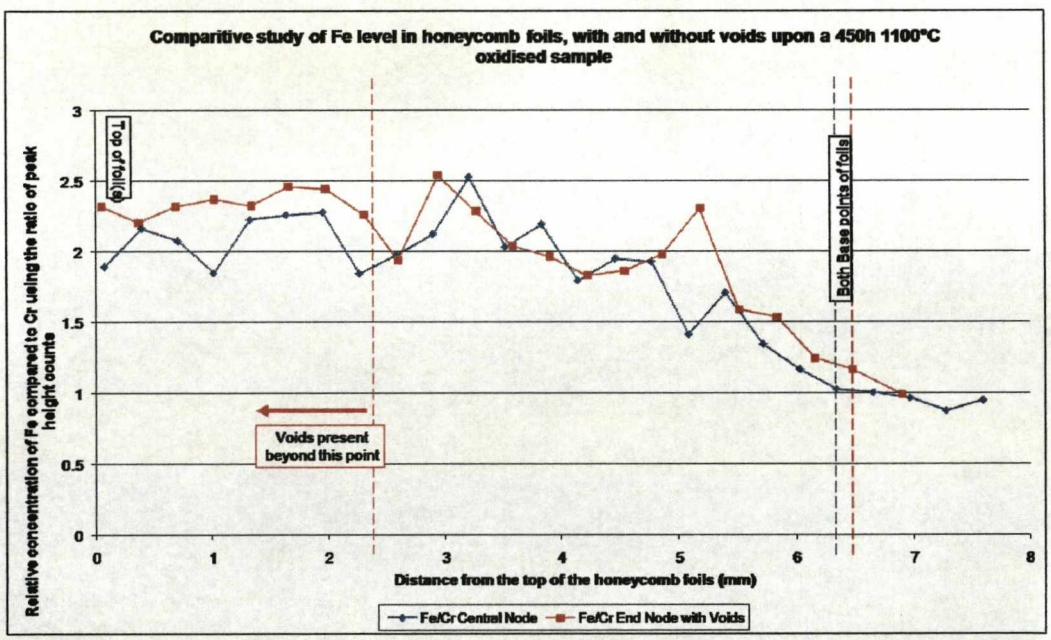
Comparitive study of Fe level in honeycomb foils, with and without voids upon a 450h 1100°C oxidised sample
Relative concentration of Fe compared to Cr using the ratio of peak height counts
Top of foil(s)
Both Base points of foils
Voids present beyond this point
Distance from the top of the honeycomb foils (mm)
Fe/Cr Central Node
Fe/Cr End Node with Voids

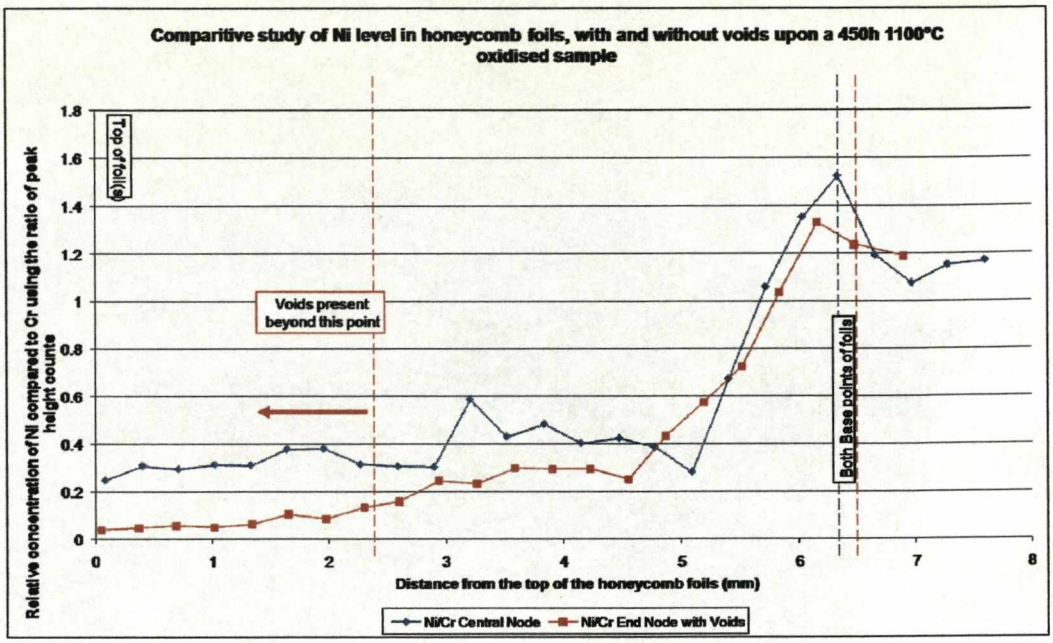

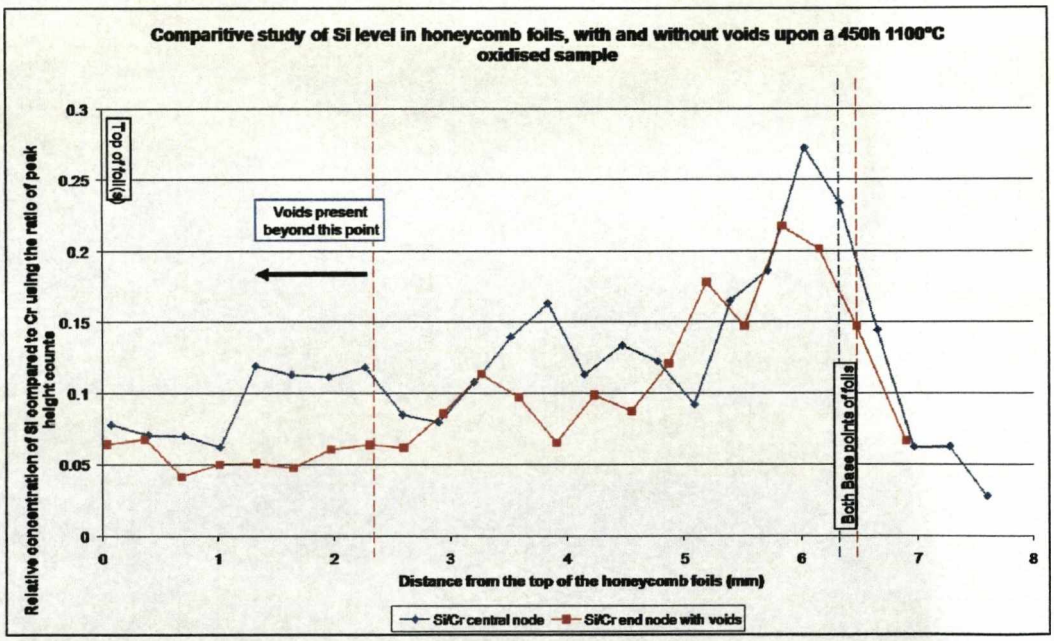

Figure 6.18: Comparative study of the diffusion profiles of Al, Fe, Ni, and Si in a adjacent honeycomb foils with and without void formation after 450 hours at 1100°C

The joining of dissimilar metals has always been problematic [142, 148]. Many authors state the two obvious reasons for this are: a) the incompatibility of the joining techniques with one but not the other substrate, and b) the long term effects of coupling two incompatible materials e.g. diffusion at high temperatures. The design of the honeycomb abradable seal mentioned in this work is no different and is affected by the joining of the two dissimilar alloys i.e. foil (iron based) and braze (nickel-based) alloys. FeCrAl alloys are renowned for their excellent oxidation resistance and their compatibility for such applications as heating elements and automotive catalytic converters, etc [123, 166-168]. However, when confined to the abradable seal setup, their oxidation performance is dramatically reduced. The diffusion couple of braze and foils effectively reduces the overall level of aluminium in the foils, as the higher concentration of aluminium in the foils moves across into the lower concentration of the braze alloy rapidly at high temperatures.

Overall aluminium depletion from the foils is not the only effect of joining the two dissimilar alloys, but the consumption of aluminium below a critical level (either by overall consumption or localised depletion) in oxide formation is what induces the breakaway oxidation of the foils. The movement of silicon into the FeCrAl alloy foils is also shown to affect the oxidation mechanism. When significant amounts of silicon and nickel were present in the foils, interfacial void formation was observed directly beneath the alumina scales and at times prior to the critical consumption of aluminium. Silicon also had an effect on void filling, due to the thermodynamic stability of silica over chromia at 1100 and 1200°C. Unlike the lower temperature tests on foils at 900°C, the alumina scales grown above voids at 1200°C, prior to aluminium exhaustion, show the typical equiaxed and columnar grain structures of α-alumina. It is possible that the increases in Si and Ni to the foils may locally deplete aluminium near the braze regions.

The comparison of theoretical and experimental data sets for the diffusion of nickel and silicon in brazed sandwich structures does show some correlation. Although great care in producing perfectly flat sample cross-sections and careful setup of the SEM were taken, the point analysis technique could not be classed as very reliable in comparison to an EPMA (electron probe micro-analyser). The diffusion of braze alloy constituents as shown theoretically can be observed experimentally. The same theoretical calculations were used to predict that silicon can diffuse through the alloy in 21 hours and 7 minutes (76,020 seconds) if no silicon was assumed present in the FeCrAl alloy.

No interfacial voids were observed when analysing the metal-oxide interface of the brazed sandwich structures. The FeCrAl alloys used in the sandwich structures were much thicker than the thin foils, and therefore, have a greater aluminium reservoir. An α-alumina oxide of ~4μm thick was observed on the brazed sandwich structures after 300 hours at 1100°C.

Increased levels of nickel and aluminium determined by EDX coincide with one another within the brazed region after 100 hours oxidation at 1100°C on brazed sandwich structures. Initially high levels of aluminium in this region were thought to be caused by the presence of remnant oxides which had not been fluxed away sufficiently during the brazing process. However, EDX spectra were also high in nickel content and therefore suggest the possible formation of intermetallic phases; NiAl and/or Ni_3Al. No further testing of possible intermetallic phase formation was performed. Tests for longer durations did not generate any regions where high levels of nickel and aluminium coincided. The 100 hours at 1100°C brazed sandwich structure did not present high levels of Ni and Al at any other locations other than the braze.

Although not compositional, diffusion maps from honeycomb foils present large amounts of Fe, Ni, and Si diffusion across the abradable seal foils system. Al

levels were found to be slightly higher at foil tips when compared to the base of the foils above the braze region. Diffusion of Al and high temperature oxidation and the formation of Al_2O_3 are thought responsible for Al consumption near the base of the foils.

The comparison of honeycomb end foils and foils located in a more centrally location show no differences in the levels of diffusion experienced. However, Al levels do seem lower in end foils than more centralised foils. The comparison of central honeycomb foils with and without voids present also shows no difference to the levels of diffusion of Al, Fe, Ni, and Si.

An interesting observation was found when comparing experimental and theoretical diffusion results for brazed sandwich structures. Experimental results present the uneven diffusion of nickel and silicon between the two foils in a braze sandwich structure. Figure 6.7 and 6.8 show the diffusion of nickel and silicon. The 100 hour data set upon both graphs presents retarded diffusion to the right compared to the diffusion of the same alloy constituent to the foil on the left. Large amounts of remnant oxides are thought responsible for this effect. Figure 6.4 a) presents a thick band of oxide between the two brazed foils from the analysed cross-section. Images b) and c) (Figure 6.4) are from longer oxidation times of the same setups and also present remnant oxides at the braze foil interface. These oxide bands are not as thick as that seen in figure 6.4 a). This thick remnant oxide may also be partly responsible for the increased aluminium x-ray signal from the brazing interface.

6.8 Phase Analysis of Failure Region – Further Results

The Cam Scan X500 crystal probe FEG-SEM was used to map the failure region, just above the braze chamfer of the honeycomb foils using the EBSD and EDX facilities. This location of attack also coincides with the interface of nickel-rich and iron-rich regions, developed by the mating of the dissimilar alloys during brazing. Evident from this result is the diffusive reaction of the brazing alloy, resulting in the complete consumption of the honeycomb foils material within the nickel-rich brazing alloy (braze chamfered zone) and the establishment of a homogeneous nickel-based substrate at the base of honeycomb foils.

A honeycomb abradable seal sample was oxidised for 450 hours at 1200°C. EBSD and EDX mapping of the honeycomb foils was carried out in cross-section and just above the brazed chamfered zone. This position was of most interest as it is the most common site for foil rupture and honeycomb failure. Band contrast, All Euler and Phase identification maps are shown in figure 6.19. A step size of 0.7μm was used to scan the selected area. All three maps present an interface between top and bottom. In both band contrast and All Euler maps, the difference in iron-based and nickel based grain structures can be observed. The nucleation and growth of large grains are shown in the upper parts of the data maps. Grain sizes here are typical of those found after grain recrystallisation and growth in FeCrAl substrates. When considering that this section of the map would have once been two separate foils with common but individual grain structures. The capillary fill action of the brazing alloy and subsequent high temperature exposure during oxidation has caused inter-diffusion of all three parts. The resultant Fe-rich grain structure presents grain growth over all initial boundaries (foil/braze/foil interface). In comparison the lower half of these data maps present, on average, a much smaller grain

structure. Evidence of twinning is recorded in 5 of these grains, typical of that seen in Ni-based alloys and the honeycomb abradable seal base plate.

Examination of the phase identification map (Figure 6.19(c)) shows a strong yellow region. The channel 5 software identifies this region as a face centred cubic (FCC) structure of a Ni-based substrate and was indexed as a Ni superalloy. The upper region of the phase identification map is a mix of red and yellow data points. Red here is used to index the body centred cubic (BCC) structure of ferrite (FeCrAl alloy). A gradient in the mix density of index points from high to low is not observed from the FCC phase. This map suggests a significant amount of nickel diffusion into the honeycomb foils. Thus probably causing the stainless steel foils to transform from ferritic to duplex or austenitic - a BCC to FCC transformation within the crystal structure.

Figure 6.19(c) presents two distinct regions, a nickel-rich phase (yellow) and a mixed region of nickel-rich and ferrite (ferrite = red) phases. The diffusion of nickel is thought responsible for these phase changes. However the diffusion of nickel from one end of the honeycomb foils would be expected to present a gradual change (i.e. a gradient) from a nickel-rich phase to a mixed region of ferrite and Ni-rich material, rather than the distinctive boundary of the two regions presented here. The boundary between these two regions is thought to be a consequence of the automated diffraction pattern indexing used for EBSD. Limitations in the EBSD facility may cause diffraction patterns of mostly Ni-rich material and some ferrite material from the same area to be indexed as Ni-rich, and diffraction patterns of mostly ferrite material and some Ni-rich material to be indexed as entirely ferrite.

EDX maps (Figure 6.20) were used for chemical analysis of the same region. The chromium and silicon maps show an even distribution of these two elements across the interface. Aluminium is shown conclusively to be part of

the protective oxide scale generated around all parts of this region for this exposure time. Only a very weak trace of aluminium can be seen within the substrate, suggesting that the aluminium reservoir will soon be exhausted and alumina oxide formation will soon stop after 450 hours at 1200°C. The intensity of iron seems to remain constant over the entire length of the analysed region, with the possible exception of an increased level around the interface between phases. The nickel level can be interpreted as adopting a diffusion gradient into the FeCrAl foils. The greater volume of nickel is shown on the brazed side of the interface as expected.

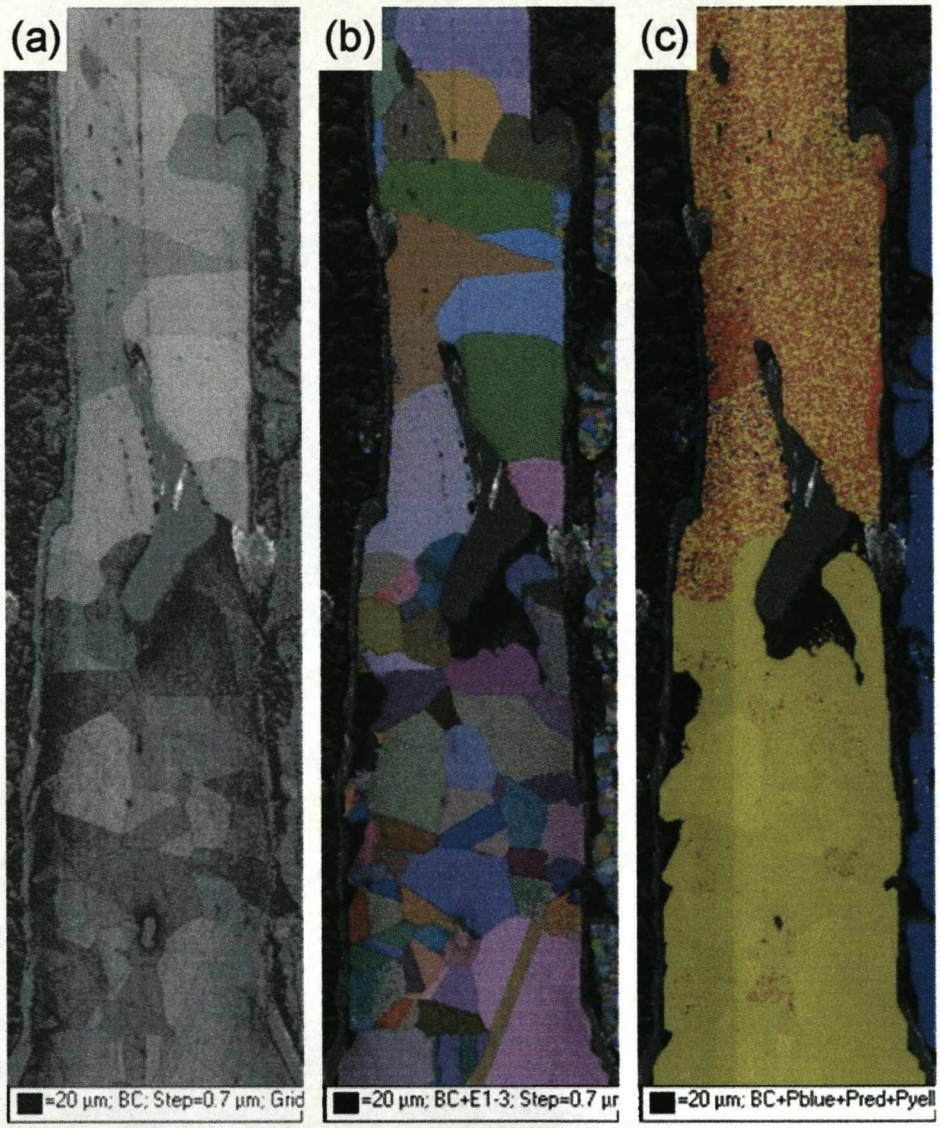

Figure 6.19: EBSD maps of a honeycomb abradable seal cross-section, oxidised for 450 hours at 1200°C. Maps recorded from just above the brazing chamfer on a double walled honeycomb foil, centrally located in the sample. Image (a) is a band contrast map, and (b) is an All Euler map. Image (c) is a phase identification map, red represents the BCC ferrite phase, and yellow represents the nickel-rich FCC phase

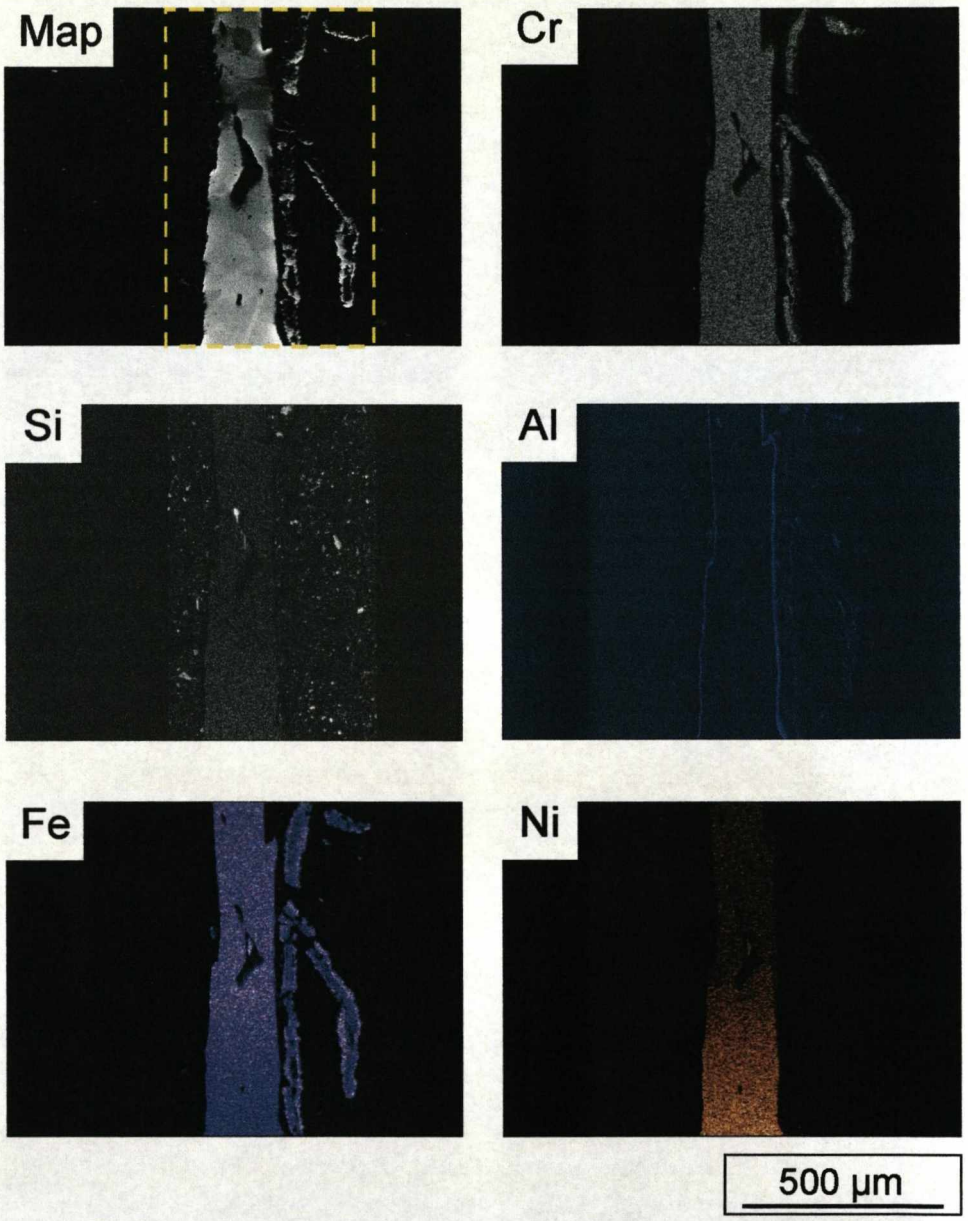

Figure 6.20: EDX maps of the region of honeycomb foils that is most prone to rupture/failure, just above the braze chamfer. These maps are to accompany the EBSD data shown in figure 6.19

The effect of brazing FeCrAl based foils with a Ni-based alloy is clearly shown in figure 6.19. Phase analysis by EBSD and EDX mapping show the extent of Ni diffusion into the foils. Honeycomb foils at approximately ¼ foil height, can be classed as having a high enough nickel content to change the ferrite structure of the foils to the duplex or austenitic phase. This also coincides with the region of most aggressive oxidation attack. The location of attack coincides with the interface of nickel-rich and iron-rich regions. Below ¼ foil height, the entire construction can be classed as nickel based. The original position of the base of the foils has been consumed by this region.

Austenitic steels yield properties such as increased strength at high temperatures and increased creep resistance. This would make such alloys incompatible for abradable seal design to avoid damage to rotor blade tips. Austenitic steels also exhibit reduced diffusion rates of alloy constituents, such as aluminium and chromium, due to its crystallographic structure [62-65]. Austenite has an FCC (face centred cubic) unit cell. Initially the FeCrAl foils would have been classed as having a matrix of ferrite. This has a BCC (body centred cubic) unit cell [21].

A small volume change is also associated with this transformation of a BCC to a FCC structure [21]. This may affect the adhesion of the oxide scale already adhered to the alloy substrate. Additionally, if high temperature creep of the alloy substrate was reduced and plastic deformation of the oxide was prevented by a thick scale, oxide scale cracking may occur as a secondary effect.

The mechanical effects of thin foil creep also require attention. Creep of thin foils at 1200°C above the anchoring point of the braze can be classed as an effect of "swaying in the wind." If the foils are of increased strength near the base, creep of the soft foil substrates above may induce alumina scale cracking at ¼ honeycomb foil height.

6.9 EBSD Results

The EBSD analysis above an unfilled void of a 70μm thick FeCrAl foil sample suggests a similar crystallographic preferred orientation between the columnar grains of the α-alumina scale and the equiaxed grains of the chromia layer formed beneath. The results presented only show a chromia layer of two grain thickness. This was typical of all FeCrAl foil samples analysed using EBSD. Both alumina columnar grains and chromia equiaxed grains are characterised with a strong "fibre" texture. This analysis of chromia and alumina crystals above a void was found to also be true for the dual layered oxide formed when adhered directly to the substrate. Further work suggests the loss of the crystallographic preferred orientation of the chromia grains as they nucleate and grow further into the voids.

At first sight our results of the crystallographic orientation of the equiaxed alumina grains are different to the findings of Prior et al [86]. They found a preferred crystal orientation developed in the equiaxed region of the α-alumina scale, and had distinct similarities with the columnar grains of the alumina scale. However those tests were carried out on alumina scales of 20μm thickness on a thick sample where the scale was still developing. In the present case, the equiaxed structure may have developed a similar texture if it had been allowed to continue to grow. Our tests analysed α-alumina scales of approximately 5μm thickness.

Further EBSD analysis of chromia void fills suggests that this fibre texture is lost as chromia formation continues within the void. Chromia void fills analysed using EBSD show a fine equiaxed grain structure, with no columnar grain structures being observed.

Analysis of most chromia void fills revealed no preferred crystallographic orientation. However, some chromia void fills do reveal a gradual loss of texture. This is found to occur during the first 3-4 layers of chromia void fill from the underside of the alumina scale.

Work by Al-Badairy et al. [87] presented the texture of α-alumina scales. The scale texture they present is independent of the underlying metal orientation, so the scale texture is not controlled by a specific orientation relationship (e.g. epitaxial) between the metal and the scale. The results from the columnar grains of alumina scales thermally grown at 1200°C on alloy MI2100 directly agree with their work. Other work presents the r-axis of sapphire (see Section 2.17.1). Sapphire has one of the lowest sonic velocities [101]. From this it is suggested that the development of texture in α-alumina scales may relate to the anisotropy of elastic properties in alumina and its relationship to the free surface. However, the more likely explanation for a strong "fibre" texture is the preferred growth modes of alumina crystals. During the initial stages of oxidation this would require the formation of layers of equiaxed alumina grains until those of the preferential alignment of the <1-101> (the r axis) perpendicular to the foil substrate formed. These preferred grains would then grow longitudinally and impinge on others to form the columnar grain structure.

The EBSD results and high resolution FEG-SEM images have shown that the microstructure of the alumina scale consists of equiaxed grains at the oxide-gas interface and columnar grain at the metal-oxide interface. This agrees with the work of many others [34, 169, 170]. These results have also shown the band of chromia, consisting of equiaxed grains, formed upon the exhaustion of aluminium from the substrate.

6.10 Columnar Grain Profiles from α-Alumina Oxide Scales – Further Results

High resolution SEM and FEG-SEM images of polished sample cross-sections were used to measure the shapes and sizes of the columnar grain structures grown within the α-alumina scale. Tests were conducted to observe any changes in size and profiles of α-alumina columnar grain structures on 70μm thin foil samples oxidised at 1200°C. Alloy MI2100 was used for this section of analysis. It was thought that if a displacement reaction within the alumina scales above voids had occurred then this would have an effect on the sizes and profiles of the columnar grains. A displacement reaction was thought possible to provide the necessary oxygen to the void, for void filling to commence.

Profiles of ten randomly selected columnar grains structures after 100, 300, 500 and 700 hours oxidation at 1200°C are show in figure 6.21. These give a typical example of the many different profiles and widths of columnar grains analysed from selected micrographs. Only ten columnar grain profiles are show on each graphical plot in order to prevent overloading the graphs with too much visual data. Columnar grain profiles shown in figure 6.21 a), b), and c) were recorded from alumina scales directly adhered to the FeCrAl alloy substrate. Figure 6.21 d) is the columnar grain profiles of grains measured above interfacial void formations. Columnar grain structures above voids are not recorded at the three other time intervals as void formation was not observed when testing MI2100 foils until after 600 hours at 1200°C.

These graphs have been plotted using 2-dimensional x and y components. Where x represents the half width of the columnar grain, whist y is the depth of where the measurement was taken with respect to the oxide-gas interface. It is hoped that the resultant graphs give the reader an idea of not only the size, but also the profiles of the columnar grains. These graphs plot the columnar grains

as symmetrical. This is not always true as grains may not be symmetrical and may also not be perfectly perpendicular to the foil substrate. The graphs are idealised representations.

The profiles of columnar grain structures directly adhered to the alloy substrate and above the layer of chromia that is detached from the alloy substrate by voids were analysed. However, this showed no real difference to the columnar grains analysed above voids after 700 hours. Images from equiaxed and columnar grain structures of alumina directly adhered to the foil substrates can be observed in figure 6.22. These MI2100 foils have been oxidised for 500 hours at 1200°C. Columnar grain structures of alumina scales were also observed on brazed honeycomb foils. However, the profiles and sizes of these grains were not recorded.

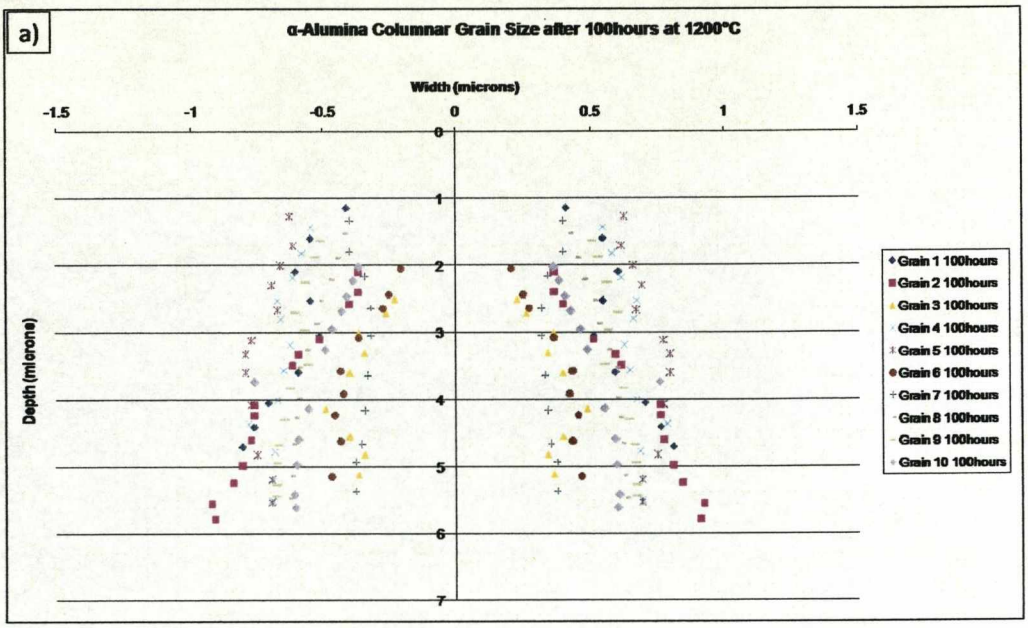
a)
α-Alumina Columnar Grain Size after 100hours at 1200°C
Width (microns)
-1.5
-1
-0.5
0
0.5
1
1.5
Depth (microns)
0
1
2
3
4
5
6
7
Grain 1 100hours
Grain 2 100hours
Grain 3 100hours
Grain 4 100hours
Grain 5 100hours
Grain 6 100hours
Grain 7 100hours
Grain 8 100hours
Grain 9 100hours
Grain 10 100hours

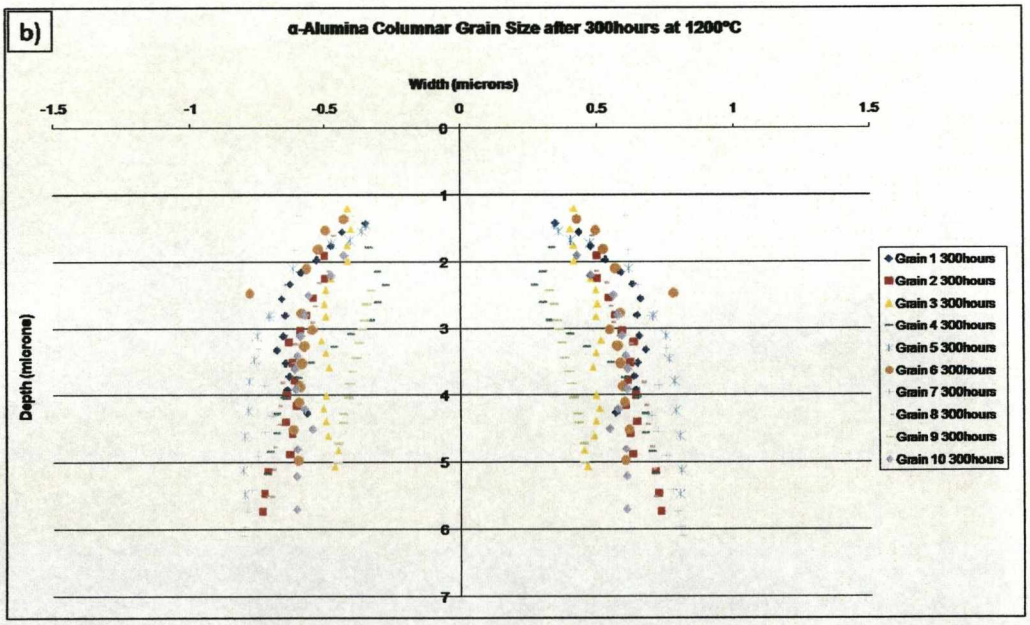
b)
α-Alumina Columnar Grain Size after 300hours at 1200°C
Width (microns)
-1.5
-1
-0.5
0
0.5
1
1.5
Depth (microns)
0
1
2
3
4
5
6
7
Grain 1 300hours
Grain 2 300hours
Grain 3 300hours
Grain 4 300hours
Grain 5 300hours
Grain 6 300hours
Grain 7 300hours
Grain 8 300hours
Grain 9 300hours
Grain 10 300hours

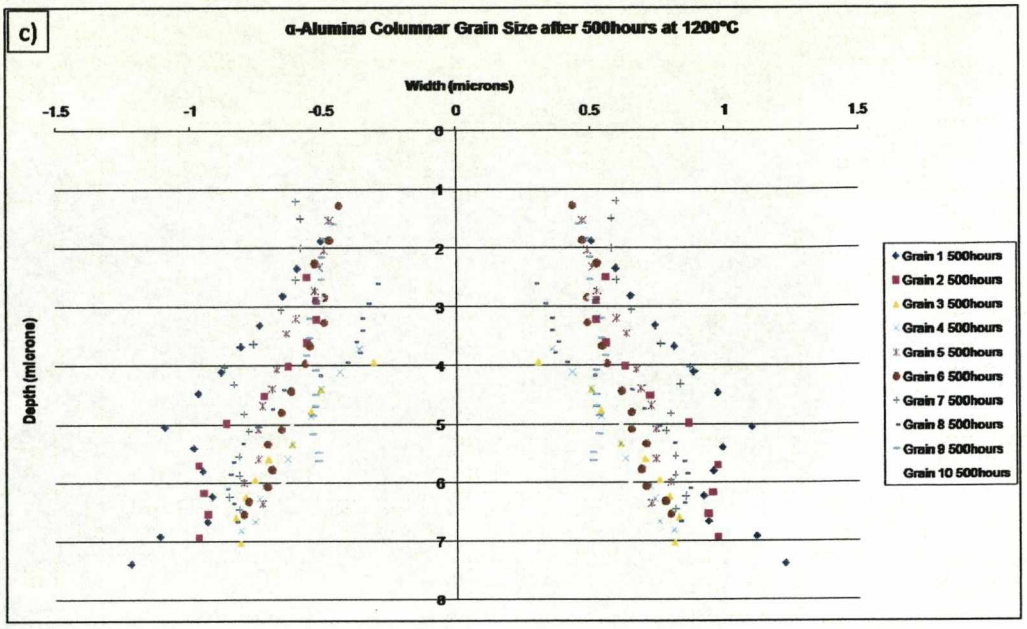

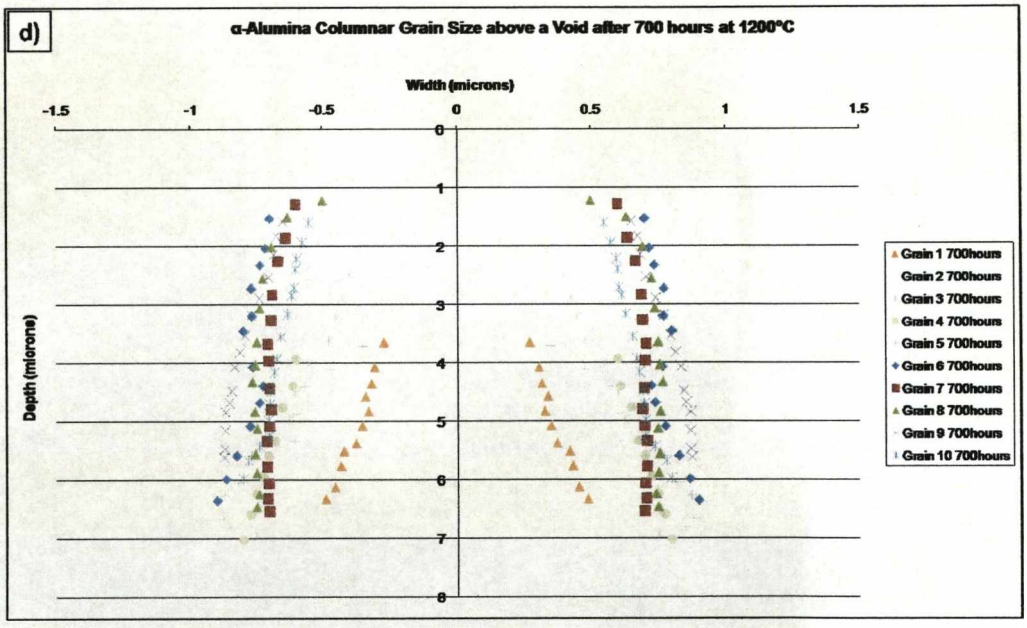

Figure 6.21: The graphical representation of α-alumina columnar grain profiles and sizes grown on MI2100 alloy foils, oxidised at 1200°C. Where a), b) and c) shows the columnar grain profiles of alumina scales directly adhered to the substrate after 100, 300 and 500 hours respectively. Image d) is the graphical representation of columnar profiles recorded above interfacial voids.

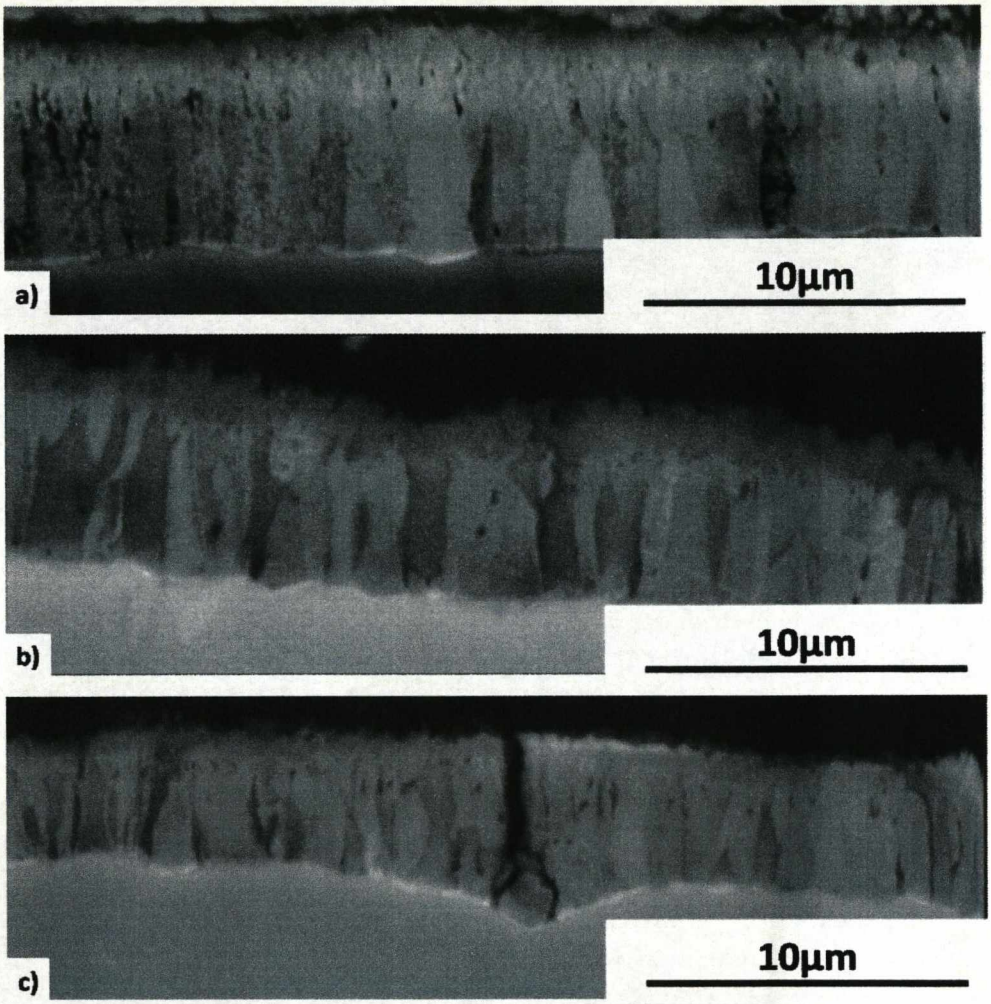

Figure 6.22: Images a), b) and c) show examples of columnar grains of α-alumina scales formed on the MI2100 alloy after 500 hours at 1200°C

A displacement reaction was regarded as a possible method of either continued alumina formation [106, 171] or chromia growth above interfacial voids. It was considered that the columnar grain profiles of the α-alumina scales, formed at 1200°C would be affected if a displacement reaction was responsible. This would present a reduction in columnar grain size near the oxide-void interface and an increase in grain size at the opposite end. Alternatively, a thickening of the equiaxed grains of alumina may have been recorded. The profiling of growing scales adhered to the substrate and above voids does not conclusively

prove this theory. Although a distinct average change in the appearance of the average width of columnar grains occurs between 500 hours and 700 hours; the profile of the grains are recorded from above voids. Widening/Coarsening of the columnar grain structures at their base after 500 hours at 1200°C on thin foil samples is observed. Wider based columnar grain profiles are not observed above interfacial voids. No change in columnar grain size near the equiaxed/columnar grain interface of the alumina occurred. Thickening of the layer of equiaxed alumina gains above voids did not occur either.

7. Conclusions and Future Work

7.1 Conclusions

7.1.1 Honeycomb Abradable Seals

- The tested honeycomb abradable seal design consisted of alloy MI2100 foils, BNi-5 braze, and a Haynes 214 base plate. Satisfactory oxidation performance of the abradable seal was recorded past 1000 hours at 1100°C in a lab air environment.

- Abradable seal failure was observed at times less than 600 hours during oxidation tests at 1200°C. Failure occurred due to FeCrAl foil detachment. The foils of the honeycomb failed at ~200-500μm above the brazed region.

- Curvature of honeycomb end foils was due to substrate alloy creep at 1200°C. This promoted increased oxide scale thickness on the outer walls of the honeycomb foils, along with increased levels of void formation. Commercial manufacturers of such abradable seals e.g. Neomet Ltd. now incorporate end foils of double thickness to prevent end foil degradation.

- Void formation, filling and alumina scale cracking above voids was extensive near the region of honeycomb foil failure. Voids were found to fill with silica. This is a consequence of brazing using a silicon rich filler metal.

- Voids appear to be much larger than vacancy voids. The size of interfacial voids recorded from selected positions of honeycomb foil cross-sections are at least one order of magnitude larger than those expected due to vacancy condensation alone.

- Crack propagation through alumina scales above voids is thought to initiate silica void filling. Mechanical movement of the honeycomb foils i.e. creep of the alloy substrate is thought to be the main cause of alumina scale cracking and foil failure.

- The diffusion of nickel from the braze alloy has a significant effect on the honeycomb construction. Honeycomb foils, up to approximately ¼ foil height can be classed as having a high enough nickel content to change the ferrite structure of the foils to a duplex or austenitic phase. A change in volume is also associated with the BCC to FCC structural change. Shrinkage of the substrate may occur with this transformation.

- Mechanical movement of the honeycomb foils, a change in phase, and localized areas of Al depletion in the substrate alloy are thought to be responsible for the failure of the honeycomb foils.

7.1.2 Alloy MI2100: Void formation at 1200°C

- FeCrAl foils (without the influence of Si) present void formation after 500 hours at 1200°C. This length of time at 1200°C corresponds to the exhaustion of the aluminium reservoir within the substrate needed to sustain alumina formation. After the exhaustion of aluminium from the substrate, a chromia layer formation is observed directly beneath the alumina scale. At 1200°C this chromia layer is continuous and forms beneath the entire scale. Voids are always found below the chromia layer. Chromia void filling commences soon after void formation. Void filling was found to commence from the oxide surface of the void.

- The results suggest that chromium vapour transport or surface diffusion may occur across voids at 1200°C. This proposal could explain the void filling mechanism, where chromia fills the void from the underside of the oxide. This may also explain the uniform thickness of the chromia layer across the whole sample.

- If reactive elements are consumed by incorporation into alumina scales, then upon their exhaustion, scale adhesion may suffer and void formation may arise. This may occur during the formation of the chromia layer beneath the alumina.

- EBSD analysis of the chromia layer formation beneath the alumina scales of oxidised thin foils suggests a similar texture between the two oxide layers. These results were found for chromia layers formed both above voids and where the chromia layer was adhered to the FeCrAl substrate. Both alumina columnar grains and chromia equiaxed grains are characterised as having a strong fibre texture.

7.1.3 Alloy A1: Void formation at 900°C

- Void formation was recorded after only 50 hours whilst still enough aluminium remained within the metal substrate to sustain the growth of alumina.

- Vacancy condensation due to transient oxide formation is thought responsible for void formation at this temperature.

- Void filling occurs soon after void formation at this temperature. These voids are found to fill with chromia. Void filling was found to commence from the base of the alumina scale.

7.2 Future Work

- Oxidation testing of the honeycomb abradable seal, consisting of: MI2100 alloy foils, BNi-5 braze, and Haynes 214 base plate, revealed the incompatibility of joining these dissimilar alloys for operation at elevated temperatures. It is thought that the silicon content of the braze is the main issue that affects the components lifetime. Development of honeycomb abradable seals using braze alloys without silicon content are the next area of testing. Alternatives to nickel based braze filler metals have also been discussed e.g. such as cobalt. Unfortunately, no iron based braze filler metals are available that would yield satisfactory performance at elevated temperatures. It is also suggested that creep resistant alloys, such as ODS (oxide dispersion strengthened) FeCrAl alloys, or Ni-based alloys could be tested as suitable replacements to alloy MI2100. Ni-based alloys, especially, would avoid the joining of dissimilar metals. However, elevated costs would also be associated with incorporating such alloys into the honeycomb seal constructions.

- EBSD analysis of alumina scales, alumina scales above voids, dual oxide layers of alumina and chromia, and chromia filled voids revealed some excellent results. EBSD analysis of silica void fills is a possibility for further study. No epitaxial relationship is expected between the silica and alumina due to the growth direction of the silica void fill.

- Auger electron microscopy possesses resolution and chemical analysis facilities beyond the resolution of a SEM. It is proposed that auger analysis of interfacial void formations would present valuable data about void filling. Monolayer analysis of unfilled voids could reveal the initial stages of chromia or silica void filling, either on the substrate interface or on the

underside of the alumina, if charging could be avoided. These data sets would prove valuable in demonstrating the initial stages of void filling.

- Electron probe micro-analysis (EPMA) would produce diffusion profiles of a higher accuracy than those obtained during this study with the EDX point analysis technique. These diffusion profiles would provide compositional analysis of diffusion gradients over a range of test times for both brazed sandwich structures and honeycomb abradable seals. The EPMA facility could also be applied near void formations to analyse regions of localised depletion of elements in the substrate. The diffusion profiles of silicon and chromium near void formations on honeycomb foils may also yield some interesting results and may be related to void filling.

8. References

[1] J. P. Norbye; Gas Turbine Engine: Design, Development and Applications ed. 1975.

[2] G. W. Meetham; The Development of Gas Turbine Materials 1st ed. 1981, London: Applied Science.

[3] The Modern Gas Turbine Engine: How it works and How its Built, [2004]; 'Available from:' www.rolls-royce.com.

[4] N. Birks, G. H. Meier and F. S. Pettit; Introduction to the High-Temperature Oxidation of Metals Second Edition ed. 2006: Cambridge University Press.

[5] W. J. Quadakkers, D. Naumenko, E. West, V. Kochubey and L. Singheises; Oxidation of Metals (2004), Vol. 61, p.17-37

[6] R. F. Tylecote; Journal of The Iron and Steel Institute (1960), Vol. 196, p.445-453

[7] W. Smarsly, N. Zheng, C. S. Buchheim, C. Nindel, C. Silvestro, D. Sporer, M. Tuffs, K. Schreiber, C. Langlade-Bomba, O. Andersen, H. Goehler, N. J. Simms and G. C. McColvin; Functionally Graded Materials Science Forum (2005), Vol. 492-493, p.21-26

[8] N. J. Simms, J. F. Norton and G. McColvin; Materials and Corrosion-Werkstoffe Und Korrosion (2005), Vol. 56(11), p.765-777

[9] N. J. Simms, R. Newton, J. F. Norton, A. Encinas-Oropesa, J. E. Oakey, J. R. Nicholls and J. Wilber; Materials at High Temperatures (2003), Vol. 20(3), p.439-451

[10] S. C. duBois; Brazing Fundamentals: Metallurgy of Nickel-Based Brazing Filler Metals; 'Available from:' www.wallcolmonoy.com.

[11] S. Y. Liu, A. Suzumura, T. T. Ikeshoji and T. Yamazaki; JSME International Journal Series A-Solid Mechanics and Material Engineering (2005), Vol. 48(4), p.420-425

[12] H. W. Hsu and W. T. Tsai; Materials Chemistry and Physics (2000), Vol. 64, p.147-155

[13] B. Gleeson and M. A. Harper; Oxidation of Metals (1998), Vol. 49(3-4), p.373

[14] B. Li and B. Gleeson; Oxidation of Metals (2006), Vol. 65(1-2), p.101-122

[15] A. M. Huntz, V. Bague, G. Beauple, C. Haut, C. Severac, P. Lecour, X. Longaygue and F. Ropital; Applied Surface Science (2003), Vol. 207, p.255-275

[16] J. S. Dunning, D. E. Alman and J. C. Rawers; Oxidation of Metals (2002), Vol. 57(5-6), p.409

[17] D. J. Potter, H. Al-Badairy, G. J. Tatlock and M. J. Bennett; Materials and Corrosion-Werkstoffe Und Korrosion (2008), Vol. 59(5), p.414-422

[18] W. J. Quadakkers and K. Bongartz; Materials and Corrosion/Werkstoffe und Korrosion (1994), Vol. 45(4), p.232-241

[19] I. G. Wright, R. Peraldi and B. A. Pint; Materials Science Forum (2004), Vol. 461-464, p.579-590
[20] H. Al-Badairy, G. J. Tatlock and M. J. Bennett; Materials at High Temperatures (2000), Vol. 17(1), p.101-107
[21] W. D. Callister; Materials Science and Engineering : An Introduction 6th ed. 2003, New York: Wiley.
[22] C. T. Sims and W. C. Hagel; The Superalloys 1st ed. 1972, New York: Wiley.
[23] G. Strehl, D. Naumenko, H. Al-Badairy, L. M. R. Lobo, G. Borchardt, G. J. Tatlock and W. J. Quadakkers; Materials at High Temperatures (2000), Vol. 17(1), p.87-92
[24] C. Wagner; Corrosion Science (1965), Vol. 5(11), p.751-764
[25] J. C. Schaeffer, W. H. Murphy and J. L. Smialek; Oxidation of Metals (1995), Vol. 43(1-2), p.1-23
[26] D. R. Sigler; Oxidation of Metals (1988), Vol. 29(1-2), p.23-43
[27] M. J. Bennett, J. R. Nicholls, N. J. Simms, D. Naumenko, W. J. Quadakkers, V. Kochubey, R. Fordham, R. Bachorczyk, D. Goossens, H. Hattendorf, A. B. Smith and D. Britton; Materials and Corrosion (2005), Vol. 56(12), p.854-866
[28] D. R. Sigler; Oxidation of Metals (1989), Vol. 32(5-6), p.337-355
[29] S. Chevalier, C. Nivot and J. P. Larpin; Oxidation of Metals (2004), Vol. 61(3-4), p.195-217
[30] B. A. Pint; Oxidation of Metals (1996), Vol. 45(1-2), p.1
[31] P. Y. Hou; Materials and Corrosion (2000), Vol. 51, p.329
[32] R. Prescott and M. J. Graham; Oxidation of Metals (1992), Vol. 38(3-4), p.233-254
[33] V. Kochubey, H. Al-Badairy, G. Tatlock, J. Le-Coze, D. Naumenko and W. J. Quadakkers; Materials and Corrosion (2005), Vol. 56(12), p.848-853
[34] F. H. Stott and N. Hiramatsu; Materials at High Temperatures (2000), Vol. 17(1), p.93-99
[35] G. Strehl, R. Beaven, B. Lesage and G. Borchardt; Materials and Corrosion-Werkstoffe Und Korrosion (2005), Vol. 56(11), p.778-784
[36] V. Kochubey, D. Naumenko, E. Wessel, J. Le Coze, L. Singheiser, H. Al-Badairy, G. J. Tatlock and W. J. Quadakkers; Materials Letters (2006), Vol. 60(13-14), p.1654-1658
[37] V. Kochubey, H. Al Badairy, J. Le Coze, D. Naumenko, G. J. Tatlock, E. Wessel and W. J. Quadakkers; Materials at High Temperatures (2005), Vol. 22(3-4), p.461-466
[38] P. Y. Hou and J. Stringer; Journal de Physique (1993), Vol. IV(3), p.231
[39] P. Y. Hou; Proceedings of the Symposium on Fundamental Aspects of High Temperature Corrosion, Electrochemical Society, NJ (1997), Vol. 1, p.28
[40] P. Fox and G. J. Tatlock; Materials Science and Technology (1998), Vol. 4, p.439

[41] M. C. Stasik, F. S. Pettit, G. H. Meier, A. Ashary and J. L. Smialek; Scripta Metallurgica et Materialia (1994), Vol. 31(12), p.1645-1650
[42] C. H. Xu, W. Gao and H. Gong; Intermetallics (2000), Vol. 8(7), p.769-779
[43] F. A. Golightly, F. H. Stott and G. C. Wood; Oxidation of Metals (1976), Vol. 10(3), p.163-187
[44] Z. G. Yang and P. Y. Hou; Materials Science and Engineering a-Structural Materials Properties Microstructure and Processing (2005), Vol. 391(1-2), p.1-9
[45] F. H. Stott; Materials Science and Engineering (1998), Vol. 4, p.431
[46] G. C. Wood and F. H. Stott; Materials Science and Technology (1987), Vol. 3(7), p.519
[47] F. H. Stott, G. C. Wood and M. G. Hobby; (1971), Vol. 3(2), p.103-13
[48] G. C. Wood; Oxidation of Metals (1970), Vol. 2(1), p.11
[49] V. K. Tolpygo and D. R. Clarke; Acta Materialia (1999), Vol. 47(13), p.3589-3605
[50] V. K. Tolpygo and D. R. Clarke; Oxidation of Metals (1998), Vol. 49(1-2), p.187-212
[51] V. K. Tolpygo; Oxidation of Metals (1999), Vol. 51(5/6), p.449
[52] T. Ohashi and T. Harada; Oxidation of Metals (1996), Vol. 6(3-4), p.235-255
[53] D. R. Sigler; Oxidation of Metals (1993), Vol. 40(3-4), p.295-320
[54] I. Itoh, M. Fukaya, R. Hisatomi, H. Morimoto, K. Ohmura, H. Tanaka, F. Fudanki and M. Arakawa; Nippon Steel Technical Report (1995), Vol. 64, p.69-74
[55] G. Korb; New Materials by Mechanical Alloying Techniques, Arzt and Schulz ed. 1990, Oberusel: DGM.
[56] W. J. Quadakkers and M. J. Bennett; Materials Science and Technology (1994), Vol. 10(2), p.126-131
[57] M. J. Bennett; Solid State Phenomena (1995), Vol. 41, p.235-252
[58] H. E. Evans; International Materials Reviews (1995), Vol. 40(1), p.1-40
[59] J. P. Wilber, J. R. Nicholls and M. J. Bennett; Microscopy of Oxidation (1997), Vol. 3, p.207-220
[60] J. P. Wilber, M. J. Bennett and J. R. Nicholls; Materials for Advanced Power Engineering (1998), Vol. 5(Pt. II), p.835-846
[61] G. Borchardt and G. Strehl; In: H. Bode, Materials Aspects in Automotive Catalytic Converters ed. 2002, Munich, Germany: DGM.
[62] H. J. Grabke, E. M. Muller-Lorenz, S. Straub, E. Pippel and J. Woltersdorf; Oxidation of Metals (1998), Vol. 50, p.2241
[63] H. J. Grabke, E. M. Muller-Lorenz, B. Eltester, M. Lucas and D. Monceau; Steel Research (1997), Vol. 68, p.179
[64] H. J. Grabke, E. M. Muller-Lorenz, B. Eltester and M. Lucas; Materials at High Temperatures (2000), Vol. 17, p.339
[65] H. J. Grabke and E. M. Muller-Lorenz; Materials and Corrosion (1998), Vol. 49, p.317

[66] W. G. Moffatt, G. W. Pearsall and J. Wulff; The Structure and Properties of Materials, 1. Structure ed. 1964, New York: John Wilev & Sons.
[67] B. Ganser, K. A. Wynns and A. Kurlekar; Materials and Corrosion (1999), Vol. 50, p.700
[68] R. Streiff; Elevated Temperature Coatings: Science and Technology II (Eds. N.B. Dahotre, J.M. Hampikian), The Minerals, Metals & Materials Society ed. 1996.
[69] C. Sarioglu, E. Schumann, J. R. Blachere, F. S. Pettit and G. H. Meier; Materials at High Temperatures (2000), Vol. 17(1), p.109-115
[70] J. D. French, J. H. Zhao, M. P. Harmer, H. M. Chan and G. A. Miller; Journal of the American Ceramic Society (1994), Vol. 77(11), p.2857-2865
[71] B. A. Pint, A. J. Garratt-Reed and L. W. Hobbs; Oxidation of Metals (2001), Vol. 56(1-2), p.119-145
[72] G. J. Tatlock, E. G. Dyadko, S. N. Dryepondt and I. G. Wright; Metallurgical and Materials Transactions a-Physical Metallurgy and Materials Science (2007), Vol. 38A(7), p.1663-1665
[73] J. R. Nicholls, M. J. Bennett and R. Newton; Materials at High Temperatures (2003), Vol. 20(3), p.429-438
[74] J. P. Wilber, M. J. Bennett and J. R. Nicholls; Materials at High Temperatures (2000), Vol. 17(1), p.125-132
[75] A. Galerie, F. Toscan, M. Dupeux, J. Mougin, G. Lucazeau, C. Valot, A.-M. Huntz and L. Antoni; Materials Research (2004), Vol. 7(1), p.81-88
[76] P. F. Tortorelli, B. A. Pint, E. A. Kenik, K. L. More and I. G. Wright; Zurich-Uetikon, Vol. 369-3, p.337-344
[77] K. Ishii and T. Kawasaki; Journal of the Japan Institute of Metals (1992), Vol. 56(7), p.854-862
[78] N. Hiramatsu and F. H. Stott; Oxidation of Metals (1999), Vol. 51(5-6), p.479-494
[79] M. Schutze and W. J. Quaddakers; Cyclic Oxidation of High Temperature Materials, European Federation of Corrosion, Publication No. 27 ed. 1999, London: IoM Communication.
[80] M. Legall, A. M. Huntz, B. Lesage, C. Monty and J. Bernardini; Journal of Materials Science (1995), Vol. 30(1), p.201-211
[81] S. C. Tsai, A. M. Huntz and J. Philibert; Defect and Diffusion Forum (1997), Vol. 143, p.1195-1200
[82] K. Ishii, M. Kohno, S. Ishikawa and S. Satoh; Materials Transactions Jim (1997), Vol. 38(9), p.787-792
[83] A. Gil, S. Mrowec, J. Jedlinski and G. Borchardt; Solid State Ionics (1992), Vol. 58(1-2), p.13-21
[84] H. E. Evans, A. T. Donaldson and T. C. Gilmour; Oxidation of Metals (1999), Vol. 52(5-6), p.379-402
[85] D. J. Potter and G. J. Tatlock; Materials Science Forum (2008), Vol. 595-598, p.In Press

[86] D. J. Prior, H. Al-Badairy, G. G. E. Seward, C. J. Veltkamp and G. J. Tatlock; Materials Science and Technology (2006), Vol. 22, p.1316-1324
[87] H. Al-Badairy, D. J. Prior and G. J. Tatlock; Materials at High Temperatures (2005), Vol. 22(3-4), p.453-460
[88] F. A. Golightly, G. C. Wood and F. H. Stott; Oxidation of Metals (1980), Vol. 14(3), p.217-234
[89] F. A. Golightly, F. H. Stott and G. C. Wood; Journal of the Electrochemical Society (1979), Vol. 126(6), p.1035-1042
[90] F. N. Rhines and J. S. Wolf; (1970), Vol. 1(6), p.1701-10
[91] R. Prescott, D. F. Mitchell and M. J. Graham; Corrosion (Houston) (1994), Vol. 50(1), p.62-71
[92] H. M. Hindam and W. W. Smeltzer; Oxidation of Metals (1980), Vol. 14(4), p.337-349
[93] J. Smialek and R. Gibala; Diffusion Processes in Al2O3 Scales: Void Growth, Grain Growth, and Scale Growth, in High Temperature Corrosion, by R. A. Rapp, p. 274-283 ed. 1983, Housten TX: NACE.
[94] J. Doychak; Ed., Proceedings of the 42nd Annual Meeting of the Electron Microscopy Society of America (1984), Vol. 1, p.598
[95] G. C. Wood and B. Chattopadhyay; Corrosion Science (1970), Vol. 10, p.471
[96] J. L. Smialek and R. Gibala; Metallurgical Transactions (1983), Vol. 14(A), p.2143
[97] J. L. Smialek; Microstructure of Al_2O_3 Scales formed on NiCrAl Alloys, Ph.D. Thesis, Case Western Reserve University, Cleveland, OH, 1981.
[98] J. K. Doychak and T. E. Mitchell; in (1985), Boston, MA, USA: Materials Research Soc, Pittsburgh, PA, USA
[99] W. H. Gitzen; Alumina as a Ceramic Material ed. 1970, Columbus, OH: American Ceramic Society.
[100] W. T. Donlon, T. E. Mitchell and A. H. Heuer; Journal of Materials Science (1982), Vol. 17, p.1389
[101] J. M. Winey, Y. M. Gupta and D. E. Hare; Journal of Applied Physics (2001), Vol. 90(6), p.3109-3111
[102] J. R. Blachere, E. Schumann, G. H. Meier and F. S. Pettit; Scripta Materialia (2003), Vol. 49(9), p.909-912
[103] J. L. Smialek and R. Gibala; in (1983), San Diego, CA, USA: NACE, Houston, Tex, USA
[104] J. L. Smialek; Ed., Proceedings of the 42nd Annual Meeting of the Electron Microscopy Society of America (1984), Vol. 1, p.594
[105] M. W. Brumm and H. J. Grabke; Corrosion Science (1993), Vol. 34(4), p.547-561
[106] P. Y. Hou, Y. Niu and C. Van Lienden; Oxidation of Metals (2003), Vol. 59(1-2), p.41-61
[107] F. Gesmundo and P. Y. Hou; Oxidation of Metals (2003), Vol. 59(1-2), p.63-81

[108] G. J. Tatlock, H. Al-Badairy, M. J. Bennett and J. R. Nicholls; Materials at High Temperatures (2005), Vol. 22(3-4), p.467-472
[109] R. Hales, R. E. Smallman and P. S. Dobson; Proceedings of the Royal Society, A. 307 (1968), Vol., p.71
[110] D. L. Douglas; Materials Science and Engineering (1969), Vol. 3, p.255
[111] J. E. Harris; Acta Metallurgica (1978), Vol. 26(6), p.1033-1041
[112] V. Provenzano, K. Sadananda, N. P. Louat and J. R. Reed; Surface & Coatings Technology (1988), Vol. 36(1-2), p.61-74
[113] S. Perusin, B. Viguier, D. Monceau, L. Ressier and E. Andrieu; Acta Materialia (2004), Vol. 52(18), p.5375-5380
[114] M. G. C. Cox, B. McEnaney and V. D. Scott; Philosophical Magazine (1973), Vol. 28(2), p.309-319
[115] M. G. C. Cox, B. McEnaney and V. D. Scott; Philosophical Magazine (1974), Vol. 29(3), p.585-600
[116] M. G. C. Cox, B. McEnaney and V. D. Scott; Philosophical Magazine (1975), Vol. 31(2), p.331-338
[117] B. A. Pint; Oxidation of Metals (1997), Vol. 48(3-4), p.303-328
[118] B. W. Dunnington, F. H. Beck and M. G. Fontana; Corrosion Science (1952), Vol. 8, p.2-13
[119] R. F. Tylecote; Journal of The Iron and Steel Institute (1960), Vol. 196, p.135-141
[120] R. F. Tylecote; Journal of The Iron and Steel Institute (1960), Vol. 195, p.380-385
[121] J. Stringer; Metallurgical Review (1966), Vol. 11, p.113
[122] M. Skeldon, J. M. Calvert and D. G. Lees; Oxidation of Metals (1987), Vol. 28(1-2), p.109-125
[123] P. Kofstad; High Temperature Corrosion ed. 1988, London/New York: Elsevier Applied Science.
[124] J. D. Kuenzly and D. L. Douglass; Oxidation of Metals (1974), Vol. 8(3), p.139-178
[125] J. Doychak, J. L. Smialek and C. A. Barrett; Oxidation of Ni-rich Ni-Al Intermetallics, in Oxidation of High Temperature Intermetallics, T. Grobstien and J. Doychak ed. 1988, Warrendale, PA: TMS.
[126] P. Y. Hou, K. Prussner, D. H. Fairbrother, J. G. Roberts and K. B. Alexander; Scripta Materialia (1998), Vol. 40(2), p.241-247
[127] P. Y. Hou; Impurity segregation to scale/alloy interfaces and its effect on interfacial properties ed. High Temperature Corrosion and Protection of Materials 5, Pts 1 and 2. 2001, Zurich-Uetikon: Trans Tech Publications Ltd.
[128] R. A. Rapp; Metallurgical Transactions a-Physical Metallurgy and Materials Science (1984), Vol. 15(5), p.765-782
[129] J. K. Tien and F. S. Pettit; Metallurgical Transactions (1972), Vol. 3(6), p.1587-1599
[130] A. Kumar, Nasralla.M and D. L. Douglass; Oxidation of Metals (1974), Vol. 8(4), p.227-263

[131] K. L. Luthra and C. L. Briant; Metallurgical Transactions a-Physical Metallurgy and Materials Science (1988), Vol. 19(8), p.2091-2098
[132] W. D. Kingery, H. K. Bowen and D. R. Uhlmann; Introduction to Ceramics ed. 1976, New York: John Wiley and Sons.
[133] P. Y. Hou and J. Stringer; Oxidation of Metals (1992), Vol. 38(5-6), p.323-345
[134] H. J. Grabke, D. Wiemer and H. Viefhaus; Applied Surface Science (1991), Vol. 47(3), p.243-250
[135] H. J. Grabke, G. Kurbatov and H. J. Schmutzler; Oxidation of Metals (1995), Vol. 43(1-2), p.97-114
[136] P. Fox, D. G. Lees and G. W. Lorimer; Oxidation of Metals (1991), Vol. 36(5-6), p.491-503
[137] T. Maruyama, N. Fukagai, M. Ueda and K. Kawamura; Materials Science Forum (2004), Vol. 461-464, p.807-814
[138] M. Ueda, K. Kawamura and T. Maruyama; Materials Science Forum (2006), Vol. 522-523, p.37-44
[139] K. Akiba, M. Ueda, K. Kawamura and T. Maruyama; Materials Transactions (2007), Vol. 48(10), p.2753-2761
[140] N. Nesmeyanov; Vapour Pressure of the Chemical Elements ed. 1963, Amsterdam: Elsevier.
[141] J. Ehlers, D. J. Young, E. J. Smaardijk, A. K. Tyagi, H. J. Penkalla, L. Singheiser and W. J. Quaddakkers; Corrosion Science (2006), Vol. 48, p.3428-3454
[142] M. J. Fletcher; Vacuum Brazing ed. 1971, London: Mills & Boon Ltd.
[143] D. P. Sekulic, F. Gao, H. Zhao, B. Zellmer and Y. Y. Qian; Welding Journal (2004), Vol. 83(3), p.102S-110S
[144] F. M. Hosking, C. H. Cadden, N. Y. C. Yang, S. J. Glass, J. J. Stephens, P. T. Vianco and C. A. Walker; Welding Journal (2000), Vol. 79(8), p.222S-230S
[145] N. C. Cole and G. M. Slaughter; Nuclear Technology (1975), Vol. 26(2), p.183-191
[146] C. L. Bauer and G. G. Lessmann; Annual Review of Materials Science (1976), Vol. 1, p.361
[147] A. W. Society; Welding handbook Fifth ed. 1961, New York: : Phillips, Arthur L. .
[148] A. I. H. Committee; ASM Handbook Vol. 6 Welding, brazing, and soldering 10th ed. c1990-1998, OH: Materials Park.
[149] W. Tillmann, E. Lugscheider and I. Buschke; Warrendale, Vol., p.605-611
[150] P. Heinz, A. Volek, R. F. Singer, M. Dinkel, F. Pyczak, M. Goken, M. Ott, E. Affeldt and A. Vossberg; Stafa-Zurich, Vol. 273-276, p.294-299
[151] G. G. E. Seward, D. J. Prior, J. Wheeler, S. Celotto, D. J. M. Halliday, R. S. Paden and M. R. Tye; Scanning (2002), Vol. 24(5), p.232-240

[152] J. Wheeler, D. J. Prior, Z. Jiang, R. Spiess and P. W. Trimby; Contributions to Mineralogy and Petrology (2001), Vol. 141(1), p.109-124
[153] M. Bestmann and D. J. Prior; Journal of Structural Geology (2003), Vol. 25(10), p.1597-1613
[154] C. D. Storey and D. J. Prior; J. Petrology (2005), Vol. 46(12), p.2593-2613
[155] P. J. Goodhew, J. Humphreys and R. Beanland; Electron Microscopy and Analysis Third ed. 2001, London: Taylor and Francis.
[156] G. E. Lloyd; Mineralogical Magazine (1987), Vol. 51(1), p.3-19
[157] D. J. Prior, A. P. Boyle, F. Brenker, M. C. Cheadle, A. Day, G. Lopez, L. Peruzzo, G. J. Potts, S. Reddy, R. Spiess, N. E. Timms, P. Trimby, J. Wheeler and L. Zetterstrom; American Mineralogist (1999), Vol. 84(1), p.1741-1759
[158] Oxford Instruments; Electron Back-Scattered Diffraction Explained, [2008]; 'Available from:' www.ebsd.com.
[159] N. C. A. Seaton; Mechanisms of Recrystallisation in Ti-Sulc Steel, PhD Thesis, Liverpool, 2006.
[160] S. Gray, K. Berriche-Bouhanek, H. E. Evans and p. trans tech; in 6th International Symposium on High Temperature Corrosion and Protection of Materials (2004), Les Embiez, FRANCE: Trans Tech Publications Ltd
[161] R. C. Lobb, J. A. Sasse and H. E. Evans; Materials Science and Technology (1989), Vol. 5(8), p.828-834
[162] H. Al-Badairy and G. J. Tatlock; Materials at High Temperatures (2001), Vol. 18(2), p.101-106
[163] A. M. Huntz, L. Maréchal, B. Lesage and R. Molins; Applied Surface Science (2006), Vol. 252(22), p.7781-7787
[164] T. Sheppard and P. Richards; Journal of Materials Science (1987), Vol. 22(5), p.1642-1650
[165] M. S. McIntosh, T. H. Sanders and J. M. Hampikian; Modeling and Numerical Simulation of Materials Behavior and Evolution (2002), Vol. 731, p.183-188
[166] H. Bode; Metal-Supported Automotive Catalytic Converters, ed. 1997, Frankfurt: Werkstoff-Informationsgesellshaft.
[167] H. Bode; Metal-Supported Automotive Catalytic Converters (MACC 2001) ed. 2001, Frankfurt: Werkstoff-Informationsgesellshaft.
[168] G. C. Wood and F. H. Stott; Proceedings of the International Conference on High Temperature Corrosion NACE-6, San Diego California, USA (1983), Vol. 1, p.227
[169] B. A. Pint; The morphology of Al_2O_3 scales: Indicators of phase, growth mechanisms, and grain boundary segregation ed. Fundamental Aspects of High Temperature Corrosion, ed.D. A. Shores, R. A. Rapp and P. Y. Hou. 1997, Pennington: Electrochemical Society Inc.

[170] C. Mennicke, E. Schumann, M. Ruhle, R. J. Hussey, G. I. Sproule and M. J. Graham; Oxidation of Metals (1998), Vol. 49(5-6), p.455-466
[171] P. Y. Hou and K. Priimak; Oxidation of Metals (2005), Vol. 63(1-2), p.113
[172] A. Fick; Poggendorff's Annalen der Physik und Chemie (1855), Vol. 94(1), p.59
[173] W. Jost; Diffusion in Solids, Liquids, and Gases 1st ed. 1952, New York: Academic Press.
[174] G. E. Murch and A. S. Nowick; Diffusion in Crystalline Solids 1st ed. 1984, New York: Academic Press.
[175] V. Z. Bugakov; Diffusion in Metals and Alloys 1st ed. 1949, Jerusalem: Israel Program for Scientific Translations.
[176] SMILER Project No G5RD-CT-2001-00530, FP5 Growth, Final Project Review; Technische Universitat Clausthal, Julick, (2004), Unpublished Work
[177] J. J. Stephens and K. S. Weil; Brazing and Soldering, Proceedings of the 3rd International Brazing and Soldering Conference, 1 ed. 2006, San Antonio, Texas, USA: ASM International.
[178] E. A. BRANDES; Smithells metals reference book" 6th ed. 1983, London: Butterworths.

Appendix 1:

GDMS (Glow Discharge Mass Spectroscopy) analysis of alloy MI2100 composition

Fe-20Cr-5Al alloy **Model Fe-20Cr-5Al alloy**	
Element	Concentration [ppm / wt]
Mg	63
Al	Matrix
Si	~ 0.62%wt
P	130
S	1.6
Cl	0.46
Ca	5.6
Ti	85
V	590
Cr	Matrix
Mn	~ 0.11%wt
Fe	Balance
Ni	~ 0.20%wt
Cu	150
Zn	2.7
Se	2.5
Y	500
Zr	380
Nb	< 50
Mo	53
La	0.03
Hf	450
Ta	260
W	4.3
Pt	0.31

Appendix 2:

Al_2O_3 scale thickness vs aluminium consumption from alloy substrate from [20] using Equation 2-11.

$$Al_r = \frac{Al_m \cdot \rho_m \cdot x_m - 2Al_s \cdot \rho_s \cdot x_s}{\rho_m \cdot x_m - 2Al_s \cdot \rho_s \cdot x_s}$$

The following result set is based on the FeCrAl foils being approximately 100 microns thick and having a density of 7.18 x 10^6 g/m^3.

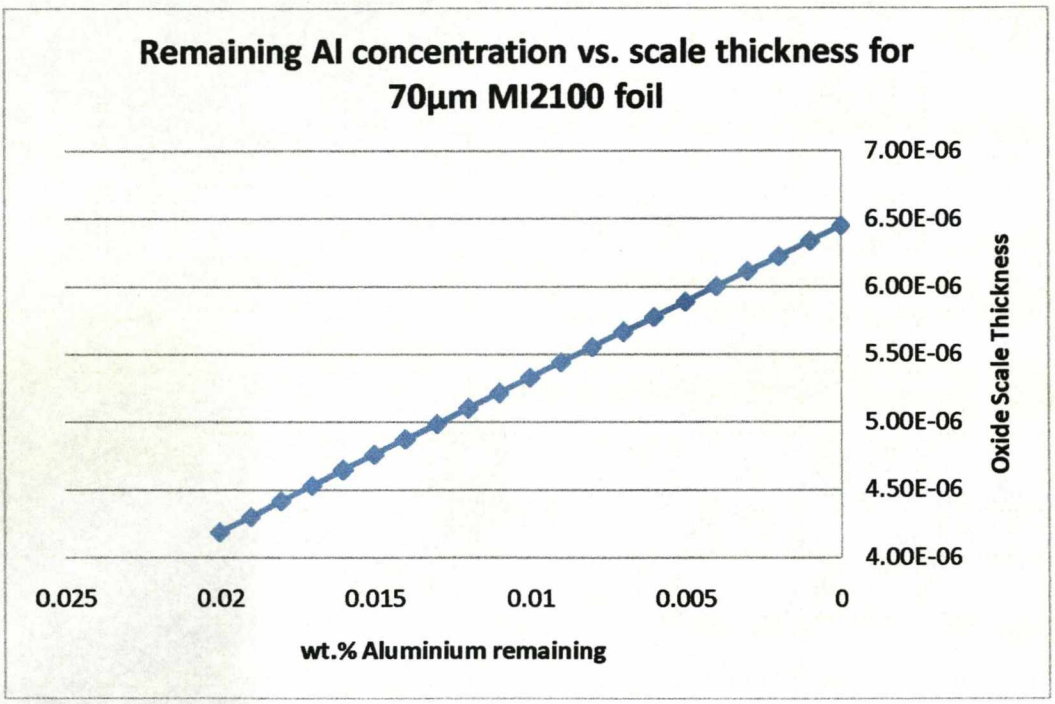

Figure Appendix 2.1: Al composition remaining in FeCrAl foils as calculated from oxide scale formation

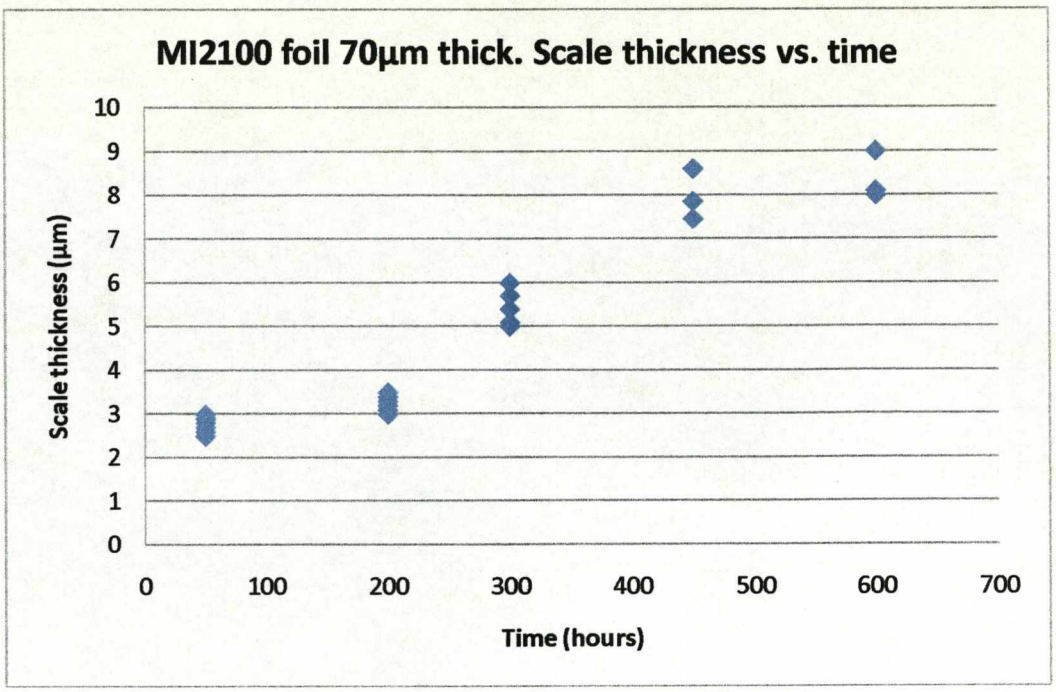

Figure Appendix 2.2: Oxide thickness vs. time. It is proposed that all the Aluminium is consumed from the substrate once the oxide scale thickness exceeds 6.5µm.

Appendix 3:

EBSD sample preparation for the examination of α-alumina scales grown during the oxidation of Fe-20Cr-5Al alloys

This method of sample preparation applies to the oxide formation on both foil and sheet.

- After oxidation and cooling of the selected sample, the entire sample is mounted in cross-section using a Buehler hot mounting press and a carbon filled epoxy resin. If the sample is a thin foil <100 microns in thickness, the sample cross-section is sandwiched between two sheets of FeCrAl material to help avoid foil distortion during the hot mounting process.
- The mounted sample is then ground back at least 3mm to obtain a cross-section unaffected by the edges of the sample. This is achieved by patiently grinding with 600 grit wet silicon carbide paper upon a spinning horizontal grinding wheel. Longer grinding times at each stage were found to be beneficial in overcoming the differential hardness between the alumina scales and soft FeCrAl substrate.
- Progressive stages of sample grinding were then carried out using 1200, 2400 and 4000 grit.
- Samples were ground manually upon the spinning grinding wheels, but with a slightly increased applied pressure. Once the certain grit stage of grinding was complete, further grinding beyond this point proved beneficial. Grinding times were almost doubled at each stage.
- As manually ground, the samples were periodically rotated by 90° on each grinding wheel.
- Samples were ultrasonically cleaned using detergent and acetone after each stage.
- Samples were then polished to 6μm and 1μm standard using diamond paste. Again a patient approach is needed, with a slightly increased pressure.
- Samples are cleaned between stages in exactly the same way as mentioned previously.
- A final polish is carried out using colloidal silica (Buehler Mastermet) 60nm standard upon an automated universal polisher. A maximum period of 20 minutes is used. This is normally the shortest stage of polishing.
- The sample is then thoroughly cleaned using detergent and acetone.
- An optical microscope is used between stages to monitor any differences in height between oxide and metallic substrate. Repeating certain stages may be necessary.

Appendix 4:

Theoretical diffusion for a brazed sandwich structure of 2 FeCrAl foils (~1mm thickness) and a nickel brazing alloy (70μm thickness)

The theoretical diffusion model used as the solution to the sandwich structure is derived from Fick's second law of diffusion (Equation A4.1) [172]. Equation A4.2 shows the derivative of Fick's second law of diffusion used as the solution to the diffusion couple. The derivation of Equation A4.2 from Equation A4.1 can be found in the texts by Jost, and Murch et al. [173-175] and is not presented here.

$$\frac{\partial c}{\partial t} = D\frac{\partial^2 c}{\partial x^2} \tag{A4.1}$$

$$C(x,t) = C_1 + \frac{C_0 - C_1}{2} \cdot \left[erf\left(\frac{h-x}{2\sqrt{Dt}}\right) + erf\left(\frac{h+x}{2\sqrt{Dt}}\right)\right] \tag{A4.2}$$

where:

x =	position within the sandwich structure (m)
t =	time (sec)
C(x, t) =	composition at position (x) and time (t)
C_1 =	composition of Ni or Si in foils at start (wt %)
C_0 =	composition of Ni or Si in braze at start (wt %)
h =	the ½ width of the braze alloy i.e. 70μm/2 (m)
erf =	error function
D =	diffusion coefficient (cm^2s^{-1})

and where D can be calculated from:

$$D = D_0 \cdot exp\left(-\frac{\Delta H_a}{RT}\right)$$

where:

D_0 =	pre-exponential diffusion factor (cm^2s^{-1})
T =	temperature (K)
R =	gas constant (8.314 J $mol^{-1}K^{-1}$)
ΔH_a =	activation enthalpy (J mol^{-1})

ΔH_a for Si = ~484 ± 135 KJ mol^{-1}
ΔH_a for Ni = ~334 ± 62 KJ mol^{-1}

D_0 for Si = ~1.088 x 10^{10} cm^2s^{-1}
D_0 for Ni = ~5.935 x 10^4 cm^2s^{-1}

The boundary conditions for the solution to the finite model are that the composition of Ni and Si outside the FeCrAl foils is zero, and that Ni and Si are not involved in any process by which they may be consumed and removed from the diffusion couple (e.g. oxidation).

Diffusion coefficients D_{Ni} and D_{Si} were obtained from the graph below. This graph was presented in the final review of the European funded SMILER Project where diffusion tests on a variety of brazed joints were performed [176]. These values are experimentally determined diffusion coefficients from a BNi-5 brazed sandwich structure using a similar FeCrAl alloy (Aluchrom YHf). Values of D_0(Ni), D_0(Si), ΔH_a(Ni), and ΔH_a(Si) were subsequently determined from this work.

The activation energy for the diffusion of Si is found to be larger than that of Ni. The activation energy for nickel diffusion is found to be comparable with the work presented in literature regarding the diffusion of nickel-rich braze filler metals [177]. The calculated activation energy for Si is comparable with activation energies presented in the literature for the diffusion of Si through Fe [178].

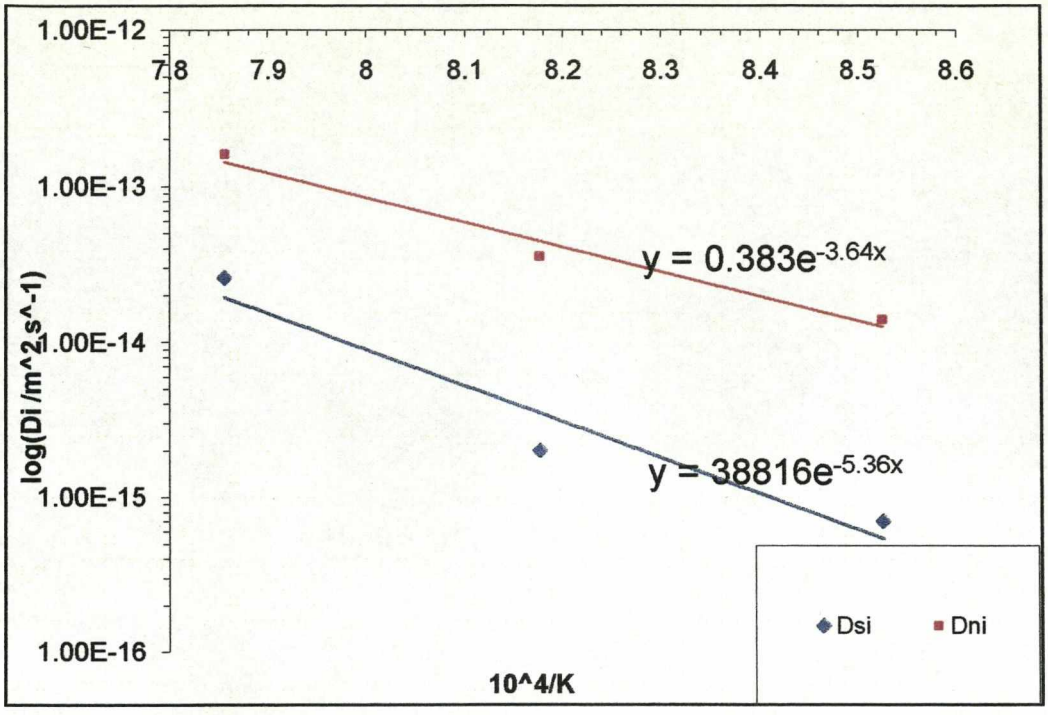

Figure Appendix 4: Graph used for establishing diffusion coefficients for Ni and Si. This figure presents experimentally calculated diffusion coefficient data over a range of temperatures